



UNICA

UNIVERSITÀ
DEGLI STUDI
DI CAGLIARI

Ph.D. DEGREE IN

Earth and Environmental Sciences and Technologies

Cycle XXXV

TITLE OF THE Ph.D. THESIS

Characterization of the CRM occurrences in ore deposits Of Sardinia

Scientific Disciplinary Sectors

Ore Geology GEO/09 – GEO/06

| | |
|----------------|------------------------------|
| Ph.D. Student: | Matteo Luca Deidda |
| Supervisor | Giovanni Battista De Giudici |
| Co-Supervisor | Stefano Naitza |

Final exam. Academic Year 2020/2021

Thesis defence: April 2023 Session

Table of content

| | |
|--------------|----|
| Introduction | VI |
|--------------|----|

Chapter I

| | |
|--|----------|
| Passive Structural Control on Skarn Mineralization Localization: A Case Study from the Variscan Rosas Shear Zone (SW Sardinia, Italy) | 8 |
|--|----------|

Published 21 February 2022 by Minerals - MDPI

| | |
|---|----|
| Abstract | 9 |
| Introduction | 9 |
| Geological Background | 10 |
| Stratigraphic Setting | 11 |
| Structural Setting | 12 |
| Ore deposits of the Sulcis Area | 13 |
| Material and Methods | 14 |
| The Rosas Shear Zone and Related Skarn Ores | 15 |
| Structure of the Rosas Shear Zone | 15 |
| Field Relationships of the Orebodies | 17 |
| Barisonis | 17 |
| Mitza Sermentus | 18 |
| S'Ega Su Forru | 19 |
| Ore Microscopy and SEM-EDS Analyses | 20 |
| Barisonis | 20 |
| Mitza Sermentus | 22 |
| S'Ega Su Forru | 24 |
| Discussion | 25 |
| Conclusions | 29 |
| References | 29 |

Chapter II

| | |
|---|-----------|
| Mineralogy of the scheelite-bearing ores of Monte Tamara, SW Sardinia: insights for the evolution of a Late Variscan W–Sn skarn system | 33 |
|---|-----------|

Published 21 November 2022 by Mineralogical Magazine - Cambridge University Press

| | |
|---|----|
| Abstract | 34 |
| Introduction | 34 |
| Geological setting | 35 |
| The San Pietro and Sinibidraxiu orebodies | 36 |
| Materials and methods | 36 |
| Mineral associations and micro-textures | 40 |
| The San Pietro skarn | 40 |
| The Sinibidraxiu orebody | 42 |
| Mineral compositions | 43 |
| Skarn minerals | 43 |
| Garnet | 43 |
| Clinopyroxene | 43 |

| | |
|--|----|
| Amphibole | 45 |
| Epidote and chlorite | 45 |
| Ore minerals (sulfides and oxides) | 45 |
| Sphalerite | 45 |
| Bi-bearing sulfosalts | 46 |
| Arsenopyrite, pyrrhotite and pyrite | 47 |
| Chalcopyrite | 47 |
| Galena | 47 |
| Stannite | 48 |
| Cassiterite | 48 |
| Scheelite | 48 |
| Discussion | 49 |
| Scheelite trace-element composition | 50 |
| Temperatures of formation | 51 |
| The prograde stage at San Pietro | 51 |
| The hydrothermal/sulfide stage at San Pietro | 52 |
| Mineralisation at Sinibidraxiu | 52 |
| Conclusions | 53 |
| References | 54 |

Chapter III

| | |
|--|----|
| Major and trace elemental composition of magnetite from Sardinia, Italy: implications on the evolution of W-Sn-bearing skarns and on the role of germanium as their marker. | 57 |
|--|----|

To be submitted to Mineralium Deposita - Springer

| | |
|--|----|
| Abstract | 58 |
| Introduction | 58 |
| Geological setting | 59 |
| Skarn ores of Southern Sardinia | 60 |
| Perda Niedda | 60 |
| Monte Tamara | 61 |
| Rosas | 61 |
| Giacurru | 62 |
| Analytical methods | 63 |
| Petrographic and textural features | 64 |
| Perda Niedda | 64 |
| Monte Tamara | 64 |
| Rosas | 66 |
| Giacurru | 66 |
| Results | 67 |
| EPMA | 67 |
| LA-ICP-MS | 67 |
| Discussion | 70 |
| Major and minor elements (EPMA) in magnetite | 70 |
| Trace-elements (LA-ICP-MS) in magnetite | 74 |
| Geochemical twins fractionation in magnetite | 76 |
| Discrimination diagram for W-Sn skarns | 77 |
| Mechanisms of formation | 81 |

| | |
|-------------|----|
| Conclusions | 84 |
| References | 85 |

Appendix I

| | |
|---|----|
| Spatial and Metallogenic Relationships between Different Hydrothermal Vein Systems in the Southern Arburèse District (SW Sardinia) | 91 |
|---|----|

Published 25 February 2021 by Environmental Science Proceedings - MDPI

| | |
|--------------------------------|-----|
| Abstract | 91 |
| Introduction | 89 |
| Materials and Methods | 95 |
| Results | 95 |
| Field Relationships | 95 |
| The Five-Element Vein-Type Ore | 96 |
| The Wolframite Ore | 97 |
| Discussion and Conclusions | 96 |
| References | 100 |

Appendix II

| | |
|--|-----|
| Bi-minerals occurrence in various ore deposits of Southern Sardinia: a short review | 102 |
|--|-----|

Published 19 April 2022, presented at EGU General Assembly 2022

| | |
|----------|-----|
| Abstract | 103 |
| Slides | 105 |

Appendix III

| | |
|---|-----|
| Towards the definition of a Sn-W-Mo late Variscan skarn-system in Southwestern Sardinia: evidence from key-areas in the Sulcis-Iglesiente district | 120 |
|---|-----|

Submitted 4 May 2022, presented at SGI-SIMP, Geoscience for a Sustainable Future, Torino, 19-21 September 2022

| | |
|----------|-----|
| Abstract | 121 |
| Slides | 122 |

| | |
|--------------------|------|
| Conclusions | CLIV |
|--------------------|------|

| | |
|-------------------------|-----|
| Acknowledgements | CLV |
|-------------------------|-----|

Introduction

This thesis is entitled “Characterization of the CRM occurrences in ore deposits of Sardinia” and its aim is to further study the geological occurrence of economic raw materials in various mineral deposits of southern and central Sardinia, with a focus on a specific class of deposit named “skarns”. In the last decades concerns have increased about the supply for specific elements and minerals, essential to high-end industrial applications and for the green-technologies transition. Starting from 2017, and updated to 2020, the European Commission defined a list of elements, namely the Critical Raw Materials (CRM) by means of two factors: economic importance and supply risk. This list includes, among others, elements such as Rare Earth Elements (REE) and lithium (Li) but also indium (In), germanium (Ge), tungsten (W), molybdenum (Mo), bismuth (Bi), niobium (Nb), tantalum (Ta), nickel (Ni) and cobalt (Co) whose supply in Europe is almost totally dependent on the import from non-EU nations, most notably China (accounting for the 69% and 93% of global W and Bi production respectively). Other elements, most notably Sn, are likely to be inducted to the CRM list in the next years. These elements usually occur in small concentrations in the crust and in most orebodies are generally subordinated to base metals like iron (Fe), lead (Pb), zinc (Zn) and copper (Cu). As a reflection of the contextualized economic demand and technologies of the past, most mining activities were mostly oriented towards the exploitation of base metals ores, usually overlooking the minor and trace concentrations of metals that are now considered critical. A re-evaluation of the CRM occurrences in old mining districts and mine wastes of Europe currently represents one of the most promising frontiers in mineral exploration and may assume a key role in reducing the supply risk.

In the framework of the re-evaluation of CRM occurrences in mine districts of the past, Sardinia, which was one of the most important mining district of Italy, is a very interesting study area due to its abundant resources, extensively mined during the 18th and 19th century, especially for Zn-Pb-Cu-Fe. The most significant mining districts were in Southern Sardinia and included the Iglesias-Sulcis and Montevecchio (Arburèse region) mines, hosting several giant Mississippi Valley Type (MVT) deposits and their associated non-sulfide ores and a 15 km long hydrothermal Zn-Pb vein system respectively. Aside from Zn-Pb MVT deposits, southern Sardinia is also characterized by several Au-As(-Sb-W), Ag-Sb, F-Ba-Pb and epithermal Cu-Au-Ag vein deposits. A further class of ore deposits is represented by Late Variscan granite-related deposits such as greisen and hydrothermal

veins, locally exploited for their molybdenite, cassiterite, wolframite and arsenopyrite mineralization and skarn deposits.

Indeed, skarns are probably the most recurrent type of ore deposits in SW Sardinia (Sulcis district), and to a lesser extent in SE and central Sardinia (Sarrabus-Gerrei; Barbagia). They typically hosted high-grade Zn-Pb-Cu-Fe mineralization, for which were historically explored and exploited. In the last years, the revitalised interest for CRM in Sardinia lead to a clearer definition of the metallogenic potential of some variscan granitic intrusion, especially for elements like Sn, Mo and W (Naitza et al., 2017).

Therefore, this project was conceived to gain further knowledge on the geological relationships, mineralogy, chemical composition and mechanisms of formation of skarn deposits of southern and central Sardinia, and to investigate their W-, Sn-, Mo-, Bi-, In- and Ge-bearing potential. Sampling and analyses have been done at the University of Cagliari in collaboration with the University of Milano, and during the six months spent abroad in Switzerland (University of Geneva, ETH Zürich) and Germany (Karlsruhe Institute of Technology, University of Tübingen). The structure of this thesis includes two published papers and one paper in the process of submission in the next months. The first article, presented in Chapter 1, provides more insights on the field and structural relationships between host rocks and skarn mineralization. The second article, in Chapter 2, is an in-depth mineralogical, petrographical and chemical characterization of two different skarn-related orebodies. The third paper draft, Chapter 3, takes the compositional features of magnetite into account in order to provide some insights on the genesis and classification of skarn deposits. Other selected works on the topic, including an extended abstract about the relationships between W-Bi-Te-Au granite-related hydrothermal veins with other Bi-Ag-Ni-Co-As mineralized systems (five-element veins), and two abstracts and their relative slide presentations, are presented in the Appendix section.

CHAPTER I

Passive Structural Control on Skarn Mineralization Localization: A Case Study from the Variscan Rosas Shear Zone (SW Sardinia, Italy)

Fabrizio Cocco*¹, Antonio Attardi¹, Matteo Luca Deidda¹, Dario Fancello¹,
Antonio Funedda¹ and Stefano Naitza¹

¹Department of Chemical and Geological Sciences, University of Cagliari, 09042, Monserrato (CA), Italy

Submitted 19 January 2022

Accepted 18 February 2022

Published 21 February 2022

Minerals - MDPI

Article

Passive Structural Control on Skarn Mineralization Localization: A Case Study from the Variscan Rosas Shear Zone (SW Sardinia, Italy)

Fabrizio Cocco , Antonio Attardi, Matteo Luca Deidda, Dario Fancello, Antonio Funedda  and Stefano Naitza 

Department of Chemical and Geological Sciences, University of Cagliari, Cittadella Universitaria, S.S. 554 Bivio per Sestu, Monserrato, 09042 Cagliari, Italy; antatt94@gmail.com (A.A.); deiddam.geo@gmail.com (M.L.D.); dario.fancello@unica.it (D.F.); afunedda@unica.it (A.F.); snaitza@unica.it (S.N.)

* Correspondence: fabrcocco@unica.it

Abstract: The case study presented here deals with the Pb-Zn-Cu skarn ores hosted in the Rosas Shear Zone (RSZ), a highly strained domain located in the external zone of the Sardinian Variscan chain. The RSZ is characterized by several tectonic slices of Cambrian limestones within a strongly folded and foliated Cambrian-Ordovician siliciclastic succession, intruded by late Variscan granites and mafic dykes. Based on geological mapping, structural and microscope analyses, our results show that the skarn ores in the RSZ are an example of passive structurally controlled mineralization. The RSZ was structured close to the brittle–ductile transition and, once exhumed to shallower crustal levels, acted as plumbing system favoring a large-scale granite-related fluid circulation. The paragenesis and the mineralization style of the skarn vary slightly according to the peculiarity of the local structural setting: a tectonic slice adjacent to the mafic dyke; an intensely sheared zone or a discrete thrust surface.

Keywords: tectonic slices; mineralization; polydeformed basement; fluid circulation; brittle–ductile transition; mafic intrusion; thermal metamorphism; exhumation; metasomatism



Citation: Cocco, F.; Attardi, A.; Deidda, M.L.; Fancello, D.; Funedda, A.; Naitza, S. Passive Structural Control on Skarn Mineralization Localization: A Case Study from the Variscan Rosas Shear Zone (SW Sardinia, Italy). *Minerals* **2022**, *12*, 272. <https://doi.org/10.3390/min12020272>

Academic Editors: Huan Li and Han Zheng

Received: 19 January 2022

Accepted: 18 February 2022

Published: 21 February 2022

Publisher's Note: MDPI stays neutral with regard to jurisdictional claims in published maps and institutional affiliations.



Copyright: © 2022 by the authors. Licensee MDPI, Basel, Switzerland. This article is an open access article distributed under the terms and conditions of the Creative Commons Attribution (CC BY) license (<https://creativecommons.org/licenses/by/4.0/>).

1. Introduction

A proper identification, quantification and exploitation of ore deposits cannot be separated from a full comprehension of the structural control of the mineralization processes. This is particularly relevant for ores hosted in polydeformed basements, where the complexity of the structural setting is emphasized by the superposition of several deformation phases. Structural controls are critical in the genesis of hydrothermal ore deposits [1]. They define the pattern, extension, and modalities of the fluid flow in crustal sectors affected by mineralizing phenomena [2–4], not only determining the emplacement mode and the geometric–dimensional aspects of the deposits, but also influencing the type of fluid–rock interactions and the chemical mechanisms that determine the compositional characters of the ores [5,6]. The tectonic regime in which the mineralizing phenomena occur determines the prevalence of (1) passive controls, in which a frequently multi-scale network of pre-existing structural discontinuities in the host rocks forms a pre-established plumbing system for circulation and entrapment of hydrothermal fluids [7,8], or (2) active controls, in which deformation of rocks and development of the structural pattern is synchronous with the emplacement of mineralized deposits and is influenced by them [8–14]. In the framework of complex structures such as polyphasic shear zones, the two control modalities can repeatedly occur in several moments, but they are frequently related to dominantly extensional regimes [7]. This view assumes a particular declination in the case of districts characterized by skarn metasomatic deposits, in which (1) magma inflow and fluid circulations are favored by opening of pathways in large scale shear zones; (2) shear zone

structural set-up through tectonic slicing and cataclastic/mylonitic zones development results in a definite control on the spatial distribution and extension of reactive lithologies (e.g., carbonate rocks), susceptible to metasomatic phenomena and ore mineralization [15].

This study is focused on the Rosas Shear zone (RSZ), in the Sulcis subregion of SW Sardinia, which is considered as a key area in the definition of deformation styles at the crustal brittle–ductile transition in the south Variscan Sardinian chain [16], but it is also relevant for ore deposits studies, as home to a historical district (Rosas mine district) marked by widespread Pb-Zn-Cu mineralized skarns. Skarn ores are located along a complex pattern of tectonic slices and brittle structures enclosed in the RSZ and related to early Permian mafic and felsic magmatic pulses associated with the emplacement of the Sulcis pluton [17]. In this study, new structural field surveys and new studies on the ore deposits were performed to investigate the relationships between the geometry and evolution of the RSZ and late Variscan magmatic and metallogenic events, highlighting the role of structural passive control in the localization of the ore deposits in the Rosas district.

2. Geological Background

The segment of the south European Variscan chain exposed in Sardinia arose from the early Carboniferous continental collision and consists of three main tectono-metamorphic zones [18] (Figure 1a): an External zone in southwestern Sardinia, a Nappe zone in south-eastern and central Sardinia, and an Axial zone in northern Sardinia. During the Variscan collision, a Barrovian-type metamorphism developed increasing northward from very low grade in the External zone, to greenschist facies in the Nappe zone, to high grade in the Axial zone ([19], and references therein). The nappes were stacked with a top-to-the-south transport direction with the exception of the uppermost tectonic unit that was thrust over the External zone with a top-to-the-west transport direction [20,21]. During the late Carboniferous-Permian, the Variscan chain was involved in the post-collisional extension, and the Sardinian basement was affected by low- and high-angle normal faults [22]. At the same time, the emplacement of the Variscan granitoids occurred, leading to HT-LP metamorphism development [23,24].

The RSZ (Figure 1b,c) is part of the External zone located at the footwall of the Arburese thrust, the regional structure that separates the Variscan External zone from the Variscan Nappe zone [25] (Figure 1b).

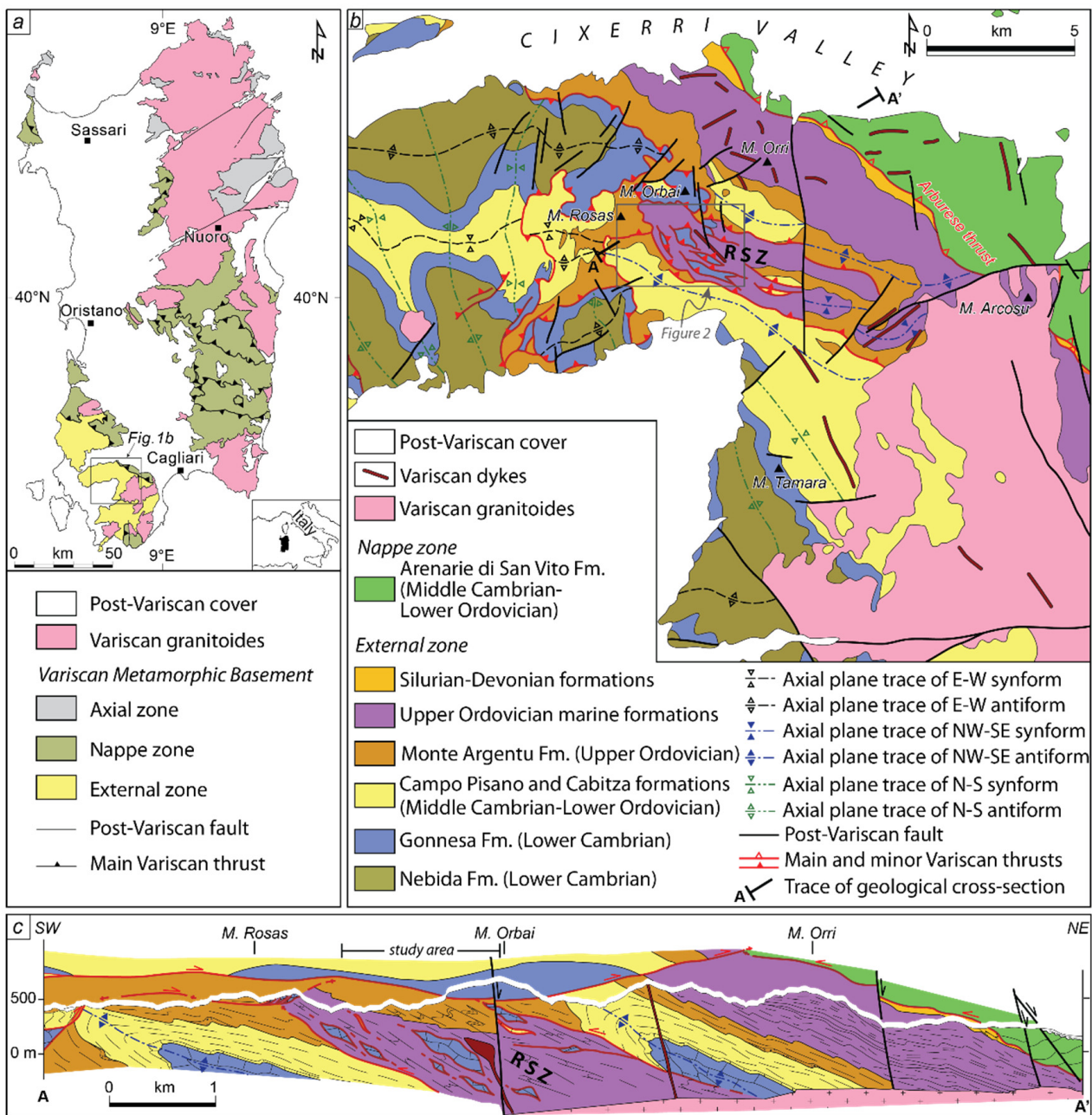


Figure 1. (a) Tectonic sketch map of the Variscan basement of Sardinia (after [26]); (b) geological sketch map of the central sector of the external zone. Location in Figure 1a. RSZ: Rosas Shear Zone. The grey box shows the location of Figure 2. (c) Geological cross-section across the Rosas Shear Zone (after [25]).

2.1. Stratigraphic Setting

The stratigraphic succession of the External zone is subdivided into two mega-sequences separated by a regional angular unconformity (Sardic Unconformity; [27]) ascribed to the Sardic Phase [28], a tectonic event related to the geodynamic processes affecting the northwestern Gondwana margin in Ordovician times [29–32].

The pre-Sardic sequence spans in age from lower Cambrian to lower Ordovician and consists of the following formations [33]: the Nebida Fm. (lower Cambrian), a 500 m thick siliciclastic succession characterized by alternating layers of sandstones and siltstones and by the occurrence of a continuous oolite level and episodic limestone intercalations; the Gonnesa Fm. (lower Cambrian), an up to 500 m thick carbonate succession mainly

made up of well-stratified dolostones and massive limestones [34]; the Campo Pisano Fm. (middle Cambrian), a 20–50 m thick succession of alternating claystones and marly limestones [35]; the Cabitza Fm. (middle Cambrian-lower Ordovician), a 400 m thick siliciclastic succession characterized by alternating layers of claystones, siltstones and fine-grained sandstones [36].

The post-Sardic sequence starts with the Monte Argentu Fm. (upper Ordovician), a siliciclastic succession highly variable in thickness, from few tens to hundreds of meters, characterized at the base by olistoliths, megabreccias and conglomerates followed up section by marine sandstones and siltstones [37]. The marine depositional environment persisted throughout the whole upper Ordovician, during which a sedimentary succession 600 m thick was deposited (Monte Orri Fm., Portixeddu Fm., Domusnovas Fm. and Rio San Marco Fm.; [38]). Finally, the younger formations involved in the Variscan deformation are the Genna Muxerru, Fluminimaggiore, and Mason Porcus fms (Silurian-Devonian in age), mainly characterized by black-shales and limestones [39], and the Pala Manna Fm. (lower Carboniferous) characterized by clastic deposits [40].

The lower Cambrian-lower Carboniferous succession was intruded during lower Permian by numerous granitoid bodies and associated mafic and felsic dikes forming the Sulcis pluton [17] that crops out few kilometers to the SE of the RSZ (Figure 1b) and most likely occurs at shallow depth beneath the Rosas mine district (Figure 1c). In southern Sardinia, the intrusion of mafic dykes is a process that lasted for a long time span, more than 10 Ma, so dykes may pre-date, be coeval or post-date the granite body intrusion [17,41]. The outermost part of the Pluton in Northern Sulcis consists of F-bearing, ferroan ilmenite-series, subaluminous I-type granites (“GS1 suite”, [17]), dated at 289 ± 1 Ma by Re-Os on molybdenite [42]. Siderophyllitic dark mica (the only mafic mineral) and ilmenite, xenotime-Y and fluorite accessory minerals are distinctive of the GS1 granites, which also keep a significant metallogenic potential, being related to many W-Sn-Mo hydrothermal deposits in southern Sardinia [43,44].

2.2. Structural Setting

The Variscan External zone suffered three main shortening events that gave rise to a fold-and-thrust belt with a complex structural setting characterized by superposed folds, fore-thrusts and back-thrusts [45–47].

The lower Cambrian-lower Ordovician sedimentary succession was affected by a compressional event related to the Sardic Phase during which E-trending folds originated according to a N-S shortening direction. The Sardic folds have a kilometric wavelength, upright axial surface without any related tectonic foliation, and close tightness, as testified by the limbs cut by the Sardic unconformity with an angle approaching 90° . An important erosion affected the folded succession so that in several areas, the upper Ordovician sedimentary deposits lie just above the lower Cambrian sandstones and limestones of the Nebida and Gonnese fms. This mainly happens in the crest of the Sardic antiforms, whereas in the hinge zone of the synforms, the lower Ordovician siliciclastic succession of the Cabitza Fm. is usually preserved [48,49].

In Carboniferous time, the entire lower Cambrian-lower Carboniferous stratigraphic succession was involved in the deformation related to the Variscan Orogeny. During the first Variscan Phase, the N-S shortening direction caused E-trending open folds that gently deformed the post-Sardic Unconformity succession and that superposed in parallel on the Sardic folds. During the second Variscan Phase, the shortening direction progressively rotated from NE–SW to E–W, originating in sequence SW-facing overturned folds and the RSZ with a top-to-the-SW transport direction, W-facing folds with a well-developed axial plane foliation, W-verging fore-thrusts and, finally, E-verging back-thrusts and E-facing back-folds [25]. The superimposition of ductile and brittle structures related to different shortening directions results in a very complex stratigraphic structural setting in which the strain partitioning separates domains of very high strain intensity from others where

the intensity of the deformation is so low that the primary characteristics of the rocks, as bedding and sedimentary structures, are fully preserved.

The RSZ is a highly strained domain consisting of a 1 km thick shear zone located few kilometers westward of the leading edge of the Nappe front. It dips toward NE and lies beneath and subparallel to the Arburese thrust. The RSZ is bounded by two thrusts that developed along the limbs of two km-scale overturned antiforms that affect the lower Cambrian-upper Ordovician succession showing a SW-facing direction [25] (Figure 1b,c). A detailed description of the complex internal structure of the RSZ and the deformation processes along with its relationships with the ore mineralization will be provided in the next paragraphs.

3. Ore Deposits of the Sulcis Area

The SW of Sardinia has been one of the most important Zn-Pb-Ag mining districts of Europe with a peak of activity during the 19th century. The northern side of the district, the Iglesias area, hosts several giant and high-grade MVT and SEDEX Zn-Pb-Fe deposits such as those exploited in the old mines of Monteponi, San Giovanni, Masua, Nebida, Monte Agruxiau, San Benedetto, Campo Pisano, Genna Luas. These deposits consist of stratabound and discordant orebodies with variable proportions of Cd-rich sphalerite, Ag-rich galena and pyrite which formed in the carbonate platform, represented by the Gonnese Formation, during Cambrian extensional tectonics [47,50]. Conversely, in the Sulcis area, the southern side of the district, skarn deposits are a frequent typology. They are genetically and spatially related with the emplacement of the GS1 suite granites and to the strong hydrothermal activity generated from intrusive bodies, which produced the aforementioned W-Sn-Mo (\pm Fe-Pb-Zn-Cu-As-F-Bi) distinctive metallogenic association. Accordingly, the mineral expression of this geochemical footprint in skarns of SW Sardinia is represented by massive magnetite-fluorite and Cu-Zn-As-Fe-Pb sulfide orebodies with, most importantly, variable concentrations of cassiterite, scheelite, Bi-Pb-Ag-sulfosalts, stannite and molybdenite. Some of these indicative minerals have been reported in various localities of SW Sardinia [44]: most notably, the occurrence of scheelite have been reported in samples from the Sa Marchesa and Monte Tamara mining areas of Sulcis [51–53], 2–10 km south from the Rosas mine area. These skarn orebodies are small in size but numerous and recurrently located along tectonic contacts, thrusts and fractures both in the carbonate rocks (Gonnese and Campo Pisano fms.) and at the contacts between carbonate and siliciclastic rocks (Nebida Fm. at the base and of Cabitza Fm. at the top). In many cases, as in the Monte Tamara area, faults appear to have provided a permeability pattern that favored the extent of hydrothermal fluids circulation in rocks and a broader development of metasomatic processes. Therefore, size and geometry of skarn orebodies, their mineral zonation and their extension at depth are controlled by these structures. These assumptions could also be extended to the more intensely deformed structural setting of the Rosas mine area (Figure 2).

The Rosas mine, active from the 19th century to the 1980s, was one of the most important of Sulcis region and comprised numerous mine workings throughout an area of roughly 6 km². Among the different mineralized bodies occurring in this area, several skarn ores were exploited extensively for their Zn-Pb sulfide contents in the mine workings of Barisonis, Mitza Sermentus, S'Ega Fogus, S'Ega Su Forru, Truba Niedda (Figure 2). Bechstadt and Boni (1994) [34] proposed an Ordovician age for the whole stratigraphic sequence, including the limestones. In more recent studies, various authors [16,25,54] interpreted the limestones as belonging to deformed portions of the lower Cambrian Gonnese Fm. enclosed inside the complex pattern of tectonic slices of RSZ, prevalently comprising elements from the upper Ordovician sequence. Indeed, the arrangement of metasomatized limestones along the NW–SE alignment of the main RSZ structure suggests a more effective structural control compared to other Sulcis areas where deformations and structural outlines are not as pervasive. Moreover, along the prosecution of the RSZ to the SE in the Campanasissa locality, other skarns are mentioned [55] close to

the contact with the GS1 intrusion. Granitoids do not crop out in the Rosas area, but their occurrence at shallow depth beneath the Rosas mine district is suggested by the widespread granite-related mineralization; Variscan magmatic rocks are represented by a swarm of mafic calc-alkaline dikes that intrude in the basement following the main tectonic lineaments, oriented NW–SE, of the RSZ. The most relevant magmatic body is a large gabbroid dike that crops out in the central part of the area, spatially associated with numerous orebodies (e.g., Barisonis mineworks) (Figure 2). For this reason, a genetic relationship between the gabbro and the skarn ores has been repeatedly inferred in the past when the mine was operating [56], but no clear evidences have been provided yet to verify this hypothesis. Cavinato (1937) [57] excluded these relationships based on considerations on skarn paragenesis and the relatively small volume of basic magmas in the area. Anyhow, the relationships between the developing of the main tectonic structures, the emplacement of the gabbro and the formation of the skarn orebodies have been further detailed in this study, in the three key areas of Barisonis, Mitza Sermentus and S'Ega Su Forru (Figure 2).

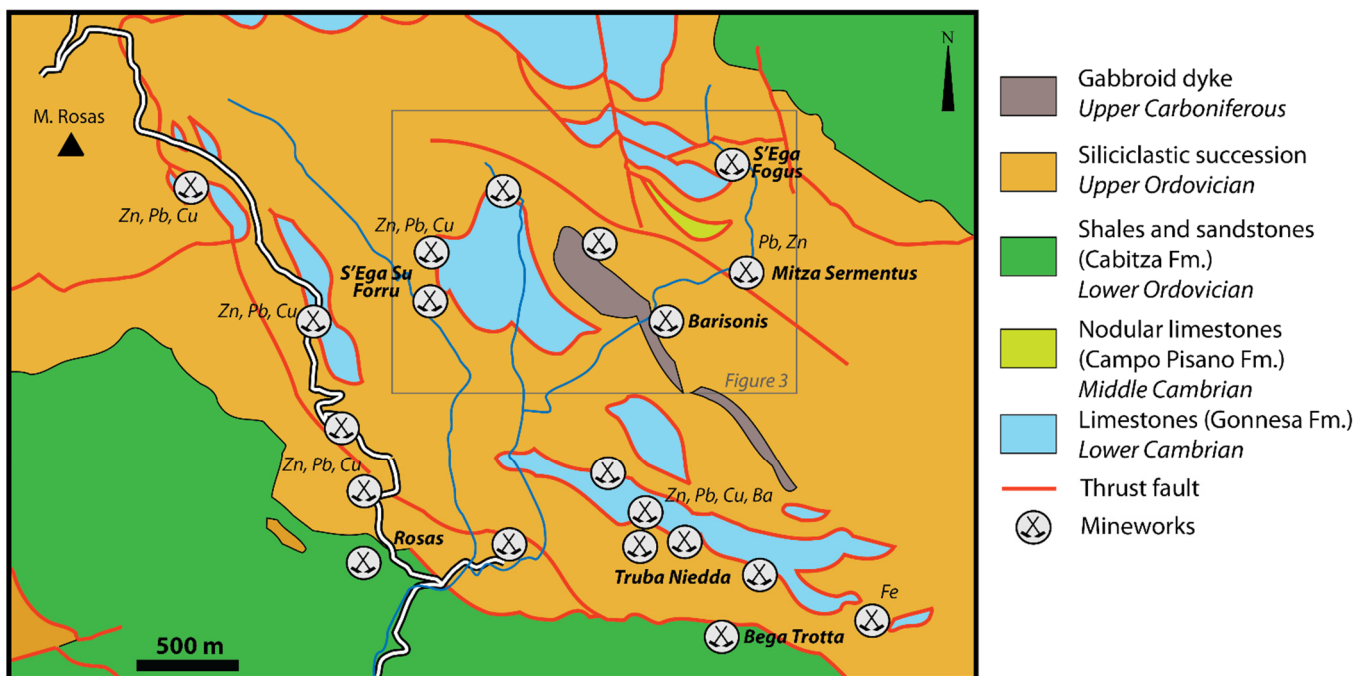


Figure 2. Geological sketch map (after [58]) and main mineworks in the Rosas district (after [54,59], modified). Location in Figure 1. The grey box shows the location of the study area in Figure 3.

4. Material and Methods

In order to infer which relationship exists between tectonic structures, magmatic intrusion and skarn ores, a geological and structural mapping at 1:5000 scale has been performed, starting from the geological map at 1:50,000 scale “Foglio 556 Assemini” [58] carried out by the Italian Geological Survey (ISPRA Carg Project; [54]). The field investigation aimed to further detail the main stratigraphic and tectonic contacts and the structural features, as foliations, folds and kinematic indicators, paying special attention to the areas where the main skarn ores were exploited.

The geological map has been validated by structural contouring, following the procedure proposed by [60]. This procedure allowed us to check the consistency of the detected tectonic contacts and to project properly them in the geological cross-sections, providing a more accurate attitude of the thrusts.

Microstructural and petrographic analyses were carried out on representative samples from the areas of Barisonis, Mitza Sermentus and S'Ega Su Forru. Thin and polished sections were firstly observed at the Department of Chemical and Geological Sciences of

Cagliari, University of Cagliari, Monserrato, Italy, under transmitted and reflected light in Optical Microscopy (OM) with a JenaLab polarizing microscope; then, SEM-EDS analyses were performed on selected samples at CESAR laboratories of Università di Cagliari, using a Quanta Fei 200 unit equipped with a ThermoFischer Ultradry EDS detector operating under both low- and high-vacuum conditions, 25–30 KeV voltage and variable spot size.

5. The Rosas Shear Zone and Related Skarn Ores

5.1. Structure of the Rosas Shear Zone

The core of the RSZ, where the large part of the addressed skarn ores are located, shows a complex internal structure characterized by several anastomosing thrusts that bound map-scale tectonic slices derived from the Gonnese, Campo Pisano, Cabitza and Rio San Marco fms. (Figure 3). Because of the intensity of the deformation, the lithostratigraphic attribution of the siliciclastic succession that wraps these tectonic slices is often difficult. However, interpreting the primary features preserved in less strained domains, the upper Ordovician Monte Orri and Monte Argentu fms have been recognized. This characterization also contributes to better define the structure of the RSZ, given information on the deformation style.

The Monte Argentu Fm. crops out in the northern sector of the study area and consists of alternating layers of conglomerates, sandstones and siltstones, where diagenetic nodules characterized by a maximum diameter of 1 cm and an elongate cigar shape occur. The Monte Orri Fm. crops out extensively in the southern sector of the study area and is mainly made up of alternating sandstones and siltstones. The stratigraphic polarity is frequently reversed because of the thrusting and also of the occurrence of large overturned folds (Figure 1c). The main feature at the outcrop scale in the siliciclastic formations is a penetrative NE-dipping cleavage along which the original bedding is transposed, although in some cases it is still possible to recognize the bedding attitude by means of chromatic and grain size variations. In this last case, isoclinal folds with NW-striking axis and NE-dipping axial plane can be identified. At micro-scale, the tectonic foliation varies from disjunctive to slaty cleavage, depending on grain size. In the higher strained zones, mm-size quartz porphyroclasts show asymmetrical sigma shapes consistent with a top-to-the-SW transport direction.

Among the others, the tectonic slices belonging to the Gonnese Fm. are the most relevant for this study because they host the skarn ores. These slices are embedded in both the Monte Argentu and Monte Orri fms and are mainly made up of gray to black massive limestones. The thrusts that bound the slices dip towards N–NE, with the top thrust generally steeper than the bottom thrust (Figure 3). The size of the slices is highly variable, ranging in length from 1 to 100 m and reaching the maximum thickness of 100 m. For instance, in the Barisonis and Mitza Sermentus mines the limestone slices are very small, only few meters thick, whereas the skarn in the S'Ega Su Forru mine is hosted in a slice more than 150 m thick (Figure 3). Contact metamorphism and sulfide disseminations on the limestones are evident in the proximity of the tectonic contacts in many cases accompanied by 1-m-thick quartz veins in the terrigenous formations. At the micro-scale, calcite shows grain size reduction and a dynamic recrystallization, leading to fine-grained calc-mylonites where asymmetric grains oblique to the main foliation reveals a top-to-the-SW sense of shear that is the same inferred from the kinematic indicators detected in the siliciclastic formations.

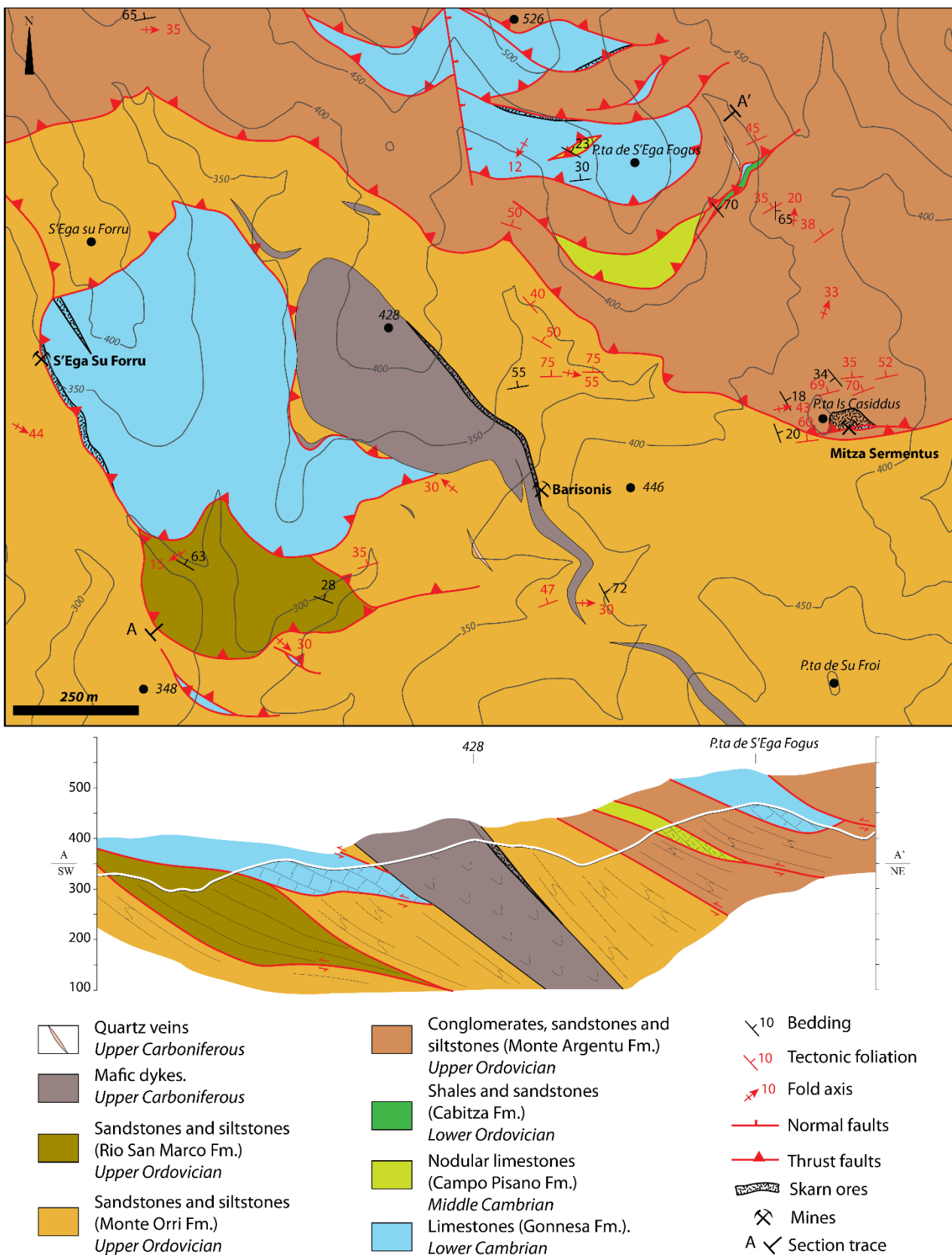


Figure 3. Geological map of the Rosas Shear Zone and geological cross-section. Location in Figure 2. Note that the limestone slices in the Barisonis and Mitza Sermentus mines are very small and have not been drawn at the scale of this map.

The occurrence of tectonic slices derived from lower Cambrian to upper Ordovician formations provides evidence of a widespread tectonic shearing and a very high displacements accommodated by slip along the foliation surfaces. As suggested by Casini et al. (2010) [16], the active behavior of the tectonic foliation is facilitated by the occurrence of detrital muscovite that, once passively rotated towards the cleavage plane, acted as microstructural lubricant favoring the sliding along each foliation plane, avoiding internal grain deformation. The main deformation mechanisms active in the RSZ include pressure solution, grain boundary sliding, deformation lamellae and mechanical twinning [16,25], suggesting that the RSZ structured near the crustal brittle–ductile transition, under sub-greenschist facies, in a depth range of 11.5–13.5 km and a temperature range of 250–300 °C [16,25]. The microstructures associated to the main foliation suggest that it must be considered as an active foliation along which part of the dislocation of the shear zone took place. A post-tectonic annealing, possibly related to the magmatic intrusion described in the follow, is reported.

The RSZ has been affected in late Carboniferous-Permian times by a gabbroid intrusion that consists of a main large mafic dike with a thickness of about 100 m and several smaller veins of metric thickness. The dike dips northeastward, subparallel to the main tectonic contacts, reaches its maximum width near Punta Atzori and thins towards SE. The top and bottom contact of the dike dip 60° and 40°, respectively, leading to a progressively thinning of the dike with depth. The whole gabbroid mass is crossed by cooling joints that dip of about 60° towards SW, perpendicular to the dike attitude. At the outcrop scale it shows a doleritic structure, dark green to dark gray in color, characterized by sub-millimetric amphibole (hornblende) and chlorite crystals. In thin section plagioclase (andesine), pyroxene (augite), hornblende, epidote, chlorite, calcite and muscovite are recognizable, arranged in ophitic texture that suggests a hypabyssal origin for the intrusion. Several minor mafic dikes, parallel to the gabbroid dyke, crop out discontinuously within the siliciclastic host rocks. The intrusion process seems to have been favored by the occurrence of the cleavage that has been exploited as surfaces of weakness by the dike swarm, although in some cases the tectonic foliation is cut across. This unequivocally demonstrates that the dyke intrusion post-dates the RSZ structuring.

5.2. Field Relationships of the Orebodies

In the following, we describe the field relationships of the orebodies in some of the most relevant mine works located in the study area, namely Barisonis, Mitza Sermentus and S'Ega su Forru (Figure 3).

5.2.1. Barisonis

The Barisonis mine site consists of a 10-m-wide stope with short galleries and dumps. The orebody is hosted in a metasomatized lens-shaped carbonate slice of the Gonnese Fm., embedded in the upper Ordovician siltstones of Monte Orri Fm. (Figure 4). On the main stope, the skarn measures 10 m in thickness and closes abruptly to the S. Although the presence of a steep dump limits its exposure at the N of the adit, the slice seemingly reduces in width and closes shortly thereafter. On the E contact, a 5–7 m thick gabbro dyke crops out between the skarn and the Monte Orri Fm. rocks. The skarn is dark green and with a visible zoning pattern represented by garnet, clinopyroxene and wollastonite bands parallel to the contacts with the gabbro and the siltstones (Figure 4). The garnet bands are mostly located at the edges of the skarn close to the host rocks. Clinopyroxene became prevalent on the garnet in a more internal zone, while wollastonite is more abundant in the inner part of the skarn. In terms of relative abundances, clinopyroxene appears as the main calc-silicate throughout the outcrop, locally forming decametric-size bands of dark green idiomorphic elongated crystals up to 5 cm in length. In the inner zones of the skarn, where calcite and quartz veins also appear, chlorite and amphibole broadly form at the expense of clinopyroxene bands. The sulfide ore hosted in the skarn consists of abundant sphalerite, chalcopyrite, galena and pyrite mostly concentrated in the upper garnet-clinopyroxene

bands. Secondary Cu-sulfides (covellite, bornite) pockets can be observed towards the inner wollastonite zone closer to the gabbro contact.



Figure 4. Lens-shaped skarn at the Barisonis mine embedded within the siliciclastic Monte Orri Fm. (MRI) and the gabbro dyke. The mineral zoning pattern is also shown.

5.2.2. Mitza Sermentus

The Mitza Sermentus old Zn-Pb mine is located on the Is Casiddu high, about 0.7 km east from Barisonis (Figure 3). It consists of a 130 m wide open pit and a 60–70 m deep system of underground levels. The main sulfide mineralization is hosted in irregular lens-shaped metasomatized carbonate slices embedded in dark shales belonging to the Monte Argentu Fm. (Figure 5). The slices display an E–W to ESE–WNW direction dipping 30–35° to the NNE. The orebodies size, extent of metasomatism and grade of mineralization increase from the top to the bottom of the pit. Small (up to 1.5 m) and barren to strongly oxidized shreds of calc-silicate hornfels prevail at the top of the sequence. Conversely, a higher grade 10 m thick massive skarn orebody is located at the bottom of the pit. The skarn features a light green color and a banded structure made of fine-grained wollastonite-clinopyroxene, epidote and chlorite. At the outcrop scale, a distinct zoning pattern is difficult to identify. Garnet occurs with small magnetite bands at the immediate contact with the shales in the upper part of the pit. Conversely, in the lower part of the pit, garnet and clinopyroxene are apparently subordinate with respect to wollastonite, and retrograde phases like epidote and chlorite are very abundant. The foremost ore minerals are here represented by chalcopyrite, sphalerite and galena with subordinate pyrite. They generally form cross-cutting veinlets, massive aggregates and disseminations in the calc-silicate gangue. The contact between the skarn and the siliciclastic formation is marked by a band of dark shales bleached and affected by intense hydrothermal alteration. Thus, a swarm of thin veinlets of chalcopyrite-sphalerite infill in the phyllites rock foliation. The veinlets are cm-scale and are often accompanied by a more competent white-greenish matrix. In the upper zone, small centimetric to decimetric arsenopyrite-pyrite lenses are emplaced along the shale foliation planes. Skarn veins also involve the mafic dikes intruding the dark shales, producing a further type of metasomatized and sulfide-mineralized rock.



Figure 5. Lens-shaped skarn lenses at the Mitza Sermentus mine embedded in the shales of the Monte Argentu Fm; red dashed line: Variscan thrust with tectonic transport direction the-top-to-the-SW (view from SW).

5.2.3. S'Ega Su Forru

The S'Ega Su Forru old mining site is located roughly 1 km NW from Barisonis (Figure 3). In this locality, a series of small and today often inaccessible galleries are widespread along a large slice of partly metasomatized Cambrian limestones embedded in the upper Ordovician siltstones and sandstones of the Monte Orri Fm. Thermal recrystallization, suggested by the white and greyish-black banded texture, is widespread throughout the limestones. Moreover, traces of thin veinlets and nests of galena-chalcopyrite-pyrite are made particularly evident by the malachite-azurite alteration of chalcopyrite. The skarn orebodies of this locality are remarkably smaller in size compared to those from Barisonis and Mitza Sermentus. In fact, the main orebody consists of a 20 cm NNW–SSE dipping skarn vein ($N330-60^\circ$) formed at the tectonic contact between marbles and siltstones (Figure 6a,b). The skarn vein has a dark greenish-grey color and a fine-grained texture, seemingly dominated by retrograde calc-silicate minerals such as epidote, amphibole and chlorite. Sulfides, among which idiomorphic crystals of pyrite and galena are the most abundant, are disseminated in the gangue. Chalcopyrite is also present, showing a deep green malachite alteration. Moving downward along the same tectonic contact, the marbles are seemingly barren. Moreover, their color changes to a brownish and vuggy, more dolomitic facies.

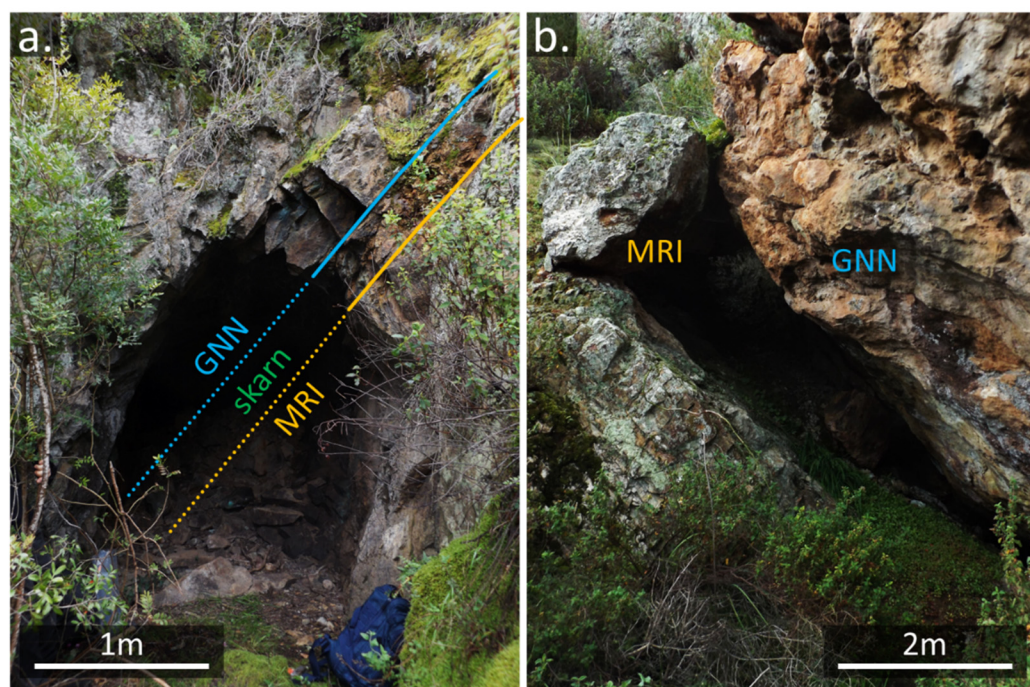


Figure 6. Relationships between the tectonic contact and the skarn mineralization at the S'Ega Su Forru locality. (a) thin skarn band (20 cm) located along the contact between a slice of recrystallized Cambrian limestone of the Gonnese Fm. (GNN) and Ordovician phyllites of the Monte Orri Fm. (MRI); (b) same contact of (a) in a lower stratigraphic position between phyllites and a more magnesian facies of the GNN, where no skarn ore has been detected.

6. Ore Microscopy and SEM-EDS Analyses

6.1. Barisonis

A total of 12 samples from Barisonis have been collected to further detail the mineral zoning of the skarn observed at the outcrop scale. The samples are representative of (a) the outer garnet zone (BS.S2.11; BS.S2.10; BS.S2.11); (b) the clinopyroxene zone (BS.S203); and (c) the inner wollastonite zone (BS.S2.04; BS.S2.05; BS.S2.06; BS.S2.08).

The mineralogy of the samples from Barisonis represents a well-developed calcsilicate assemblage. It is characterized by early wollastonite, clinopyroxene and garnets of the metasomatic, prograde stage followed by a retrograde hydrothermal alteration during which amphiboles, epidotes, chlorite, hematite and calcite were formed.

Garnets along the contacts with the wall rocks, namely the sandstones and the gabbro, form homogeneous bands of anhedral crystals. They are generally isotropic towards the core with birefringent rims (Figure 7a) that become more evident where the hydrothermal alteration is more advanced and retrograde calcsilicates (chlorite and amphiboles) develop at the edges of crystals and between the rims. From EDS analyses, their compositions range from almost pure andradite (Adr_{97}) to grossular-dominant ($\text{Grs}_{72-67}\text{Adr}_{24-27}$) with minor spessartine components (Sps_{1-3}). A transitional oscillatory zoning of alternating Fe-rich and Al-rich garnet is commonly found. Clinopyroxenes essentially belong to the hedenbergite term (14–16 wt.% of Fe and 0–3 wt.% of Mg) with appreciable manganese contents up to 5 wt.%. Amphiboles from the inner zone of the orebody fall in the field of the ferroactinolite-actinolite series (up to 20 wt.% Fe). Their composition is arguably inherited by the hedenbergitic clinopyroxene, more abundant than diopside. In fact, extensive substitution of amphiboles over clinopyroxene crystals is evident. Quartz and calcite are widespread and testify a strong carbonation of calc-silicate phases. Wollastonite, in particular, is completely substituted by needle-shaped quartz and very fine-grained calcite (Figure 7b). Millimeter-scale seams of massive chlorite are also typical of this zone, frequently enveloping sub-millimetric crystals of rutile with titanite reaction rims.

Conversely, rounded and “worm-like” chlorite aggregates with distinct blue birefringence are associated with magnetite and cassiterite veinlets in a quartz-fluorite gangue. Moreover, interstitial spatic calcite and quartz-fluorite veins and pockets occur in the lower-central parts of the outcrop. The mineralizing stages closes with the formation of quartz and calcite, cementing all the previously formed minerals.

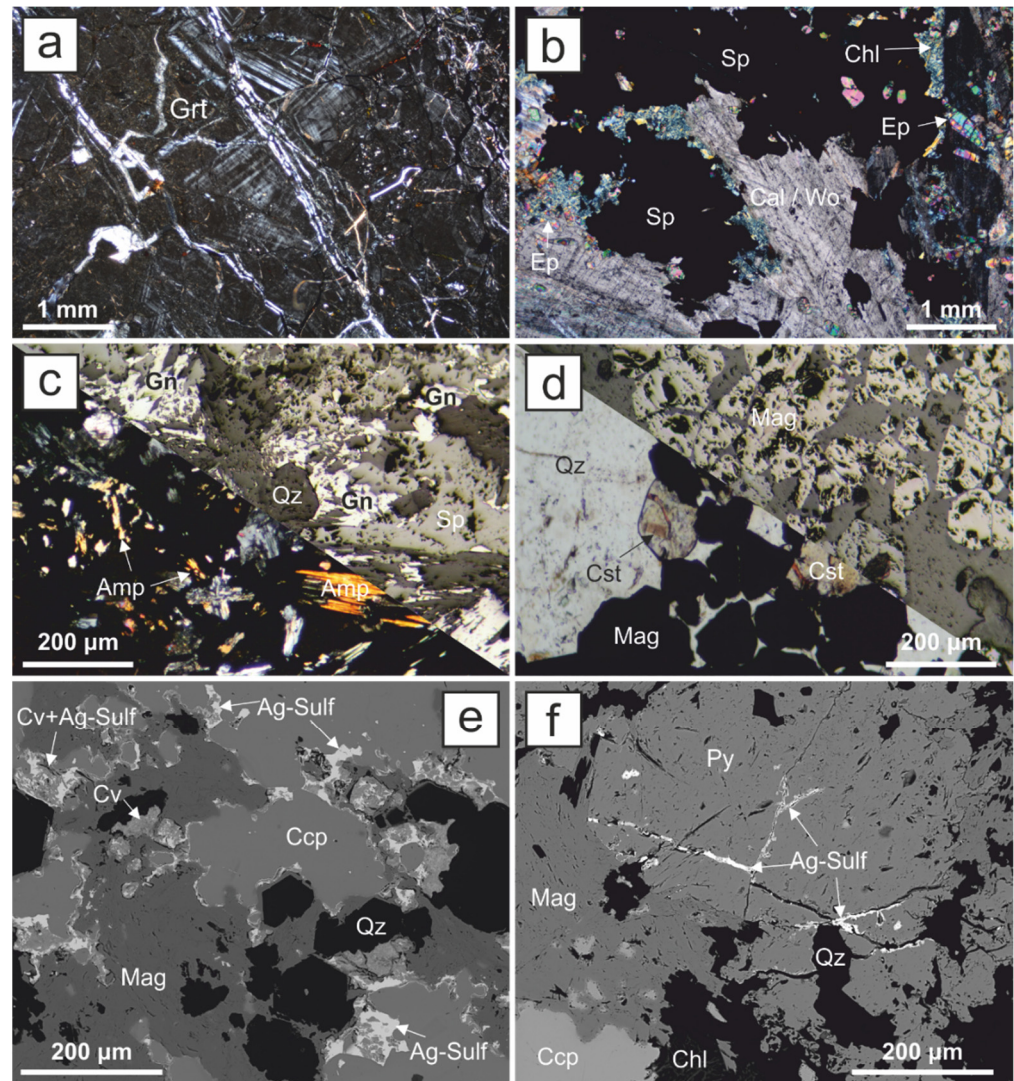


Figure 7. Photomicrographs of the Barisonis orebody. The mineral assemblages include (a) garnets with birefringent rims; (b) epidote, chlorite and calcite pseudomorphs with interstitial sphalerite; (c) interstitial sulfides in the amphibole-quartz matrix; (d) magnetite with subordinate cassiterite in fluorite-quartz veins; (e) chalcopyrite-magnetite zones with thin rims of covellite and Ag-sulfides (acanthite-argentite); (f) Ag-sulfides and covellite veinlets cross-cutting pyrite. Grt = garnet; Amp = amphibole; Wo = wollastonite; Chl = chlorite; Ep = epidote; Qz = quartz; Cal = calcite; Mag = magnetite; Cst = cassiterite; Sp = sphalerite; Ccp = chalcopyrite; Gn = galena; Py = pyrite; Cv = covellite; Ag-Sulf = acanthite-argentite.

The ore minerals of Barisonis are magnetite, cassiterite, bismuthinite, sphalerite, chalcopyrite, bornite, tetrahedrite, pyrite, galena, covellite and argentite-acanthite. Magnetite occurs in parallel seams of sub-millimetric euhedral-to-subhedral crystals in a quartz-fluorite and chlorite assemblage. Moreover, these crystals are often enveloping smaller hematite grains and have a skeletal structure. Hematite and goethite are also commonly found within fractures of garnets. Idiomorphic cassiterite crystals, up to 200 µm in size,

have also been found leaning on the edges of magnetite (Figure 7d). The formation of sulfides clearly postdates the retrograde stage as suggested by their recurrence in the intergranular spaces in chlorite-epidote-calcite and amphiboles aggregates (Figure 7b,c). Where retrograde alteration is not developed, sulfides are deposited in the intergranular spaces between prograde calcsilicates. Based on the abundance of inclusions and Fe contents, two sphalerite types can be distinguished. The first type is characterized by abundant chalcopyrite and pyrrhotite inclusions, a darker color and higher Fe contents (4–7 wt.%). The chalcopyrite-pyrrhotite inclusions are usually smaller along the edges of sphalerite crystals and become larger and more randomly distributed at the core. Conversely, the absence of inclusions, the brownish-red colors and the negligible Fe contents are characteristics of sphalerites of the second type. Chalcopyrite forms abundant anhedral grains and veinlets usually adjacent to sphalerite in the chlorite-titanite matrix and cross-cutting veinlets in garnet. Galena and pyrite are also interstitial to the retrograde skarn assemblage and surrounded by the previous sulfides. In addition, small grains of secondary Cu-sulfides such as bornite, chalcocite and thin veinlets of covellite formed at the expense of chalcopyrite. Secondary Ag-sulfides, which may be attributed to argentite or acanthite (Ag₂S), have been identified in several micrometer-sized anhedral crystallites both disseminated within the Zn-Cu-Pb-Fe sulfides and in the covellite veinlets cross-cutting pyrite and chalcopyrite (Figure 7e,f). Moreover, native-Au particles smaller than 10 µm have also been occasionally detected in the quartz matrix. The formation of goethite and cuprite rims on magnetite-pyrite and chalcopyrite, respectively, is related to a supergene stage.

6.2. Mitza Sermentus

Five samples from the Mitza Sermentus locality have been studied with the aim of highlighting the main differences between skarns formed on the limestone slices (MS.01; MS.02b; MS.3b; MS.04) and on mafic dykes (MS.3a). The formers are mainly characterized by clinopyroxene and wollastonite as the prevalent prograde minerals; garnets have been occasionally identified as isolated and strongly altered crystals, therefore with a certain degree of uncertainty. The most recurrent assemblage is characterized by bands of chlorite and calcite pseudomorphs after wollastonite (Figure 8b). These minerals often envelop fragmented individuals and aggregates of clinopyroxenes, epidotes and the relict garnets. Amphiboles and epidotes are usually more abundant where clinopyroxene alteration is more advanced. Occasionally, apatite and plagioclase have also been identified as accessory minerals. The ore minerals are sphalerite, chalcopyrite, pyrrhotite, pyrite and galena. Sphalerite occurs as interstitial grains characterized by moderately abundant chalcopyrite and pyrrhotite inclusions, usually randomly distributed. Occasionally, in the same way as the Fe-rich generation of the Barisonis samples, these inclusions are finer at the boundaries and larger at the core of sphalerite crystals. Chalcopyrite forms as void-filling grains in the matrix often associated with sphalerite. In the latter case, chalcopyrite corrodes and substitutes sphalerite as suggested by reaction gulfs at their boundaries. Subsequently, pyrite and galena are formed. Accessory minerals are tetrahedrite and bornite, usually observed at the edges of chalcopyrite. Calcite and quartz are the latest to form.

The sample MS.3a represents the contact between a skarn vein and the dark shale wall-rock in which the mineralized vein is enclosed (Figure 8a), adjacent to a metasomatized mafic dike (MS.3b). The shale matrix mainly consists of muscovite, chamosite and interstitial quartz arranged along a mylonitic foliation with folds and crenulation bands. Accessory minerals are represented by K-feldspar, plagioclase, clinozoisite, titanite and calcite. The mineralized zone is a centimeter-wide vein parallel to the main foliation. The contact with the skarn vein is marked by a band of a Ba-rich silicate phase in large (up to 3 mm) anhedral to subhedral crystals (Figure 8c,e). The EDS spectra point towards armenite, a rare silicate with the $\text{BaCa}_2\text{Al}_6\text{Si}_9\text{O}_{30} \cdot 2(\text{H}_2\text{O})$ formula, which is believed to form after hydrothermal alteration of baryte or Ba-rich feldspars; the armenite occurrence has been conclusively confirmed by XRPD analyses on the veinlets [59]. Occasional smaller armenite crystals also occur in the phyllite. The mineral assemblage is made of clinopyrox-

ene, amphibole, epidote, chlorite and wollastonite, the latter occasionally overgrown by pseudomorphic calcite. Accessory minerals are titanite, apatite, pumpellyite, armenite and barite (Figure 8c).

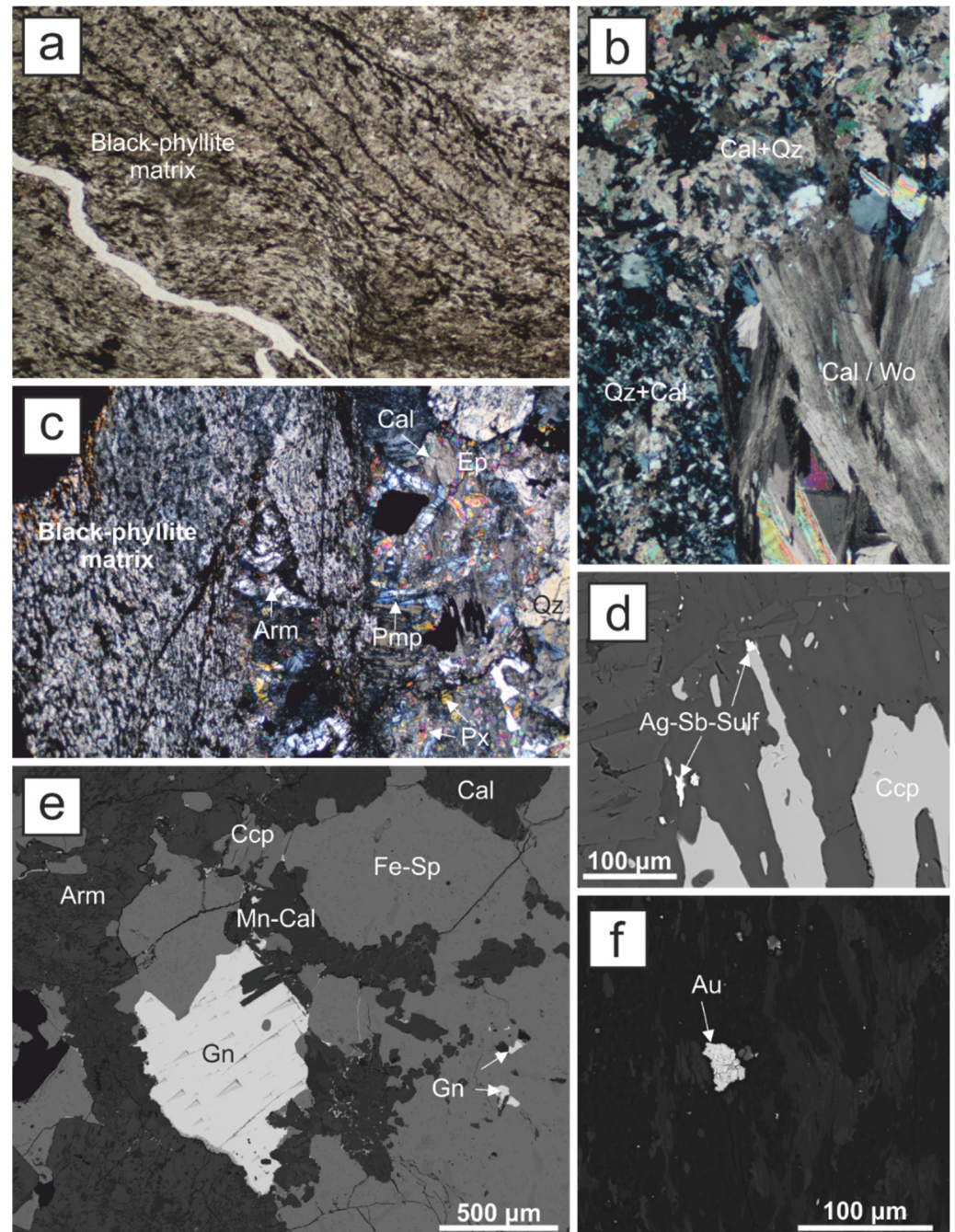


Figure 8. (a) Photomicrographs of the Mitza Sermentus orebody in the proximity of the black-phyllite host rock. Black domains are the mylonitic foliation. Mineral assemblages include (b) calcite-quartz replacing wollastonite; (c) chalcopyrite veinlets in a pyroxene-epidote-quartz-calcite gangue with subordinate pumpellyite, armenite, titanite and apatite; (d) Ag-sulfantimonides (tetrahedrite) grains associated with chalcopyrite; (e) galena, chalcopyrite and sphalerite in the armenite-rich zones; (f) native Au grains in the titanite, armenite, chlorite, epidote matrix. Mn-Cal = manganocalcite; Arm = armenite; Pmp = pumpellyite; Fe-Sp = Fe-rich sphalerite; Ag-Sb-Sulf = Ag-sulfantimonides (tetrahedrite); Au = native gold.

Similar to the BS samples, the ore minerals mainly consist of galena, sphalerite, chalcopyrite and pyrite. The first minerals to form in the crystallization sequence of sulfides are sphalerite and chalcopyrite, followed by galena and late pyrite. Chalcopyrite is also found in sparse inclusions within sphalerite, suggesting their partial timing overlap or the presence of two generations of chalcopyrite. Moreover, and similar to the BS samples, Ag-sulfosalts and Au have also been found (Figure 8d,f). Here, though, the former are more abundant and host a significant amount of antimony (up to 11 wt.% of Sb), therefore suggesting their occurrence in the form of tetrahedrite over Ag-sulfides. Small particles (up to 20 μm) of native Au have been recognized in the titanite, armenite, chlorite, epidote matrix (Figure 8f). Later veins of quartz, calcite and manganocalcite intrude both the phyllite and the mineralized vein.

6.3. S'Ega Su Forru

Due to the limited size of the S'Ega Su Forru mineralized vein, one sample (namely FOR1) was chosen as representative of this orebody. It consists of a matrix made up by calc-silicate minerals as prograde clinopyroxene of the diopside-hedenbergite series slightly enriched in Mn (up to 2.5 wt%), partially replaced by amphibole, epidote and chlorite. The ore minerals mainly consist of base metal sulfides as sphalerite, pyrite, chalcopyrite and galena. A peculiar feature of this mineralization, not found in the other outcrops within the Rosas mine area, is the presence of Ni-Co-Fe sulfarsenides (Figure 9a–c). Indeed, SEM-EDS analyses revealed the presence of small (5–15 μm) subrounded and idiomorphic grains of Co-Ni-Fe sulfarsenides, sometimes isolated, some others grouped in small clusters, disseminated around the calcsilicate matrix and as tiny inclusions in pyrite. The composition of these phases is characterized by almost constant contents of As (40–42 wt.%) and S (20–22 wt.%) indicating a As:S = 1:1 molar ratio (mono-sulfarsenides). Conversely, the contents of Co, Ni and Fe are strongly variable from one point to another, with Co ranging between 16 and 29 wt.%, Ni 3–11 wt.% and Fe 4–8 wt.%. Co is inversely related to both Ni and Fe, whereas a clear correlation between Ni and Fe is not observed. In addition, traces of Zn and Cu are locally found. The As/S constant ratio and the continuous variation of Co, Ni and Fe point towards a mixture of glaucodot ((Co,Fe)AsS) and gersdorffite (NiAsS). Pyrite also forms idiomorphic cubic crystals up to 0.4 mm locally with Ni-Co-Fe arsenides and sphalerite inclusions. Chalcopyrite can be found as anhedral grains at contact with pyrite. Inclusions are rare and consist mostly of micro-scale individuals of sphalerite and pyrite. Sphalerite forms large anhedral grains cross-cutting chalcopyrite. Its dark color is due to Fe contents up to 10%; traces of Mn have also been detected; “chalcopyrite disease” [61] textures are very frequent. The size of the chalcopyrite inclusions increases towards the center portion of sphalerite grains where pyrite inclusions have also been recurrently observed. Galena grains fill the intergranular spaces between previous sulfides, often producing fractures on sphalerite and chalcopyrite (Figure 9b,c). Small aggregates of hematite lamellae form at the expense of pyrite crystals and represent the late stage of the ore minerals formation.

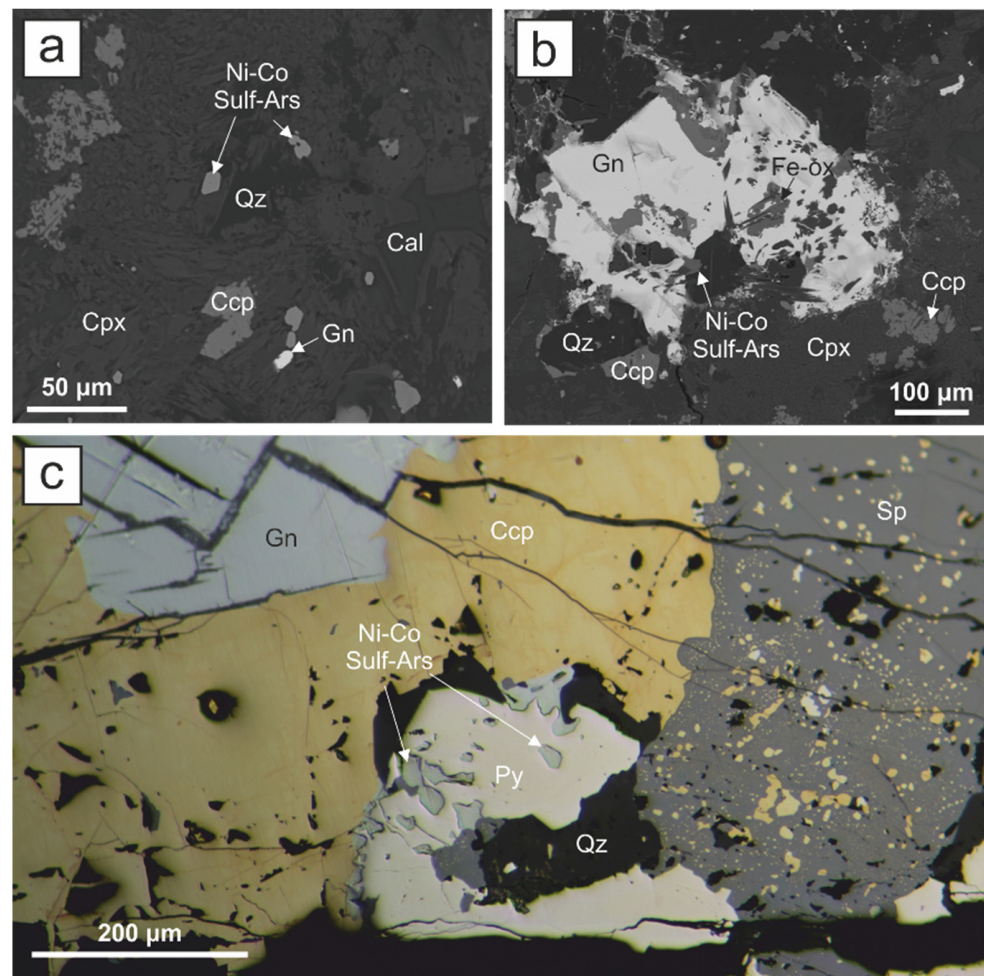


Figure 9. Photomicrographs of the S'Ega Su Forru vein: (a) a clinopyroxene-quartz-calcite matrix with base metal sulfides and Ni-Co-Fe sulfarsenides; (b) galena and Fe-oxides (goethite-hematite) enveloping Ni-Co sulfarsenide crystals; (c) Ni-Co sulfarsenides enclosed in pyrite with sphalerite, chalcopyrite and galena. Cpx = clinopyroxene; Ni-Co-Sulf-Ars = Ni-Co sulfarsenides; Fe-Ox = Fe-oxides (goethite-hematite).

7. Discussion

In the following, we discuss how the deformation events led to the structural setting that favored the fluid circulation and mineralization in the RSZ and how localized contact metamorphism and widespread metasomatic processes gave rise to the peculiar paragenesis of skarn ores in the Rosas mining district.

The tectonic slices of limestones embedded within a highly sheared siliciclastic succession are the main structural feature of the study area, and they constitute widespread discontinuities that had allowed the fluid circulation and the skarn ore mineralization. The structuring of the plumbing system of the RSZ reflects a progressive deformation occurred in a compressive setting that led, in sequence, to the development of recumbent folds and related axial plane cleavage, thrusts development and bedding transposition along the tectonic foliation. It is in this context that the tectonic slices took place, most probably by means of thrusts that enucleated shearing the stratigraphic contacts in the overturned limbs of the recumbent folds [62,63], separating large portions of limestones and translating them within the siliciclastic succession. Note that the limestones are lower Cambrian in age, and the siliciclastic succession is upper Ordovician in age, and no evidence of older siliciclastic formations occurs in the RSZ, except for a small slice of Cabitza Fm. This suggests a remarkable displacement and/or a scarce thickness of the Cabitza Fm. above the limestones,

likely because of the erosion related to the Sardinian Phase [33,38]. The thrusts envelop the limestone slices with an anastomosed geometry and played the role of preferential conduits for fluids because they are zone of weakness with higher permeability than the surrounding rocks [64,65].

The compressive regime is followed by extension processes due to the chain's collapse that led to the exhumation of the RSZ to shallower structural levels; during this stage, folds with horizontal axial plane developed, affecting mainly the weaker siliciclastic succession and its cleavage. The decreasing of the lithostatic stress as exhumation progresses, as well as the weakness induced by the penetrative cleavage, favored the intrusion of mafic dykes that postdate the compressive phases, as testified by the fact that the dyke is not foliated. The attitude of the mafic dykes is parallel to the general setting of the RSZ, suggesting that their intrusion exploited this large discontinuity. Locally, however, the dykes cut across the cleavage no more favorably oriented because they are affected by syn-exhumation folds, demonstrating that the mafic dyke intrusion postdate also the exhumation phases.

Thus, the network of thrusts and the increased permeability provided by the pervasive foliation allowed the fluids to rise from deeper levels and to reach the limestones. The tectonic slices acted as a trap for the mineralizing fluids, due to the higher reactive potential of the carbonate rocks [15].

Metamorphic and metasomatic processes selectively affected the carbonate tectonic slices, originating several skarn-type orebodies. In general, mineralized rocks display the mineralogical assemblages and textures of Fe-Cu-Zn skarns, with relics of anhydrous calcic phases related to the prograde metamorphic stage (andradite/grossular anisotropic garnet, clinopyroxene, wollastonite), frequently enclosed in a mass of hydrated phases (actinolitic amphibole, epidote) and magnetite related to the retrograde metasomatic stage, in turn followed by chlorite, sulfides, quartz and calcite associated to the hydrothermal stage. Sulfide ores predominantly consist of sphalerite, chalcopyrite and galena, with abundant pyrite and pyrrhotite and minor tetrahedrite and Ag-sulfosalts.

The style of the skarn mineralization in the three studied examples, namely Barisonis, Mitza Sermentus and S'Ega Su Forru, slightly varies according to the local structural framework where the orebodies are emplaced: small limestones slices adjacent to the mafic dyke (Barisonis); small limestones slices embedded in a highly sheared siliciclastic succession (Mitza Sermentus); a discrete thrust fault at the bottom of larger limestone slice (S'Ega Su Forru). In the following, these differences are discussed.

In the Barisonis mineworking, the skarn developed in a carbonate slice directly in contact with the mafic dyke and is characterized by a clear and well-developed zoning pattern. Considering that such a stratigraphic relationship and zonation have not been observed in other skarns of the RSZ, we can speculate a correlation between the potential contact metamorphism induced by the mafic dyke emplacement and the zoning pattern. In particular, contact metamorphism effects might have given rise, at the gabbro-carbonate tectonic slices contacts, to the metric to decametric garnet, pyroxene and wollastonite mineralogical zonation recognized in the Barisonis mineworking. Retrograde and ore-bearing hydrothermal stages display mineral associations and textures that suggest a common origin with the other studied mineralization in the area.

The style of mineralization in Mitza Sermentus area is characterized by several metasomatized carbonate lenses, metasomatized mafic dikes and thin mineralized veinlets parallel to the tectonic foliation. This area is structurally located close to the thrust that emplaced the Monte Argentu Fm. above the Monte Orri Fm. This shear zone is not as discrete as the thrusts that bound the carbonate tectonic slices, most probably because it developed at the contact with weak siliciclastic formations and the shortening has been accommodated in a wide zone where the mylonitic foliation acted as an active foliation [25]. This allowed the mineralizing fluids to precipitate extensively within the foliation planes, originating a peculiar mineralization style where no evidence of metamorphic zonation can be found. This style of mineralization could be confused with a stratabound type, misinterpreting

the tectonic foliation as a bedding, or as a stockwork type, nor recognizing the structural control and so leading to a wrong prospection of the orebody.

The orebody in S'Ega Su Forru mine is smaller than those of Barisonis and Mitza Sermentus and consists of a 20 cm thick vein located at the tectonic contact between the carbonate slice and the siliciclastic succession of the Monte Orri Fm. In this case, the structural control of the mineralization is strictly related to the fault damage zone of the bottom thrust of the slices, where the flow of the mineralized fluid is enhanced by the higher permeability.

The field surveys and the observations above about the three different styles of mineralization pointed out the tight structural controls on skarn and ore localization and distribution.

The structural and mineralogical data suggest that the structural evolution and its control on the ore mineralization distribution evolved in three stages (Figure 10): (1) the first stage is the structuring of the plumbing system of the RSZ as a consequence of the collisional phases related to the Variscan Orogeny. The pressure solution and grain boundary sliding deformation mechanisms that accommodated the strain in the RSZ suggest P-T conditions in the range of 3–3.5 kbar, thus we can consider a depth of about 11.5–13.5 km, and a temperature of 250–300 °C [16]. (2) The second stage concerns the intrusion of the mafic dyke and its related swarm of small veinlets. In particular, the 100-m-thick mafic dyke induced a contact metamorphism aureole whose zonation is recognizable only in some of the skarns. The intrusion of the mafic dyke occurred probably during the extensional phases related to the collapse of the Variscan chain that allowed the re-using of previous structures (foliation and thrust) as normal faults or extensional joint, at very shallow crustal structural levels. (3) The third stage reflects a larger scale, extensive magmatic fluid circulations that involved the structures of the RSZ and gave rise to the skarn ore mineralization. Infilling of metasomatic fluids in carbonate tectonic slices occurred along faults, also aided by metasomatic reactions and by the increase in permeability due to alteration of prograde stage minerals. Metasomatic reactions also involved mafic rocks, producing a mineral association of chlorite, epidote, plagioclase, K-feldspar and pumpellyite with accessory armenite, titanite and apatite. This mineral association allows us to ascribe the metamorphic and metasomatic processes to P-T conditions that do not exceed pressure of 2 kbar, so few kilometers in depth, and a temperature range of roughly 200–350 °C [66,67].

The causative intrusions related to skarn ores belong to the GS1 suite [17] of early Permian (289 Ma) ilmenite-series, ferroan granites which intrude the RSZ about 3 km east from the studied area, beneath which the granites are most probably present as well. The geochemical signatures and mineralogical associations of the skarn ores (e.g., presence of fluorite and cassiterite) are significant elements in favor of the metallogenic relationship with the GS1 granites. The Fe-Cu-Zn skarn ores of Rosas are best interpreted as distal orebodies whose localization is controlled by inherited structures, connected to large-scale circulation of granite-related fluids in the km-sized plumbing system represented by the RSZ.

The emplacement of the skarns of the RSZ mine district is an example of a passive structural control of ore mineralization localization. The main evidences are (1) the orebodies aligned with the main structural features, thrusts and tectonic foliation, both at cartographic and outcrop scale; (2) the orebodies show no deformation neither evidence of preferential orientation at thin section scale; (3) the plumbing system has been structured at crustal structural levels definitely deeper than that where the formation of the skarn occurred, which is very shallow and in a completely different tectonic scenario.

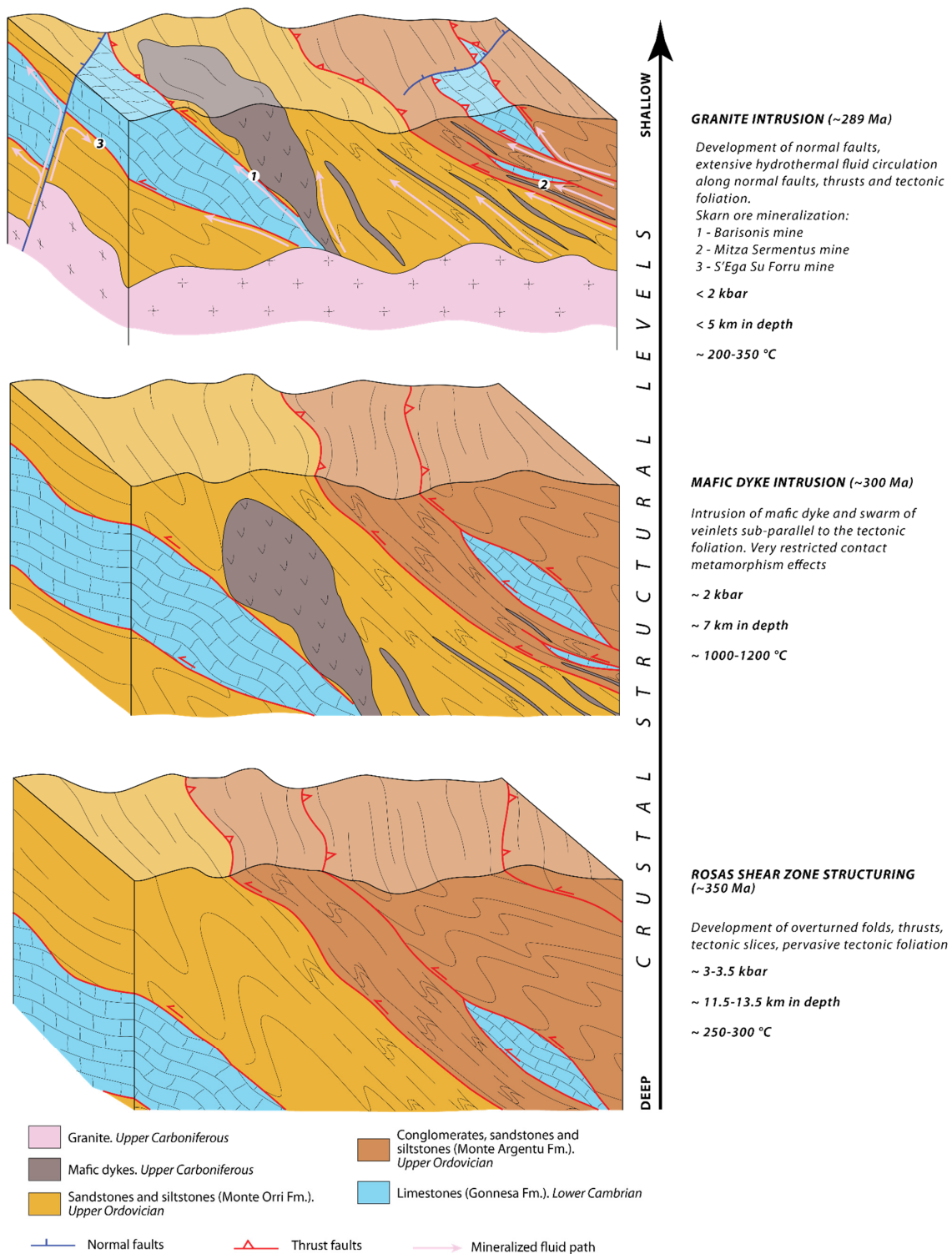


Figure 10. Cartoon showing the tectonic evolution and the passive structural control on the skarn ore mineralization in the Barisonis (1), Mitza Sermentus (2) and S'Ega Su Forru (3) mines. The plumbing system is inherited from the structuring of the Rosas Shear Zone at deep structural levels. Once exhumed at shallow structural levels, the Rosas Shear Zone acted as weakness and permeable zone favorable for the intrusion of mafic dyke and, soon after, for extensive granite-related fluid circulation. The ages of each step are supposed taking into account the available dating in the Sardinian basement of the regional metamorphism (~350 Ma, [68]), mafic dyke intrusion (~300 Ma, [41,69,70]) and granite intrusion (~289 Ma [17,42]).

8. Conclusions

The field survey and structural analysis in the RSZ and ore microscopy and SEM-EDS analysis allowed us to better characterize the skarn deposits in the Rosas mining district, excluding any sedimentary process involved in the genesis of the ores as proposed up to now.

The skarn ores in the RSZ mining district are an example of passive structurally controlled mineralization localization in polydeformed basements. The structuring of the RSZ during the collisional phases of the Variscan Orogeny originated at the brittle–ductile transition crustal level and acted as the plumbing system exploited, at shallower crustal levels, during the extensional phases related to the collapse of the Variscan chain, by the mafic dyke intrusion and by extensive magmatic fluid circulation related to the granite emplacement. In addition to the different crustal levels of the plumbing system structuring and ores emplacement, the passive structural control on the mineralization location and distribution is testified by the same attitude between the orebodies and the structures and by the lack of deformation in the mafic dyke and skarn. The paragenesis of the ores and the mineralization style varies slightly according to the local structural setting where skarns took place: a carbonate tectonic slice adjacent to the mafic dyke; an intensely sheared zone; a discrete thrust fault surface.

The intrusion of the mafic dyke generated a local-scale contact metamorphic aureole on the limestone slices (for instance in the Barisonis skarn) that, once affected by the subsequent metasomatic processes, gave rise to a well recognizable zonation pattern in the skarn ores and to the occurrence of peculiar minerals in the mafic protolith. The limited extent of thermal metamorphism induced by mafic dykes, despite their likely high temperature, can be explained by the quick cooling of these relatively small bodies.

Finally, the results suggest that the understanding of the structural style and its control in the ore mineralization localization is essential for a proper identification, quantification and exploitation of economically relevant ore minerals, especially in complex structural settings of polydeformed basements.

Author Contributions: Conceptualization, S.N., A.F., A.A., F.C., M.L.D. and D.F.; methodology, A.A., M.L.D., D.F., S.N., F.C. and A.F.; microscope analysis, A.A., M.L.D., D.F. and S.N.; field investigation, A.A., A.F., S.N., M.L.D. and F.C.; data curation, F.C., A.A., M.L.D., D.F., A.F. and S.N.; writing—original draft preparation, F.C., A.A., M.L.D., D.F. and S.N.; writing—review and editing, S.N. and A.F.; supervision, S.N. and A.F.; funding acquisition, A.F. and S.N. All authors have read and agreed to the published version of the manuscript.

Funding: This work was supported by Fondazione di Sardegna (research program: “Sustainable land management: the tools of geology for the environment”—CUP F75F21001270007), and Regione Autonoma della Sardegna (research program: “Il blocco Sardo-Corso: area chiave per la ricostruzione della geodinamica varisica”—CUP J81G17000110002). Matteo Luca Deidda gratefully acknowledges Sardinia Regional Government for the financial support of his PhD scholarship (P.O.R. Sardegna F.S.E. Operational Programme of the Autonomous Region of Sardinia, European Social Fund 2007–2013—Axis IV Human Resources, Objective 1.3, Line of Activity 1.3.1.).

Data Availability Statement: Not applicable.

Acknowledgments: We thank two anonymous reviewers for their careful comments and suggestions that improved the quality of the paper. We acknowledge the CeSAR (Centro Servizi d’Ateneo per la Ricerca) of the University of Cagliari, Italy, for SEM analysis.

Conflicts of Interest: The authors declare no conflict of interest.

References

1. Cox, S.F.; Knackstedt, M.A.; Braun, J. Principles of structural control on permeability and fluid flow in hydrothermal systems. In *Structural Controls on Ore Genesis*; Richards, J.P., Tosdal, R.M., Eds.; Reviews in Economic Geology; Society of Economic Geologists: Littleton, CO, USA, 2001; Volume 14, pp. 1–24.
2. Cathles, L.M. Fluid flow and genesis of hydrothermal ore deposits. In *Economic Geology 75th Anniversary Volume, 1905–1980*; Society of Economic Geologists: Littleton, CO, USA, 1981; pp. 424–457. [[CrossRef](#)]

3. Caine, J.S.; Evans, J.P.; Forster, C.B. Fault zone architecture and permeability structure. *Geology* **1996**, *24*, 1025–1028. [[CrossRef](#)]
4. Ingebritsen, S.E.; Appold, M.S. The physical hydrogeology of ore deposits. *Econ. Geol.* **2012**, *107*, 559–584. [[CrossRef](#)]
5. Ord, A.; Lester, D.R.; Hobbs, B.E. The mechanics of hydrothermal systems: I. Ore systems as chemical reactors. *Ore Geol. Rev.* **2012**, *49*, 1–44. [[CrossRef](#)]
6. Lester, D.R.; Ord, A.; Hobbs, B.E. The mechanics of hydrothermal systems: II. Fluid mixing and chemical reactions. *Ore Geol. Rev.* **2012**, *49*, 45–71. [[CrossRef](#)]
7. Chauvet, A. Structural Control of Ore Deposits: The Role of Pre-Existing Structures on the Formation of Mineralised Vein Systems. *Minerals* **2019**, *9*, 56. [[CrossRef](#)]
8. Funedda, A.; Naitza, S.; Butta, C.; Cocco, F.; Dini, A. Structural Controls of Ore Mineralization in a Polydeformed Basement: Field Examples from the Variscan Bacca Locci Shear Zone (SE Sardinia, Italy). *Minerals* **2018**, *8*, 456. [[CrossRef](#)]
9. Sibson, R.H. Earthquake rupturing as a mineralizing agent in hydrothermal systems. *Geology* **1987**, *15*, 701–704. [[CrossRef](#)]
10. Sibson, R.H. Fault-valve behavior and the hydrostatic lithostatic fluid pressure interface. *Earth Sci. Rev.* **1992**, *32*, 141–144. [[CrossRef](#)]
11. Hodgson, C.J. The structure of shear-related, vein-type gold deposits: A review. *Ore Geol. Rev.* **1989**, *4*, 231–273. [[CrossRef](#)]
12. Stephens, J.R.; Mair, J.R.; Oliver, N.H.L.; Hart, C.J.R.; Baker, T. Structural and mechanical controls on intrusion-related deposits of the Tombstone Gold Belt, Yukon, Canada, with comparisons to other vein-hosted ore-deposit types. *J. Struct. Geol.* **2004**, *26*, 1025–1041. [[CrossRef](#)]
13. Cox, S.F. Coupling between Deformation, Fluid Pressures, and Fluid Flow in Ore-Producing Hydrothermal Systems at Depth in the Crust. In *Economic Geology 100th Anniversary Volume, 1905–2005*; Society of Economic Geologists: Littleton, CO, USA, 2005; pp. 39–75. [[CrossRef](#)]
14. Cox, S.F. Injection-Driven Swarm Seismicity and Permeability Enhancement: Implications for the Dynamics of Hydrothermal Ore Systems in High Fluid-Flux, Overpressured Faulting Regimes—An Invited Paper. *Econ. Geol.* **2016**, *111*, 559–587. [[CrossRef](#)]
15. Meinert, L.D.; Dipple, G.M.; Nicolescu, S. World Skarn Deposits. In *Economic Geology 100th Anniversary Volume, 1905–2005*; Society of Economic Geologists: Littleton, CO, USA, 2005; pp. 299–336. [[CrossRef](#)]
16. Casini, L.; Funedda, A.; Oggiano, G. A balanced foreland–hinterland deformation model for the Southern Variscan belt of Sardinia, Italy. *Geol. J.* **2010**, *45*, 634–649. [[CrossRef](#)]
17. Conte, A.M.; Cuccuru, S.; D’Antonio, M.; Naitza, S.; Oggiano, G.; Secchi, F.; Casini, L.; Cifelli, F. The post-collisional late Variscan ferroan granites of southern Sardinia (Italy): Inferences for inhomogeneity of lower crust. *Lithos* **2017**, *294–295*, 263–282. [[CrossRef](#)]
18. Carmignani, L.; Carosi, R.; Di Pisa, A.; Gattiglio, M.; Musumeci, G.; Oggiano, G.; Pertusati, P.C. The Hercynian chain in Sardinia (Italy). *Geodin. Acta* **1994**, *7*, 31–47. [[CrossRef](#)]
19. Franceschelli, M.; Puxeddu, M.; Cruciani, G. Variscan metamorphism in Sardinia, Italy: Review and discussion. *J. Virtual Explor.* **2005**, *19*, 1–36. [[CrossRef](#)]
20. Conti, P.; Patta, E.D. Large-scale Hercynian West-directed tectonics in southeastern Sardinia (Italy). *Geodin. Acta* **1998**, *11*, 217–231. [[CrossRef](#)]
21. Conti, P.; Carmignani, L.; Funedda, A. Change of nappe transport during the Variscan collisional evolution of central-southern Sardinia (Italy). *Tectonophysics* **2001**, *332*, 255–273. [[CrossRef](#)]
22. Conti, P.; Carmignani, L.; Oggiano, G.; Funedda, A.; Eltrudis, A. From thickening to extension in the Variscan belt-kinematic evidence from Sardinia (Italy). *Terra Nova* **1999**, *11*, 93–99. [[CrossRef](#)]
23. Rossi, P.; Cocherie, A. Genesis of a Variscan batholith: Field, petrological and mineralogical evidence from the Corsica-Sardinia batholith. *Tectonophysics* **1991**, *195*, 319–346. [[CrossRef](#)]
24. Casini, L.; Cuccuru, S.; Puccini, A.; Oggiano, G.; Rossi, P. Evolution of the Corsica–Sardinia Batholith and late-orogenic shearing of the Variscides. *Tectonophysics* **2015**, *646*, 65–78. [[CrossRef](#)]
25. Funedda, A. Foreland- and hinterland-verging structures in fold-and-thrust belt: An example from the Variscan foreland of Sardinia. *Int. J. Earth Sci.* **2009**, *98*, 1625–1642. [[CrossRef](#)]
26. Carmignani, L.; Oggiano, G.; Funedda, A.; Conti, P.; Pasci, S. The geological map of Sardinia (Italy) at 1:250,000 scale. *J. Maps* **2016**, *12*, 826–835. [[CrossRef](#)]
27. Teichmüller, R. Zur Geologie der Thyrenisgebietes. Teil 1: Alte und junge Krunstenbewegungen im südlichen Sardinien. *Ges. Der Wiss. Zu Göttingen* **1931**, *3*, 857–950.
28. Stille, H. Bemerkungen betreffend die “sardische Faltung” und den Ausdruck “ophiolitisch”. *Z. Geol. Ges.* **1939**, *91*, 771–773.
29. Von Raumer, J.F.; Stampfli, G.M.; Arenas, R.; Sánchez Martínez, S. Ediacaran to Cambrian oceanic rocks of the Gondwana margin and their tectonic interpretation. *Int. J. Earth Sci.* **2015**, *104*, 1107–1121. [[CrossRef](#)]
30. Cocco, F.; Oggiano, G.; Funedda, A.; Loi, A.; Casini, L. Stratigraphic, magmatic and structural features of Ordovician tectonics in Sardinia (Italy): A review. *J. Iber. Geol.* **2018**, *44*, 619–639. [[CrossRef](#)]
31. Cocco, F.; Funedda, A. The Sardinic Phase: Field evidence of Ordovician tectonics in SE Sardinia, Italy. *Geol. Mag.* **2019**, *156*, 25–38. [[CrossRef](#)]
32. Oriolo, S.; Schulz, B.; Geuna, S.; González, P.D.; Otamendi, J.E.; Sláma, J.; Druguet, E.; Siegesmund, S. Early Paleozoic accretionary orogens along the Western Gondwana margin. *Geosci. Front.* **2021**, *12*, 109–130. [[CrossRef](#)]
33. Pillola, G.L.; Leone, F.; Loi, A. The Cambrian and Early Ordovician of SW Sardinia. *G. Di Geol.* **1998**, *60*, 25–38.

34. Bechstädt, T.; Boni, M. *Sedimentological, Stratigraphical and ore Deposits Field Guide of the Autochthonous Cambro-Ordovician of Southwestern Sardinia*; (Technical Periodicals) Descriptive Memories of the Geological Map of Italy; Istituto Superiore per la Protezione e la Ricerca Ambientale: Rome, Italy, 1994; Volume 48, 434p.
35. Elicki, O.; Pillola, G.L. Cambrian microfauna and palaeoecology of the Campo Pisano Formation at Gutturu Pala (Iglesiente, SW Sardinia, Italy). *Bollettino della Società Paleontologica Italiana* **2004**, *43*, 383–401.
36. Gandin, A. Depositional and paleogeographic evolution of the Cambrian in south-western Sardinia. In *Correlation of Prevariscan and Variscan Events of the Alpine-Mediterranean Mountain Belt*; IGCP Project No. 5—Newsletter; Sassi, F.P., Bourrouilh, R., Eds.; Institute of Mineralogy Petrology, University of Padua: Padua, Italy, 1989; Volume 7, pp. 151–166.
37. Laske, R.; Bechstädt, T.; Boni, M. The post-Sardic Ordovician series. In *Sedimentological, Stratigraphical and Ore Deposits Field Guide of the Autochthonous Cambro-Ordovician of Southwestern Sardinia*; Memorie Descrittive della Carta Geologica, d'Italia; Bechstädt, T., Boni, M., Eds.; Servizio Geologico d'Italia: Rome, Italy, 1944; pp. 115–146.
38. Leone, F.; Ferretti, A.; Hammann, W.; Loi, A.; Pillola, G.L.; Serpagli, E. A general view on the post-Sardic Ordovician sequence from SW Sardinia. *Rend. Soc. Paleontol. Ital.* **2002**, *1*, 51–68.
39. Gnoli, M.; Kříž, J.; Leone, F.; Olivieri, R.; Serpagli, E.; Storch, P. Lithostratigraphic units and biostratigraphy of the Silurian and early Devonian of Southwest Sardinia. *Boll. Della Soc. Paleontol. Ital.* **1990**, *29*, 11–23.
40. Barca, S.; Forci, A.; Forci, A. I depositi sinorogenici ercinici del Sulcis (Sardegna sud-occidentale). *Boll. Della Soc. Geol. Ital.* **1998**, *117*, 407–419.
41. Secchi, F.; Naitza, S.; Oggiano, G.; Cuccuru, S.; Puccini, A.; Conte, A.M.; Giovanardi, T.; Mazzucchelli, M. Geology of late-Variscan Sàrrabus pluton (south-eastern Sardinia, Italy). *J. Maps* **2021**, *17*, 591–606. [[CrossRef](#)]
42. Boni, M.; Stein, H.J.; Zimmerman, A.; Villa, I.M. Re-Os age for molybdenite from SW Sardinia (Italy): A comparison with $^{40}\text{Ar}/^{39}\text{Ar}$ dating of Variscan granitoids. In *Mineral Exploration and Sustainable Development*; Eliopoulos, D.G., Ed.; Millpress: Rotterdam, The Netherlands, 2003; pp. 247–250.
43. Naitza, S.; Oggiano, G.; Cuccuru, S.; Casini, L.; Puccini, A.; Secchi, F.; Funedda, A.; Tocco, S. Structural and magmatic controls on Late Variscan Metallogenesis: Evidences from Southern Sardinia (Italy). In Proceedings of the 13th Biennial SGA Meeting, Nancy, France, 24–27 August 2015; Volume 1, pp. 161–164.
44. Naitza, S.; Conte, A.M.; Cuccuru, S.; Oggiano, G.; Secchi, F.; Tecce, F. A Late Variscan tin province associated to the ilmenite-series granites of the Sardinian Batholith (Italy): The Sn and Mo mineralisation around the Monte Linas ferroan granite. *Ore Geol. Rev.* **2017**, *80*, 1259–1278. [[CrossRef](#)]
45. Carmignani, L.; Cocozza, T.; Ghezzi, P.C.; Pertusati, P.C.; Ricci, C.A. Outlines of the Hercynian Basement of Sardinia. In *Guide-book to the Excursion on the Paleozoic basement of Sardinia*; IGCP Project No. 5—Newsletter; Università di Siena: Siena, Italy, 1986; pp. 11–21.
46. Carosi, R.; Musumeci, G.; Pertusati, P.C.; Carmignani, L. The Hercynian backthrusts of eastern Iglesias (SW Sardinia): An example of inversion tectonics. In *Contributions to the Geology of Italy with Special Regard to the Paleozoic Basement*; IGCP No., 276—Newsletter; Carmignani, L., Sassi, F.P., Eds.; Università di Siena: Siena, Italy, 1992; pp. 97–105.
47. Cocco, F.; Funedda, A. Mechanical influence of inherited folds in thrust development: A case study from the Variscan fold-and-thrust belt in SW Sardinia (Italy). *Geosciences* **2021**, *11*, 276. [[CrossRef](#)]
48. Pasci, S.; Pertusati, P.C.; Salvadori, I.; Murtas, M. I rilevamenti CARG del foglio geologico 555 “Iglesias” e le nuove implicazioni strutturali sulla tettonica della “Fase Sarda”. *Rend. Online Della Soc. Geol. Ital.* **2008**, *3*, 614–615.
49. ISPRA. Carta Geologica d'Italia Alla Scala 1:50,000. Foglio 555 IGLESIAS. Available online: https://www.isprambiente.gov.it/Media/carg/555_IGLESIAS/Foglio.html (accessed on 16 January 2022).
50. Boni, M.; Balassone, G.; Iannace, A. Base metal ores in the lower Paleozoic of southwestern Sardinia. *Soc. Econ. Geol. Spec. Publ.* **1996**, *4*, 18–28. [[CrossRef](#)]
51. Valera, R.; Zuffardi, P. Segnalazione di Scheelite in taluni adunamenti metamorfici della Sardegna (Nota preliminare). *Res. Ass. Min. Sarda* **1968**, *73*, 62–64.
52. Valera, R.; Zuffardi, P. La geochimica del tungsteno nel Paleozoico della Sardegna. *Rend. Soc. Ital. Mineral. Petrol.* **1970**, *26*, 815–830.
53. Pirri, I.V. Il giacimento a blenda, galena, calcopirite di Sa Marchesa nel Sulcis (Sardegna). *Boll. Soc. Ital. Sci. Nat.* **1971**, *62*, 505–549.
54. Funedda, A.; Carmignani, L.; Pasci, S.; Patta, E.D.; Uras, V.; Conti, P.; Sale, V. Foglio 556 ASSEMINI. In *Note Illustrative della Carta Geologica d'Italia alla Scala 1:50,000, Servizio Geologico d'Italia*; Istituto Poligrafico e Zecca dello Stato: Roma, Italy, 2009; p. 192.
55. Valera, R. Appunti sulla morfologia, termometria e composizione delle inclusioni fluide di fluoriti sarde. *Rend. Soc. Ital. Mineral. Petrol.* **1974**, *30*, 459–480.
56. Borghesan, E.C. Giacimenti misti di galene e blende del tipo di metasomatismo di contatto fra intrusione basica e calcare. *Res. Ass. Min. Sarda* **1935**, *40*, 9–13.
57. Cavinato, A. Cenno su un'area metamorfica e sulla genesi e significato di una metallizzazione. *Res. Ass. Min. Sarda* **1937**, *41*, 5–29.
58. ISPRA. Carta Geologica d'Italia Alla Scala 1:50,000. Foglio 556 ASSEMINI. Available online: https://www.isprambiente.gov.it/Media/carg/556_ASSEMINI/Foglio.html (accessed on 16 January 2022).
59. Poll, J.J.K. The Geology of the Rosas-Terraseo area (Sulcis, South Sardinia). *Leidse Geol. Meded.* **1966**, *35*, 117–208.
60. Tearpock, D.J.; Bischke, R.E. *Applied Subsurface Geological Mapping with Structural Methods*, 2nd ed.; Prentice Hall: Upper Saddle River, NJ, USA, 2002; p. 822.

61. Fancello, D.; Deidda, M.L.; Attardi, A.; Cocco, F.; Funedda, A.; Naitza, S. Armenite: A really rare mineral? In Proceedings of the 3rd European Mineralogical Conference EMC, Cracow, Poland, 29 August–2 September 2021; Volume 127.
62. Barton, P.B.; Bethke, P.M. Chalcopyrite disease in sphalerite: Pathology and epidemiology. *Am. Mineral.* **1987**, *72*, 451–467.
63. Poblet, J.; Lisle, R.J. Kinematic evolution and structural styles of fold-and-thrust belts. *Geol. Soc. Lond. Spec. Publ.* **2011**, *349*, 1–24. [[CrossRef](#)]
64. Butler, R.; Bond, C. Chapter 9—Thrust systems and contractional tectonics. In *Regional Geology and Tectonics*, 2nd ed.; Scarselli, N., Adam, J., Chiarella, D., Roberts, D.G., Bally, A.W., Eds.; Elsevier: Amsterdam, The Netherlands, 2020; pp. 149–167. [[CrossRef](#)]
65. Labaume, P.; Sheppard, S.; Moretti, I. Fluid flow in cataclastic thrust fault zones in sandstones, Sub-Andean Zone, Southern Bolivia. *Tectonophysics* **2001**, *340*, 141–172. [[CrossRef](#)]
66. Muñoz-López, D.; Cruset, D.; Cantarero, I.; Benedicto, A.; John, C.M.; Travé, A. Fluid Dynamics in a Thrust Fault Inferred from Petrology and Geochemistry of Calcite Veins: An Example from the Southern Pyrenees. *Geofluids* **2020**, *2020*, 815729. [[CrossRef](#)]
67. Yardley, B.; Warren, C. (Eds.) *An Introduction to Metamorphic Petrology*, 2nd ed.; Cambridge University Press: Cambridge, UK, 2021; Volume 334. [[CrossRef](#)]
68. Del Moro, A.; Di Pisa, A.; Oggiano, G.; Villa, I.M. Isotopic ages of two contrasting tectono-metamorphic episodes in the Variscan chain in northern Sardinia. In Proceedings of the Geologia del Basamento Italiano, Convegno in Memoria di Tommaso Cocozza, Siena, Italy, 21–22 March 1991; Volume 33–35.
69. Dack, A. Internal Structure and Geochronology of the Gerrei Unit in the Flumendosa Area, Variscan External Nappe Zone, Sardinia, Italy. Ph.D. Thesis, Boise State University, Boise, Idaho, 2009; p. 116.
70. Brotzu, P.; Callegari, E.; Secchi, F.A. The search for the parental magma of the high-K calc-alkaline igneous rock series in the southernmost Sardinia Batholith. *Per. Mineral.* **1994**, *62*, 253–280.

CHAPTER II

Mineralogy of the scheelite-bearing ores of Monte Tamara, SW Sardinia: insights for the evolution of a Late Variscan W–Sn skarn system

Matteo L. Deidda^{1*}, Stefano Naitza¹, Marilena Moroni², Giovanni B. De Giudici¹, Dario Fancello¹, Alfredo Idini¹ and Andrea Risplendente²

¹ Department of Chemical and Geological Sciences, University of Cagliari, 09042, Monserrato (CA), Italy
² Dipartimento di Scienze della Terra, Università degli Studi di Milano, Via Luigi Mangiagalli, 34, 20133 Milano MI, Italy

Submitted 28 March 2022
Accepted 18 October 2022
Published 21 November 2022

Mineralogical Magazine – Cambridge University Press



Article

Mineralogy of the scheelite-bearing ores of Monte Tamara, SW Sardinia: insights for the evolution of a Late Variscan W–Sn skarn system

Matteo L. Deidda^{1*} , Stefano Naitza¹ , Marilena Moroni², Giovanni B. De Giudici¹ , Dario Fancello¹ , Alfredo Idini¹ and Andrea Risplendente²

¹Dipartimento di Scienze Chimiche e Geologiche, Università degli Studi di Cagliari, Cittadella Universitaria, Blocco A, 09042 Monserrato CA, Italy; and ²Dipartimento di Scienze della Terra, Università degli Studi di Milano, Via Luigi Mangiagalli, 34, 20133 Milano MI, Italy

Abstract

Southwestern Sardinia, Italy, hosts several skarn, W–Sn–Mo greisen and hydrothermal deposits related to a 289±1 Ma Late Variscan granite suite. Among them, the most representative scheelite-bearing skarns belong to the San Pietro and Sinibidraxiu localities, in the Monte Tamara area, Sulcis region. The San Pietro deposit is a typical calc-silicate skarn whereas Sinibidraxiu is a sharply bounded orebody hosted in a marble unit. Optical petrographic observations and compositional data of major and trace elements were obtained for samples from both localities. San Pietro data suggests evolution from an oxidising prograde skarn stage (andradite–diopside, hematite and scheelite), to progressively more reducing conditions from the early retrograde (magnetite–cassiterite) to the late sulfide stage (arsenopyrite, stannite, molybdenite, Bi sulfosalts and Zn–Cu–Pb–Fe sulfides); Sinibidraxiu has diffuse carbonate–quartz intergrowths pseudomorphic over an early mineral assemblage with fibrous habit, followed by abundant ore mineral precipitation under reducing conditions (scheelite, arsenopyrite and Pb–Zn–Cu–Fe sulfides). Geothermometers indicate a comprehensive temperature range of 460–270°C for the sulfide stages of both deposits. The differences between the two deposits might be controlled by the distance from the source intrusion coupled with the different reactivity of the host rocks. The San Pietro mineralogy represents a more proximal skarn, contrasting with more distal mineralogical and chemical features characterising the Sinibidraxiu orebody (lack of Mo–Sn–Bi phases; LREE–MREE–HREE signature of scheelite). This investigation contributes for the first time to the identification of a W–Sn skarn system in SW Sardinia, thereby suggesting the Monte Tamara area and its surroundings as favourable for further exploration.

Keywords: Late Variscan, tin, tungsten, skarn system, hydrothermal, scheelite, cassiterite, stannite geothermometer, arsenopyrite geothermometer, SW Sardinia

(Received 28 March 2022; accepted 18 October 2022; Accepted Manuscript published online: 21 November 2022; Associate Editor: Irina O Galuskina)

Introduction

Skarns are a common class of ore deposits and are generally classified into seven major types of economic significance on the basis of the dominant economic metal (Fe, Au, Cu, Zn, W, Sn, Mo skarns; Einaudi *et al.*, 1981; Meinert *et al.*, 2005). In each major skarn type, their particular ore mineral associations, relative abundances and mineral composition are strongly dependent on the metallogenic features of the parental intrusions (Meinert *et al.*, 2005; Chang *et al.*, 2019). Skarn deposits are typically regarded as relevant sources of strategic and critical elements (Meinert *et al.*, 2005; Chang *et al.*, 2019; US Geological Survey, 2021). This has triggered new interest in these deposits in different European districts in which the historical mining areas host

numerous, poorly exploited and/or underexplored skarns; among them, W- and Sn-bearing skarns, which are typically poorly constrained in many Variscan regions of Europe (Burisch *et al.*, 2019). In the ore districts of SW Sardinia, W-bearing skarns hosted in the Palaeozoic basement and related to Late Variscan granitoids are mentioned only in older literature (Valera And Zuffardi, 1968, 1970; Valera, 1970; Venerandi Pirri, 1971; Verkaeren and Bartholomé, 1979; Aponte *et al.*, 1988), where scheelite was reported as an accessory mineral in association with Pb–Zn–Cu sulfide and Fe-oxide ores. Moreover, numerous old mine reports indicate only small amounts of scheelite in ore and in dressing plant concentrates, and the presence of cassiterite in the skarn ores is noted repeatedly in reports by mineral collectors (Brizzi *et al.*, 1992a, 1992b; Olmi *et al.*, 1995).

New research themes for critical raw materials in Sardinia (Naitza *et al.*, 2019) have revitalised interest in a broad re-examination of already known skarn-related deposits and mineral occurrences. Similarly, investigations of a Late Variscan

*Author for correspondence: Matteo L. Deidda, Email: deiddam.geo@gmail.com

Cite this article: Deidda M.L., Naitza S., Moroni M., De Giudici G.B., Fancello D., Idini A. and Risplendente A. (2023) Mineralogy of the scheelite-bearing ores of Monte Tamara, SW Sardinia: insights for the evolution of a Late Variscan W–Sn skarn system. *Mineralogical Magazine* 1–23. <https://doi.org/10.1180/mgm.2022.119>

F-bearing, ilmenite-series (Ishihara, 1981) ferroan granite suite, exposed extensively in SW Sardinia (GS1 suite: Conte *et al.*, 2017) and accompanied by Sn–W–Mo mineralisation, confirmed the metallogenic potential of this setting (Naitza *et al.*, 2015; Naitza *et al.*, 2017). The area of Monte Tamara, located in the southern part of SW Sardinia (Sulcis region), displays some of the most interesting and least known occurrences of W- and Sn-bearing Pb–Zn–Cu sulfide and Fe-oxide skarns, related spatially and possibly genetically to GS1 suite ferroan granites. This investigation provides the first detailed characterisation of the main occurrences of the Monte Tamara area and their different mineral parageneses, with the objective of better understanding the formation processes of the mineralisation, defining the spatial evolution of the skarn system and obtaining useful indications for W and Sn exploration in the Sardinian Variscan districts.

Geological setting

The Monte Tamara area is located in the Sulcis region, the SW edge of Sardinia, which represents a foreland area in the Southern Variscan chain (Rossi *et al.*, 2009). In the Sulcis region, two main Palaeozoic deformations occurred: (1) an initial kilometre-scale E–W trending syncline–anticline fold system

related to the Early–Middle Ordovician ‘Sardic Phase’ (Cocco *et al.*, 2018, 2022b, and references therein); (2) a Variscan multi-stage folding, resulting in amplification of the previous E–W structures followed by N–S and NNE–SSW-trending folds (Arthaud, 1963; Poll and Zwart, 1964; Funedda, 2009). The Variscan structures affect two main very low-grade sedimentary mega-sequences separated by an angular unconformity (‘Sardic unconformity’; Stille, 1939). The first Early Cambrian–Early Ordovician mega-sequence (Coccozza, 1979) includes two siliciclastic units (Nebida Formation and Cabitza Formation), a thick carbonate unit (Gonnesa Formation), and a thin nodular silty limestone unit (Campo Pisano Formation). The Gonnesa Formation is the host of the large MVT Pb–Zn sulfide deposits of the Iglesiente–Sulcis district (Boni *et al.*, 1996). The second mega-sequence is a thick Middle–Late Ordovician siliciclastic sequence (Leone *et al.*, 1991), capped by Silurian–Early Devonian carbonaceous black shales and limestones.

The Monte Tamara area is located in the Early Cambrian–Early Ordovician pre-Variscan low-grade metasedimentary sequence, arranged in a large N–S anticline–syncline fold system related to the Variscan stage (Fig. 1). From the bottom to the top, the folding system includes meta-sandstones of the Nebida Formation (early Cambrian) overlapped by carbonate rocks of

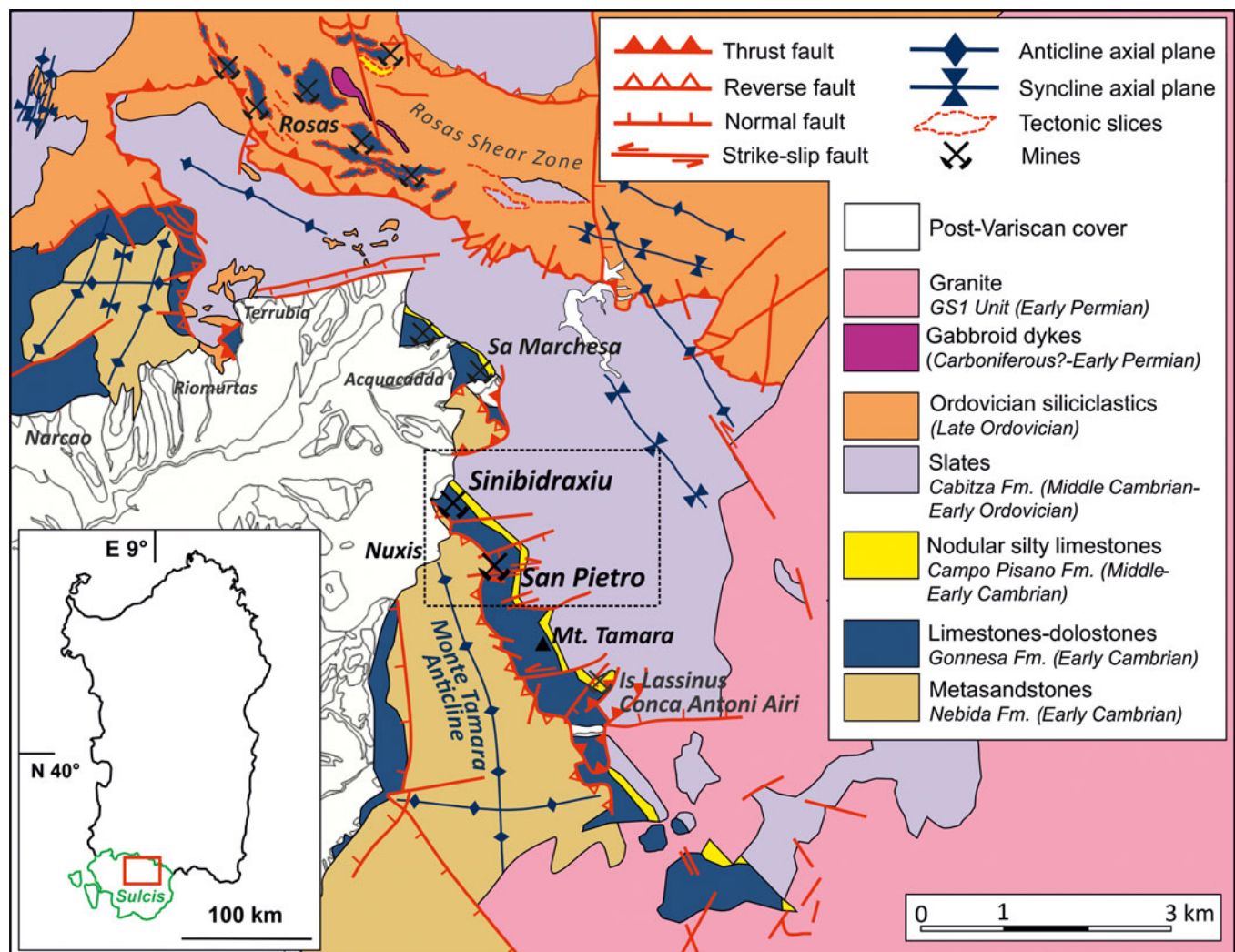


Fig. 1. Simplified geological map of the Monte Tamara area, SW Sardinia; the San Pietro and Sinibidraxiu abandoned mines are highlighted by the black rectangle.

the Gonnese Formation (early Cambrian), nodular silty limestones of the Campo Pisano Fm (middle–early Cambrian) and slates from the Cabitza Formation (middle Cambrian–early Ordovician). Tectonic contacts between these formations are produced by low-angle NNW–SSE striking reverse faults and later steeply dipping NE–SW striking normal faults (Barca *et al.*, 2009). During Late Variscan post-collisional stages the Sulcis region, including the Monte Tamara area, was intruded by a granite suite ('GS1 suite', Conte *et al.*, 2017). The GS1 suite consists of F-bearing, ferroan ($\text{FeO}/[\text{FeO} + \text{MgO}] > 0.90$) ilmenite series, slightly peraluminous monzogranites and leucogranites (Conte *et al.*, 2017). Relevant accessory minerals are ilmenite, xenotime-Y and fluorite. Intrusive bodies are affected locally by alkaline metasomatism and greisenisation with associated Mo–W–Sn mineralisation (Naitza *et al.*, 2017). The suite was emplaced at shallow crustal levels (~ 1 kbar; Conte *et al.*, 2017) in the Early Permian (289 ± 1 Ma by Re–Os on molybdenite; Boni *et al.*, 2003), forming extended low-angle-dipping bodies under the metasedimentary formations (Naitza *et al.*, 2017). As a result, evidence for contact-metamorphism (spotted schists, marbles, skarns and hornfelses on the Nebida, Gonnese-Campo Pisano and Cabitza Formations) and skarn mineralisation is common. Skarn deposits in this region are located typically along pre-existing Variscan structures and tectonic contacts between carbonate and siliciclastic units. These structural relationships are particularly evident in the neighbouring, highly-deformed Rosas mine area, where numerous mineralised skarns occur in limestone–dolostone tectonic slices throughout the Ordovician siliciclastic sequence (Cocco *et al.*, 2022a; Funedda, 2009).

The San Pietro and Sinibidraxiu orebodies

The Monte Tamara area hosts numerous mineworkings among which the most important were the San Pietro and Sinibidraxiu historic mines. These have been active since the late 19th Century until the second half of the 20th Century and exploited Zn–Pb–Cu–As ores. Although the presence of scheelite was known (Valera and Zuffardi, 1968, 1970; Valera, 1970) its occurrence remained uncharacterised and both deposits have been described generically as skarn-type (Salvadori and Zuffardi, 1961). However, despite many similarities, the San Pietro and Sinibidraxiu orebodies exhibit significant differences in terms of geometry, texture, gangue and mineral assemblages.

The San Pietro mine (Fig. 1) consisted of five underground mining levels through a vertical depth of ~ 70 m (Fig. 2a). The mine exploited a 0.5–5 m thick and irregular, steeply dipping band of dark green skarn (Fig. 3a) located between the meta-sandstones (Nebida Formation) and greyish black marbles (Gonnese Formation) with disseminated Zn–Pb–Cu sulfides and narrow subvertical veins. Well-exposed mineralised skarn outcrops are limited to an open excavation and a stope close to a shaft at the top of the mine (level 377 in Fig. 2a). The ore is a 5 m thick, NW–SE striking and steeply SW-dipping band, consisting of four main zones (1–4 in Fig. 3a). From the meta-sandstones to the marbles: the first zone (1) is a 50 cm thick garnet–clinopyroxene–wollastonite skarn band with magnetite, chalcopyrite and scheelite; followed by (2) a zone of 30 cm thick magnetite and sphalerite band in a garnet and amphibole gangue; (3) the magnetite band grades towards an arsenopyrite–sphalerite–chalcopyrite–galena zone; and (4) towards the contact with the marbles, a 30 cm thick band of massive magnetite hosts

subordinate chalcopyrite and mm-scale dispersed crystals of scheelite (observed under short-wave UV light) in an amphibole gangue. Due to the inaccessibility of underground mineworks and to the scarcity of skarn outcrops, hand specimens from the lower parts of the orebody (Fig. 2a) were collected from small ore stockpiles in front of the main adits. They include medium- to coarse-grained dark green garnet, clinopyroxene and wollastonite rocks with magnetite and chalcopyrite cross-cutting veinlets and disseminations of millimetric crystals of scheelite. Chalcopyrite, galena and sphalerite are commonly found as space-filling veins and grains in garnet–clinopyroxene specimens, and in retrograde amphibole- and epidote-rich facies. Specimens from the massive sulfide veins include fine- to medium-grained aggregates of chalcopyrite, sphalerite, arsenopyrite, galena and pyrite, commonly intergrown with magnetite. Secondary Fe–Cu–Zn–As minerals are common and renowned among mineralogists and mineral collectors (<https://www.mindat.org/loc-56421.html>: San Pietro Mine, Tamara Mountain, Nuxis, South Sardinia Province, Sardinia, Italy).

The Sinibidraxiu mine is located on the NW edge of the Monte Tamara ridge, ~ 2 km north of the San Pietro mine (Fig. 1). The mine can be accessed underground by an E–W stope of 200 m in length, excavated primarily in the Cambrian carbonate rocks of the Gonnese Formation (Fig. 2b). The thermal recrystallisation increases eastwards, and limestone–dolostone grade into marbles with sporadic disseminations of Zn–Pb sulfides. In the main orebody is a 1 m thick and 4 m large, vertical and flattened chimney hosted in dolomitic marbles. This is located at the intersection between two NNE–SSW and ESE–WSW striking fractures (Fig. 2b), and extends for ~ 60 m upwards to the surface, where it presents as a small gossan deposit. In the underground exposure, five zones (1–5 in Fig. 3b) can be recognised. Zone 1 is a 30 cm thick arsenopyrite + scheelite + Ca–Mg-carbonates association. Arsenopyrite is the most abundant mineral occurring as lustrous grey, idiomorphic and centimetre-sized crystals, intergrown with carbonates and milky-white idiomorphic scheelite crystals. Scheelite ranges from few mm to 2 cm in size and can be distinguished from carbonates under short-wave ultraviolet light. In the 20 cm thick-zone 2, arsenopyrite, carbonates and quartz are the most abundant minerals, with subordinate scheelite and sphalerite. Arsenopyrite, less abundant than in zone 1, is enclosed in a pale greenish carbonates and quartz matrix forming large radiate/fibrous aggregates. Scheelite here occurs as millimetre- to centimetre-sized grains, scattered irregularly inside the carbonates–quartz aggregates. Arsenopyrite decreases gradually towards zone 3 in favour of a sphalerite \pm scheelite association in the carbonates–quartz matrix, here assuming a brownish-green colour and forming larger radiate aggregates (2 cm in diameter). Centimetre-sized grains of dark sphalerite are observed at the core of the aggregates, resembling cockade-type textures. Scheelite disseminations within these cockades become more sporadic. Zone 4 is an arsenopyrite + calcite veinlet marking the contact between the ore and marbles. Lastly, irregular veinlets and pockets of massive sulfides of zone 5, consisting of sphalerite, arsenopyrite, chalcopyrite, galena and pyrite associated with calcite–dolomite and baryte, crosscut the other associations. The macroscopic features of the ores in representative samples are shown in Fig. 4.

Materials and methods

Two main sites of the Monte Tamara area have been surveyed and sampled in this study: the San Pietro mine and the Sinibidraxiu

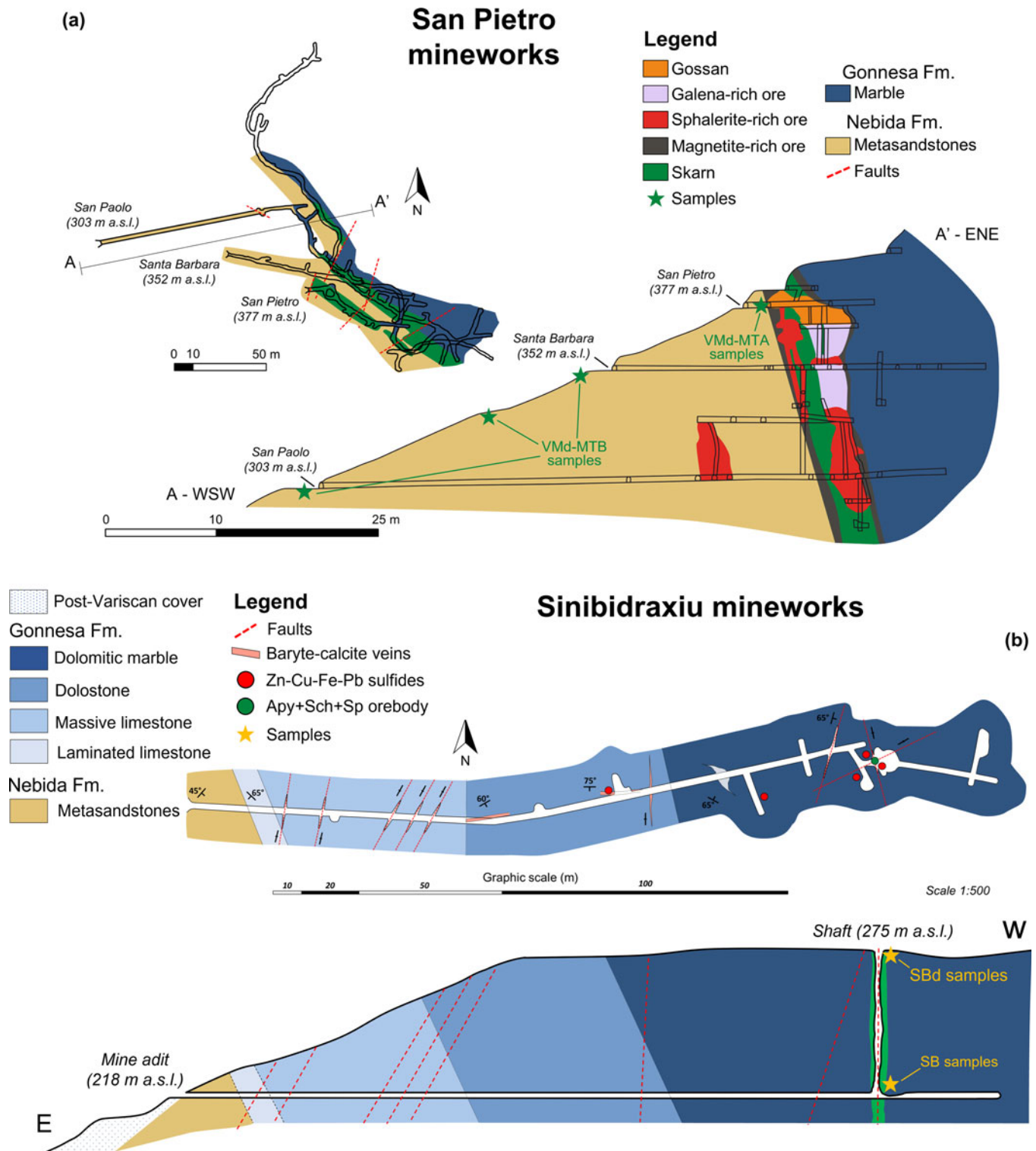


Fig. 2. Geological sketches and cross-sections of the San Pietro (a) and Sinibidraxiu (b) mines with sampling points indicated in the cross-sections. At San Pietro, VMd samples were collected from mine dumps across all levels of the mine; MTB and MTA samples belong to the lower and upper levels respectively. At Sinibidraxiu, SB samples were collected from the outcrops at the lower level of the mine; SBd samples were collected from the mine dumps at the upper level. In (a) the plant and the projection of the mineworks in the A-A' cross-section have been modified after Salvadori and Zuffardi (1961) and old mine maps, respectively. Mineral abbreviations (Warr, 2021): Apy = arsenopyrite; Sch = scheelite; Sp = sphalerite.

mine. Broad sampling from skarn and wall-rock outcrops, mine dumps and from the ores exposed in underground stopes was carried out. In each locality, preliminary evaluation for the presence of scheelite in the exposed ores was performed with a short-wave

ultraviolet-light torch. After field observations (Fig. 3), a selection of more than a hundred samples was made on the basis of their macroscopical features of mineralisation and texture (Fig. 4, Supplementary table S0). After the sampling, 23 thin sections,

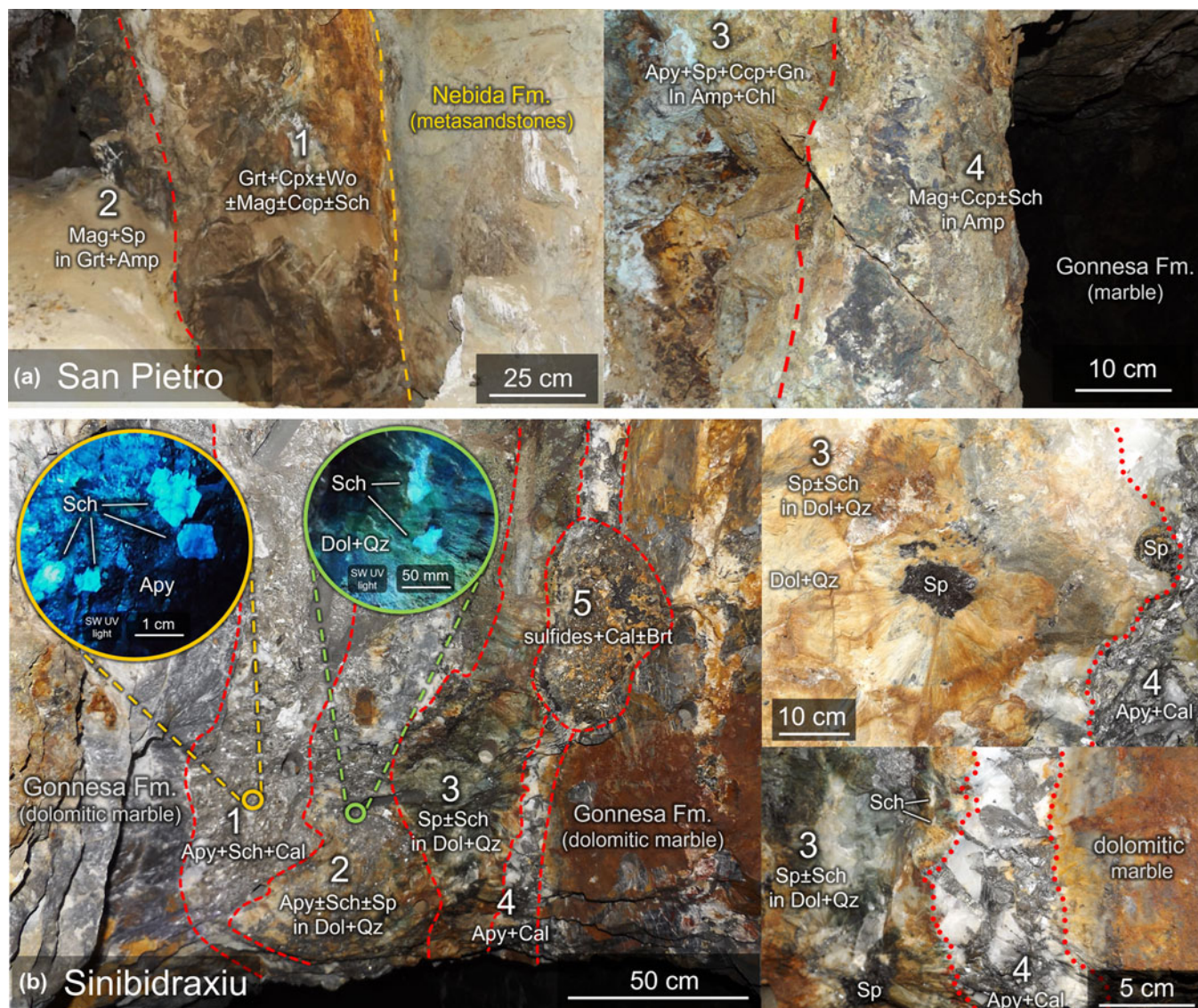


Fig. 3. Macroscopic zonation of the orebodies based on the occurrence of the major phases. At San Pietro (a), four main assemblages can be recognised and consist of: (1) magnetite + chalcopyrite ± scheelite in a garnet + clinopyroxene ± wollastonite gangue; (2) magnetite + sphalerite in a garnet + amphibole gangue; (3) arsenopyrite + sphalerite + chalcopyrite + galena in an amphibole + chlorite gangue; (4) magnetite + chalcopyrite ± scheelite in amphibole gangue. At Sinibidraxiu, five zones have been recognised: (1) arsenopyrite + scheelite and calcite; (2) arsenopyrite ± scheelite ± sphalerite in a dolomite–quartz gangue; (3) sphalerite ± scheelite in a dolomite–quartz gangue; (4) arsenopyrite and calcite; (5) sulfides (arsenopyrite, sphalerite, chalcopyrite, galena) in a calcite–baryte gangue. For each zone of the two deposits, the corresponding thin sections, polished mounts and polished slabs are reported in Supplementary Tables. Mineral abbreviations (Warr, 2021): Grt = garnet; Cpx = clinopyroxene; Wo = wollastonite; Amp = amphibole; Chl = chlorite; Mag = magnetite; Sch = scheelite; Apy = arsenopyrite; Sp = sphalerite; Ccp = chalcopyrite; Gn = galena; Cal = calcite; Dol = dolomite; Qz = quartz; Brt = baryte.

three polished slabs and 20 polished mounts were made from San Pietro (labelled VMD, MTB and MTA); six thin sections and 15 polished mounts were made from Sinibidraxiu (labelled SB and SBd). Thin sections and polished rock chips were investigated by optical microscopy in transmitted and reflected light and selected samples underwent scanning electron microscopy (SEM) analyses at CESAR laboratories of Università di Cagliari, using a Quanta FEI 200 unit equipped with a Thermo Fischer Ultradry EDS detector under low-vacuum conditions, 25–30 KeV voltage and 0.3–0.5 torr variable pressure. Quantitative wavelength dispersion spectrometry (WDS) microanalyses of sulfides, oxides and silicates were performed by means of a JEOL JXA–8200 electron probe equipped with five wavelength-dispersive spectrometers at the Dipartimento di

Scienze della Terra, Università Statale di Milano. The elements analysed with standards (pure metal or mineral), analytical/spectral lines, monochromators and detection limits in brackets are: Zn (Zn, $K\alpha$, LIFH, 650); Fe (fayalite, $K\alpha$, LIFH, 330); Cd (Cd, $L\alpha$, PET, 280); Cu (Cu, $K\alpha$, LIFH, 550); Ag (Ag, $L\alpha$, PET, 260); Ni (nickeline, $K\alpha$, LIFH, 350); Co (Co, $K\alpha$, LIFH, 350); Ge (Ge, $L\alpha$, TAP, 230); In (In, $L\alpha$, TAP, 600); Mn (rhodonite, $K\alpha$, LIFH, 350); Pb (galena, $M\alpha$, PET, 450); Sn (Sn, $L\alpha$, TAP, 350); Bi (Bi, $M\alpha$, PET, 330); Sb (Sb, $L\alpha$, TAP, 450); As (nickeline, $L\alpha$, TAP, 200); Te (Te, $L\alpha$, TAP, 500); S (pyrite, $K\alpha$, PET, 100); Se (HgSe, $K\alpha$, LIFH, 200); Ca (grossular, $K\alpha$, PETH, 140); Si and Al (grossular, $K\alpha$, TAP, 200 and 140); Na (omphacite, $K\alpha$, TAP, 240); K (K-feldspar, $K\alpha$, PETH, 170); Mg (olivine, $K\alpha$, TAP, 200); Ti (ilmenite, $K\alpha$, PETJ, 220); Cr (Cr, $K\alpha$, PETJ, 400); V

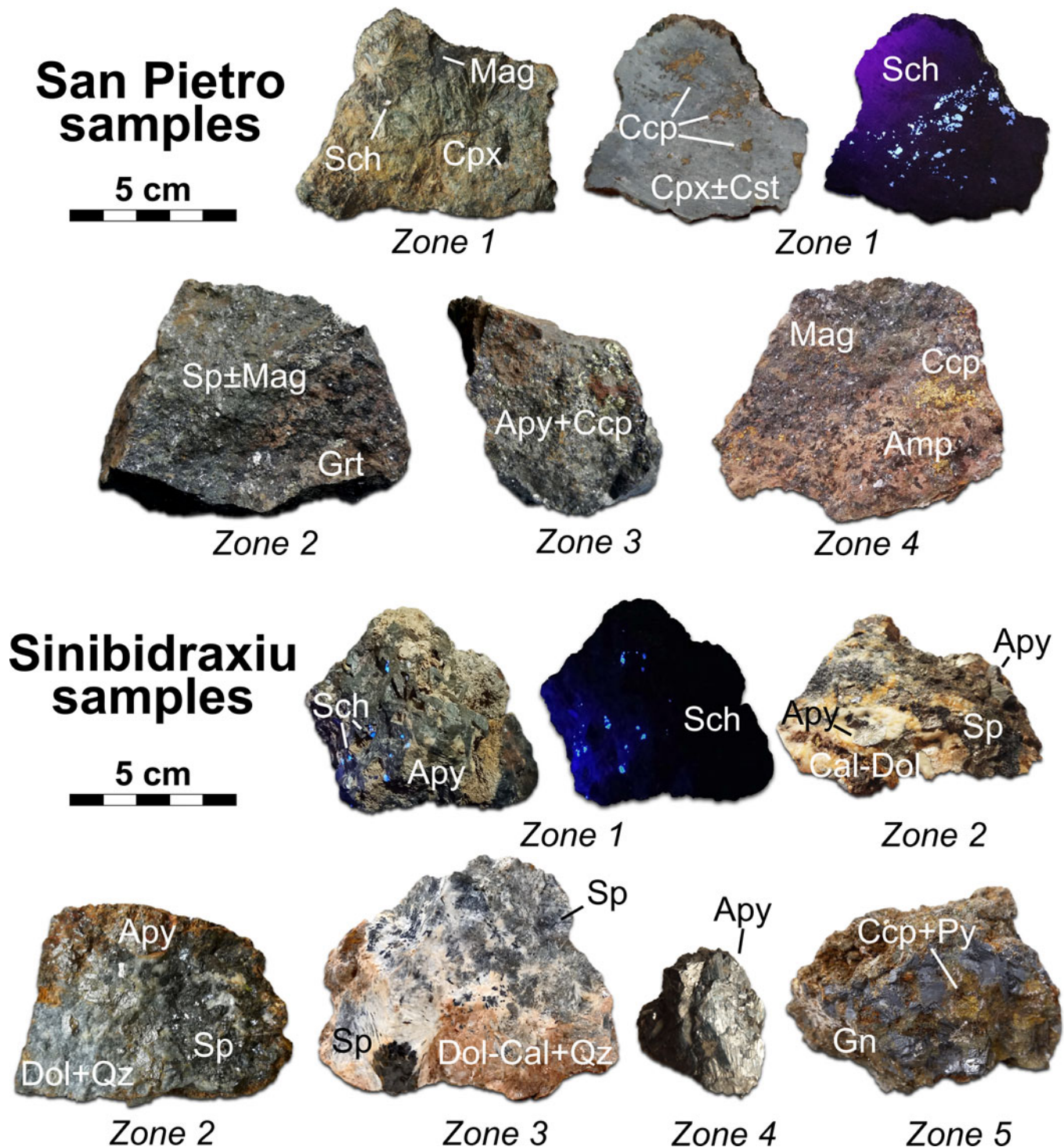


Fig. 4. Representative specimens from each zone of the San Pietro and Sinibidraxiu orebodies from which the samples indicated in Supplementary Tables have been selected. Mineral abbreviations (Warr, 2021): Grt = garnet, Cpx = clinopyroxene; Amp = amphibole; Chl = chlorite; Mag = magnetite; Sch = scheelite; Apy = arsenopyrite; Sp = sphalerite; Ccp = chalcopyrite; Gn = galena; Py = pyrite; Cal = calcite; Dol = dolomite; Qz = quartz; Brt = baryte.

(V, $K\alpha$, LIFH, 350); and W (W, $L\alpha$, LIFH, 2000). The analytical conditions for the electron beam were: accelerating voltage = 15 kV, beam current = 5 nA, beam diameter = 1–2 μm , counting time of 30 s on peak and 10 s on background for each element. Elemental concentrations were determined after applying the $\varphi(\rho z)$ algorithm and corrections for X-ray fluorescence, absorption, atomic number (Z) and matrices, and by evaluating spectral

interferences. Analyses were performed after verifying that $I_{x\text{std}}/I_{\text{std}}$ was 1.00 ± 0.01 for each element, where $I_{x\text{std}}$ was the intensity of the analysed standard and I_{std} the intensity of the same standard checked after calibration for each element. Quantitative, *in situ* trace-element analysis of scheelite crystals from Monte Tamara and Sinibidraxiu were performed by means of an inductively coupled mass spectrometer Thermo Fisher Scientific iCAP

RQ quadrupole coupled with a Teledyne Cetac Technologies Analyte Excite 193 nm excimer laser, equipped with a HelEx 2 volume sample cell. These instruments are located at the LASA laboratories, Earth Science Department, State University of Milano. Diameters of laser spots were of 40 μm . The repetition rate was of 10 Hz with a fluence of 2 J/cm². The analytical routine included the acquisition of a background signal for 40 s, then analysis with laser ablation for 60 s, followed by 20 s of line purification. The NIST612 glass was used as the primary standard and the BCR-2g glass as a secondary standard. The Ca content determined by microprobe analysis was used as the internal standard for correcting the differences in performance in the ablation between the glass standards and the minerals. The software *Glitter* (Griffin *et al.*, 2008) was employed for the revision of the signals from the spectrometer, the recalculation and the data elaboration. The following elemental isotopes were analysed: ⁷Li, ⁹Be, ¹¹B, ²⁵Mg, ²⁹Si, ³¹P, ⁴³Ca, ⁴⁴Ca, ⁴⁵Sc, ⁴⁹Ti, ⁵¹V, ⁵³Cr, ⁵⁵Mn, ⁵⁹Co, ⁶⁰Ni, ⁶⁵Cu, ⁶⁶Zn, ⁶⁹Ga, ⁷³Ge, ⁷⁵As, ⁷⁷Se, ⁸⁵Rb, ⁸⁸Sr, ⁸⁹Y, ⁹⁰Zr, ⁹³Nb, ⁹⁵Mo, ¹¹¹Cd, ¹¹³In, ¹¹⁵In, ¹¹⁸Sn, ¹²¹Sb, ¹³³Cs, ¹³⁷Ba, ¹³⁹La, ¹⁴⁰Ce, ¹⁴¹Pr, ¹⁴⁶Nd, ¹⁴⁹Sm, ¹⁵¹Eu, ¹⁵⁷Gd, ¹⁵⁹Tb, ¹⁶³Dy, ¹⁶⁵Ho, ¹⁶⁷Er, ¹⁶⁹Tm, ¹⁷³Yb, ¹⁷⁵Lu, ¹⁷⁷Hf, ¹⁸¹Ta, ¹⁸²W, ²⁰⁵Tl, ²⁰⁸Pb, ²⁰⁹Bi, ²³²Th and ²³⁸U. Precision was better than 5% for rare earth elements (REE), large ion lithophiles and high-field-strength elements and better than 10% for other elements. Accuracy was within 2 σ of the preferred values. Mineral abbreviations throughout the text are used according to Warr (2021). The compositional data are shown in detail in Tables S1–14 in the Supplementary materials.

Mineral associations and micro-textures

The San Pietro orebody features a wide variety of gangue, ore minerals and micro-textures. Samples from zone 1 (Figs 3a–4)

of San Pietro include garnet, clinopyroxene, wollastonite, hematite, magnetite, scheelite, chalcopyrite, chlorite, amphibole, epidote, cassiterite, native Bi, bismuthinite, Bi–Pb–Ag–Cu sulfosalts, calcite and quartz. The association of zone 2 includes garnet, clinopyroxene, amphibole, carbonates, magnetite, sphalerite and subordinate hematite, chalcopyrite, cassiterite and stannite. In zone 3, amphibole, chlorite, sphalerite, chalcopyrite, arsenopyrite, cassiterite, stannite, molybdenite, native Bi, bismuthinite, Bi–Pb–Ag–Cu sulfosalts, galena, pyrrhotite, pyrite, marcasite and secondary Zn–Pb–Cu phases have been identified. The mineral association of zone 4 includes clinopyroxene, amphibole, magnetite, sphalerite, galena, chalcopyrite and pyrrhotite.

Compared to San Pietro, the orebody of Sinibidrauli is characterised by a simpler mineralogy. Moreover, the overall textural features of each mineral appear more homogeneous throughout the different zones identified in the underground exposure (Figs 3b–4). The mineral assemblage from zones 1 to 5 includes calcite–dolomite, quartz, arsenopyrite, scheelite, galena, sphalerite, chalcopyrite, pyrrhotite, pyrite and marcasite.

The San Pietro skarn

The mineral assemblage of zone 1 includes a wide variety of calc-silicates. Garnet is abundant and forms aggregates of idiomorphic crystals with anomalous birefringence characterised by sector and concentric patterns (Fig. 5a). Clinopyroxene is the most common calc-silicate, and forms millimetre to centimetre sized idiomorphic crystals (Fig. 5c), arranged in radiating or felt-like aggregates with interstitial calcite, scheelite (Fig. 5d) and, locally, fluorite (Fig. 5e). Tiny idiomorphic inclusions are enclosed occasionally in garnet rims. Epidote, chlorite (Fig. 5h) and semi-opaque carbonate aggregates (Fig. 5b) occur where garnet is more altered, whereas amphibole-rich (Fig. 5g) aggregates are

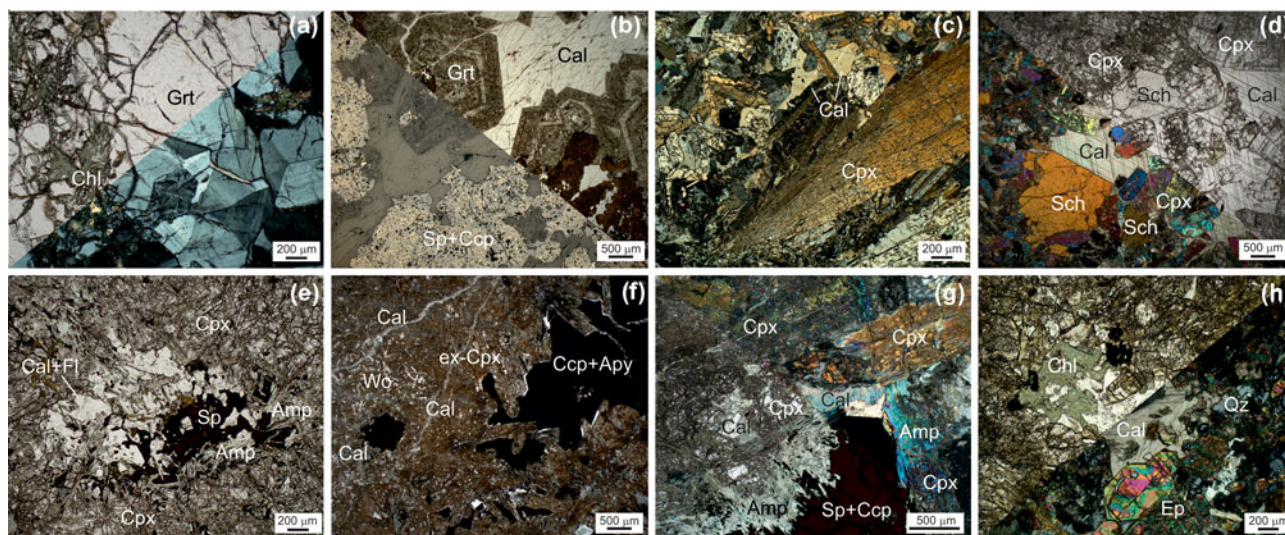


Fig. 5. Photomicrographs of prograde and retrograde mineral assemblages in the San Pietro skarn deposit: (a) fresh, anisotropic grossular garnet with minimal alteration by late epidote and chlorite (zone 1, sample MTB4; transmitted light, combined parallel and crossed nicols); (b) anisotropic, partly retrogressed andradite garnet with interstitial calcite, and replacement by sphalerite (+ chalcopyrite + magnetite) aggregates (zone 2, sample MTA3D; TL-RL, PN); (c) coarse-grained euhedral diopside with interstitial calcite (zone 1, sample VMD5b; TL, XN); (d) coarse-grained euhedral diopside intergrown with scheelite and calcite (zone 1, sample VMD5b; TL, comb PN-XN); (e) felt-like aggregate of fine-grained acicular diopside with interstitial calcite and fluorite, with blebby sphalerite intergrown with actinolite (zone 2, sample MTA4; TL, PN); (f) altered diopside groundmass enveloping scarce fibrous wollastonite and cross-cut by calcite veinlets; the interstitial chalcopyrite–arsenopyrite–molybdenite aggregates are rimmed by quartz (zone 3b, sample MTB1; TL, PN); (g) fine-grained acicular actinolite rimming interstitial sulfide (sphalerite–chalcopyrite) aggregates interstitial to coarse-grained diopside (zone 1, sample VMD5b; TL, comb. PN-XN); (h) aggregates of euhedral epidote deeply replacing grossular together with fine-grained chlorite (sample MTB4; TL, comb. PN-XN). Mineral abbreviations (Warr, 2021): Grt = garnet; Cpx = clinopyroxene; Wo = wollastonite; Ep = epidote; Amp = amphibole; Chl = chlorite; Sch = scheelite; Apy = arsenopyrite; Sp = sphalerite; Ccp = chalcopyrite; Fl = fluorite; Cal = calcite; Qz = quartz.

associated with altered clinopyroxene. Wollastonite and vesuvianite are rare. Scheelite is usually found in clinopyroxene-rich facies and consists of millimetre- to centimetre-sized subhedral and fractured individuals and aggregates, associated commonly with magnetite, chalcopyrite and cassiterite (Fig. 5d and 6a). Magnetite is very common in clinopyroxene-rich facies, occasionally forming fibrous aggregates replacing hematite ('mushketovite') or, more commonly granular aggregates associated with massive chalcopyrite, at margins of scheelite. Native Bi and Bi sulfosalts can be found as tiny inclusions in altered garnet, scheelite (Fig. 6f), and calcite and as disseminations in the clinopyroxene-rich facies with scheelite and magnetite–chalcopyrite (Fig. 6a). Cassiterite occurs as subordinate individuals scattered along the contacts between scheelite and magnetite–chalcopyrite and between clinopyroxene–amphibole and sulfides (Fig. 6b–e).

In zone 2, amphibole and carbonates are widespread and overgrow clinopyroxene (e.g. Fig. 5e) and garnet (Fig. 5b). Magnetite is abundant and occurs as radial aggregates (mushketovite) typically intergrown with galena. Cassiterite occurs as rare micro-inclusions (Fig. 6m–p) in sphalerite, usually

associated with magnetite. Hematite is observed occasionally as tiny relics in sphalerite. Sphalerite forms intergrowths with the amphibole–carbonate gangue, usually enveloping magnetite and galena. It features a variably patterned 'chalcopyrite disease' (Barton and Betkhe, 1987) with minor pyrrhotite micro-inclusions (Fig. 5b and 6l–n) and stannite blebs (Fig. 6l). Bismuth phases are rare in the sphalerite-rich samples, whereas scheelite appears to be absent.

The mineral association of zone 3 features sulfide-rich aggregates intergrown in the amphibole–chlorite and carbonate matrix overgrowing clinopyroxene (Fig. 5f). The main sulfide assemblage consists of sphalerite–chalcopyrite–galena ± pyrite aggregates (zone 3a). However, a chalcopyrite ± arsenopyrite with scarce sphalerite assemblage prevails locally (zone 3b). Compared to zone 2, sphalerite is associated more commonly with pyrite rather than magnetite, and hematite, cassiterite and stannite inclusions were not found. Where chalcopyrite and arsenopyrite become more prominent (zone 3b), native Bi and Bi sulfosalts occur commonly in peculiar round or egg-shaped aggregates enclosed by molybdenite 'rings' (Fig. 6h,i) and cassiterite is overgrown

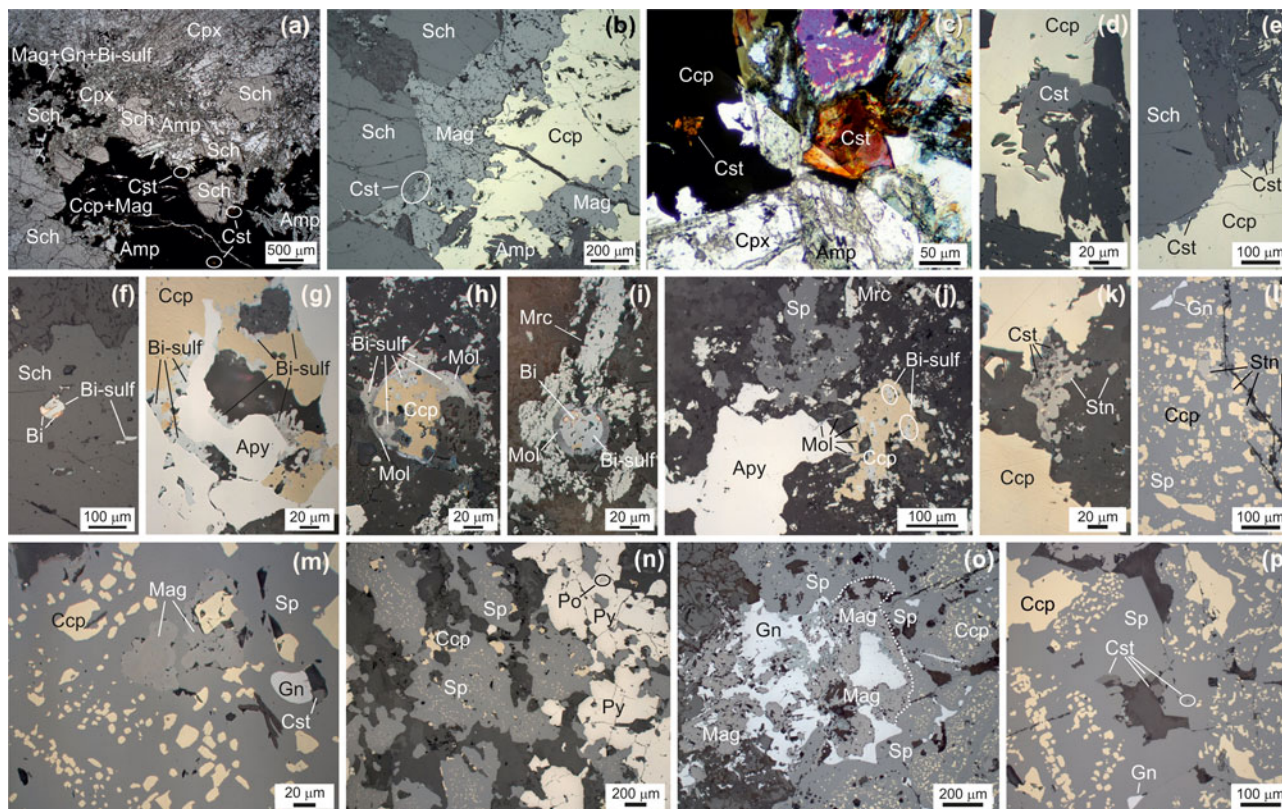


Fig. 6. Photomicrographs of ore minerals in the San Pietro skarn deposit. (a) scheelite intergrown with fibrous clinopyroxene, magnetite–chalcopyrite aggregates (with blebs of galena and Bi sulfosalts) rimmed by fibrous amphibole (zone 1, sample VMD5b; TL, PN); (b) cassiterite inclusions in magnetite intergrown with chalcopyrite and scheelite (zone 1, sample VMD5b; RL, PN); (c) cassiterite crystals associated with chalcopyrite and enclosed in the clinopyroxene matrix (zone 1, sample VMD5a TL, comb. PN–XN); (d,e) cassiterite aggregates intergrown with chalcopyrite and amphibole and rimming scheelite grains (zone 1, sample VMD5b; RL, PN); (f) native Bi and bismuthinite micro-inclusions in scheelite (zone 1, sample VMD5b; RL, PN); (g) Bi-rich sulfosalts intergrowths with chalcopyrite and arsenopyrite in the Cu-rich ore facies (zone 3b, sample MTB1; RL, PN); (h,i) ring-like molybdenite intergrown with Bi phases, chalcopyrite and marcasite, replacing pyrrhotite (zone 3b, sample MTB1; RL, PN); (j) arsenopyrite–chalcopyrite ore with Bi-rich sulfosalts (intergrown with galena), molybdenite and shredded sphalerite aggregate in carbonate-rich gangue (zone 3b, sample MTB1; RL, PN); (k) stannite crust-like aggregates replacing small cassiterite grains in the Cu-rich arsenopyrite-bearing ore facies (zone 3b, sample MTB1; RL, PN); (l) blebby stannite micro-inclusions in sphalerite with chalcopyrite disease in the Zn-rich ore facies (zone 2, sample MTA2; RL, PN); (m) sphalerite with chalcopyrite disease intergrown with granular magnetite (showing slight optical zoning), galena and cassiterite, in the pyrite-free Zn-rich ore facies (zone 2, sample MTA3; RL, PN); (n) intergrowths of sphalerite, chalcopyrite and pyrite (with few pyrrhotite relics) in magnetite-free, Zn-rich ore facies (sample MTB3; RL, PN); (o) magnetite–galena intergrowths in sphalerite-rich ore facies (zone 2, sample MTA3; RL, PN); (p) fine-grained euhedral cassiterite intergrown with sphalerite in sphalerite–magnetite ore facies (zone 2, sample MTA3; RL, PN). Mineral abbreviations (Warr, 2021): Cpx = clinopyroxene; Amp = amphibole; Sch = scheelite; Mag = magnetite; Cst = cassiterite; Bi = native bismuth; Ccp = chalcopyrite; Sp = sphalerite; Apy = arsenopyrite; Po = pyrrhotite; Bi-sulf = bismuth sulfosalts; Mol = molybdenite; Stn = stannite; Py = pyrite; Gn = galena; Mrc = marcasite.

occasionally by stannite aggregates (Fig. 6k). Galena and marcasite–pyrite overgrowing pyrrhotite are subordinate.

In zone 4 the gangue consists mostly of amphibole forming felt-like aggregates surrounding relic grains of clinopyroxene. Magnetite is widespread and occurs as mushketovite fibrous aggregates and massive aggregates, frequently enclosing anhedral galena grains with reabsorbed edges. However, galena also occurs at the edges of magnetite. Sphalerite with ‘chalcopyrite disease’ with the same features of zone 2 and 3 is also often found, whereas chalcopyrite and pyrite are very subordinate.

The Sinibidraxiu orebody

The gangue of the Sinibidraxiu orebody (zones 2–3) is fine-grained, semi-opaque and brownish. The characteristic

cockade-type textures observed in outcrops and hand samples consist of fibrous aggregates of fine-grained carbonates and quartz (Fig. 7a). Very fine-grained fibrous quartz is locally recrystallised to coarser clear, irregular aggregates associated generally with sulfide patches (Fig. 7b,c). Spathic calcite is commonly observed in the intergranular spaces between arsenopyrite, sphalerite and the gangue (zones 1–4). Among the ore minerals, arsenopyrite is by far the most abundant in zones 1 and 2, where it occurs as coarse-grained idiomorphic crystals (Fig. 7f). In zone 1, arsenopyrite is centimetre sized and inclusion-free, with interstitial sphalerite along fractures, whereas in zone 2 it contains abundant micro-inclusions of galena, sphalerite (Fig. 7g), and fibre-shaped inclusions of dolomite–quartz, occasionally extensively replaced by sphalerite and galena (Fig. 7g,h). Scheelite usually occurs as idiomorphic individuals (zones 1–3) associated with

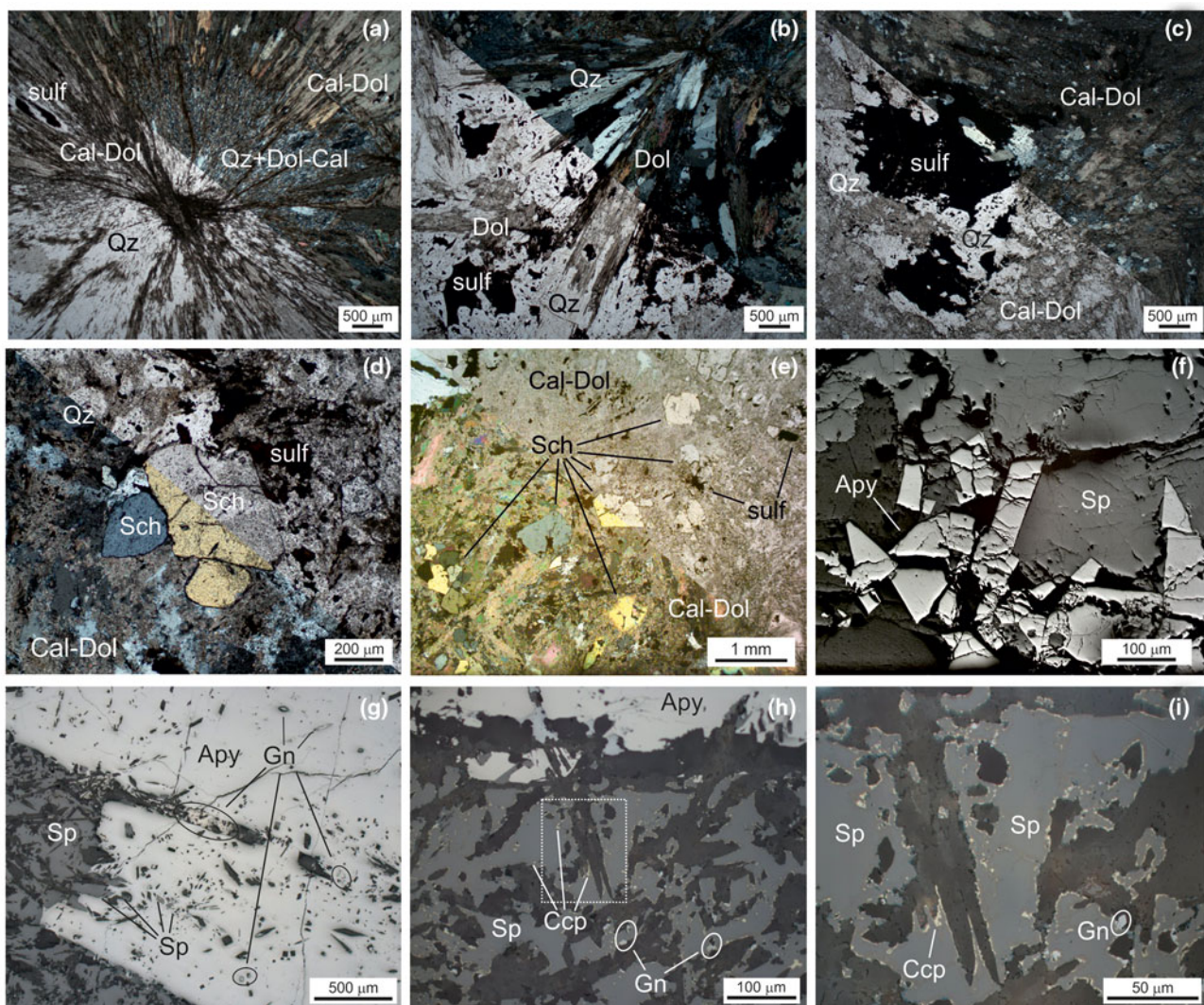


Fig. 7. Photomicrographs of gangue and ore mineral assemblages at the Sinibidraxiu skarn deposit: (a) fine-grained turbid dolomite and quartz replacing fibrous aggregates with interstitial sulfides enveloped in quartz (sample SB-c1; TL, comb. PN-XN); (b,c) sulfide patches interstitial to, and overgrowing, fibrous aggregates extensively replaced by fine-grained dolomite–quartz (sample SB-d; TL, comb. PN-XN); (d,e) idiomorphic scheelite crystals disseminated in the dolomite–quartz matrix (zone 3, samples SB11A and SB11B; TL, comb. PN-XN); (f) idiomorphic, fractured arsenopyrite surrounded by sphalerite (zone 2, sample SB8E; RL, PN); (g) arsenopyrite containing micro-inclusions of sphalerite, of galena and very abundant inclusions of the fibrous gangue (zone 2, sample SB12; RL, PN); (h) sphalerite–arsenopyrite border zone, rich in fibrous inclusions (zone 2, sample SB12; RL, PN); (i) close-up view of contacts between sphalerite and carbonate–quartz fibres: zones of higher transparency and dissemination of chalcopyrite and galena micro-grains mark the sphalerite–matrix contacts and microfractures (zone 2, sample SB12; RL, PN). Mineral abbreviations (Warr, 2021): Cal = calcite; Dol = dolomite; Qz = quartz; Sch = scheelite; Apy = arsenopyrite; Sp = sphalerite; Ccp = chalcopyrite; Gn = galena; Po = pyrrhotite; Py = pyrite; sulf = sulfides.

arsenopyrite (zone 1) and locally arranged in oriented seams and disseminations in the carbonate–quartz gangue (zones 2–3; Fig. 7d,e). Pyrrhotite, typically altered to fine-grained pyrite–marcasite intergrowths, has been observed occasionally at the edges of arsenopyrite (zone 2) or enclosed in chalcopyrite–galena aggregates. Sphalerite occurs as aggregates at the margins and in fractures of arsenopyrite (zone 1–2; Fig. 7f) and as interstitial to, and enveloping, the carbonate–quartz gangue (zones 2–3–4; Fig. 7g–i). In the first association, chalcopyrite and pyrrhotite inclusions are rare, whereas in the latter chalcopyrite–galena and subordinate pyrrhotite–pyrite–marcasite micro-inclusions are more common. Inclusions are distributed irregularly and concentrated at the sphalerite margins along the contact with the carbonate–quartz gangue (zone 2; Fig. 7i). This feature is also accompanied by a more pronounced transparency of sphalerite. Galena occurs as small, disseminated blebs and as large, network-like aggregates surrounding arsenopyrite crystals (zone 2), and disseminated variably elsewhere in the gangue and intergrown with sphalerite (zones 2–3–4; Fig. 7g–i). Chalcopyrite and pyrite–marcasite are interstitial to the carbonate–quartz gangue.

The paragenetic schemes for the San Pietro and Sinibidraxiu mineralisation, as deduced by the mineral assemblages and related textural features, are presented in Fig. 8.

Mineral compositions

Samples from San Pietro and Sinibidraxiu were investigated initially by SEM using energy dispersive spectroscopy (EDS) for semi-quantitative analysis and compositional maps, whereas quantitative mineral compositions were determined by electron probe microanalyses (EPMA) and laser-ablation inductively coupled mass spectrometry (LA-ICP-MS) on a selected set. Due to its paragenetic complexity, a larger set of samples from San Pietro has been analysed. The mineral composition of skarn and ore minerals (Tables S1–14 in Supplementary materials) are presented below for each mineral group, with comparisons for ore minerals between the different localities.

Skarn minerals

Garnet

Garnet crystals from San Pietro, are characterised either by concentric or sector birefringence (Table S1). The garnets belong to the grossular–andradite solid solution, though with a clear compositional distinction (Fig. 9a,b) between the sector zoned MTB4 garnet (Fig. 5a), enriched variably in the grossular end-member (82.4–33.7% Grs, 63.2–13.1% Adr and 3.0–1.6% Sps), and the concentrically zoned garnet from zone 2 (MTA3d sample; Fig. 5b), which plots close to the pure andradite end-member (99.6–93.5% Adr; 4.3–0% Grs; 3.0–0.4% Sps). In the MTB4 garnet the variations in the grossular, or Al_2O_3 , component reflect distinct core-to-rim zoning (Fig. 9b). Of the accessory elements, Ti (Fig. 9c) also displays a variable distribution in the MTB4 garnet compared to the restricted field for the MTA3d andradite, whereas Mn and Sn display similar ranges of variation in the two main garnet varieties (Fig. 9d,e). The garnet sporadically displays W contents above the EPMA detection limit (2000 ppm). The few data for the rare garnet in pyroxene-dominated skarn facies of zone 1 (sample VMd5b) show affinities with the grossular-enriched population. Notably, each garnet is Sn-enriched, with some maximum contents over 1 wt.% SnO_2 . In the element-distribution X-ray maps and profiles across the

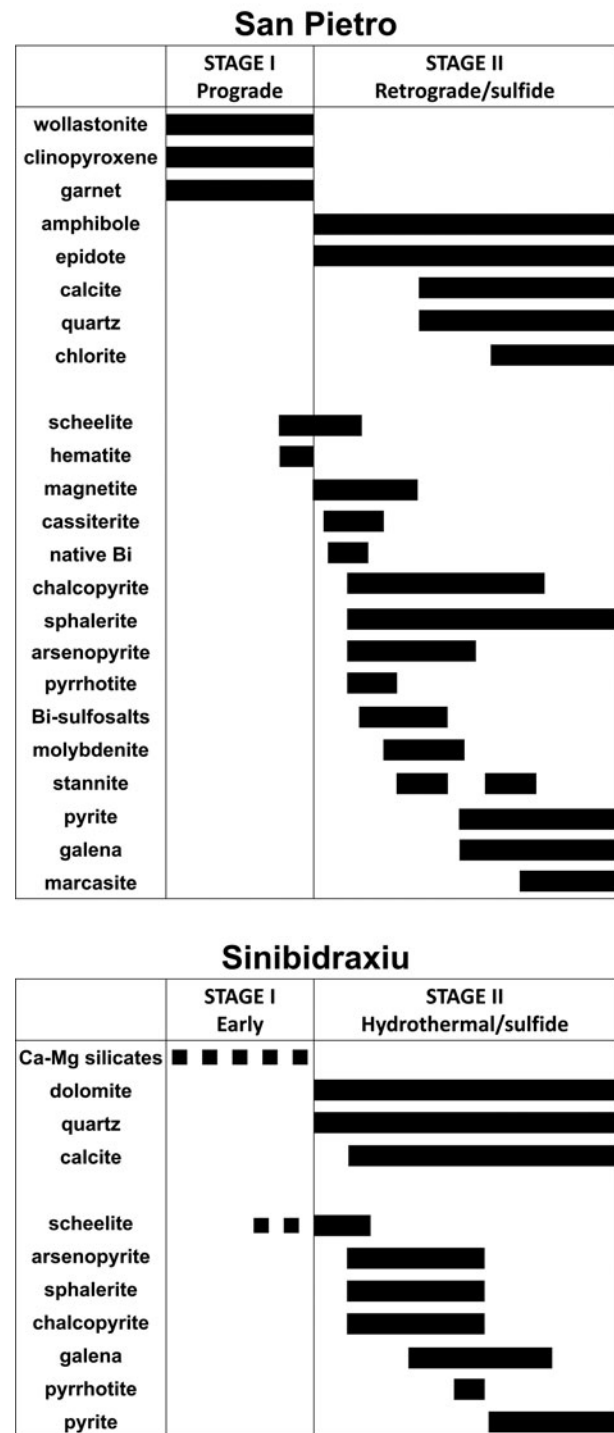


Fig. 8. Paragenetic sequence of the San Pietro and Sinibidraxiu orebodies.

garnet (Fig. 10), the Sn enrichments appear to correlate positively with Fe and negatively with Ti.

Clinopyroxene

All San Pietro clinopyroxene from zone 1 (Table S2), independently of grain size, are essentially diopside (Fig. 11a), with low Mn contents (rarely > 1 wt.% MnO; Fig. 11b,c). The Sn contents commonly exceed the microprobe detection limit of 350 ppm, and range from frequently >0.1 wt.% to 0.36 wt.% SnO_2 (Fig. 11c).

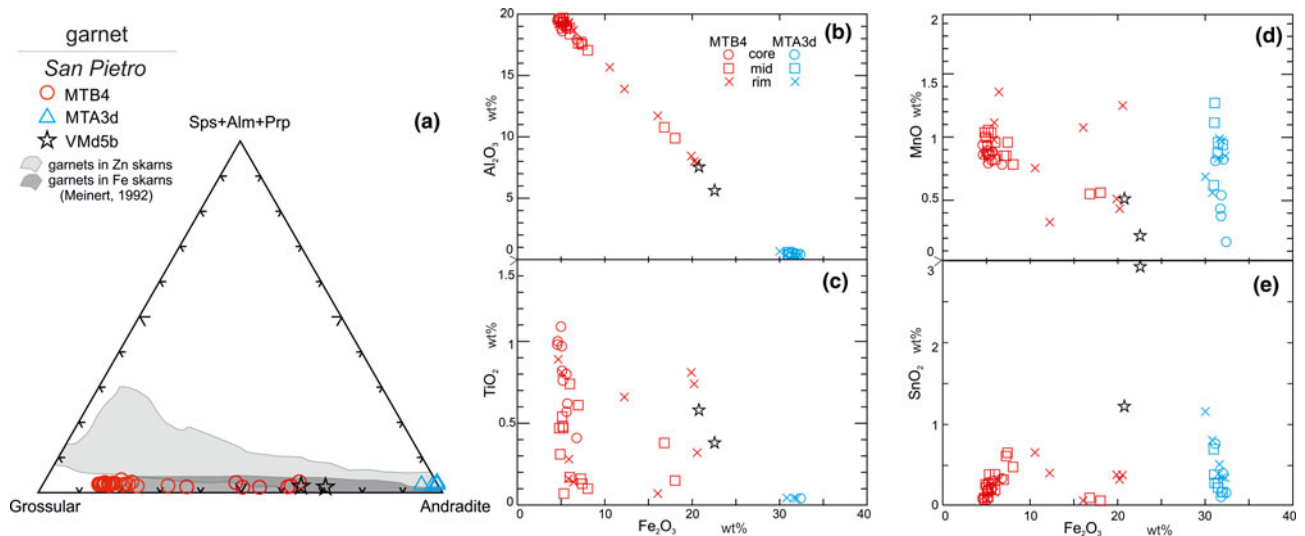


Fig. 9. Ternary (a) and binary compositional diagrams (b–e) for garnet from garnet-rich (MTB4, MTA3d) and garnet-poor (VMd5b) samples from the San Pietro skarn. Symbols in the binary diagrams represent data points from cores to rims.

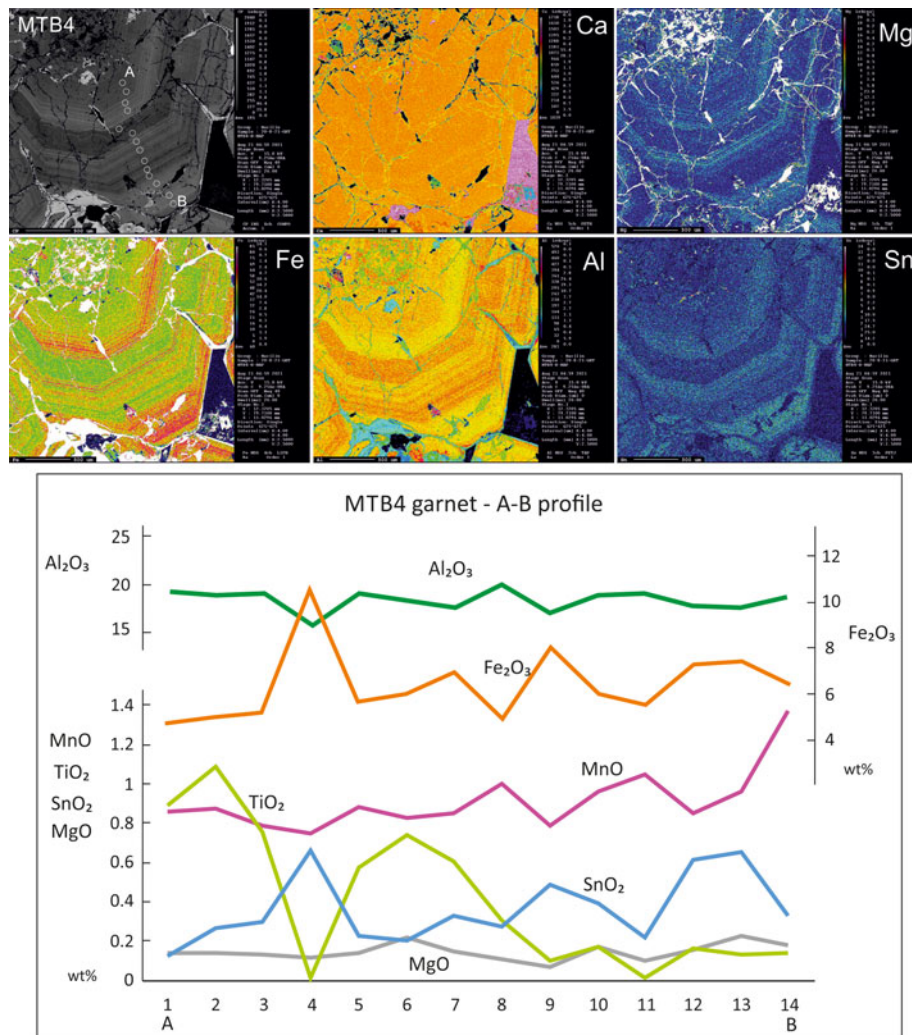


Fig. 10. Element distribution EPMA X-Ray maps from core to rim for one of the sector-zoned garnets in sample MTB4. The A–B profile in the BSE image shows the location of analytical points for data given in the graph.

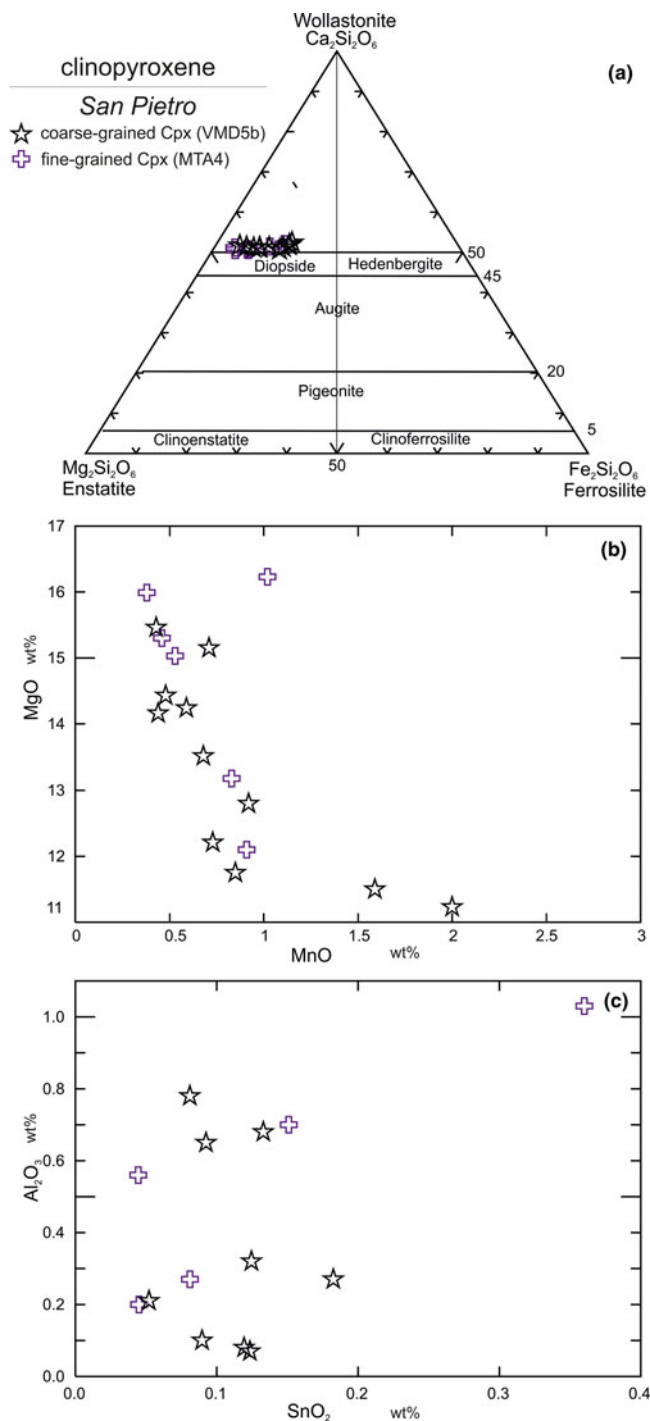


Fig. 11. Ternary (a) and binary compositional diagrams (b,c) for clinopyroxene from the San Pietro skarn, with grain size ranging from coarse (sample VMD5b) to fine (sample MTA4).

Amphibole

The limited compositional data (Table S3) for amphibole replacing coarse and fine grained clinopyroxene in zone 1 of the San Pietro skarn indicates they are all actinolite (Fig. 12a,b) with Sn contents up to 0.13 wt.% in some examples.

Epidote and chlorite

Epidote and minor chlorite occur as replacement phases on garnet in the San Pietro skarn. Epidote (Table S4) belongs to the

Fe-rich epidote end-member, with a minor piemontite component (Pmt₅₋₁₅) and notable concentrations of Sn (often > 0.1 wt.% SnO₂), probably inherited from the garnet substrate. Preliminary data for associated fine-grained chlorite aggregates (Table S5) indicate clinochlore compositions (e.g. Deer *et al.*, 1962), with low Sn, though Mn contents are similar to the original garnet (~1 wt.% MnO).

Ore minerals (sulfides and oxides)

Sphalerite

Sphalerite is the main sulfide ore mineral in the San Pietro skarn and displays variable compositional features (Table S6). On the basis of the Fe contents, three groups of sphalerite are distinguished (Fig. 13a). The Fe-rich group, with 11–13 wt.% Fe, is represented by sphalerite in the sphalerite–chalcopyrite–galena ± pyrite aggregates (zone 3a; sample MTB3) of San Pietro and by the cores of sphalerite from Sinibidraxiu (zone 3; sample SB12). The mildly ferriferous group, containing 4–8 wt.% Fe, corresponds to sphalerite of the chalcopyrite–scheelite-rich (zone 1; sample VMD5b), magnetite-rich (zones 2–3b; samples MTA3, MTA2, MTB1), and the chalcopyrite-rich (zone 3a; sample MTB1) assemblages of San Pietro. A third, Fe-poor group, characterised by 1.7–0.5 wt.% Fe, belongs to the chalcopyrite-rich assemblage of San Pietro (zone 3a), and the inclusion-rich rims of Sinibidraxiu sphalerite (zones 3–4, sample SB12). Cadmium values in San Pietro sphalerite (av. 1 wt.%) show a negative correlation with Zn (Fig. 13b), with the most Fe-rich sphalerite displaying the highest Cd contents (up to 1.7 wt.%). In contrast, Cd contents of Sinibidraxiu sphalerite are markedly lower (up to 0.5 wt.%) and unrelated to their Fe contents. A positive correlation with Fe, involving all analysed grains, can be observed for Mn (Fig. 13c), with sphalerite from Sinibidraxiu attaining the highest Mn contents (0.4–0.5 wt.%). The San Pietro sphalerite appear to be mildly cobaltiferous, whereas Ni rarely exceeds detection limits. Cobalt-bearing sphalerite occurs especially in the scheelite–chalcopyrite (zone 1; sample VMD5b) and in the sphalerite–magnetite ore facies (zones 2–3b; samples MTA3, MTA2, MTB1), where Co is commonly above the 350 ppm detection limit and may attain peak values >0.3 wt.% Co. Sporadic Co enrichments are also found in Sinibidraxiu sphalerite. Overall, both San Pietro and Sinibidraxiu sphalerite has low indium and tin contents. Indium is never above the EPMA detection limit, whereas Sn is found as sporadic enrichments (up to 0.27 wt.% Sn) mainly in the San Pietro sphalerite of the sphalerite–magnetite ore facies (zones 2–3b; samples MTA3, MTA2, MTB1). This is probably related to micro-inclusions of cassiterite and stannite. Germanium was detected sporadically below 0.1 wt.% in the San Pietro sphalerite cores of the chalcopyrite–scheelite (zone 1; sample VMD5b) and the sphalerite–magnetite ore facies (zones 2–3b; samples MTA3, MTA2, MTB1). Bismuth displays variable, although commonly high, concentrations (up to 0.3 wt.% Bi) in sphalerite from San Pietro and Sinibidraxiu (Fig. 13d); Ag is typically below the detection limit and locally up to 0.14 wt.%. Bismuth and Ag concentrations are coupled with variable Pb contents (up to 0.2 wt.%). The Bi, Ag and Pb contents of sphalerite are probably related to the presence of (sub-) micro-inclusions of the Bi–Pb–Ag–Cu sulfosalts (Lockington *et al.*, 2014), similar to those identified in the San Pietro ore (see below).

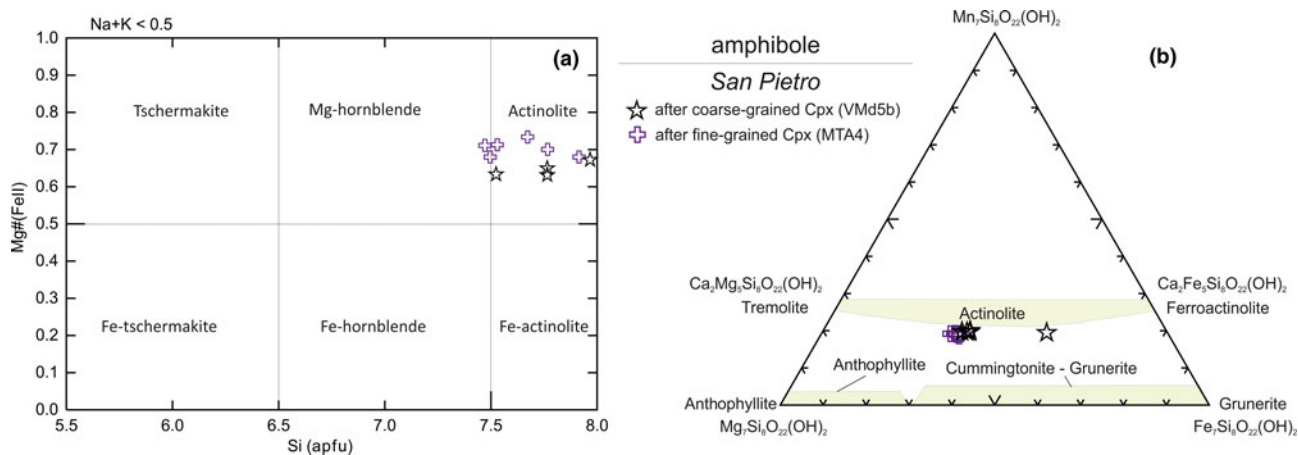


Fig. 12. Amphibole compositions of the San Pietro skarn according to the binary classification diagram (a) by Leake *et al.* (2003) and to the ternary diagram for Fe–Mn amphiboles (b) by Hawthorne *et al.* (2012).

Bi-bearing sulfosalts

Samples from San Pietro show a complex association of accessory Cu–Ag–Pb–Bi sulfosalts (Table S7), represented in the Ag + Cu vs. Bi + Sb vs. Pb ternary diagram (Fig. 14; Ivashchenko, 2021; Damian *et al.*, 2008; Voudouris *et al.*, 2008). On the basis of their different Bi–Ag–Pb–S quantitative ratios (Moelo *et al.*,

2008 and references therein), bismuthinite (Bi_2S_3), ‘phase 88.6’ ($\text{Cu}_{0.33}\text{Pb}_{0.33}\text{Bi}_{7.67}\text{S}_{12}$, Ciobanu and Cook, 2000), pekoite ($\text{PbCuBi}_{11}\text{S}_{16}\text{Se}_2$), cosalite ($\text{Pb}_2\text{Bi}_2\text{S}_6$), salzburgite–paarite ($\text{Cu}_{1.6}\text{Pb}_{1.6}\text{Bi}_{6.4}\text{S}_{12}$ – $\text{Cu}_{1.7}\text{Pb}_{1.7}\text{Bi}_{6.3}\text{S}_{12}$), gustavite ($\text{PbAgBi}_3\text{S}_6$), beryrite ($\text{Cu}_3\text{Ag}_2\text{Pb}_3\text{Bi}_7\text{S}_{16}$), xilingolite–lillianite ($\text{Ag}_x\text{Pb}_{3-2x}\text{Bi}_{2+x}\text{S}_6$ – $\text{Pb}_3\text{Bi}_2\text{S}_6$) ourayite ($\text{Pb}_4\text{Ag}_3\text{Bi}_5\text{S}_{13}$) and cupropavonite

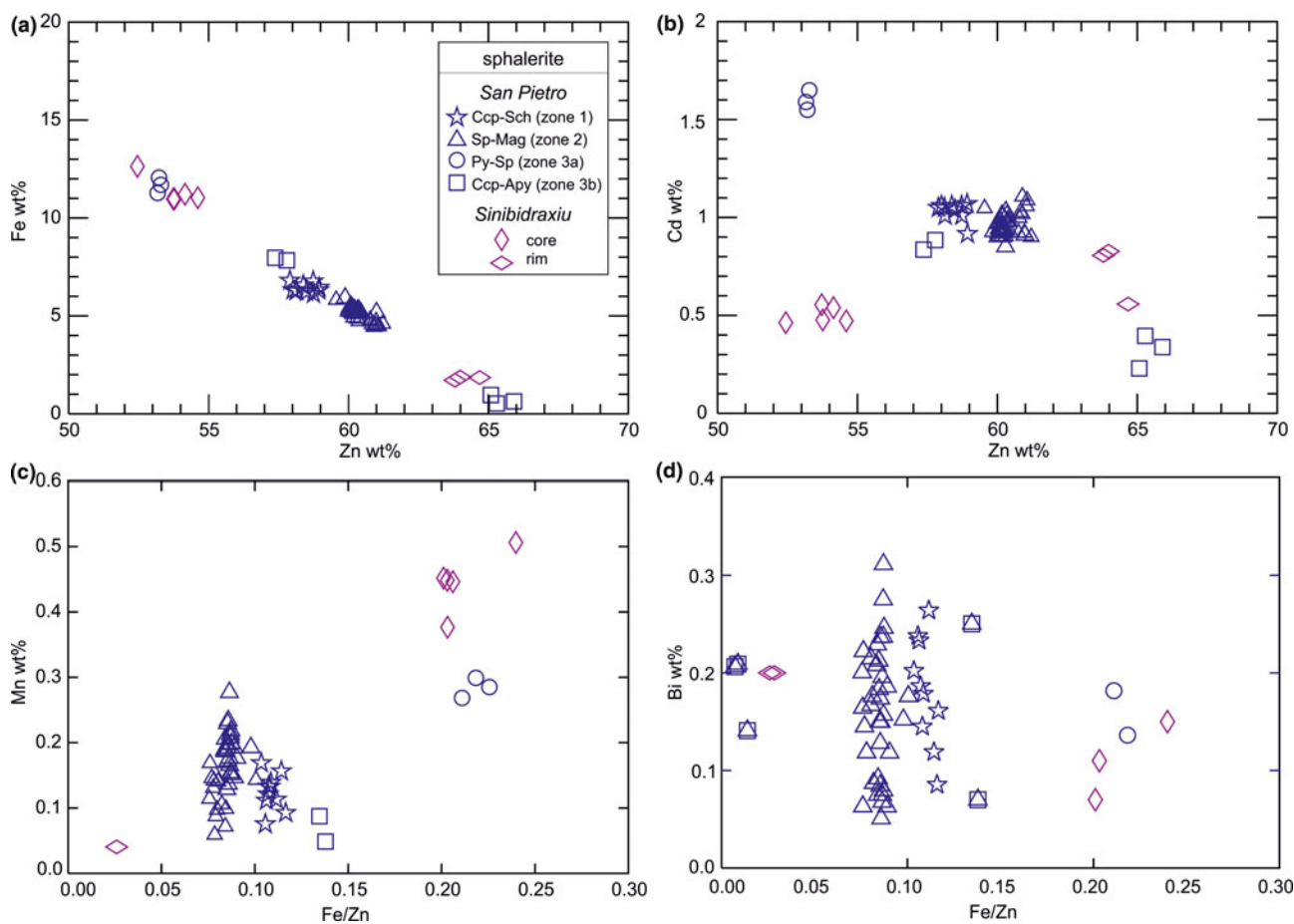


Fig. 13. Plots of sphalerite compositions (wt.%) for the San Pietro and Sinibidraxiu skarn deposits: (a,b) binary diagrams of major (Zn, Fe and Cd); and (c–f) selected accessory components (Mn, Bi) vs. Fe/Zn. The different symbols for San Pietro sphalerite correspond to the zones 1–2–3a–3b of the orebody; the symbols for Sinibidraxiu sphalerite refer to the core and rim composition.

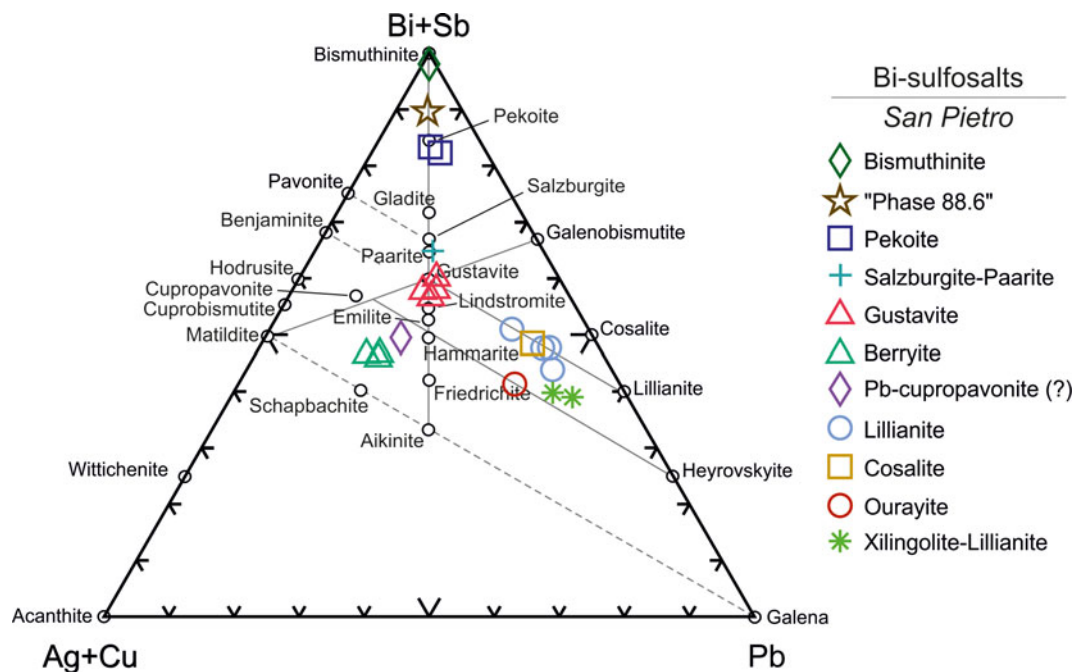


Fig. 14. Ternary diagram representing the compositions of the Bi-bearing sulfosalts detected in zone 3 of the San Pietro skarn (modified after Ivashchenko, 2021; Damian et al., 2008; Voudouris et al., 2008).

($\text{Cu}_{0.9}\text{Ag}_{0.5}\text{Pb}_{0.6}\text{Bi}_{2.5}\text{S}_5$) were identified. Bismuthinite occurs in both chalcopyrite–scheelite (zone 1; sample VMd5b) and sphalerite–pyrite ore facies (zone 3a; sample MTB3), whereas the other Bi phases occur in the chalcopyrite-rich facies only (zone 1–3a; samples VMd5b–MTB1). All the Bi phases display a mildly seleniferous character, with average Se contents of 0.58 wt.% and maximum at 1.5 wt.% Se. Maximum values were recorded in bismuthinite, which occasionally contains Pb (4 wt.%) or Cu (1 wt.%) contamination due to intergrowths with galena or chalcopyrite. Pekoite ($\text{PbCuBi}_{11}\text{S}_{16}\text{Se}_2$) is characterised by localised Sn maximum contents of 0.18 wt.%, probably due to contamination by the common stannite blebs in the chalcopyrite host. A phase with a composition intermediate between bismuthinite and pekoite was identified as the ‘phase 88.6’ ($\text{Cu}_{0.33}\text{Pb}_{0.33}\text{Bi}_{7.67}\text{S}_{12}$; Moelo et al., 2008 and references therein). One spot analysis showed a correspondence with the composition of salzburgite–paarite ($\text{Cu}_{1.58-1.67}\text{Fe}_{0.03-0.01}\text{Pb}_{1.65-1.72}\text{Bi}_{6.38-6.3}\text{S}_{12-12.06}$). Cosalite ($\text{Pb}_2\text{Bi}_2\text{S}_6$) has a Pb deficit (1.73 atoms per formula unit) coupled with a slight enrichment in Cu (0.35 apfu) which may be attributed to a Pb^{2+} – Cu^+ coupled substitution with Bi^{3+} (Moelo et al., 2008). At least five Ag-bearing sulfosalts were detected, with Ag ranging between 3.3 and 7.8 wt.%. Spots on gustavite ($\text{PbAgBi}_3\text{S}_6$) reveal variable Cu enrichments (locally >1 wt.%). Gustavite and berryite ($\text{Cu}_3\text{Ag}_2\text{Pb}_3\text{Bi}_3\text{S}_{16}$) display the highest Ag contents, with similar contents averaging 7.4 wt.% Ag. Lillianite was recognised on the basis of the $\text{Ag}_x\text{Pb}_{3-2x}\text{Bi}_{2+x}\text{S}_6$ structural formula proposed by Moelo et al. (2008), whereas phases corresponding closer to the lillianite simplified formula ($\text{Pb}_3\text{Bi}_2\text{S}_6$) were attributed generically to the xilingolite–lillianite polymorphs. The other identified phases, though with a certain degree of uncertainty, include ourayite ($\text{Pb}_4\text{Ag}_3\text{Bi}_5\text{S}_{13}$) with a Pb-enrichment over Ag ($\text{Pb}_{5.08}\text{Ag}_{1.88}\text{Bi}_{4.95}\text{S}_{13}$), and cupropavonite ($\text{Cu}_{0.9}\text{Ag}_{0.5}\text{Pb}_{0.6}\text{Bi}_{2.5}\text{S}_5$) with an excess of 0.3 apfu of Pb over Cu ($\text{Cu}_{0.68}\text{Ag}_{0.65}\text{Pb}_{0.94}\text{Bi}_{2.23}\text{S}_5$).

Arsenopyrite, pyrrhotite and pyrite

Arsenopyrite (Table S8) approaches its theoretical composition with slight variations on the As contents (33.2–33.9 at.% at San Pietro; 32.4–33.1 at.% at Sinibidraxiu) and more pronounced variations for Fe, particularly in the San Pietro samples (28.3–33.6 at.% Fe), compared to Sinibidraxiu (31.2–34 at.% Fe). The most significant accessory element in the Fe-poor arsenopyrites is Co, with higher average values at San Pietro (1.8 wt.%, maximum 5.4 wt.% Co) compared to Sinibidraxiu (average 0.61 wt.%, maximum 3.3 wt.% Co). Contents of Se occasionally attain 0.2 wt.%. Pyrrhotite and pyrite from San Pietro and Sinibidraxiu (Table S8) are low in Se (close to or below the 200 ppm detection limit), however tend to be Co-bearing; up to 0.2 and 0.16 wt.% Co for San Pietro pyrrhotite and pyrite, respectively, and 0.12 wt.% Co for the Sinibidraxiu pyrite. The high Bi and Pb contents (> 0.1 wt.%), in pyrite and pyrrhotite from San Pietro and in pyrrhotite from Sinibidraxiu, might result from micro-inclusions of Bi and Pb phases.

Chalcopyrite

Chalcopyrite occurs in variable amounts in the various ore facies of the San Pietro skarn, although its composition appears to be rather constant (Table S9). Small amounts of Zn (1–1.7 wt.%) are recorded only in chalcopyrite inclusions in sphalerite. Cobalt, Pb and Te are detected sporadically, whereas Bi is commonly well above the EPMA detection limit (up to 0.28 wt.% Bi).

Galena

The analysed galena from Sinibidraxiu and San Pietro (Table S10) contain Bi, Ag and Se as the main trace elements. Of these, Bi is the most abundant (up to 1.48 wt.% in San Pietro) and detected in all analyses from both localities, although galena from Sinibidraxiu exhibits lower contents relative to San Pietro. Selenium enrichments characterise only galena from San Pietro

(from 0.06 to 0.4 wt.% Se). A maximum value of 0.12 wt.% Te was detected in galena from San Pietro, and is probably due to micro-inclusions of Bi tellurides (George *et al.*, 2015).

Stannite

The general compositions of stannite from the San Pietro skarn (Table S11) are compatible with mildly Zn-bearing phases within the solid solution between pure stannite ($\text{Cu}_2\text{FeSnS}_4$) and k esterite ($\text{Cu}_2\text{ZnSnS}_4$) end-members. Figure 15 shows that stannite data plot into two separate clusters: the blebs from the chalcopyrite–arsenopyrite ore facies (zone 3b; sample MTB1) all plot close to the stannite end-member, whereas the more dispersed cluster plotting closer to the ferrok esterite end-member ($\text{Cu}_2(\text{Fe,Zn})\text{SnS}_4$) corresponds to blebs from the sphalerite–magnetite ore facies (zone 2; sample MTA2). The main trace elements of the San Pietro stannite, which is devoid of In, are represented by Te (avg. 0.3 wt.%), Bi (avg. 0.13 wt.%) and Se (avg. 0.1 wt.%), which are recorded consistently in all analyses, and by Pb peaks (below 0.2 wt.%).

Cassiterite

The compositions of cassiterite (Table S12) were determined by EMPA on small single grains occurring in the chalcopyrite–scheelite (zone 1; sample VMd5b), chalcopyrite–arsenopyrite (zone 3a; sample MTB1) and sphalerite–magnetite (zone 2–3b; samples MTA2–MTA3) ore facies of San Pietro. Indium contents in cassiterite attain 0.3 wt.% In_2O_3 with an average of 0.14 wt.%. Other detected minor and trace elements are Fe, Zn and Te. Iron (expressed both as ferrous and ferric oxide in Table S12) occurs in variable amounts, from below 0.1 up to 2.9 wt.% Fe_2O_3 , unevenly distributed in cassiterite grains from different ore facies (Fig. 16b). Zinc shows distribution trends similar to In (Fig. 16a), whereas Te contents (Fig. 16c) were only detected in the cassiterite grains belonging to the sphalerite–magnetite and chalcopyrite–arsenopyrite ore facies, where accessory stannite (also Te bearing) is widespread.

Scheelite

Analyses on scheelite were performed by EPMA and LA-ICP-MS on samples from San Pietro (zone 1; sample VMd5b) and Sinibidraxiu (zone 3; sample SB11). In terms of major elements, the scheelite crystals are compositionally similar in both sites (Table S13), without appreciable zoning. However, subtle-to-remarkable differences were revealed by LA-ICP-MS data (Table S14), particularly for Mo, Y and REE contents. The San Pietro scheelite is moderately enriched in Mo (ranging between 737 and 2467 ppm, avg. 1593 ppm Mo) compared to Sinibidraxiu scheelite (ranging between 6.3 and 42 ppm, avg. 21 ppm Mo) with no rim-to-core variations (Fig. 17a). Yttrium and REE show an opposite trend, as the $\Sigma\text{REE}+\text{Y}$ contents in the Sinibidraxiu scheelite are remarkably higher (from 62 to 564 ppm, avg. 386 ppm) than those in the San Pietro scheelite (range 3–31 ppm, av. 19 ppm). The Y/Ho ratios are markedly higher at Sinibidraxiu than in San Pietro and they exhibit a good linear correlation (Fig. 17b). The chondrite-normalised REE distribution patterns for both San Pietro and Sinibidraxiu scheelite show a seagull-wing-like shape with distinct negative Eu anomaly (Fig. 17d). The Eu anomaly ($\text{Eu}/\text{Eu}^* = \text{Eu}/[(\text{Gg-Sm})^{1/2}]$) is slightly more pronounced for the Sinibidraxiu scheelite (average Eu/Eu^* of 0.06 and up to 0.16) compared to the San Pietro scheelite (avg. of 0.24 and up to 0.35). Moreover, the San Pietro scheelite displays profiles characterised by light

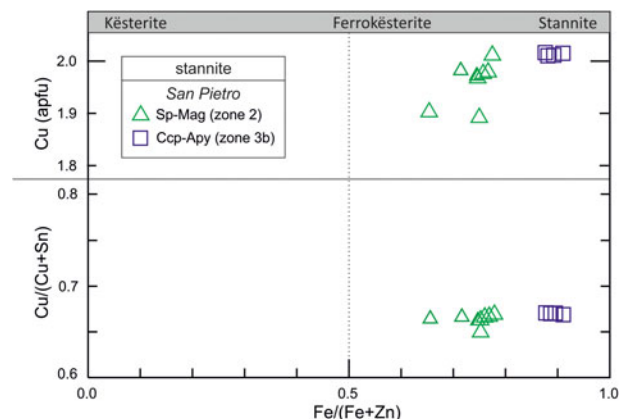


Fig. 15. Compositions of stannite from zones 2 and 3b of San Pietro skarn as functions of Cu (apfu) and Cu/(Cu + Zn) vs. Fe/(Fe + Zn) (after Petruk, 1973).

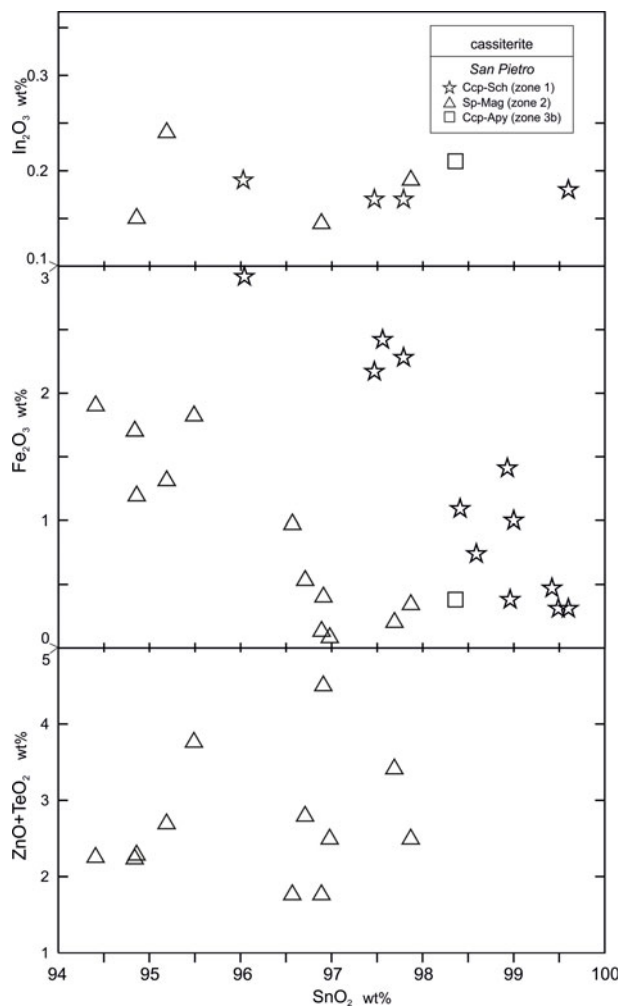


Fig. 16. Compositions of accessory elements (wt.% oxides) in cassiterite grains from the chalcopyrite–scheelite (zone 1), sphalerite–magnetite (zone 2) and chalcopyrite–arsenopyrite (zone 3b) ore facies of the San Pietro skarn.

versus heavy REE (LREE vs. HREE) enrichments. Other minor differences in trace-element concentrations involve Nb–Ta and As. Niobium, paired with Ta, is mildly enriched in the San Pietro scheelite (avg. 8.8 ppm Nb and 0.07 ppm Ta) compared to

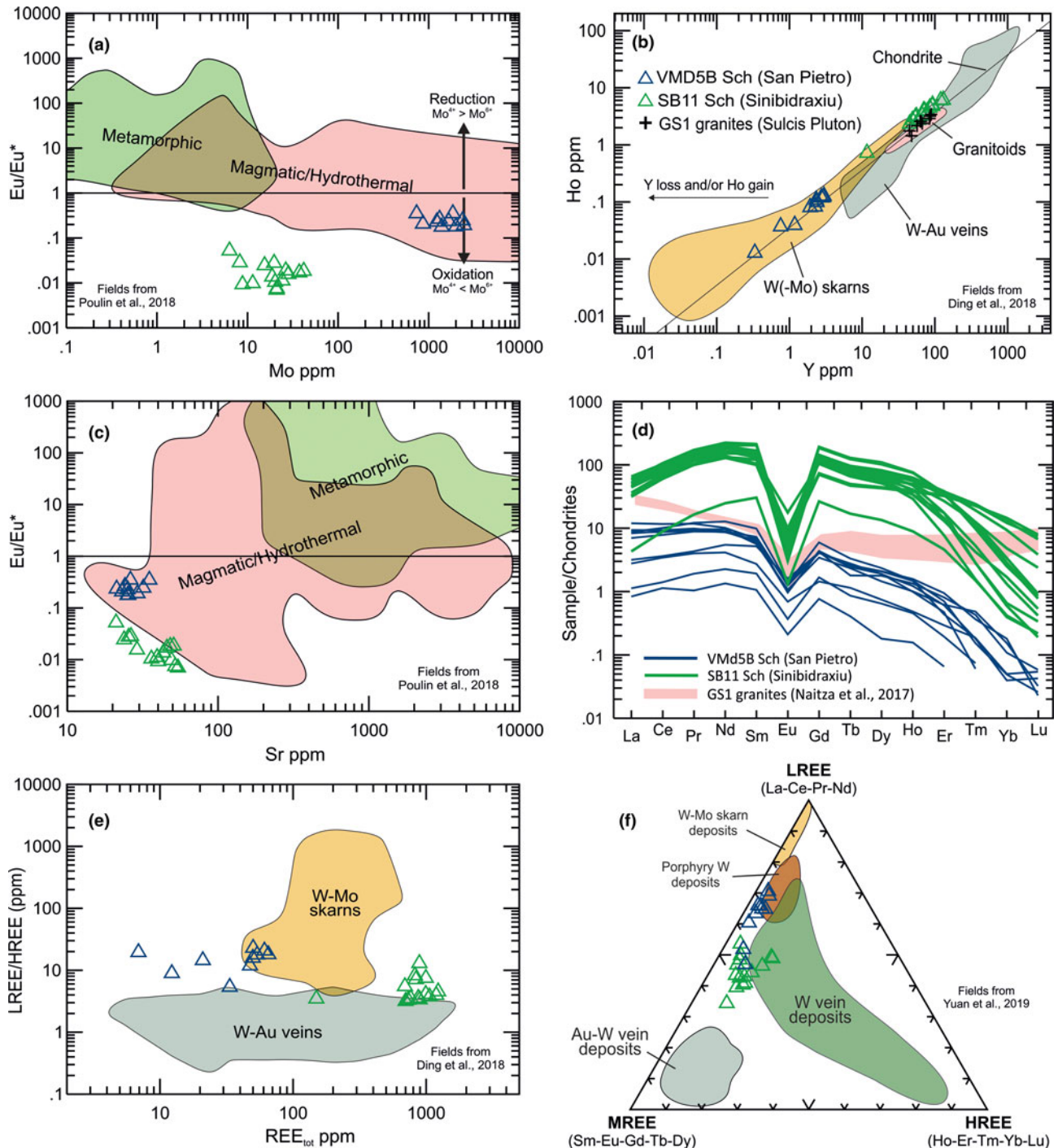


Fig. 17. Binary, spider and triangular composition diagrams for scheelite from the Sinibidraxiu and San Pietro ores: (a) Mo vs. Eu/Eu^* (modified after Poulin *et al.*, 2018); (b) Y vs. Ho (modified after Ding *et al.*, 2018); (c) Sr vs. Eu/Eu^* (modified after Poulin *et al.*, 2018); (d) chondrite-normalised (Sun and McDonough, 1989) REE distribution patterns and comparison with the GS1 granite in the Sulcis area (modified after Naitza *et al.*, 2017); (e) total REE vs. LREE/HREE (modified after Ding *et al.*, 2018); (f) normalised LREE-MREE-HREE contents (modified after Song *et al.*, 2014, Yuan *et al.*, 2019).

Sinibidraxiu (avg. 2.5 ppm Nb and 0.015 ppm Ta). Arsenic contents are generally low, although slightly more enriched in the San Pietro scheelite (from 2.4 to 8.24 ppm, avg. 4.5 ppm As) compared to the Sinibidraxiu scheelite, where As is typically below the detection limit and rarely exceeds 1 ppm. Scheelite from both sites are Sr poor (average Sr values below 40 ppm, Fig. 17c) and Mn poor. Manganese is slightly more enriched (avg. 2.25 ppm Mn) in the Sinibidraxiu scheelite compared to San Pietro (avg. 0.54 ppm Mn).

Discussion

The orebodies at the San Pietro and Sinibidraxiu mines display clear differences in the skarn mineralogy and ore mineral associations. The San Pietro orebody is characterised by multi-stage formation of a prograde assemblage (garnet, clinopyroxene, hematite, scheelite), affected by retrograde alteration (amphibole, epidote, chlorite) and oxide and sulfide mineralisation (magnetite,

cassiterite, Bi phases, Cu–Fe–Zn sulfides, molybdenite, stannite and galena). This succession of temperature- and time-controlled assemblages is different at Sinibidraxiu. Here, an early-stage calc-silicate assemblage, forming radiate and fibrous aggregates, was probably extensively replaced by a hydrothermal assemblage (carbonates–quartz), coinciding with the ore mineral deposition (arsenopyrite, scheelite, sphalerite). However, several common features allow us to bring the two ore deposits into a common framework. These are: (1) a similar metallogenic signature, with the occurrence in both ores of variable amounts of scheelite, as well as arsenopyrite, sphalerite and other base metal sulfides (chalcopyrite, galena, pyrrhotite, pyrite); (2) a similar role of the pre-existing structural framework in focusing fluids during the mineralising processes; and (3) allegedly, the same granite intrusion source (the GS1 intrusive suite of Conte *et al.*, 2017). However, regardless of these similarities, an important difference exists in the host rocks. At San Pietro, the skarn orebody formed at the contact between a siliciclastic unit and a carbonate formation whereas at Sinibidraxiu the orebody is confined entirely to the carbonate host. At both localities, the carbonate rocks are metamorphosed to marbles. The migration of fluids in the host rocks might have occurred by infiltration along major structures, represented by tectonised stratigraphic contacts at San Pietro and mutually cross-cutting faults at Sinibidraxiu. The sub-vertical dip of these structures had a crucial role in controlling the extent of metasomatic processes and determining the steep shape of the orebodies. Thus, although limited to 1–5 m thickness, they are most probably characterised by a depth-controlled zonation regulated by the fluid flow (Meinert *et al.*, 2005). These features are, in general terms, comparable to vein–skarn types (Meinert *et al.*, 2005).

For the San Pietro orebody, field and analytical evidence display a marked zonation pattern from hornfelses to marbles within a garnet–clinopyroxene–wollastonite zone. In contrast, such a prograde mineralogy and zonation has not been observed at Sinibidraxiu, where only marbles can be recognised at the contact with the orebody. However, textural evidence from the carbonates and quartz gangue such as the very fine grain size and intimate association of unusual fibrous textures, suggest replacement of pre-existing radiating aggregates of possible Ca and/or Ca–Mg silicate precursor(s) such as wollastonite and/or diopside–tremolite. In both localities, the circulation of hydrothermal fluids produced the substitution of early calc-silicate assemblages in favour of newly formed hydrous calc-silicates at San Pietro and carbonates plus quartz at Sinibidraxiu. Most ore minerals appear to be part of such retrograde assemblages, essentially confirming the evolutionary trends observed by Aponte *et al.* (1988) for other skarn occurrences in SW Sardinia. The complex variations in skarn mineralogy and composition recognised by our optical microscopy, SEM-EDS, EPMA and LA-ICP-MS studies provide data, which allow us to outline below possible evolutionary paths for the mineralising stages in different parts of the Monte Tamara skarn system.

Scheelite trace-element composition

Scheelite compositions have been used increasingly as a method for determining the origin and the physicochemical characters of fluids and the processes of formation of the orebodies (Liu *et al.*, 2019; Yuan *et al.*, 2019; Ding *et al.*, 2018; Poulin *et al.*, 2018). Accordingly, our scheelite LA-ICP-MS data allowed us to obtain many useful indications for sources of ore-forming elements and for mineralising processes at San Pietro and

Sinibidraxiu. The scheelite display seagull-wing-shaped REE chondrite-normalised distribution patterns (Fig. 17d), indicative of a magmatic source of fluids (Poulin *et al.*, 2018). As compared to those reported in literature for GS1 granites (Naitza *et al.*, 2017), chondrite-normalised REE contents are slightly to moderately lower at San Pietro and remarkably higher at Sinibidraxiu. Both scheelites display similar convex REE distribution patterns, as opposed to the concave patterns of GS1 granites. These differences may be indicative of REE fractionation under the prevailing hydrothermal conditions, arguably corresponding to greisenisation processes following granite emplacement. Hence, comparing the patterns of scheelite and the greisenised facies of the GS1 could provide clearer indications as to their genetic relationships (Poulin *et al.*, 2018). The magmatic source is also confirmed by the Sr vs. Eu/Eu* diagram (Fig. 17c; Poulin *et al.*, 2018) in which both scheelites lie in the magmatic field (San Pietro) or very close to it (Sinibidraxiu). The trace-element composition of scheelite, specifically REE contents and proportions, also provided useful qualitative indications about the ore forming processes. Scheelite from both orebodies have very low HREE contents with respect to LREE and middle REE (MREE) (Fig. 17f; Song *et al.*, 2014; Yuan *et al.*, 2019). However, the same diagram shows that scheelite from San Pietro are relatively enriched in LREE; a feature more distinctive of scheelite from W porphyry and W–Mo skarn deposits. In contrast, the relatively higher MREE of Sinibidraxiu scheelite are associated more usually with W vein deposits. A further indication of different mineralisation environments is provided by trends in the Ho vs. Y diagram (Fig. 17b; Ding *et al.*, 2018) and the REE_{tot} vs. LREE/HREE (Fig. 17e; Ding *et al.*, 2018) diagrams. In these diagrams, San Pietro scheelite plots in or close to the W–Mo skarn field, whereas Sinibidraxiu scheelite falls very close to the granitoid field and within the W–Au hydrothermal veins field. Within a single skarn system model for the Monte Tamara area, data plotted in these diagrams might indicate a continuum from proximal W–Mo skarn deposits (San Pietro) to more distal W hydrothermal vein deposits (Sinibidraxiu). Sinibidraxiu scheelite have REE contents one order of magnitude higher than those of San Pietro scheelite. As REE substitute for Ca²⁺, such enrichment indicates that at the stage of formation, scheelite was the most effective REE ‘scavenger’ in the mineral assemblage of the orebody, in agreement with the absence of other potential REE-bearing minerals such as epidote, garnet or fluorite. Although crystallised in different environments, scheelite from San Pietro and from Sinibidraxiu share similar Eu/Eu* < 1 ratios (Fig. 17a–c), whereas relative Mo enrichments observed at San Pietro indicate formation under oxidising conditions (Poulin *et al.*, 2018). In fact, Mo⁶⁺ substitutes commonly for W⁶⁺ in oxidised environments, whereas Mo⁴⁺ precipitates readily as molybdenite under reducing conditions and in the presence of S. Arsenic is another common trace element whose presence in scheelite depends strongly on redox conditions. As-bearing scheelite are also generally formed in oxidising conditions due to As⁵⁺ substitutions for W⁶⁺. In contrast under reducing conditions, As is not incorporated in the scheelite lattice due to the difference in ionic radii between W⁶⁺ and As²⁺ or As³⁺ (Poulin *et al.*, 2018). In the case of Monte Tamara, As is enriched only in San Pietro scheelite (from 2.4 to 8.2 ppm As) and is generally below the detection limit (locally up to 1.8 ppm) in Sinibidraxiu scheelite. Therefore, the As–Mo contents and the Eu/Eu* < 1 ratios at San Pietro clearly record oxidising conditions. In contrast, despite the Eu/Eu* < 1 ratios, the low Mo and As contents in Sinibidraxiu scheelite, together with the widespread occurrence of arsenopyrite, strongly suggest a formation under at least moderately reducing conditions.

Temperatures of formation

Temperature changes are one of the main controlling parameters in skarn formation. As a general feature, skarns are the result of fluid–rock interactions evolving from a prograde stage of temperature increase to a retrograde stage of decreasing temperature. The retrograde/sulfide stage of mineralisation corresponds to the peak of activity of hydrothermal fluids that produce hydrous minerals as overgrowths on prograde mineral associations and may precipitate sulfides and other ore minerals. To assess the temperature of the retrograde/sulfide stage in Monte Tamara skarns, the arsenopyrite, stannite and chlorite geothermometers were applied. The arsenopyrite thermometer (Kretschmar and Scott, 1976; Sharp *et al.*, 1985) has been used for San Pietro and Sinibidraxiu arsenopyrite–pyrrhotite–pyrite mineral assemblages (Fig. 18a), Arsenopyrite coexisting with pyrrhotite (then altered to pyrite) in the San Pietro ore has an As content in the range 33.2–33.9 at.%, corresponding to a temperature range of 460–425°C. These temperatures are slightly higher than those reported for skarn retrograde stages worldwide (Meinert *et al.*, 2005) and suggest the early formation of arsenopyrite at the boundary between prograde and retrograde stages. At Sinibidraxiu, lower temperatures have been obtained with respect to those of San Pietro, in fact, the As contents in Sinibidraxiu arsenopyrite are within the 32.3–33.1 at.% range, corresponding to temperatures of 400–375°C. The range of temperatures of the sulfide stage of San Pietro was further constrained using the stannite–sphalerite geothermometer (Shimizu *et al.*, 2008; Shimizu and Shikazono, 1985; Nekrasov *et al.*, 1979), based on the Fe and Zn exchange between coexisting stannite and sphalerite (Fig. 18b). For its application, stannite aggregates, locally overgrowing cassiterite in the arsenopyrite–chalcopyrite-rich ore facies (zone 3b) and stannite blebs exsolved with chalcopyrite in sphalerite in the cassiterite-bearing sphalerite–magnetite-rich ore facies (zone 2)

were considered. In addition to textural features, a relationship between stannite and cassiterite in both assemblages was considered because both share detectable Te contents. The obtained values form two clusters at different temperatures (Table S11). The first group is represented by stannite blebs in sphalerite in the sphalerite–magnetite ore facies (zone 2), which are characterised by temperature ranges of 315–284°C. The second group is represented by the stannite aggregates locally rimming cassiterite in the arsenopyrite-rich ore facies (zone 3b) which provided temperatures of 270–255°C. Such a range might be compatible with the common crustiform texture of stannite in the arsenopyrite–chalcopyrite ore facies. The stannite geothermometer thus suggests that there may be two distinct generations of stannite as also indicated by the slight compositional differences between them. Moreover, the stoichiometry of chlorite from the San Pietro retrograde assemblages, characterised by $Al(IV) > 1.9$ and $Fe/(Fe+Mg) > 0.3$, allowed the application of the geothermometer proposed by Kranidiotis and MacLean (1987), according to which a temperature range of 290–315°C was obtained for late-stage hydrothermal alteration of garnet following the initial replacement by epidote + calcite. This temperature range is markedly lower than that of arsenopyrite (460–425°C) though shows a good correspondence with the stannite blebs in sphalerite (315–284°C). Thus, the different temperatures of formation for arsenopyrite and chlorite contribute to bracketing the progression and the cooling path of retrograde alteration to which the polyphase ore mineralisation at San Pietro is related.

The prograde stage at San Pietro

In skarn systems, the oscillatory zoning in garnet reflects compositional variations in mineralising fluids, due to alternating disequilibrium and steady-state processes during infiltration into

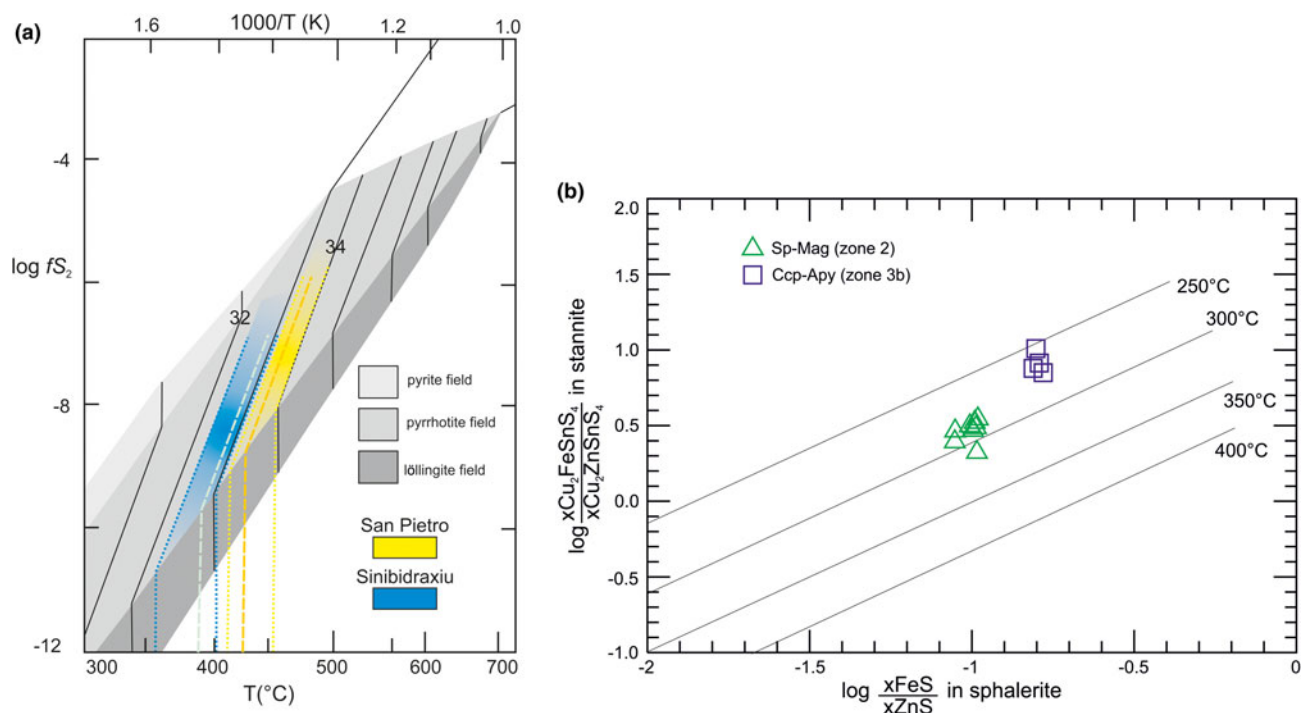


Fig. 18. Arsenopyrite (a, Sharp *et al.*, 1985; Kretschmar and Scott, 1976) and stannite–sphalerite (b, Shimizu *et al.*, 2008; Shimizu and Shikazono, 1985; Nekrasov *et al.*, 1979) geothermometers and calculations of the temperatures of the retrograde/sulfide stages at San Pietro and Sinibidraxiu (a) and San Pietro (b).

the wall rocks (Park *et al.*, 2017, 2019; Zhu *et al.*, 2021). Abundant oscillatory-zoned grossular and andradite garnet are characteristic of the prograde-stage mineral association of San Pietro skarn. Microprobe data confirmed that: (1) in grossular, zoning corresponded to slight core/rim and rim/rim Al_2O_3 and Fe_2O_3 variations, overall leading to andradite-rich (Fe^{3+} rich) compositions; (2) both andradite and grossular garnet are variably enriched in Sn (0.4 wt.% SnO_2 on average, with maxima over 1 wt.%); and (3) Sn enrichments tend to characterise the mid to marginal portions of the zoned crystals. Overall, these features suggest precipitation from an oxidising fluid, characterised by increasing Fe^{3+} activity. In SW Sardinia, a similar trend of late Fe enrichment in the prograde stage is reported for skarns in the San Leone mine area, Eastern Sulcis (Verkaeren and Bartholomè, 1979), also related to the GS1 suite granites (Naitza *et al.*, 2017). In the San Pietro skarn, under oxidising conditions and temperatures $> 460^\circ\text{C}$ (arsenopyrite geothermometer), Sn contents in garnet also increased progressively due to Sn^{4+} incorporation in octahedral sites in substitution of Fe^{3+} (Eadington and Kinealy, 1983; Galuskina *et al.*, 2010). Sporadic W peaks recorded in garnet in the San Pietro skarn might result from W^{6+} competing with REE in the garnet lattices (Zhu *et al.*, 2021). Diopside exhibits lower, although equally remarkable Sn contents (commonly 0.1 wt.% SnO_2 , with maxima at 0.36 wt.%). Similarly to other W and W–Sn skarn deposits worldwide, in San Pietro the crystallisation of scheelite appears to correspond to the waning stage of prograde skarn (Kwak and Tan, 1981; Zaw and Singoyi, 2000; Zhu *et al.*, 2021). Both Mo-bearing scheelite (Kwak, 1987; Zaw and Singoyi, 2000) and hematite (further pseudomorphed by magnetite) confirm the early oxidising nature of mineralising fluids in this stage. Moreover, the fine-grained fluorite interstitial to unaltered clinopyroxene suggest that F^- was present in the fluids during the prograde stage. This characteristic could relate to greisenisation processes in the more proximal, and unexposed, parts of the skarn system, which may have been of critical importance in conveying new contributions of metals from the consolidating granite outwards (Meinert, 1997).

The hydrothermal/sulfide stage at San Pietro

Both San Pietro and Sinibidraxiu skarns display abundant evidence of intense, locally pervasive retrogression of the prograde assemblages, thereby testifying a continuous intake of magmatic fluids from the consolidating granites. The growth of the coarse-grained prograde minerals enhanced the porosity of the skarns, improving the circulation of these fluids. Simultaneously, extensive alteration might have been favoured by the increase of reactive surfaces. In the San Pietro orebody, multiple pulses of fluids resulted initially in diffuse formation, at decreasing temperatures, of hydrous silicates, dominated by amphibole, epidote and chlorite, at the expense of clinopyroxene and garnet. The hydrothermal alteration of primary skarn minerals is also related to abundant precipitation of magnetite, which may indicate definite physicochemical changes in mineralising solutions, most notably variations of the redox conditions. The formation of magnetite, e.g. by substitution of early hematite (mushketovite), represents a change towards relatively more reducing conditions, below the Hematite–Magnetite buffer. The newly formed retrograde silicates partially-inherited the Sn signature of prograde silicates. This is best exemplified by epidote, whose SnO_2 contents are commonly > 0.1 wt.%. Tin might have been available for structural

substitutions in silicates (e.g. $\text{Sn}^{4+} + \text{Ti}^{4+} \rightarrow \text{Al}^{3+} + \text{Fe}^{3+}$, also with Fe^{2+} incorporation, in clinzoisite: Ordosch *et al.*, 2019), until the establishment of favourable physicochemical conditions for cassiterite (nearly simultaneous with magnetite) and, subsequently, stannite precipitation. Notably, a source of Sn derived from the alteration of the garnet–clinopyroxene skarn, is also testified by diffuse, fine-grained cassiterite, together with scheelite, along corroded garnet rims. The concurrent sulfur increase in fluids during retrogression stabilised different sulfide assemblages. The first to form are pyrite-free sulfide assemblages, and include arsenopyrite, chalcopyrite, sphalerite, pyrrhotite, galena and Bi sulfosalts, locally surrounded by peculiar molybdenite ring-shaped aggregates. They correspond to a lower sulfur fugacity and higher temperature (arsenopyrite at $460\text{--}425^\circ\text{C}$; Fig. 18a) and are coprecipitated with accessory cassiterite. Sphalerite is ubiquitous although dominant in the magnetite-rich and in the final, pyrite-rich ore facies. The composition of sphalerite is highly variable in terms of Fe content, probably due to internal zoning of grains, reflecting fluctuations in the hydrothermal fluid conditions. A few irregular sphalerite aggregates in the early sulfide facies do not conform to the general Mn-rich character, typical of high-temperature sphalerite (Frenzel *et al.*, 2016). Stannite was observed in the earlier, pyrite-free assemblages, although with two distinct textures, compositions and temperature ranges. As stated above, the stannite geothermometer (Fig. 18b) indicates that two distinct generations of stannite might have formed at different temperatures. The higher temperature range ($315\text{--}284^\circ\text{C}$) is representative of stannite exsolved with chalcopyrite blebs in the sphalerite–magnetite-rich ore, and sporadic inclusions of cassiterite crystals are enclosed in chalcopyrite of this assemblage. The lower temperature range ($270\text{--}255^\circ\text{C}$) corresponds to crustiform stannite overgrowing corroded remnants of cassiterite in the arsenopyrite–chalcopyrite ore facies. As further evidence of late-stage alteration, early pyrrhotite is locally altered to spongy pyrite–marcasite. Distribution, textures and preliminary compositional data for cassiterite (Fig. 16) suggest a protracted time span of crystallisation during the hydrothermal stage, as suggested by the rather high Fe contents (Lerouge *et al.*, 2017).

Mineralisation at Sinibidraxiu

Compared to the San Pietro skarn, a distinct feature of the Sinibidraxiu orebody resides in the different prograde effects represented by only marble formation in the host rock. However, the gangue of the orebody is essentially composed of microscopic intergrowths dolomite–calcite and quartz, arranged as fibrous textures or irregular aggregates visible on outcrops. These might suggest hydrothermal substitution of pre-existing aggregates by the dolomite–calcite–quartz assemblage. In this case, fibrous silicates (e.g. wollastonite, diopside or tremolite) could have formed under higher temperatures than those of the early hydrothermal stage (arsenopyrite, $400\text{--}375^\circ\text{C}$). Thus, the hypothetical stages of formation of the Sinibidraxiu vein could be: (1) a first stage of formation of Ca and/or Ca–Mg fibrous silicates at temperatures $\sim 550\text{--}400^\circ\text{C}$ (Bucher and Grapes, 2011); (2) a hydrothermal stage, characterised initially by a widespread pseudomorphic substitution of fibrous silicates by dolomite–quartz and calcite roughly simultaneous with, or slightly preceding, the precipitation of arsenopyrite and sphalerite at temperatures of $400\text{--}375^\circ\text{C}$. This evolution is also indicated by the carbonate–quartz substitution of fibre-shaped inclusions in arsenopyrite and sphalerite, and by the peculiar low-Fe zones of Fe-rich sphalerite,

resembling reaction rims with such carbonate–quartz inclusions (Fig. 7g–i). Chalcopyrite aggregates are then formed, followed by galena, pyrrhotite and pyrite. Therefore, considering the lower temperature value obtained from arsenopyrite (Fig. 18) the Cu–Pb–Fe sulfides assemblage should have formed at temperatures <375°C. As discussed above, scheelite might have formed under at least moderately reducing conditions. The overall reducing character of the fluid is represented by the abundant arsenopyrite and Zn–Pb–Cu–Fe sulfides assemblage throughout the orebody and from the low As and Mo contents of scheelite.

The limited ore mineral association at Sinibidraxiu (scheelite–arsenopyrite–sphalerite, chalcopyrite, galena, pyrrhotite and pyrite) could result from a hydrothermal fluid with different characteristics to the fluid that formed the San Pietro ore. In fact, the Sinibidraxiu mineralising fluid was able to mobilise tungsten and LREE–MREE, but not Sn–Bi–Mo. The W and Sn decoupling has been observed in many W–Sn–Mo hydrothermal systems (Li *et al.*, 2021), including in those of SW Sardinia (e.g. Monte Linas district: Deidda *et al.*, 2021; Naitza *et al.*, 2017). As a result, tungsten minerals (e.g. wolframite) are rarely associated with cassiterite within the same part of the orebody (Liu *et al.*, 2021), being instead associated more commonly with molybdenite and Bi phases.

In the case of Sinibidraxiu, the absence of Sn–Bi–Mo minerals can be explained with a possible precipitation of cassiterite, molybdenite and Bi-bearing phases at greater depths in a skarn ore with similar features and evolutive paths to the San Pietro orebody. However, the distribution of W–Sn–Mo–Bi in the orebody may have been also controlled by intricate variations of many physiochemical parameters in the mineralising fluids such as chlorinity, f_{O_2} and availability of OH[−] complexes in the fluid (Liu *et al.*, 2021; Zajacz, 2008), all of which could be further affected by the increase of the fluid–rock reaction rate as the skarn alteration front progresses over time.

Conclusions

This investigation provided the first detailed characterisation of the mineral assemblages, paragenetic sequences and mineral composition of scheelite-bearing skarns in Sardinia. On the basis of observations and data the following conclusions can be drawn.

Mineralisation of the Monte Tamara area can be classified as oxidised (Meinert *et al.*, 2005), W-bearing vein skarns with

localised zones of enrichment of cassiterite, Bi sulfides and sulfosalts, and molybdenite.

The location and geometries of the skarn orebodies of the area are controlled strongly by the structural setting. This is exemplified by the elongated, lens-shaped and sub-vertical vein skarns along the tectonised stratigraphic contact between marbles and sandstones at San Pietro and by the sub-vertical chimney along mutually crossing faults in marbles at Sinibidraxiu.

Both orebodies record a multistage evolution, marked by mineral assemblages formed under hypo- to mesothermal conditions. At San Pietro, the prograde stage developed at temperatures of >460°C, then decreased progressively from 460–435°C (arsenopyrite), to 315–284°C (stannite inclusions in sphalerite), 315–290°C (chlorite alteration of garnet) and 270–255°C (stannite aggregates corroding cassiterite) during the retrograde/sulfide stage. The thermal evolution of the Sinibidraxiu orebody is less defined, however temperatures of >400°C can be inferred to the alleged Ca and/or Ca–Mg silicates initial stage, followed by arsenopyrite (–scheelite–sphalerite and dolomite–quartz alteration) at 400–375°C and base metal sulfides at <375°C.

The physicochemical conditions in the fluid changed progressively over time. At San Pietro, the general behaviour of redox-sensitive elements (e.g. Fe³⁺ → Fe²⁺ and Mo⁶⁺ → Mo²⁺) in the ore minerals records initial oxidising conditions (e.g. hematite crystallisation, andradite, lack of hedenbergite) during the prograde stage. The early As- and Mo-bearing scheelite with Eu/Eu* < 1, associated with magnetite, suggests a gradual transition from mildly oxidising to progressively reducing conditions coupled with an increase in sulfur fugacity, resulting in deposition of molybdenite and base-metal sulfides. The Sinibidraxiu orebody records moderately reducing initial conditions, indicated by scheelite with low As and Mo, though with Eu/Eu* < 1, evolving towards reducing conditions during arsenopyrite and base-metal sulfides formation.

The orebodies clearly show their magmatic affinity (Fig. 17). However, they are representative of different local geological controls of formation, mostly regulated by the distance from the source intrusion, within the same larger-scale W–Sn skarn system. The San Pietro orebody (Fig. 19a) and its mineralogical and compositional features suggest formation at more proximal environments very similar to other skarns worldwide (e.g. lower MREE in scheelite; presence of magnetite–cassiterite–molybdenite and Bi phases; garnet–clinopyroxene–wollastonite gangue, etc.).

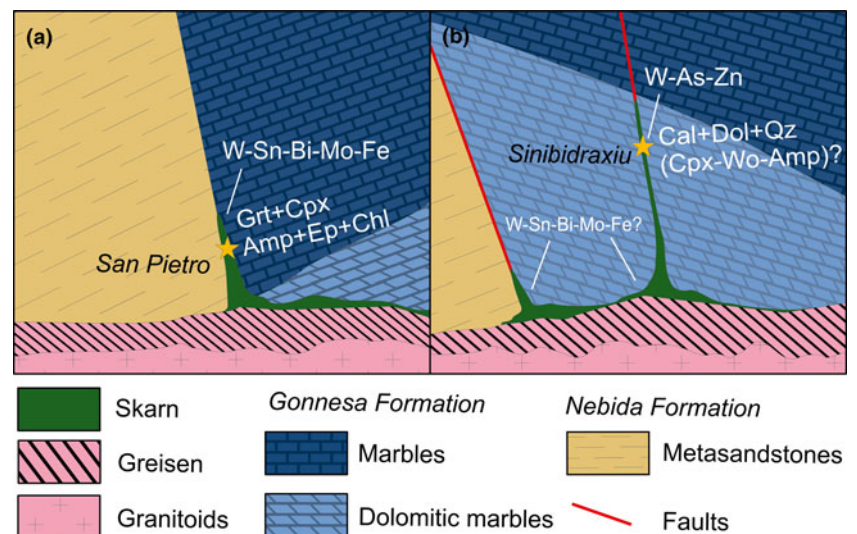


Fig. 19. Hypothetical representation of the different depth-regulated zones of the Monte Tamara skarn mineralisation system with respect to the alleged parental GS1 granites, emplaced at <2 kbar: (a) the San Pietro orebody represents a more proximal ore, including phases such as scheelite, cassiterite, molybdenite and Bi-bearing sulfosalts in a clinopyroxene–garnet skarn; and (b) the Sinibidraxiu ore has hydrothermal characters attributable to more distal environments, as suggested by the absence of molybdenite, cassiterite and Bi-bearing sulfosalts, probably deposited in deeper-seated skarns, similarly to San Pietro.

In contrast, the Sinibidraxiu orebody (Fig. 19b) is seemingly more closely related to a hydrothermal-vein environment distal to the intrusion (e.g. high MREE proportions in scheelite; absence of cassiterite–molybdenite and Bi phases; strong hydrothermal dolomite–quartz pseudomorphic substitution of fibrous silicates).

As a final consideration, the overall characteristics of both orebodies provided important guides for W, Sn and other critical raw material mineral exploration in the numerous, analogous occurrences across SW Sardinia. Moreover, this investigation supports the possibility of undiscovered mineralised outcrops and deeper-seated bodies of economic interest, particularly for W, in the whole area surrounding Monte Tamara. From a geological standpoint, this hypothesis is further supported by the structural setting of the orebodies as: (1) fault systems had a crucial role in favouring the circulation of metasomatic and ore mineralising fluids, even at large distances and along channel ways scattered along marbles; (2) the Variscan thrust-faults might have produced important ‘permeability limits’ at depth (e.g. due to tectonic repetitions) therefore potentially increasing the reaction rate between fluids and the carbonate host rocks; and (3) the large antiformal–synformal structure may have acted as a large trap, similar to some relevant W-skarn mineral deposits worldwide (e.g. the E orebody in the Cantung deposit: Mathieson and Clark, 1984; Rasmussen *et al.*, 2011).

Acknowledgements. M.L.D. gratefully acknowledges Sardinia Regional Government for financial support of his PhD scholarship (P.O.R. Sardegna F.S.E. Operational Programme of the Autonomous Region of Sardinia, European Social Fund 2007–2013 – Axis IV Human Resources, Objective 1.3, Line of Activity 1.3.1.), CESA (E58C16000080003) from RAS and RAS/FdS (F72F16003080002) grants and the CeSAR (Centro Servizi d’Ateneo per la Ricerca) of the University of Cagliari, Italy, for SEM analysis. M.M. gratefully acknowledges Dr. Gianluca Sessa for assistance in scheelite trace-element analyses at the LA-ICP-MS laboratory acquired thanks to the Progetto di Eccellenza (PRODE) funds awarded to the Earth Science Department, State University of Milano. We sincerely thank the Principal Editor Roger Mitchell, Associate Editor Irina O Galuskina, Eimear Deady and an anonymous reviewer for improving this paper with their critical reading and constructive comments.

Supplementary material. To view supplementary material for this article, please visit <https://doi.org/10.1180/mgm.2022.119>

Competing interests. The authors declare none.

References

- Aponte F, Balassone G., Boni M., Costamagna L. and Di Maio G. (1988) Variscan Skarn Ores in South-West Sardinia: their relationships with Cambro-Ordovician stratabound deposits. *Rendiconti della Società Italiana di Mineralogia e Petrologia*, **43**, 445–462.
- Arthaud F. (1963) Un exemple de tectoniques superposées dans le Paléozoïque de l’Iglesiente (Sardaigne). *Comptes Rendus de la Société Géologique de France*, **9**, 303–304.
- Barca S., Serri R., Rizzo R., Forci A., Calzia P. and Pertusati P.C. (2009) *Foglio 565 CAPOTERRA*. Note Illustrative della Carta Geologica d’Italia alla scala 1:50.000, Servizio Geologico d’Italia, Rome.
- Barton P.B. and Bethke P.M. (1987) Chalcopyrite disease in sphalerite: Pathology and epidemiology. *American Mineralogist*, **72**, 451–467.
- Boni M., Iannace A. and Balassone G. (1996) Base metal ores in the lower Palaeozoic of South-Western Sardinia. *Society of Economic Geologists, Economic Geology 75th Anniversary Volume*, **4**, 18–28.
- Boni M., Stein H.J., Zimmermann A. and Villa, I.M. (2003) Re-Os age for molybdenite from SW Sardinia (Italy): a comparison with ⁴⁰Ar/³⁹Ar dating of Variscan granitoids. Pp. 247–250 in: *Mineral Exploration and Sustainable Development*. Proceedings 7th Biennial SGA Meeting, Athens, Greece.
- Brizzi G.C., Scanu S., Stara P. and Tanca G. (1992a) I minerali del giacimento di Monte Tamara (Nuxis) – I° parte. *Rivista Mineralogica Italiana*, **3**, 167–180.
- Brizzi G.C., Scanu S., Stara P. and Tanca G. (1992b) I minerali del giacimento di Monte Tamara (Nuxis) – II° parte. *Rivista Mineralogica Italiana*, **4**, 237–248.
- Bucher K. and Grapes R. (2011) Metamorphism of dolomites and limestones. Pp. 225–255 in: *Petrogenesis of Metamorphic Rocks* (Bucher K. and Grapes R., editors). Springer, Berlin.
- Burisch M., Gerdes A., Meinert L.D., Albert R., Seifert T. and Gutzmer J. (2019) The essence of time – fertile skarn formation in the Variscan Orogenic Belt. *Earth and Planetary Sciences Letters*, **519**, 165–170.
- Chang Z., Shu Q. and Meinert L.D. (2019) Skarn Deposits of China. *SEG Special Publications*, **22**, 189–234.
- Ciobanu C.L. and Cook N. (2000) Intergrowths of bismuth sulphosalts from the Ocna de Fier Fe-skarn deposit, Banat, Southwest Romania. *European Journal of Mineralogy*, **12**, 899–917.
- Cocco F., Oggiano G., Funedda A., Loi A. and Casini L. (2018) Stratigraphic, magmatic and structural features of Ordovician tectonics in Sardinia (Italy): a review. *Journal of Iberian Geology*, **44**, 619–639.
- Cocco F., Attardi A., Deidda M.L., Fancello D., Funedda A. and Naitza S. (2022a) Passive structural control on skarn mineralization localization: A case study from the Variscan Rosas Shear Zone (SW Sardinia, Italy). *Minerals*, **12**, 272.
- Cocco F., Loi A., Funedda A., Casini L., Ghienne J-F, Pillola G.L., Vidal M., Meloni M.A. and Oggiano G. (2022b) Ordovician tectonics of the South European Variscan realm: new insights from Sardinia. *International Journal of Earth Sciences*, <https://doi.org/10.1007/s00531-022-02250-w>
- Cocozza T. (1979) The Cambrian of Sardinia. *Memorie della Società Geologica Italiana*, **20**, 163–187.
- Conte A.M., Cuccuru S., D’Antonio M., Naitza S., Oggiano G., Secchi F., Casini L. and Cifelli F. (2017) The post-collisional late Variscan ferroan granites of southern Sardinia (Italy): Inferences for inhomogeneity of lower crust. *Lithos*, **294–295**, 263–282.
- Damian G., Ciobanu C.L., Cook N.J. and Damian F. (2008) Bismuth sulphosalts from the galena-matildite series in the Cremoncea vein, Şuior, Baia Mare district, Romania. *Neues Jahrbuch für Mineralogie – Abhandlungen*, **185**, 199–213.
- Ding T., Ma D., Lu J. and Zhang R. (2018) Garnet and scheelite as indicators of multi-stage tungsten mineralization in the Huangshaping deposit, southern Hunan province, China. *Ore Geology Reviews*, **94**, 193–211.
- Eadington, P.J. and Kinealy, K. (1983) Some aspects of the hydrothermal reactions of tin during skarn formation. *Journal of the Geological Society of Australia*, **30**, 461–471.
- Einaudi M.T., Meinert L.D. and Newberry R.J. (1981) Skarn deposits. *Society of Economic Geologists, Economic Geology 75th Anniversary Volume*, **1981**, 317–391.
- Frenzel M., Hirsch T. and Gutzmer J. (2016) Gallium, germanium, indium, and other trace and minor elements in sphalerite as a function of deposit type – A meta-analysis. *Ore Geology Reviews*, **76**, 52–78.
- Funedda A. (2009) Foreland- and hinterland-verging structures in fold-and-thrust belt: An example from the Variscan foreland of Sardinia. *International Journal of Earth Sciences*, **98**, 1625–1642.
- Galuskina I., Galuskin E.V., Dzierzanowski P., Gazeev V.M., Prusik K., Pertsev N.N., Winiarski A., Zadov A.E. and Wrzalik R. (2010) Toturite Ca₃Sn₂Fe₂SiO₁₂ – a new mineral species of the garnet group. *American Mineralogist*, **95**, 1305–1211.
- George L., Cook N.J., Ciobanu C.L. and Wade B.P. (2015) Trace and minor elements in galena: A reconnaissance LA-ICP-MS study. *American Mineralogist*, **100**, 548–569.
- Griffin W.L., Powell W.J., Pearson N.J. and O’Reilly S.Y. (2008) GLITTER: data reduction software for laser ablation ICP-MS. Pp. 204–207 in: *Laser Ablation-ICP-MS in the Earth Sciences*. Mineralogical Association of Canada short course series, 40.
- Hawthorne F.C., Oberti R., Harlow G.E., Maresch W.V., Martin R.F., Schumacher J.C. and Welch M.D. (2012) Nomenclature of the amphibole supergroup. *American Mineralogist*, **97**, 2031–2048.

- Ishihara S. (1981) The granitoid series and mineralization. *Society of Economic Geologists, Economic Geology 75th Anniversary Volume*, **1981**, 458–484.
- Ivashchenko V.I. (2021) Rare-Metal (In, Bi, Te, Se, Be) Mineralization of Skarn Ores in the Pitkäranta Mining District, Ladoga Karelia, Russia. *Minerals*, **11**, 124.
- Kranidiotis, P. and MacLean, W.H. (1987) Systematics of chlorite alteration at the Phelps Dodge massive sulfide deposit, Matagami, Quebec. *Economic Geology*, **82**, 1898–1911.
- Kretzmar U. and Scott S.D. (1976) Phase relations involving arsenopyrite in the system Fe-As-S and their application. *The Canadian Mineralogist*, **14**, 364–386.
- Kwak T.A.P. (1987) *W-Sn Skarn Deposits and Related Metamorphic Skarns and Granitoids*. Developments in Economic Geology, **24**, Elsevier, pp. 451.
- Kwak T.A.P. and Tan T.H. (1981) The geochemistry of zoning in skarn minerals at the King Island (Dolphin) Mine. *Economic Geology*, **76**, 468–497.
- Leake B.E., Woolley R.A., Birch D.W., Burke J.A.E., Ferraris G., Grice D.J., Hawthorne C.F., Kisch J.H., Krivovichev G.V., Schumacher C.J., Stephenson C.N. and Whittaker W.J.E. (2003) Nomenclature of amphiboles: additions and revisions to the international Mineralogical Association's 1997 recommendations. *The Canadian Mineralogist*, **41**, 1355–1362.
- Leone F., Hamman W., Laske R., Serpagli E., and Villas E. (1991) Lithostratigraphic units and biostratigraphy of the post-sardic Ordovician sequence in south-west Sardinia. *Bollettino della Società Paleontologica Italiana*, **30**, 201–235.
- Lerouge C., Gloaguen E., Wille G. and Bailly L. (2017) Distribution of In and other rare metals in cassiterite and associated minerals in Sn±W ore deposits of the western Variscan Belt, *European Journal of Mineralogy*, **29**, 739–753.
- Liu B., Li H., Wu Q.H., Evans N.J., Cai J.Y., Jiang J.B. and Wu J.H. (2019) Fluid evolution of Triassic and Jurassic mineralization in the Xitian ore field, South China: Constraints from scheelite geochemistry and microthermometry. *Lithos*, 1–15, 330–331.
- Liu X., Whang W. and Zhang D. (2021) The mechanisms forming the five-floor zonation of quartz veins: a case study in the Piaotang tungsten-tin deposit, Southern China. *Minerals*, **11**, 883.
- Lockington J.A., Cook N.J. and Ciobanu C.L. (2014) Trace and minor elements in sphalerite from metamorphosed sulphide deposits. *Mineralogy and Petrology*, **108**, 873–890.
- Mathieson G.A. and Clark A.H. (1984) The Cantung E zone scheelite orebody, Tungsten, Northwest Territories: A revised genetic model. *Economic Geology*, **79**, 883–901.
- Meinert L.D. (1995) Compositional variation of igneous rocks associated with skarn deposits – Chemical evidence for a genetic connection between petrogenesis and mineralisation, in Magmas. Pp. 401–408 in: *Fluids, and Ore deposits* (J F H Thompson, editor). Mineralogical Association of Canada Short Course series **23**. Mineralogical Association of Canada, Québec.
- Meinert L.D. (1997) Application of skarn deposit zonation models to mineral exploration. *Exploration and Mining Geology*, **6**, 185–208.
- Meinert L.D., Dipple G.M. and Nicolescu S. (2005) World Skarn Deposits. *Society of Economic Geologists, Economic Geology 100th Anniversary Volume*, **2005**, 299–336.
- Moelo Y., Makovicky E., Mozgova N.N., Jambor J.L., Cook N., Pring A., Paar W., Nickel E.H., Graeser S., Karup-Møller S., Balic-Žunic T., Mumme W.G., Vurro F., Topa D., Bindi L., Bente K. and Shimizu M. (2008) Sulfosalts systematics: a review. Report of the IMA Commission on Ore Mineralogy. *European Journal of Mineralogy*, **20**, 7–46.
- Naitza S., Oggiano G., Casini L., Cuccuru S., Funedda A., Secchi G. and Tocco S. (2015) Structural and magmatic controls on late Variscan metallogenesis: evidences from Southern Sardinia (Italy). Pp. 161–164 in: *Source, Transport and Metal deposits*. Proceedings of 13th Biennial SGA Meeting, Nancy, France, Vol. 1.
- Naitza S., Conte A.M., Cuccuru S., Oggiano G., Secchi F. and Tecce F. (2017) A Late Variscan tin province associated to the ilmenite-series granites of the Sardinian Batholith (Italy): The Sn and Mo mineralisation around the Monte Linas ferroan granite. *Ore Geology Reviews*, **80**, 1259–1278.
- Naitza S., Fadda S., Fiori M., Peretti R. and Secchi F. (2019) The metallogenic potential of an old European mining region: the case of Sardinia (Italy). Pp. 1458–1461 in: *Life with Ore Deposits on Earth*. Proceedings of 15th Biennial SGA Meeting, Glasgow, UK, Vol. 4.
- Nekrasov I.J., Sorokin V.I. and Osadchii E.G. (1979) Fe and Zn partitioning between stannite and sphalerite and its application in geothermometry. *Physics and Chemistry of the Earth*, **11**, 739–742.
- Olmi F., Sabelli C., Santucci A. and Brizzi G. (1995) Minerali rari in Sardegna. *Rivista Mineralogica Italiana*, **1**, 9–42.
- Ordosch A., Raith J.G., Schmidt S. and Aupers K. (2019) Polyphase scheelite and stanniferous silicates in a W(-Sn) skarn close to Felbertal tungsten mine, Eastern Alps. *Mineralogy and Petrology*, **113**, 703–725.
- Park C., Coi W., Kim H., Park M.-H., Kang I.-M. and Lee H.-S. (2017) Oscillatory zoning in skarn garnet: Implications for tungsten ore exploration. *Ore Geology Reviews*, **89**, 1006–1018.
- Park C., Park C., Song Y. and Choi S.-G. (2019) Sequential trace element analysis of zoned skarn garnet: implications for multi-stage fluxing and flow of magmatic fluid into a skarn system, *Lithos*, 350–351, 105–213.
- Venerandi Pirri I. (1971) Il giacimento a blenda, galena, calcopirite di Sa Marchesa nel Sulcis (Sardegna). *Bollettino della Società Italiana di Scienze Naturali*, **62**, 505–549.
- Poll J.J.K. and Zwart H.J. (1964) On the tectonics of the Sulcis area, S Sardinia. *Geologie en Mijnbouw*, **43**, 144–146.
- Poulin R.S., Kontak D.J. and McDonald A. (2018) Assessing scheelite as an ore-deposit discriminator using its trace-element and REE chemistry. *The Canadian Mineralogist*, **56**, 265–302.
- Rasmussen K.L., Lents D.R., Falck H. and Pattison D.R.M. (2011) Felsic magmatic phases and the role of late-stage aplitic dykes in the formation of the world-class Cantung Tungsten skarn deposit, Northwest Territories, Canada. *Ore Geology Reviews*, **41**, 75–111.
- Rossi P., Oggiano G. and Cocherie A. (2009) A restored section of the “southern Variscan realm” across the Corsica-Sardinia microcontinent. *Comptes Rendus Geoscience*, **341**, 224–238.
- Salvadori I. and Zuffardi P. (1961) Il giacimento di Monte Tamara. *Resoconti dell'Associazione Mineraria Sarda*, **65**(7).
- Sharp D.Z., Essene E.J. and Kelly W.C. (1985) A Re-Examination of the Arsenopyrite Geothermometer: Pressure Considerations and Applications to Natural Assemblages. *The Canadian Mineralogist*, **23**, 517–534.
- Shimizu M. and Shikazono N. (1985) Iron and zinc partitioning between coexisting stannite and sphalerite: a possible indicator of temperature and sulfur fugacity. *Mineralium Deposita*, **20**, 324–320.
- Shimizu M., Shimizu M. and Tsunoda K. (2008) Physicochemical environment of formation of tin sulfide-bearing deposits in Japan. *Far Eastern Studies*, **7**, 23–40.
- Song G., Qin K., Li G., Evans N.J. and Chen L. (2014) Scheelite elemental and isotopic signatures: Implications for the genesis of skarn type W-Mo deposits in the Chizhou Area, Anhui Province, Eastern China. *American Mineralogist*, **99**, 303–317.
- Stille H. (1939) Bemerkungen betreffend die “Sardische Faltung” und den Ausdruck “ophiolitisch”. *Zeitschrift Deutschen Geologischen Gesellschaft*, **91**, 771–773.
- Sun S.-s. and McDonough W.F. (1989) Chemical and isotopic systematics of oceanic basalts: implications for mantle composition and processes. Pp. 313–345 in: *Magmatism in the Ocean Basins* (Saunders, A.D. and Norry, M.J., editors). Geological Society, London, Special Publications, **42**. <https://doi.org/10.1144/GSL.SP.1989.042.01.19>.
- US Geological Survey (2021) Deposit Classification Scheme for the Critical Minerals Mapping Initiative Global Geochemical Database. *U.S. Geological Survey Open-File Report 2021-1049*, pp. 70.
- Valera R. (1970) La scheelite: una nuova prospettiva nella giacimentologia sarda. *Resoconti dell'Associazione Mineraria Sarda*, **75**(8).
- Valera R. and Zuffardi P. (1968) Segnalazione di Scheelite in taluni adunamenti metamorfici della Sardegna (Nota preliminare), *Resoconti dell'Associazione Mineraria Sarda*, **73**(7), 62–64.
- Valera R. and Zuffardi P. (1970) La geochimica del tungsteno nel Paleozoico della Sardegna, *Rendiconti della Società Italiana di Mineralogia e Petrologia*, **26**, 815–830.
- Verkaeren J. and Bartholomé P. (1979) Petrology of the San Leone Magnetite Skarn (S.W. Sardinia). *Economic Geology*, **74**, 53–66.
- Voudouris P., Melfos V., Spry P.G., Bonsall T.A., Tarkian M. and Solomos Ch. (2008) Carbonate-replacement Pb-Zn-Ag±Au mineralization in the Kamariza area, Lavrion, Greece: Mineralogy and thermochemical conditions of formation. *Mineralogy and Petrology*, **94**, 85–10.

- Warr L.N. (2021) IMA-CNMNC approved mineral symbols. *Mineralogical Magazine*, **85**, 291–320.
- Yuan L., Chi G., Wang M., Li Z., Xu D., Deng T., Geng J. and Hu M. and Zhang L. (2019) Characteristics of REEs and trace elements in scheelite from the Zhuxi W deposit, South China: Implications for the ore-forming conditions and processes. *Ore Geology Reviews*, **109**, 585–597.
- Zajacz Z., Halter W.E., Pettko T. and Guillong M. (2008) Determination of fluid/melt partition coefficients by LA-ICPMS analysis of co-existing fluid and silicate melt inclusions: Controls on element partitioning. *Geochimica et Cosmochimica Acta*, **72**, 2169–2197.
- Zaw K. and Singoyi B. (2000) Formation of magnetite-scheelite skarn mineralization at Kara, Northwestern Tasmania: evidence from mineral chemistry and stable isotopes. *Economic Geology*, **95**, 1215–1230.
- Zhu D.-P., Li H., Algeo T.J., Jiang W.-C. and Wang C. (2021) The prograde-to-retrograde evolution of the Huangshaping skarn deposit (Nanling Range, South China). *Mineralium Deposita*, **56**, 1087–1110.

CHAPTER III

Major and trace elemental composition of magnetite from Sardinia, Italy: implications on the evolution of W-Sn-bearing skarns and on the role of germanium as their marker.

Matteo L. Deidda¹, Alfredo Idini¹, Kalin Kouzmanov², Florence Begue², Lorenzo Tavazzani³, Aratz Beranoaguirre⁴, Sebastian Staude⁵, Clifford Patten⁴, Marilena Moroni⁶, Giovanni B. De Giudici¹, Stefano Naitza^{1*}

¹ Department of Chemical and Geological Sciences, University of Cagliari, 09042, Monserrato (CA), Italy

² Department of Earth Sciences, University of Geneva, CH-1205 Geneva, Switzerland

³ ETH Zürich, Department of Earth Sciences, Institute for Geochemistry and Petrology, Zürich, Switzerland

⁴ Institute of Applied Geosciences, Chair of Geochemistry and Economic Geology, Karlsruhe Institute of Technology, 76131 Karlsruhe, Germany

⁵ Department of Geosciences, University of Tübingen, Schnarrenbergstrasse 94-96, 72076 Tübingen, Germany

⁶ Dipartimento di Scienze della Terra, Università degli Studi di Milano, Via Luigi Mangiagalli, 34, 20133 Milano MI, Italy

To be submitted for

Mineralium Deposita – Springer

Major and trace elemental composition of magnetite from Sardinia, Italy: implications on the evolution of W-Sn-bearing skarns and on the role of germanium as their marker.

Matteo L. Deidda¹, Alfredo Idini^{1*}, Kalin Kouzmanov², Florence Begue², Lorenzo Tavazzani³, Aratz Beranoaguirre⁴, Sebastian Staude⁵, Clifford Patten⁴, Marilena Moroni⁶, Giovanni B. De Giudici¹, Stefano Naitza¹.

Abstract: Magnetite is one of the most recurrent minerals in skarns. In the last decade, research focused on its composition as useful tool to deepen the classification of ore deposits. This work combined a detailed petrographic study with the major and trace elemental composition with the aim of characterizing the evolution stages recorded by magnetite in skarns. The most abundant trace elements detected in studied magnetites are germanium, tin and tungsten up to 20, 1000 and 80 ppm respectively. The T_{Mg-Mag} geothermometer values indicate a formation under isothermal conditions, with an evolution from prograde (585-687°C) to retrograde stages (512-454°C) of skarn evolution. Tin contents in magnetite increased during the prograde stage along with Sn-rich rims of garnet. The retrograde stage is marked by fluorite, cassiterite and Sn-poor magnetite. This study points out that the Ga and Ge contents could be used to discriminate W-Sn skarns from Fe skarns.

Introduction

Magnetite (Fe_3O_4) is a ubiquitous mineral that forms in many geological environments and under different conditions. It belongs to the oxyspinel group and is characterized by an inverse-spinel structure with a AB_2O_4 general formula, where the site A is occupied by Fe^{2+} and B by Fe^{3+} . The spinel structure is remarkably flexible, leading to extensive solid solution with other spinel end members (Bosi et al. 2019). Bivalent cations like Mg^{2+} , Zn^{2+} , Co^{2+} , Ni^{2+} , V^{2+} , Mn^{2+} typically substitute for Fe^{2+} in the A site, whereas trivalent cations like Al^{3+} , Mn^{3+} , Ga^{3+} , V^{3+} , Cr^{3+} substitute for Fe^{3+} in the B site. Other isomorphic series with the end members of the ulvöspinel subgroup may occur and, in this case, the A and B site are respectively occupied by tetravalent and bivalent cations, like the well-known solid solution magnetite-ulvöspinel (Fe_2TiO_4) (Bosi et al. 2019). Investigations based on its physical and thermodynamic properties, as well as its compositional features have been carried out to investigate various processes in many geological settings. For instance, the magnetite vs ilmenite occurrence in granitoid rocks has been extensively used to define the

oxidizing vs reducing conditions of granitic rocks and the metallogenic relationships with redox-sensitive elements (e.g., Sn) in the associated ore deposits (Ishihara, 1981). In fact, magnetite occurs in many ore deposit classes worldwide, including banded iron formation (BIF), iron oxide copper gold deposit (IOCG), porphyry copper gold (PCG), hydrothermal veins, skarn deposits, volcanogenic massive sulphide (VMS), Ni-Co and platinum group elements (PGE) and some rarer and more peculiar deposits such as the Kiruna-type and Ti-V-Fe ores (Dupuis and Beaudoin 2011; Boutroy et al. 2014; Dare et al. 2014, 2015; Nadoll et al. 2014; Hu et al. 2015; Wen et al. 2017). As a proxy of redox conditions, in the last decades magnetite has been used for the estimation of oxygen fugacity in silicate rocks using the fayalite-magnetite-quartz buffer (FMQ; Frost 1991), as well as the ilmenite-magnetite thermometer and oxybarometer (ILMAT, Lepage 2003) and geothermometers based on Mg contents (Canil and Lacourse 2020). In most recent years, the trace-elemental composition of magnetite has been increasingly applied to discriminate, and possibly classify, different classes of ore

deposits and to highlight their sources and mechanisms of formation (Dupuis and Beaudoin 2011; Boutroy et al. 2014; Dare et al. 2014, 2015; Nadoll et al. 2014; Hu et al. 2015; Wen et al. 2017). In skarn deposits magnetite is usually one of the most abundant minerals, together with garnet and clinopyroxene, locally forming massive and continuous bodies at the contact with granites. Driven by the current needs of strategic and critical raw materials, recent studies have concerned the Variscan mineralized skarn deposits of Sardinia, one of the historical mining districts of Europe. These relatively poorly studied deposits (Verkaeren and Bartholomé 1979; Aponte et al. 1988; Protano et al. 1996), partly exploited in the past for base metals, are currently under investigation for their Sn, W, Bi, Mo, In, Ge and REE contents. In these studies, the paragenetic constraints of magnetite are characterized in more detail, revealing a close association with prograde and retrograde calc-silicates and both cassiterite and scheelite (Naitza et al. 2017; Deidda et al. 2022; Cocco et al. 2022). However, only a few of them stressed the attention on mineral chemistry and related petrological constraints. The aim of this research is to provide a first elemental characterization of magnetite from four Sn-W(-Mo-Bi)-bearing skarns of Sardinia and to identify a set of geochemical markers which could be applied as an exploration tool for these skarns. In three of the studied Variscan skarns (Perda Niedda, Monte Tamara, Rosas; SW Sardinia), characterized by similar geological settings, Sn, W, Mo and Bi ore minerals are already documented. A further Variscan skarn ore from a different setting (Giacurru; E Sardinia) has been used as a counterpart to verify possible geochemical similarities or differences.

Geological setting

Sardinia represents a southern segment of the European Variscan chain and its structure can be subdivided into three main tectono-metamorphic domains. Such domains include, from south to north: 1. an External Zone at the SW (Sulcis-Iglesiente and Arburese regions); 2. A Nappe Zone at the SE and Central parts (Sarrabus-Gerrei and Barbagia regions); 3. an Axial Zone at the North. According to this division, the Cambrian to Permian sedimentary formations of the pre-Variscan succession are affected by variably intense regional metamorphism and deformations. The External Zone is affected by very low-grade regional metamorphism and by overall mild E- to W-facing foldings. The local development of km-scale shear zones at (e.g., the Rosas Shear Zone) causes more pervasive deformations such as overturned foldings, mylonitic foliation and tectonic slices (Cocco et al. 2022). In the Nappe Zone the pre-Variscan succession is affected by more intense deformations along a N-S direction of shortening and regional-scale thrusts that produce repetitions and tectonic units (Meana Sardo unit, Gerrei unit, M. Grighini unit Riu Gruppa unit). A later E-W direction of shortening is displayed by the Sarrabus-Arburèse unit, the uppermost tectonic unit of the nappe stack. Towards the Axial Zone metamorphism increases from S to N from a medium grade Barrovian-type zonation to HTHP metamorphism (amphibolite-retrogressed granulites and migmatites) along the so-called Posada Asinara Line. The extensional regime in the late-Variscan stages favoured the emplacement of the wide and composite Sardinian Batholith, outcropping from Corsica to the south of Sardinia (Rossi and Cocherie 1991), particularly along late-Variscan shear zones (Casini et al. 2015). In southern Sardinia the late- to post-Variscan intrusives include three distinct suites (GS1, GS2, GS3; Conte et al. 2017), dated overall in

the 295-277 Ma interval (Secchi et al. 2021, and references therein). Particularly, the GS1 suite has been regarded as the intrusive event causative of the several granite-related mineralization of the area (Naitza et al. 2017). From a petrogenetic standpoint, the GS1 unit consists of slightly peraluminous, ferroan, porphyritic leucogranites with accessory xenotime-Y and fluorite (Conte et al. 2017; Naitza et al. 2017). Due to its emplacement at shallow crustal levels (< 2 kbar) and the low-dipping, sub-horizontal geometries of the intrusive bodies, contact-metamorphic effects on the pre-Variscan units can be observed continuously over large areas. These features, as well as their reducing character (ilmenite series), the spread evidence of greisenisation (e.g., alkali metasomatism, biotite alteration, sericitization, chloritization and reabsorption gulfs in quartz) and the spatial correlation with the ores, are common among granites associated with Sn(-W) mineralization worldwide (Pirajno 2009).

Skarn ores of Southern Sardinia

In Southern Sardinia, GS1 suite-related mineralized skarns commonly occur in carbonate rocks of the pre-Variscan sedimentary units. They are particularly numerous in SW Sardinia, where skarns are most frequently formed in i) early Cambrian massive limestones and dolostones (Gonnesa Group, Pillola et al. 1991), in ii) fine-grained limestone lenses in early Cambrian metasandstones (Nebida Group, Punta Manna Fm; Pillola et al. 1991) and, subordinately, in iii) middle Cambrian nodular silty limestones (Campo Pisano formation; Eliko and Pillola 2004). During skarn-forming processes, metasomatic fluids circulation was often aided by pre-existing structures along lithological and tectonized contacts between carbonate and sandstones/schists (Cocco et al. 2022; Deidda et al. 2022). This host rock variability led to different gangue mineral assemblages, respectively characterized by: i)

coarse-grained garnet-clinopyroxene, with amphibole-chlorite alteration and subordinate epidote (Perda Niedda, Monte Tamara, Rosas (Naitza et al. 2017; Cocco et al. 2022; Deidda et al. 2022); ii) fine grained epidote-chlorite-calcite with subordinate garnet (Aponte et al. 1988); iii) clinopyroxene-epidote-chlorite-quartz (Monte Tamara; Deidda et al. 2022). The ore mineral assemblages commonly include sphalerite, galena, magnetite, arsenopyrite, chalcopyrite and pyrite; fluorite is common and locally abundant. Together with As-Cu-Fe, elements such as Sn-W-Mo-Bi-In form a representative assemblage in skarn mineralization spatially and genetically associated to the GS1 intrusive suite (Deidda et al. 2022). Therefore, mineral phases as scheelite and cassiterite can be locally abundant, along with traces of molybdenite, stannite, native Bi, bismuthinite and Bi-Pb-Cu sulfosalts.

Perda Niedda

The Perda Niedda old mine (Fig.1a) comprises an area of roughly 30 km² at the contact between marbles derived from the Lower Cambrian carbonates of the Gonnesa Group, Upper Ordovician siliciclastic rocks of the M.te Argentu formation and the Oridda intrusion GS1 leucogranites (Naitza et al., 2017). In this area, the leucogranites are characterized by a porphyritic texture, characterized mostly by K-feldspar (orthoclase and microcline), Na-plagioclase (Ab₇₅₋₈₅), quartz with resorbed edges, white mica and biotite, often chloritized; ilmenite and xenotime are common accessories. Various grades of greisenisation can be observed, the most intense occurring as dark greyish veins mainly composed of white mica and chlorite, cross-cutting the pinkish less altered granite. They become more frequent towards the contact with marbles. At the contact with marbles, the skarn primarily consists of coarse-grained, green and idiomorphic andradite-grossular garnets, with

very subordinate clinopyroxene. Advanced retrograde alteration deeply affected the skarn, testified by the pervasive substitution of garnet and pyroxene by amphibole (tremolite-actinolite), biotite and chlorite-fluorite-magnetite aggregates; talc and serpentine were occasionally observed. The ores consist of massive magnetite and octahedral fluorite bodies, cross-cut by massive quartz veins, interspersed between the greisenised granites and the marbles. The mineralized skarn locally displays a particular “wrigglite-type” finely layered texture (Kwak and Askins 1981) consisting of mm-to cm-sized layers of magnetite-cassiterite-sphalerite intercalated with quartz-fluorite-biotite-chlorite (Naitza et al. 2017). Cassiterite is present also in the fluorite-rich bodies and in the quartz veins. Sulfides are generally subordinate, essentially including (in order of abundance), sphalerite, chalcopyrite, marcasite, galena. Very late idiomorphic pyrite grows on magnetite. Mineral associations equilibria and available fluid inclusions data constrain the Perda Niedda skarn mineralizing stages in the 500-200 °C interval (Aponte et al. 1988).

Monte Tamara

The Monte Tamara area is characterized both by typical calc-silicate skarns (San Pietro mine) and hydrothermal arsenopyrite-scheelite-sphalerite (Sinibidraxiu mine) orebodies. The San Pietro skarn is a 5 m thick subvertical orebody located at the contact between the Lower Cambrian Gonnese Group marbles and the Nebida Group sandstones (Fig1b); the spatial relationships with granites of the GS1 suite outcropping a few kilometres to the SE (Sulcis intrusion: Conte et al. 2017), are not directly visible. The orebody basically consists of sphalerite-galena-chalcopyrite and arsenopyrite pockets in a calc-silicate skarn. The foremost skarn minerals are diopside and grossular-andradite garnet; occasionally, in the more altered

facies, epidote, amphibole (tremolite-actinolite), chlorite, calcite and quartz become more abundant. The complex mineral associations and variability of the orebody can be summarized in two main assemblages: a) scheelite-magnetite-chalcopyrite-cassiterite disseminations in the diopside-garnet skarn facies; b) a sulfide-rich assemblage consisting of magnetite-arsenopyrite-sphalerite-chalcopyrite, with subordinate amounts of cassiterite-stannite, Bi-phases and molybdenite in the retrogressed calc-silicate facies (Deidda et al. 2022). The paragenetic sequence displays a polyphase formation of grossular-andradite, diopside and scheelite during the prograde stage, followed by the formation of retrograde calc-silicates (epidote, amphibole, chlorite and calcite-quartz), magnetite, cassiterite and sulfides during the hydrothermal stage. Temperatures of formation have been calculated to constraint the early-mid hydrothermal stage between 460-425°C (arsenopyrite geothermometer) and 315-255°C (stannite geothermometer; Deidda et al. 2022).

Rosas

Located about 7 km NW from Monte Tamara, the Rosas mine area (Fig.1c) is also characterized by numerous skarn orebodies situated in the same carbonate unit of the Gonnese Group. An higher grade of deformation, related to a brittle-ductile shear zone (Rosas Shear Zone, RSZ (Funedda 2009; Cocco et al. 2022) characterize the pre-Variscan successions in this area, where frequent carbonate tectonic slices are embedded in Ordovician siliciclastic rocks. Due to this strong structural control, the area is interpreted as a distal portion of a wider skarn system where hydrothermal fluids circulation occurred for larger distances from an inferred GS1 source (Sulcis intrusion), aided by deep faults and thrusts. The same structural setting favoured the emplacement

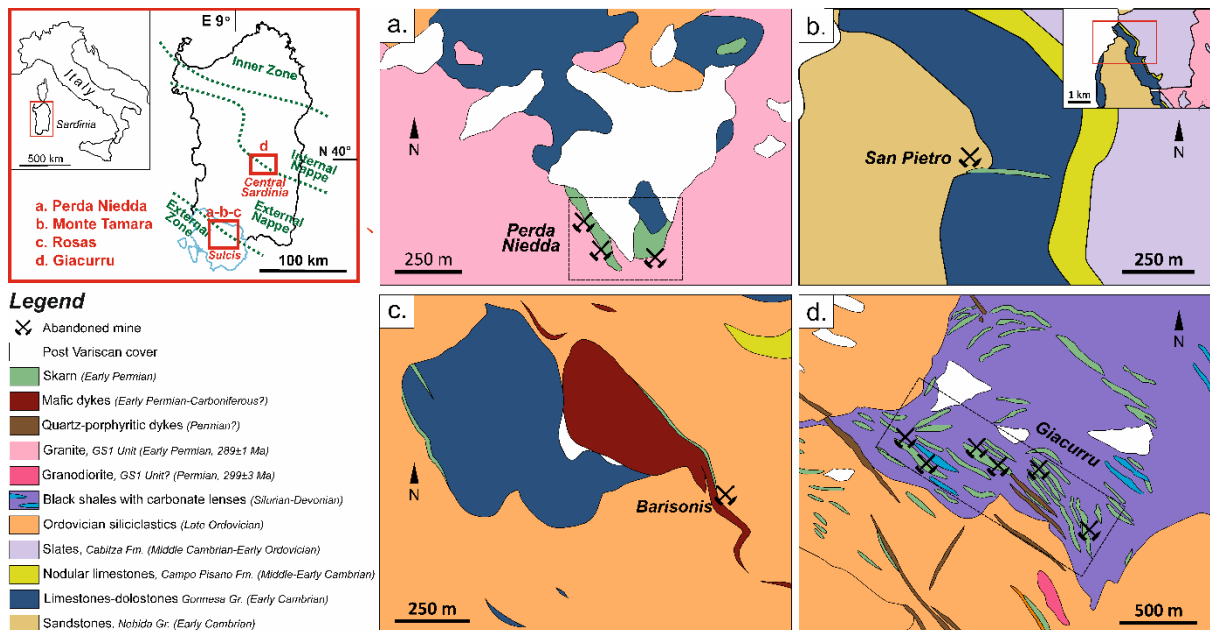


Figure 1 – Lithologic sketch maps of the studied areas in SW and Central Sardinia, Italy. The skarn ores of the Perda Niedda (a), Monte Tamara (b, mod. after [Deidda et al. 2022](#)) and Rosas (c, mod. after [Cocco et al. 2022](#)) old mining areas are formed after metasomatism on Cambrian carbonates of the Gonnessa Group. The Rosas skarn is located in a small limestone slice at the contact with a mafic dyke. Skarns from the Giacurru old mining area (d, mod. after [Meloni et al. 2017](#)) are located along carbonate lenses hosted in a black shales unit.

of several mafic calc-alkaline bodies of gabbroid-spessartitic composition, which crosscut the pre-Variscan basement as a swarm of NW-trending dykes. Field and mineralogical evidences indicate that the emplacement of mafic bodies preceded the skarn mineralization throughout the area ([Cocco et al., 2022](#)). Among the different mineralized skarns in Rosas, the Barisonis skarn orebody is one of the most representative. The skarn is formed on a carbonate slice embedded in Ordovician siliciclastics; a gabbroid dyke emplaced along one of the bordering faults of the metasomatized carbonate lens. The skarn is mostly characterized by idiomorphic and coarse-grained hedenbergite (up to 5 wt% of Mn) with grossular-andradite thinner bands towards the edges of the skarn orebody. Epidote and amphibole are common, while chlorite is rarer and associated with titanite and relict rutile crystals. The orebody occurs in the middle portion of the skarn and consists of massive sphalerite, galena and chalcopyrite, with local zones of enrichment in covellite and bornite. Magnetite and

cassiterite are closely associated with veinlets of quartz-fluorite-chlorite. Bismuthinite, tetrahedrite, argentite-achantite and gold blebs sporadically occur towards the contact with the gabbroid dyke.

Giacurru

The Giacurru old mining area (also known as *Perdabila*; [Fig.1d](#)), is located in the Barbagia region of central Sardinia. It is considered the largest magnetite-bearing skarn of Sardinia, with around 80,000 tons of ore reserves ([Meloni et al. 2017](#)). As typical of the Nappe Zone of Sardinian Variscan belt, deformations are more pervasive and regional metamorphism reaches the greenschist facies. A pre-Variscan Cambrian-Early Devonian succession, definitely different from that occurring in SW Sardinia ([Loi et al. 2023](#)) is isoclinally folded and frequently displays higher deformation zones marked by mylonitic foliation. Small intrusive bodies of a fine grained equigranular granodiorite (U-Pb age of 299 ± 3 Ma; [Meloni et al. 2017](#)) crop out for a few hundreds of square meters, but the widespread contact metamorphism of the

area suggest the presence of a larger intrusive body at depth. The skarn ores are located along the hinge of a late-Variscan antiformal fold and consist in a series of lens-shaped bodies formed after Silurian carbonate lenses embedded in a black shale succession (“Scisti a Graptoliti Auct.” Formation). Ordovician-Silurian meta-basite rocks are locally also affected by metasomatism and spatially associated with the skarn-lenses field. The prograde mineralogy of the skarn is mostly dominated by andradite (with minor spessartite and pyrope components) and hedenbergite-diopside (with minor johannsenite); actinolite and epidote constitute the retrograde calc-silicate assemblage (Meloni et al. 2017). The ore minerals mostly include massive magnetite, sphalerite, galena, chalcopyrite and pyrite. To some extent, the Giacurru mineralisation has been previously linked to the nearby Funtana Raminosa mineralization, also classified as skarn-type (Protano et al. 1996).

Analytical methods

A total of 19 magnetite-bearing skarn samples, collected from outcrops and mine dumps from the four different localities, have been investigated (Table S1). Among those, 14 samples are representative of skarns of the SW Sardinia district (PN3-PN5, PN7, PN10, PN11, PN-W, PNB1, PN28B from Perda Niedda; VMd5b, VMd8c, VMd9, MTA3D, MTA6 from Monte Tamara; BS.S2.02 from Rosas), whereas 5 samples represent magnetite-bearing skarns from Central Sardinia (GIAC1, GIAC2a, GIAC2b, GIAC3, GIAC4 from Giacurru). A larger number of samples from SW Sardinia district was chosen to have a more comprehensive overview of magnetite in skarns associated with the documented W-, Sn-, Mo- and Bi-minerals, that are the markers of the same metallogenic source (granites of the GS1 unit), and with the same carbonate protolith (Gonnesa Gr.).

Each sample has been first characterized by means of Transmitted and Reflected Light Optical Microscope to identify gangue and ore minerals and their textural and paragenetic features. For a further detailed characterization, SEM-EDS analyses and BSE imaging have been done to observe compositional zoning and to evaluate the presence of micro- and nano-inclusions. The major and minor elemental composition has been investigated by means of electron probe microanalysis (EPMA) using a JEOL 8200 Superprobe at the University of Geneva (Switzerland) and a JEOL JXA-8230 at the University of Tübingen (Germany). On both analytical setups, the analyses have been conducted in wavelength-dispersive (WD) mode under 20 kV accelerating voltage, 20 nA beam current and using a focused beam. Counting times of 16/8 s (peak/background) for main elements and 30/15 s for trace elements were used. We measured the following elements and their characteristic X-Ray peaks, which were standardized with in-house standards of silicate, oxide or pure metal composition: Al ($K\alpha$), Sn ($L\alpha$), Si ($K\alpha$), Fe ($K\alpha$), Ti ($K\alpha$), Mn ($K\alpha$), Mg ($K\alpha$), Cr ($K\alpha$), Ta ($L\alpha$), Nb ($L\alpha$), W ($L\alpha$), Zn ($K\alpha$), V ($K\alpha$). Some elements (W, Zn, Nb, Ta) were usually close to or below the detection limit in the first analytical runs therefore we excluded them from the following analyses (labelled n.a., standing for not analyzed). Counting times on the peak were set to 30s and the background, before and after the peak, was measured during, 15s. The precision is typically between 0.5 and 5% for major elements and can be up to 10% for elements at concentration lower than 0.1%. Representative results are presented in Table 1 and all results in wt% and atoms per formula unit (apfu), as well as detection limits, are provided in Tables S2-3.

Magnetite trace element analyses were performed on thin sections by laser ablation-inductively coupled plasma-mass

spectrometry (LA-ICP-MS) at the ERDW department of ETH Zurich (Switzerland) and at the department of Karlsruhe Institute of Technology (Germany) using an ASI RESOLUTION S-155 excimer (ArF, 193 nm) laser ablation system coupled to a Thermo Element XR sector-field ICP-MS and a Teledyne 193 nm Excimer Laser coupled to a ThermoFisher Element XR sector-field ICP-MS respectively. Variable spot sizes of 25 and 43 μm and 5.0-8.0 Hz repetition rate with a laser energy density on sample surface of ca. 3.5-5 J/cm^2 were used for ablation of unknowns and reference materials. The ablation aerosol was mixed in the fast washout S-155 ablation cell (Laurin Technic) with carrier gas consisting of helium (ca. 0.5 L min^{-1}) and make-up gas consisting of argon (ca. 1 L min^{-1}) and nitrogen (2 mL min^{-1}). The ablated aerosol was then homogenized by flushing through an in-house built squid device before introduction into the plasma torch. The single collector sector-field MS is equipped with a high-capacity (80 $\text{m}^3 \text{h}^{-1}$) interface pump. Detailed instrumentation and data acquisition parameters are summarized in Tab. S5 of Electronic Supplementary Material following reporting standards of Horstwood et al. (2016). The list of analysed elements and isotopes includes: ^7Li , ^9Be , ^{11}B , ^{23}Na , ^{25}Mg , ^{27}Al , ^{29}Si , ^{31}P , ^{33}S , ^{35}Cl , ^{39}K , ^{43}Ca , ^{44}Ca , ^{45}Sc , ^{47}Ti , ^{51}V , ^{53}Cr , ^{55}Mn , ^{57}Fe , ^{59}Co , ^{60}Ni , ^{63}Cu , ^{65}Cu , ^{66}Zn , ^{69}Ga , ^{72}Ge , ^{73}Ge , ^{74}Ge , ^{75}As , ^{77}Se , ^{78}Se , ^{85}Rb , ^{88}Sr , ^{89}Y , ^{90}Zr , ^{93}Nb , ^{95}Mo , ^{107}Ag , ^{111}Cd , ^{113}In , ^{115}In , ^{118}Sn , ^{121}Sb , ^{133}Cs , ^{137}Ba , ^{139}La , ^{140}Ce , ^{141}Pr , ^{146}Nd , ^{147}Sm , ^{151}Eu , ^{157}Gd , ^{158}Gd , ^{159}Tb , ^{161}Dy , ^{165}Ho , ^{167}Er , ^{169}Tm , ^{172}Yb , ^{175}Lu , ^{177}Hf , ^{181}Ta , ^{183}W , ^{197}Au , ^{202}Hg , ^{208}Pb , ^{209}Bi , ^{232}Th , ^{238}U . Dwell times were set to 11 ms for all analyzed masses. Calibration and data quality checking was done using the SRM-NIST610 and SRM-NIST612 silicate glasses (Jochum et al., 2011) and the certified glass reference materials GSD-1G (Guillong et al. 2005) BCR-2G, BIR-1G and BHVO-2G (Gao et al. 2002). The quoted uncertainties for each analysis correspond to the internal (2σ)

statistical error and analytical reproducibility propagated by quadratic addition. The data are reported in Table S5 in the Electronic Supplementary Material.

Petrographic and textural features

Perda Niedda

In the Perda Niedda skarn orebody, magnetite hand-specimens are very abundant, occasionally forming aggregates of idiomorphic crystals up to 3 mm in the chlorite matrix. A first type of magnetite texture (MagA) consists of corroded rounded individuals with high porosity and very abundant calc-silicate inclusions forming massive aggregates (Fig.2a; PN5). Occasionally, MagA with radial fractures is surrounded by sphalerite (PN-W, PNB1). A second texture (MagB) is the most recurrent throughout the examined samples and its main features are the idiomorphic octahedral habit, the compositional zoning and the less abundance of inclusions. It occurs a) in aggregates overgrowing the corroded rounded MagA (Fig.2a; PN5), b) as inclusions in the rims of green, idiomorphic and zoned garnet (Fig.2b; PN3), c) associated with pervasively altered garnet, substituted by amphibole, chlorite, phlogopite, fluorite and cassiterite (Fig.2d; PN10, PN11) as well as d) in "wrigglite"-type facies (Fig.2c; Kwak and Askins 1981, Naitza et al. 2017), with cassiterite at its edges, fluorite, quartz and chlorite.

Monte Tamara

Magnetite from Monte Tamara occurs in the massive bodies at the selvages of the main orebody, in association with sphalerite-galena and as tiny seams in the diopside-rich matrix together with scheelite-chalcopyrite-cassiterite. Three main magnetite textures have been

distinguished. The first (Mush) is represented by fibrous mushketovite aggregates with hematite relics (Fig.2e), usually associated with partially altered grossular-andradite garnet and unaltered, coarse-grained diopside (VMd9; MTA6). The second texture (MagA) includes anhedral to euhedral individuals often associated with sphalerite, chalcopryite, galena and scheelite-cassiterite. Typical features of MagA are both the very dense and “graphic” zoning patterns, corresponding to abundant μ -scale galena grains inclusions. It is frequently

observed in: a) aggregates of 10 μ m idiomorphic crystals coating mushketovite in the unaltered garnet (Fig.2e; VMd8c; MTA6) and b) in crystals surrounded by MagB in the unaltered clinopyroxene facies (VMd5b; VMd9). A third texture (MagB) includes aggregates with the same “graphic” zoning patterns of MagA but less galena inclusions (VMd9-VMd5b-MTA3D). Due to the absence of galena inclusions, zoning is much more regular (VMd9). It is often found in the diopside-amphibole facies, associated with scheelite-cassiterite-chalcopryite facies (Fig.2f-g;

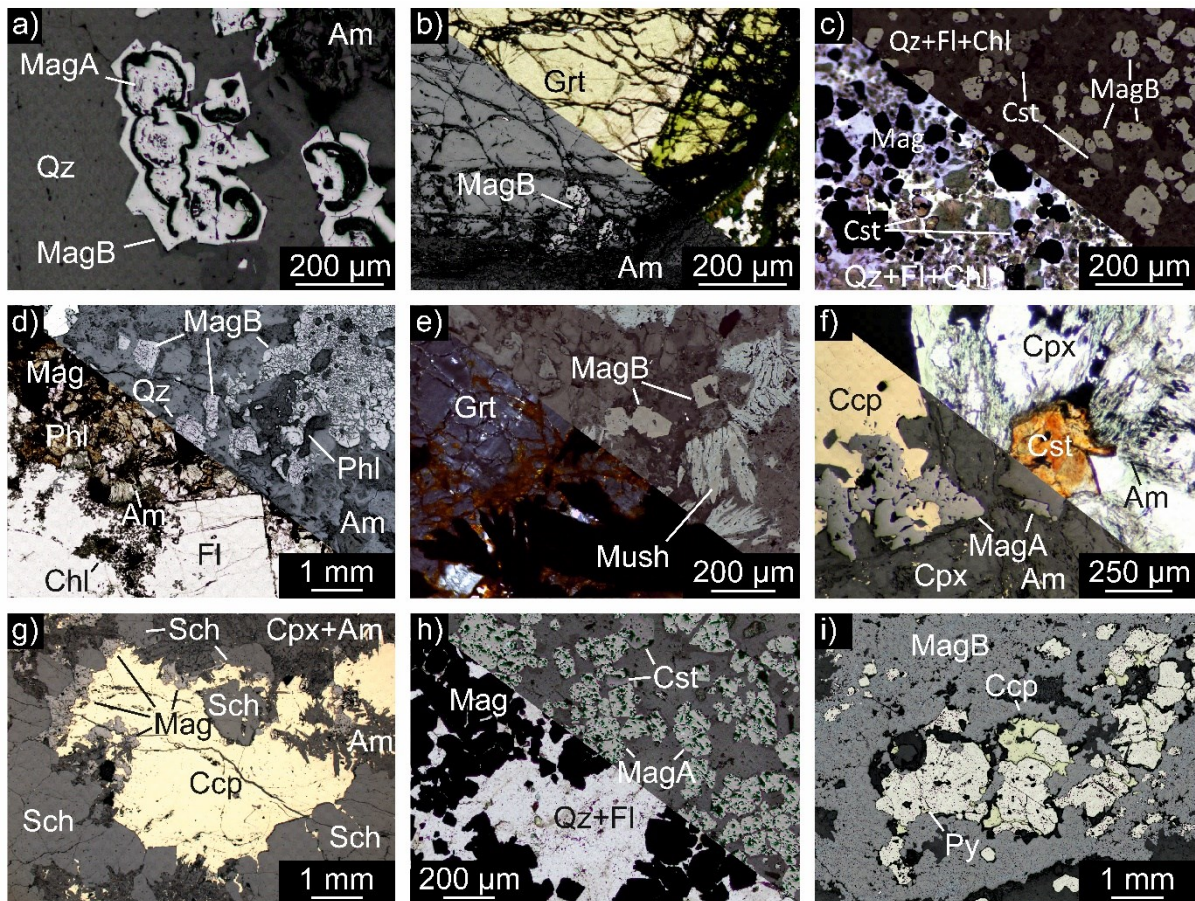


Figure 2 – Photomicrographs of representative samples from the Perda Niedda, Monte Tamara, Rosas and Giacurru: (a) rounded and corroded MagA surrounded by MagB idiomorphic crystals (Perda Niedda, PN5, 10x, RL); (b) idiomorphic magnetite (MagB) enclosed in the rim of garnet (Perda Niedda, PN3, 10x, combined TL-RL); (c) “wrigglite”-type association of idiomorphic/subhedral magnetite with cassiterite, fluorite, quartz and chlorite (Perda Niedda, PN28B, 5x combined TL-RL); (d) idiomorphic magnetite in association with phlogopite, chlorite, amphibole and fluorite (Perda Niedda, PN11, 5x, combined TL-RL); (e) mushketovite with hematite relics and idiomorphic magnetite (MagB) in unaltered garnet assemblage (Monte Tamara, MTA6, 10x, combined TL-RL); (f-g) magnetite associated with scheelite, cassiterite and chalcopryite in a clinopyroxene-amphibole gangue (Monte Tamara, VMd5b, 5x, combined TL-RL); (h) “wrigglite”-type association of magnetite, cassiterite, quartz and fluorite (Rosas, BS.S2.02, 10x, combined TL-RL); (i) porous magnetite aggregate (MagB) enveloping pyrite and chalcopryite (Giacurru, GIAC2b, 2.5x, RL). Mag= magnetite; Mush = mushketovite; Cst = cassiterite; Sch = scheelite; Grt = garnet; Cpx = clinopyroxene; Am = amphibole; Chl = chlorite; Phl = phlogopite; Qz = quartz; Fl = fluorite; Ccp = chalcopryite; Py = pyrite.

VMd9-VMd5b; Deidda et al. 2022). When they coexist, MagB envelops inclusion-rich grains of MagA (VMd9).

Rosas

Magnetite from Rosas the Barisonis skarn outcrop (MagA) is confined in a small cassiterite, quartz, fluorite and chlorite veinlet hosted in a hedenbergite-rich skarn facies (BS.S2.02; Cocco et al. 2022). It occurs in oriented seams of subhedral crystals of 500 μm in size, closely associated with cassiterite in a quartz-fluorite-chlorite gangue, very similarly to the Perda Niedda wriggilite-like facies

(Fig.2h). It often occurs as isolated individuals, locally forming small aggregates, interspersed in quartz and fluorite. The surface is usually fresh with no inclusions and porosity; zoning is not visible. Cassiterite is up to 200 μm in size and grows at the edges of magnetite (Cocco et al. 2022).

Giacurru

At Giacurru, magnetite occurs in two textures. The first is Mush forming at the expense of tiny relict lamellae of hematite (GIAC2b). Also, small (1-2 μm) calc-silicate inclusions are present.

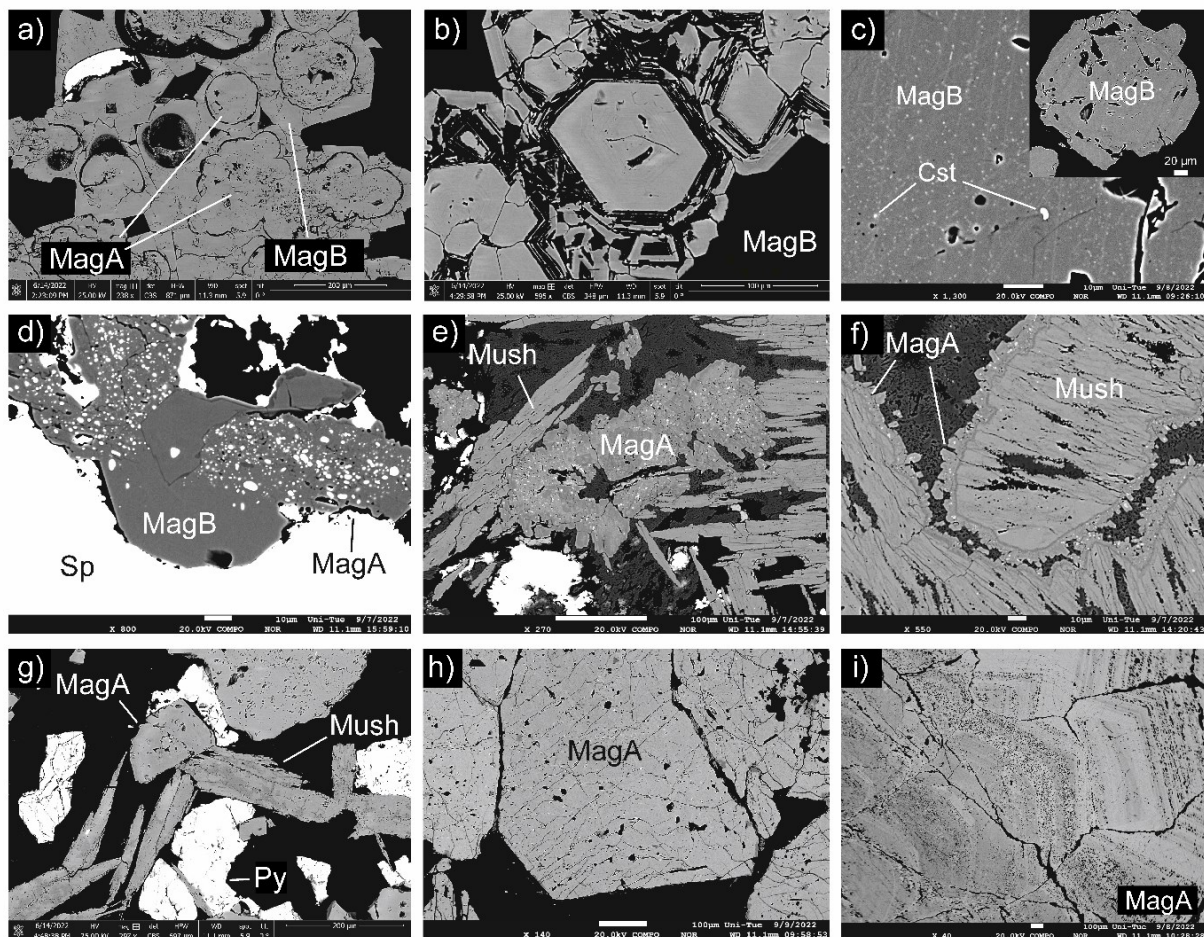


Figure 3 – Textural features of MagA and MagB observed in BSE images: (a) detail of the rounded and corroded MagA and idiomorphic MagB features (Perda Niedda, PN5); (b) idiomorphic and weakly zoned MagB (Perda Niedda, PN3); (c) idiomorphic/subhedral MagB from the wriggilite-facies, exhibiting abundant nano- and micro-scale cassiterite grains (Perda Niedda, PNB1); (d) Abundant sulfide inclusions, mostly composed by galena, of MagA overgrown by inclusion-poor MagB (Monte Tamara, MTA3D); (e-f) inclusion-rich MagA growing at the edges of mushketovite (Monte Tamara, MTA6); (g) idiomorphic/subhedral MagA growing at the edges of mushketovite (Giacurru, GIAC2a); (h) idiomorphic and fractured MagA (Giacurru, GIAC4); (i) dense zoning patterns and growth zones of idiomorphic MagA (Giacurru, GIAC3). Mag= magnetite; Mush = mushketovite; Cst = cassiterite; Py = pyrite.

The second generation (MagA) is the foremost type of magnetite throughout all samples, often associated with mushketovite in a clinopyroxene, epidote, vesuvianite and amphibole skarn facies and enveloped in sphalerite and pyrite. It is characterized by aggregates with very abundant calc-silicate inclusions of clinopyroxene, vesuvianite, epidote, amphiboles and carbonates (Fig.2i; GIAC2a-GIAC2b-GIAC3-GIAC4). Such aggregates are generally irregular and fractured; hematite patches and oriented lamellae can be observed along fractures (GIAC2a-GIAC2b-GIAC1). Towards the outer edges of MagA aggregates, though, idiomorphism is more accentuated as well as concentric zoning patterns (GIAC1-GIAC3-GIAC4). Calc-silicate inclusions are locally abundant (GIAC3). Isolated subhedral crystals form at the contact with mushketovite needles; pyrite grows in turn on the edges of both mushketovite and MagA (GIAC2a).

Results

The average EPMA and LA-ICP-MS data for each thin section and deposit are presented in Tables 1 and 2 respectively. All the results and detection limits for each EPMA and LA-ICP-MS spot, for a total number of 505 and 488 respectively, are presented in Tables S2-5-6-7 in the Supplementary Data.

EPMA

The major and minor average composition of all magnetite samples show that the Fe content ranges from around 69 wt% (VMd5a) to 72 wt% (PN28B), close to its stoichiometric value. Among minor elements, Si shows the highest values in all samples (up to 1.05 wt% in VMd9) except one (0.07 wt% in PN28B). Manganese ranges from 0.03 (PN3) to 0.71 wt%

(PNB1), attaining anomalous values of 4.57 wt% (GIAC4). Magnesium is generally lower than Mn and ranges from 0.03 (VMd8c-BS.S2.02) to 0.25 wt% (PN5). Comparable values have been detected for Sn (from 0.01 to 0.27 wt% in VMd5a and VMd9, respectively) and Al (from 0.02 to 0.12 wt% in PN10-PN11-BS.S2.02 and PN3, respectively). In some samples, Sn values are below the detection limit (MTA3D, GIAC1, GIAC2b, GIAC4). Other elements, such as Ti, Cr and Ta are frequently below the detection limit, or generally in the order of hundreds of ppm (up to 0.05 wt% of Ti; up to 0.02 wt% of Cr; up to 0.06 wt% of Ta). Vanadium, Zn, Nb and W have also been analysed (Table S2) but, since their values were usually below the detection limit, they have been omitted from Table 1.

LA-ICP-MS

The resulting intensities from LA-ICP-MS analyses were subsequently processed offline with Lolite v. 4.5. software (Paton et al. 2011). The synthetic glass NIST SRM610 (Jochum et al. 2011) was used as primary reference material for trace element quantification and instrumental drift correction using conventional standard-sample bracketing. The Fe contents obtained by EPMA were used as internal standard for relative sensitivity corrections. The analyzed In intensities on masses 113 and 115, respectively, were corrected for polybaric interferences by subtracting the contribution of ^{113}Cd and ^{115}Sn , respectively, based on the measured ^{111}Cd and ^{118}Sn intensities and using natural isotope ratios for Cd and Sn recommended by IUPAC. A careful observation of the time-resolved signal has been done to find the most representative portions of each magnetite spectrum, excluding the contribution of micro-

Table 1 – Average EPMA results for each thin section and deposit, including the calculated temperatures. Full data are available in Tables S2-3-4 of the ESM.
 bdl = below detection limit; n.a. = not analyzed;

| Sample | PN3 | PN5 | PN10 | PN11 | PN-W | PN28B | PNB1 | VMd5a | VMd8c | VMd9 | MTA3D | MTA6 | BS.S2.02 | GIAC1 | GIAC2a | GIAC2b | GIAC3 | GIAC4 | Perda Niedda | Monte Tamará | Rosas | Giaccurru |
|------------------------------------|-------|--------|-------|--------|--------|--------|--------|-------|-------|-------|--------|--------|----------|-------|--------|--------|--------|--------|--------------|--------------|-------|-----------|
| Spots | 32 | 36 | 22 | 18 | 41 | 24 | 51 | 19 | 16 | 30 | 21 | 39 | 14 | 11 | 81 | 29 | 8 | 13 | 224 | 125 | 14 | 142 |
| <i>wt%</i> | | | | | | | | | | | | | | | | | | | | | | |
| Ta ₂ O ₅ | 0.04 | 0.03 | 0.07 | 0.04 | bdl | n.a. | n.a. | 0.07 | 0.04 | 0.05 | bdl | bdl | 0.04 | n.a. | n.a. | n.a. | n.a. | n.a. | 0.04 | 0.05 | 0.04 | n.a. |
| Nb ₂ O ₅ | n.a. | n.a. | n.a. | bdl | bdl | n.a. | n.a. | bdl | n.a. | n.a. | bdl | bdl | bdl | n.a. | n.a. | n.a. | n.a. | n.a. | n.a. | n.a. | bdl | n.a. |
| SiO ₂ | 1.45 | 2.07 | 1.72 | 1.46 | 1.45 | 0.16 | 1.90 | 2.21 | 1.42 | 2.26 | 0.63 | 1.23 | 0.19 | 0.14 | 0.20 | 1.18 | 0.66 | 0.21 | 1.46 | 1.55 | 0.19 | 0.48 |
| TiO ₂ | bdl | 0.02 | 0.01 | 0.04 | 0.03 | 0.03 | 0.09 | 0.02 | 0.01 | 0.01 | bdl | 0.03 | 0.04 | 0.25 | 0.08 | 0.02 | 0.23 | 0.09 | 0.04 | 0.02 | 0.04 | 0.14 |
| SnO ₂ | 0.12 | 0.06 | 0.05 | 0.15 | 0.07 | 0.26 | 0.07 | 0.01 | 0.02 | 0.34 | bdl | 0.03 | 0.21 | bdl | 0.03 | bdl | 0.03 | bdl | 0.11 | 0.10 | 0.21 | 0.03 |
| Al ₂ O ₃ | 0.22 | 0.05 | 0.03 | 0.04 | 0.08 | 0.06 | 0.13 | 0.14 | 0.06 | 0.17 | 0.06 | 0.17 | 0.04 | 0.62 | 0.23 | 0.12 | 1.36 | 0.47 | 0.09 | 0.12 | 0.04 | 0.56 |
| Cr ₂ O ₃ | 0.02 | 0.02 | bdl | bdl | bdl | bdl | bdl | bdl | 0.01 | 0.02 | bdl | bdl | bdl | 0.01 | bdl | 0.02 | bdl | bdl | n.a. | 0.01 | bdl | 0.02 |
| Fe ₂ O ₃ | 65.24 | 64.31 | 64.25 | 66.18 | 65.85 | 69.17 | 64.72 | 62.36 | 64.68 | 62.41 | 68.33 | 66.16 | 67.44 | 66.63 | 68.64 | 64.76 | 66.07 | 68.47 | 65.68 | 64.79 | 67.44 | 66.91 |
| MgO | 0.23 | 0.42 | 0.48 | 0.10 | 0.06 | 0.10 | 0.09 | 0.25 | 0.05 | 0.11 | 0.23 | 0.17 | 0.05 | 0.03 | 0.18 | 0.15 | 0.49 | 0.15 | 0.21 | 0.16 | 0.05 | 0.20 |
| MnO | 0.03 | 0.04 | 0.10 | 0.80 | 0.72 | 0.39 | 0.91 | 0.18 | 0.24 | 0.31 | 0.12 | 0.22 | 0.37 | 0.30 | 0.31 | 0.06 | 0.24 | 0.10 | 0.43 | 0.21 | 0.37 | 0.20 |
| FeO | 32.17 | 33.19 | 32.14 | 32.29 | 32.40 | 30.95 | 32.79 | 32.83 | 32.23 | 33.11 | 31.45 | 32.10 | 30.33 | 30.87 | 31.11 | 31.76 | 31.62 | 31.43 | 32.28 | 32.34 | 30.33 | 31.36 |
| Total | 99.51 | 100.20 | 98.86 | 101.11 | 100.66 | 101.12 | 100.70 | 98.08 | 98.77 | 98.80 | 100.83 | 100.10 | 98.71 | 98.86 | 100.78 | 98.06 | 100.71 | 100.92 | 100.33 | 99.37 | 98.71 | 99.90 |
| <i>wt%</i> | | | | | | | | | | | | | | | | | | | | | | |
| Ta | 0.03 | 0.02 | 0.06 | 0.03 | bdl | n.a. | n.a. | 0.05 | 0.03 | 0.04 | bdl | bdl | 0.03 | n.a. | n.a. | n.a. | n.a. | n.a. | 0.04 | 0.04 | 0.03 | n.a. |
| Nb | bdl | n.a. | n.a. | bdl | bdl | n.a. | n.a. | bdl | n.a. | n.a. | bdl | bdl | bdl | n.a. | n.a. | n.a. | n.a. | n.a. | nr | bdl | bdl | n.a. |
| Si | 0.68 | 0.97 | 0.81 | 0.68 | 0.68 | 0.07 | 0.89 | 1.04 | 0.66 | 1.05 | 0.29 | 0.58 | 0.09 | 0.07 | 0.09 | 0.55 | 0.31 | 0.10 | 0.68 | 0.72 | 0.09 | 0.22 |
| Ti | bdl | 0.01 | 0.01 | 0.02 | 0.02 | 0.02 | 0.05 | 0.01 | 0.01 | 0.01 | bdl | 0.02 | 0.03 | 0.15 | 0.05 | 0.01 | 0.14 | 0.05 | 0.02 | 0.01 | 0.03 | 0.08 |
| Sn | 0.10 | 0.05 | 0.04 | 0.12 | 0.06 | 0.21 | 0.05 | 0.01 | 0.02 | 0.27 | bdl | 0.03 | 0.16 | bdl | 0.02 | bdl | 0.03 | bdl | 0.09 | 0.08 | 0.16 | 0.03 |
| Al | 0.12 | 0.03 | 0.02 | 0.02 | 0.04 | 0.03 | 0.07 | 0.08 | 0.03 | 0.09 | 0.03 | 0.09 | 0.02 | 0.33 | 0.12 | 0.06 | 0.72 | 0.25 | 0.05 | 0.06 | 0.02 | 0.30 |
| Cr | 0.02 | 0.01 | bdl | bdl | bdl | bdl | bdl | bdl | 0.01 | 0.01 | bdl | bdl | bdl | 0.01 | bdl | 0.01 | bdl | bdl | 0.01 | 0.01 | bdl | 0.01 |
| Fe | 70.64 | 70.78 | 69.93 | 71.39 | 71.24 | 72.44 | 70.76 | 69.13 | 70.30 | 69.39 | 72.24 | 71.22 | 70.74 | 70.60 | 72.19 | 69.98 | 70.79 | 72.32 | 71.02 | 70.46 | 70.74 | 71.18 |
| Mn | 0.03 | 0.04 | 0.10 | 0.62 | 0.55 | 0.30 | 0.71 | 0.14 | 0.19 | 0.24 | 0.10 | 0.17 | 0.29 | 0.23 | 0.24 | 0.06 | 0.18 | 4.57 | 0.34 | 0.17 | 0.29 | 1.06 |
| Mg | 0.14 | 0.25 | 0.29 | 0.06 | 0.04 | 0.06 | 0.05 | 0.15 | 0.03 | 0.07 | 0.14 | 0.10 | 0.03 | 0.02 | 0.11 | 0.09 | 0.30 | 0.09 | 0.13 | 0.10 | 0.03 | 0.12 |
| Fe ³⁺ /Fe ²⁺ | 2.03 | 1.94 | 2.00 | 2.05 | 2.03 | 2.24 | 1.97 | 1.90 | 2.01 | 1.88 | 2.17 | 2.06 | 2.22 | 2.16 | 2.21 | 2.04 | 2.09 | 2.18 | 2.03 | 2.00 | 2.22 | 2.13 |
| <i>°C</i> | | | | | | | | | | | | | | | | | | | | | | |
| T _{Mg-Mag} | 595 | 653 | 674 | 511 | 490 | 521 | 506 | 604 | 454 | 504 | 583 | 562 | 473 | 440 | 554 | 554 | 562 | 549 | 564 | 541 | 470 | 532 |
| Δ+ | 60 | 66 | 69 | 52 | 50 | 53 | 52 | 61 | 47 | 52 | 59 | 57 | 49 | 46 | 56 | 56 | 57 | 56 | 58 | 55 | 48 | 54 |
| Δ- | 57 | 62 | 64 | 50 | 48 | 50 | 49 | 58 | 45 | 49 | 56 | 54 | 46 | 43 | 53 | 53 | 54 | 53 | 54 | 52 | 46 | 51 |

Table 2 – Average LA-ICP-MS results of the most representative elements in magnetite from each sample and deposit. Full data are available in Tables S5-6-7 of the ESM.

| Sample | Perda Niedda | | | | | Monte Tamara | | | | | Rosas | Giacurru | | | Perda Niedda | Monte Tamara | Rosas | Giacurru |
|----------------------|--------------|-------|------|-------|-------|--------------|-------|-------|-------|-------|----------|----------|--------|-------|--------------|--------------|-------|----------|
| | PN5 | PN10 | PN11 | PN-W | PN28B | VMd5a | VMd8c | VMd9 | MTA3D | MTA6 | BS.S2.02 | GIAC2a | GIAC2b | GIAC3 | | | | |
| Spots | 26 | 42 | 66 | 22 | 40 | 33 | 13 | 12 | 28 | 30 | 56 | 59 | 30 | 41 | 196 | 116 | 56 | 130 |
| <i>ppm</i> | | | | | | | | | | | | | | | | | | |
| Li | 12 | 32 | 11 | 9 | 1 | 3 | 3 | 4 | 3 | 8 | 3 | 6 | 2 | 5 | 13 | 4 | 3 | 4 |
| Be | 32 | 65 | 74 | 94 | 28 | 2 | 2 | 3 | 8 | 2 | 29 | 0 | 2 | 1 | 59 | 3 | 29 | 1 |
| Al | 1130 | 1642 | 2509 | 839 | < Av. | 818 | 966 | 2377 | 1279 | 543 | 361 | 2278,94 | 1200 | 12573 | 1530 | 1197 | 361 | 6887 |
| Ti | 53 | 135 | 44 | 43 | 1642 | 50 | 12 | 53 | 61 | 63 | 126 | 2694 | 16 | 298 | 383 | 48 | 126 | 1002 |
| V | 32 | 17 | 17 | 3 | 65 | 10 | 20 | 33 | 12 | 11 | 30 | 9 | 11 | 39 | 27 | 17 | 30 | 19 |
| Cr | 11 | 4 | 7 | < Av. | 20 | < Av. | 2 | 3 | < Av. | 126 | 27 | 91 | 3 | 10 | 10 | 43 | 27 | 35 |
| Mn | 3319 | 3493 | 4810 | 6383 | 3500 | 1193 | 2095 | 3153 | 1610 | 1942 | 2610 | 3516 | 1056 | 1886 | 4301 | 1999 | 2610 | 2153 |
| Co | < Av. | < Av. | 2 | < Av. | 18 | 34 | 22 | 192 | 11 | 8 | 14 | 88 | 27 | 48 | 10 | 53 | 14 | 54 |
| Ni | < Av. | 8 | 6 | 2 | 18 | 24 | 33 | 90 | 15 | 42 | 36 | 147 | 36 | 140 | 8 | 41 | 36 | 108 |
| Ga | < Av. | < Av. | 21 | < Av. | 20 | 11 | < Av. | < Av. | < Av. | < Av. | 13 | 50 | < Av. | < Av. | 20 | < 11 | 13 | 50 |
| Ge | 59 | 41 | 13 | 19 | 13 | 6 | 7 | 12 | 8 | 10 | 15 | 5 | 9 | < Av. | 29 | 9 | 15 | 7 |
| Y | 4 | 4 | 2 | 1 | 1 | 0 | 3 | 4 | 1 | 1 | 1 | < Av. | 3 | 0 | 2 | 2 | 1 | 1 |
| Zr | 15 | 11 | 1 | 1 | 1 | 0 | 2 | 2 | 1 | 1 | 0 | 1 | 10 | 2 | 6 | 1 | 0 | 4 |
| Nb | 2 | 1 | 1 | 0 | 0 | 0 | 1 | 2 | 1 | 0 | 1 | 3 | 1 | 2 | 1 | 1 | 1 | 2 |
| Y | 4 | 4 | 2 | 1 | 1 | 0 | 3 | 4 | 1 | 1 | 1 | < Av. | 3 | 0 | 2 | 2 | 1 | 1 |
| Sn | 1098 | 852 | 1756 | 331 | 431 | 14 | 97 | 211 | 1072 | 37 | 1180 | 153 | 10 | 30 | 894 | 286 | 1180 | 64 |
| Ho | < Av. | 0 | 0 | 0 | 0 | 0 | 0 | 0 | 0 | 0 | 0 | 0 | 0 | 0 | 0 | 0 | 0 | 0 |
| Hf | 1 | 0 | 0 | < Av. | 0 | 0 | 0 | 0 | 0 | 0 | 0 | 0 | 0 | 0 | 0 | 0 | 0 | 0 |
| Ta | 0 | 0 | 0 | 0 | 0 | < Av. | 0 | 0 | 0 | 0 | 0 | 0 | < Av. | 0 | 0 | 0 | 0 | 0 |
| W | 15 | 8 | 12 | 2 | 1 | 5 | 148 | 5 | 36 | 218 | 19 | 4 | 15 | 1 | 8 | 83 | 19 | 6 |
| (La/Lu) _n | 0 | 2 | 7 | 1 | 1 | n/a | 8 | 7 | 1 | 1 | 3 | n/a | 1 | 2 | 3 | 6 | 3 | 1 |
| Nb/Ta | 68 | 9 | 22 | 7 | 2 | n/a | 14 | 15 | 6 | 2 | 10 | 24 | n/a | 16 | 13 | 8 | 10 | 16 |
| Zr/Hf | 22 | 25 | 24 | n/a | 9 | 7 | 13 | 12 | 6 | 6 | 16 | 37 | 27 | 20 | 18 | 9 | 16 | 26 |
| Y/Ho | n/a | 81 | 27 | 18 | 12 | 6 | 679 | 345 | 31 | 10 | 19 | n/a | 146 | 9 | 39 | 63 | 19 | 74 |

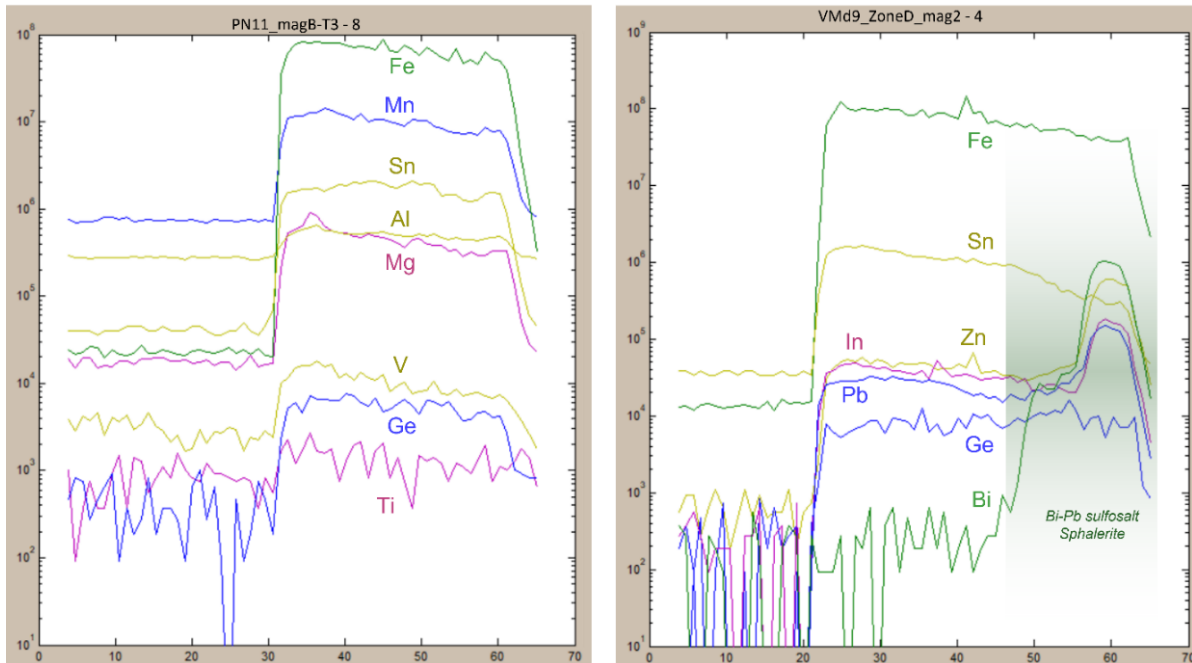


Figure 4 – Representative LA-ICP-MS time-resolved signals of magnetite. On the left, a signal with no inclusions showing the cps of the main detected trace elements including Sn and Ge. On the right, an example of signal contamination by secondary Zn-In a Bi-Pb signals from a sphalerite and sulfosalt inclusions respectively. The inclusion-contaminated portion of the signal have been excluded from the data reduction process.

inclusions and, at the same time, for their qualitative identification (Fig.4).

The average trace-elemental composition of magnetite samples from all deposits confirms that Mn, Al, Sn are the most represented minor elements, as well as newly analysed Ca and K. Manganese concentrations range from 1056 ppm (GIAC2b) up to 6383 ppm (PN-W) which are similar between all samples. Aluminum values are comprised between 138 to 2508 ppm, though in some cases being below the detection limit (PN28B) and exceeding 12000 ppm in one sample (GIAC3). Values of Ca are ranging from 545 ppm (BS.S2.02) to 2849 ppm but more frequently below the detection limit (PN-W, PN28B, MTA3D, MTA6, GIAC2a, GIAC3) with respect to Mn and Al. Differently, the average Sn concentrations are always above the detection limit and ranging from 10 (GIAC2b) to 1756 ppm (PN11). Zinc (45-1632 ppm), Cu (0-1612 ppm), Pb (4-13974 ppm) and Bi (0-1389 ppm) have also been frequently detected. The highest As, Se and Mo values (528 ppm of As; 120 ppm of Se; 144 ppm of Mo) have been detected in

samples with high Zn, Cu, Pb and Bi (VMd9). Tungsten is low (1-15 ppm; GIAC3-PN5), though its average concentrations are higher in two samples (148-218 ppm of W; VMd8c-MTA6). Concentrations of Ti are in the range of 12 (VMd8c) and 2694 ppm (GIAC2a), whereas V concentrations are much more constant and generally lower (2-65 ppm). Chromium is low, ranging from 2 (VMd8c) to 91 (GIAC2a) and below the detection limit in two samples (PN-W, VMd5a, MTA3D). Germanium average concentrations range from 5 (GIAC2a) up to 59 ppm (PN5). Niobium (0-3 ppm), Ta (0 ppm), Zr (0-15 ppm), Hf (0-1 ppm), Y (0-4 ppm), Ho (0 ppm) are usually low.

Discussion

Major and minor elements (EPMA) in magnetite

The partitioning of total Fe content into Fe²⁺ and Fe³⁺ and the calculation of the apfu of each magnetite EPMA spot have been done using the ILMAT calculation spreadsheet (Lepage 2003). The relative

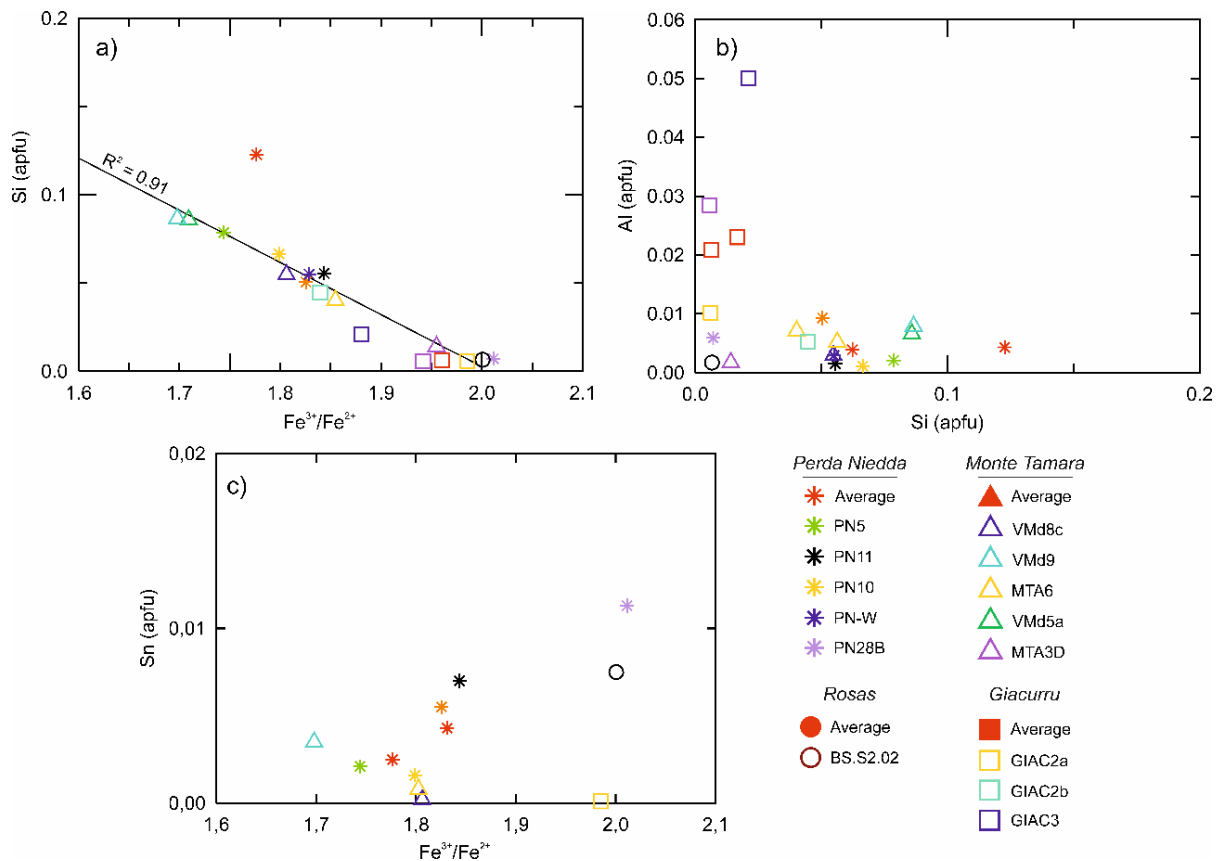


Figure 5 – In (a), the linear correlation between Si apfu versus the Fe³⁺/Fe²⁺ apfu ratio indicating the double substitution $2[M^{3+}] \rightleftharpoons [M^{4+}] + [M^{2+}]$, mechanism further supported by the antagonist correlation between Al³⁺ and Si⁴⁺ apfu (b). In (c), the weak correlation between Sn apfu and the Fe³⁺/Fe²⁺ apfu ratio is shown.

apfu values are reported in Table D1. As previously highlighted, the Fe wt% contents are overall close to the stoichiometric value. However, the average values of the Fe³⁺/Fe²⁺ apfu ratios are more often lower than the theoretical value of Fe³⁺/Fe²⁺ = 2 (Fig.5a). All deposits show in fact a negative correlation between Si apfu contents and the Fe³⁺/Fe²⁺ ratio, with a linear correlation coefficient of R² = 0.91. This evidence could be explained as a coupled substitution. Magnetite, as a member of the spinel-subgroup, can host double diadochy as stated in the new IMA-approved classification (Bosi et al. 2019), producing a transition from a spinel-subgroup structure (A²⁺B₂³⁺O₄) to the structure of the ulvospinel subgroup (A⁴⁺B₂²⁺O₄). In our samples this mechanism is best represented as a Si⁴⁺ substitution for an [M²⁺] in the A site, whereas Fe²⁺ substitutes

for an [M³⁺] in the B site. This is further supported by the antagonist correlation between Si and Al³⁺ (Fig.5b), representing the lack of [M³⁺] in the ulvospinel subgroup type-structure. Tin concentrations have been detected in all samples and the average values exhibit a small variability (0.1-0.27 wt%). The apfu contents have been calculated assuming that Sn is present in its tetravalent form, accordingly to many authors (Nistor 1975, Hernandez-Gomez et al. 2001, 2006, Wang et al. 2012). However, Sn⁴⁺ apfu contents show a weak positive correlation (R² = 0.31) with the Fe³⁺/Fe²⁺ ratio (Fig.5c). Therefore, Sn could not be clearly related to the same double substitution mechanism of Si, suggesting that more investigations on its oxidation state could provide more elucidations on this redox sensible element.

On the basis of the Mg content, detected in

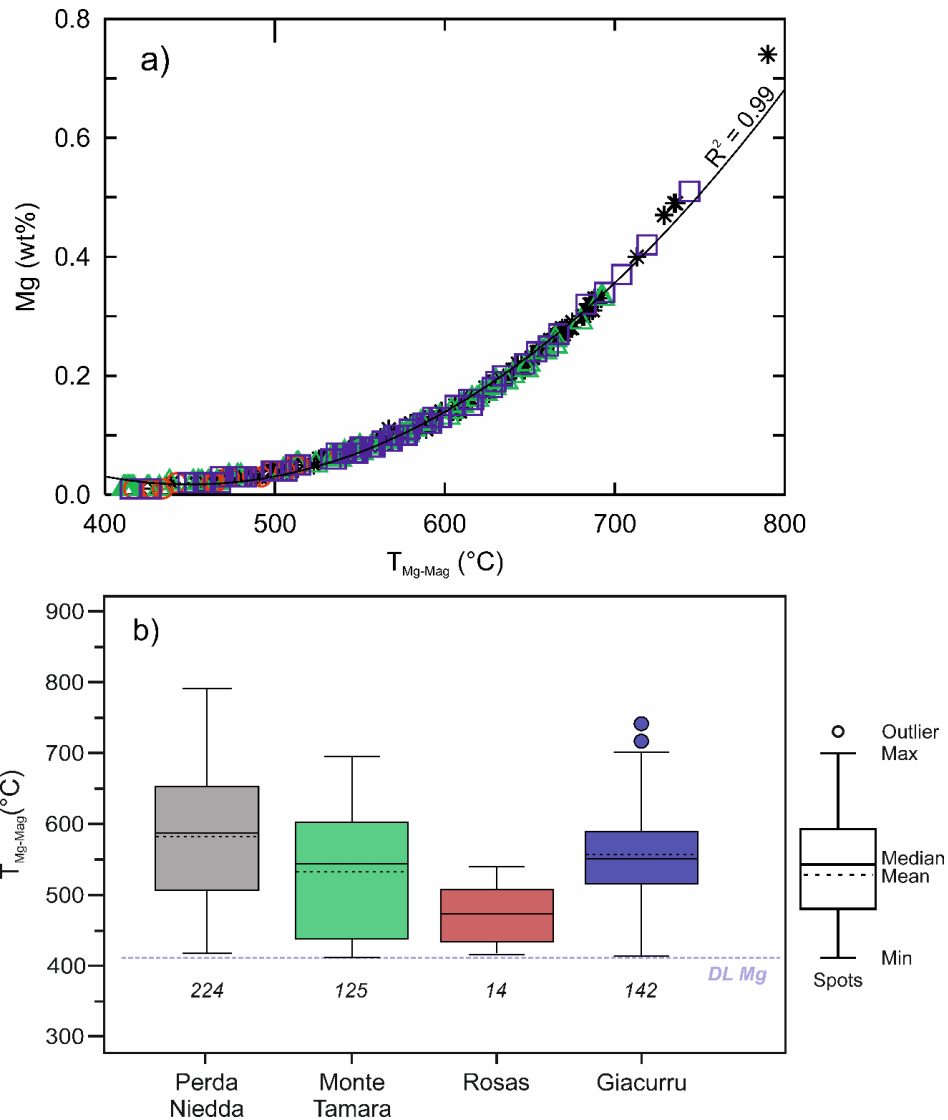


Figure 6 - In (a) it curve of Mg wt% and the calculated temperatures with the T_{Mg-Mag} equation proposed by [Canil and Lacourse \(2020\)](#). In (b) boxplots of the average temperatures for each deposit.

all of the 18 thin sections for a total of 164 point analysis, the T_{Mg-Mag} geothermometer ([Canil and Lacourse 2020](#)), based on the $X_{Mg} = Mg/(Mg+Fe)$, has been applied. A check on the applicability of this thermometer has been given by plotting the Mg wt% content versus the calculated T (°C) ([Fig.6a](#)). The strong direct correlation ($R^2 = 0.99$) between temperature values and the Mg wt% proves that the proposed equation by [Canil and Lacourse \(2020\)](#) is a very powerful tool even if only the Mg wt% content is considered. The average temperature for each sample and deposits are presented in

[Table 1](#) while the statistic distribution of the whole range of values of each deposit are presented in [Fig.6b](#). The minimum temperature value, around 400°C for all deposits, is due to the detection limit of Mg of WD-EPMA analyses. The average temperature of magnetite from each deposit ranges from 470° to 564°C. At Perda Niedda, the average temperature is 564°C within a range of 500-650°C of the 50% of the samples; at Monte Tamara the average is 541°C within a range of 450-600°C; at Rosas is 450-500°C; at Giacurru is 532°C within a 520-580°C range. Such a distribution indicates that magnetite from

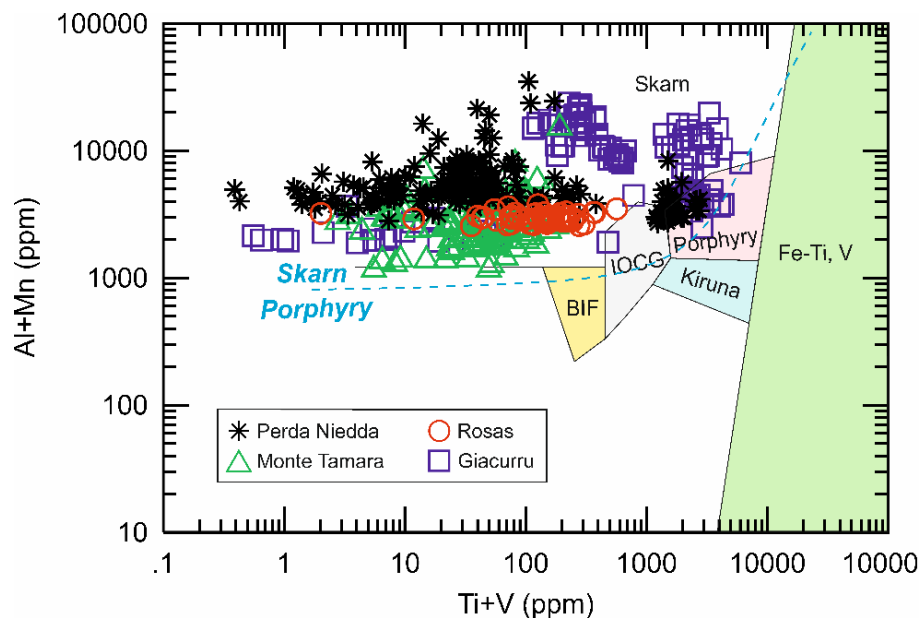


Figure 7 – Magnetite classification diagram based on their Al+Mn versus Ti+V contents (mod. after Dupuis and Beaudoin 2011 and Nadoll et al. 2014). All samples from this study lie within the skarn field, though with a variability in the Ti+V concentrations.

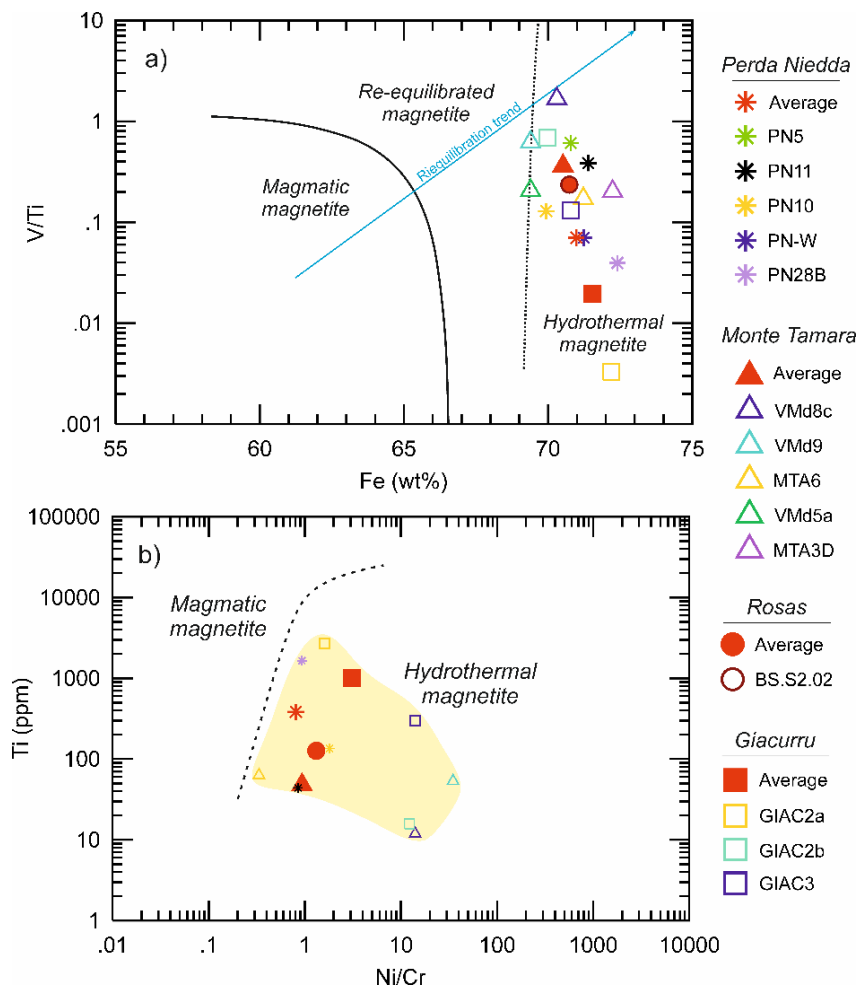


Figure 8 – Magnetite discrimination diagrams highlighting the hydrothermal character of each deposit. In a) V/Ti ppm ratio versus Fe wt% (mod. after Wen et al. 2017) and in (b) Ti ppm versus the Ni/Cr ppm ratio (mod. after Dare et al. 2014).

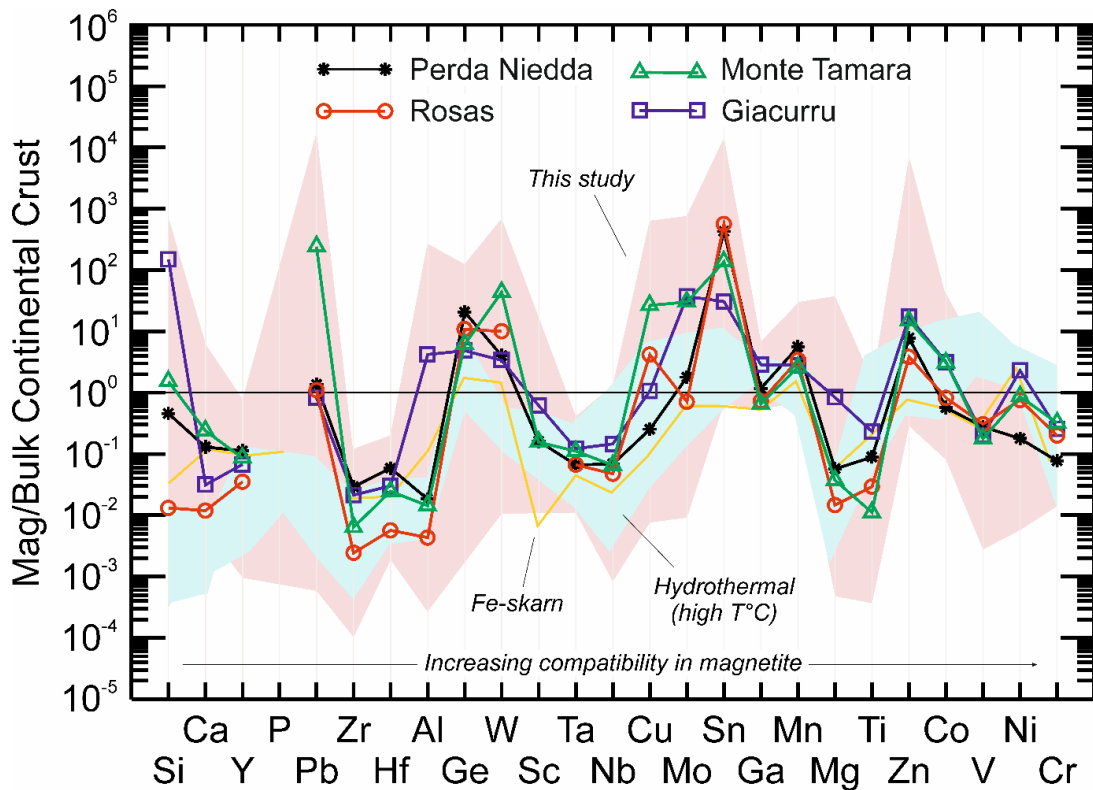


Figure 9 – Multi-trace element spider diagram (mod. after Dare et al. 2014) for magnetite from skarn ores of Sardinia, normalized to the Bulk Continental Crust (Rudnick and Gao 2003). The average values of each deposit from this study (see legend) and their overall distribution (pink field) are compared to literature data (Dare et al. 2014) for magnetite from Fe skarns (orange line) and high temperature hydrothermal deposits (light blue field). With respect to the compared data, samples from Sardinia are most notably enriched in Ge, W and Sn.

all the deposits formed under isothermal conditions.

Trace-elements (LA-ICP-MS) in magnetite

In the last decades, the trace elemental composition of magnetite has been increasingly used to classify and discriminate different types of deposits. Following this direction, the trace-elemental concentrations in this study (presented in Table 2 and in the ESM) have been plotted using different discrimination diagrams. A first characterization has been done using the Ti+V versus Al+Mn diagram proposed by Dupuis and Beaudoin (2011) and Nadoll et al. (2014), which shows that all the samples fall within the skarn field (Fig.7). Among all the samples, some Perda Niedda and Giacurru samples are quite enriched in Ti (Table 2), therefore plotting at the border of the Fe-Ti, V field. To

further classify the origin of skarn magnetite, the V/Ti ratio versus Fe wt% shows that they have a strong affinity for hydrothermal ore deposits rather than their formation in magmatic environments and no significant re-equilibration could occur (Fig.8a; Wen et al. 2017). The same consideration can be drawn from the Ti ppm versus the Ni/Cr ratio diagram (Fig.8b; Dare et al. 2014).

The diagram in Fig.9, which shows the normalized concentration (Rudnick and Gao, 2003) of increasingly compatible elements in magnetite (Dare et al. 2014), displays some similarities and differences between Fe-skarns and the W-Sn-bearing skarns of Sardinia. As highlighted by Dare et al. (2014), the enrichments of elements in magnetite from skarn deposits and hydrothermal environments are independent from the theoretical compatibility, resulting in a chainsaw

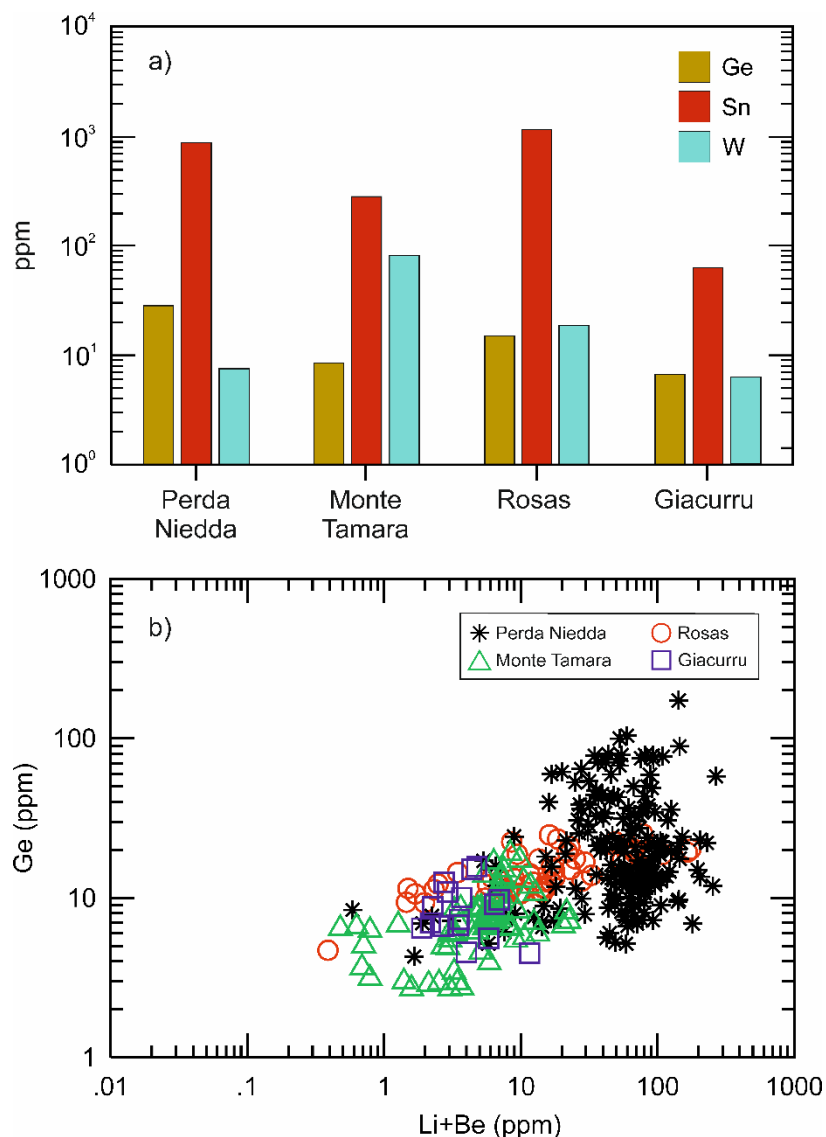


Figure 10 – Average Ge, Sn and W contents of magnetite from the Perda Niedda, Monte Tamara, Rosas and Giacurru skarns (a). In (b), the positive correlation between Ge and Li+Be concentrations indicates a magmatic origin of Ge.

shape of the spider pattern. As an opposite example, magnetite formed in magmatic environments tend to be enriched in the more compatible elements. Accordingly, the average composition of samples from W-Sn-bearing skarns Sardinia shows a trend more closely related with those of magnetite formed in hydrothermal-high temperature and Fe-skarn settings worldwide. Namely, a very good correspondence of Y, Ta, Nb, Ga, Mn, Mg, V, Ni, Cr values between our samples and Fe-skarn deposits can be observed. However, the major difference, commonly shared by all the four studied deposits, resides in the

higher concentrations of Ge, W and Sn. Such enrichments are overall comparable for the Perda Niedda, Monte Tamara, Rosas and Giacurru deposits (Fig.10a). Tin clearly shows the highest values, being around two and three orders of magnitude higher than those reported for Fe-skarns and those of the average crust respectively. Similarly, W is up to two orders of magnitude higher at Monte Tamara, allegedly reflecting the presence of variable concentrations of scheelite within the magnetite-rich zones of the skarn (Deidda et al. 2022). Moreover, as a trademark association of metals, the

presence of W- and Sn-rich magnetite confirms the relationships between this skarn system and the GS1 granites (Naitza et al. 2017; Cocco et al. 2022a; Deidda et al. 2022). Finally, the presence of anomalous Ge contents, being one order of magnitude higher than the bulk continental crust and Fe-skarns, represents a novelty for skarns of Sardinia and for the metal endowment linked to the GS1. This is quite important considering that, due to its supply risk, germanium is considered as a critical material both in Europe (Bobba et al. 2020) and in the United States (US Geological Survey 2021). The clear positive correlation between Ge and Li+Be concentrations (Fig.10b) point towards a magmatic source of the mineralization, probably related with greisenizing processes (Pirajno, 2009).

Geochemical twins fractionation in magnetite

The behaviour of the three geochemical twin couples Y/Ho, Nb/Ta and Zr/Hf in magnetite are here discussed to evaluate if and how its crystallization process follows the CHARAC (CHARGE-and-RADIUS-Controlled) ranges (Atanasova et al. 2020; Ranta et al 2018; Bau 1996; Green 1995). In order to evaluate possible fractionation mechanisms, magnetite samples have been compared to the GS1 granite (Naitza et al. 2017; Fig.11). The Y/Ho ratio of the GS1 fall perfectly in in the CHARAC range, indicating that the crystallization of the granitic suite is not affected by Y/Ho decoupling in the fractionation process. Magnetite from Giacurru, Monte Tamara and, in part, Perda Niedda overlap the GS1, while others (PN10-VMd9) show a strong increasing Y/Ho ratio. That decoupling process is controlled by a higher concentration of Y (see Table S5), usually correlating to high F⁻ activity in

hydrothermal fluids (Veksler et al., 2005). In fact the YF₂⁻ complex is strongly favoured than HoF₂⁻ (Bau and Dulski 1995). From this point of view, the two trends shown by magnetite are likely the result of two crystallization stages. The first trend, that has the higher Y concentration, includes magnetite not evidently associated with fluorite. Since fluorite is one of the most important sinks for Y over Ho (Bau 1996), such evidence could be explained by the presence in the hydrothermal solution of YF₂⁻ simultaneously to the formation of calc-silicate minerals. Therefore Ca²⁺ is not available for fluorite precipitation. The second trend, represented by samples within the CHARAC field (PN11, PN-W, PN28B), indicates that no significant decoupling agents are present, even though magnetite from these samples is associated with fluorite. A possible explanation could be that magnetite precipitated in presence of CaF⁻ complexes, which have a role in segregating Y, but before fluorite precipitation. Conversely, a magnetite forming after fluorite precipitation should be in fact depleted in Y and inherit a lower Y/Ho ratio (Bau and Dulski, 1995).

The Nb/Ta and Zr/Hf ion pairs ratio of the GS1 are both slightly lower than the CHARAC ranges. This may be due to the crystallization in the parental magma of GS1 of Ti-minerals (e.g. rutile and ilmenite) which are known to fractionate the HFSE (Linnen et al., 2013; Horng & Hess, 2000; Green 1995). This is in agreement with the ilmenite-series classification of the GS1 suite (Naitza et al., 2017; Conte et al, 2017). The Zr/Hf ratio in magnetite mostly falls within the CHARAC, being occasionally slightly depleted in Zr. This general trend confirms the relationship with the GS1 source. The Nb/Ta ratio is instead usually higher than the GS1. However, samples

from Monte Tamara fall within the CHARAC, whereas Perda Niedda shows two different trends. The first is characterized by an increasing Nb/Ta ratio, that is due to the low Ta concentrations detected in our samples. The second trend is determined by lower Nb concentrations. This two opposite behaviours could be also controlled by the hydrothermal activity of F^- and O^{2-} that, depending on the overall physio-chemical

conditions, may preferentially favour the mobilization of either Nb or Ta (Akinfiiev et al. 2020 and references therein).

Discrimination diagrams for W-Sn skarns

Aside from classifying different ore deposit types, the trace elemental composition of magnetite in skarns proved to be useful to constrain the mechanisms of formation (Xie et al. 2017; Wen et al. 2017; Chen et al. 2020; Sarjoughian et al. 2020; Dong et al.

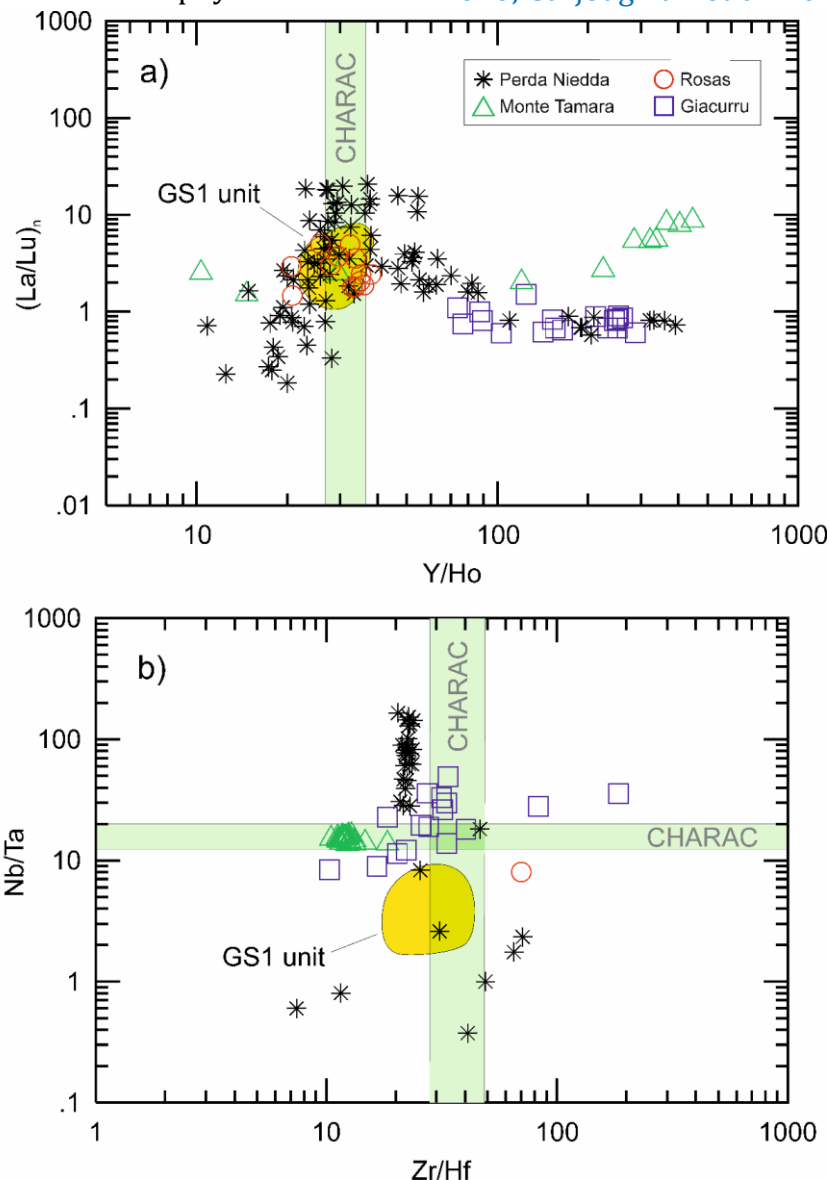


Figure 11 – Comparative diagrams between magnetite from skarn ores of Sardinia and the GS1 unit (Naitza et al. 2017) and the CHARAC ratio of geochemical twin pairs (Bau 1995; Bau 1996; Green 1995; Atasanova 2020). In (a), the $(La/Lu)_N$ normalized values (Sun and McDonough, 1989) versus Y/Ho ratio shows that magnetite below the CHARAC represent a formation during or after Y fractionation in fluorite, and a trend driven by higher Y contents which indicate a fluoride-rich hydrothermal fluid before Y fractionation in fluorite. In (b) magnetite samples show that the crystallization has followed the Zr/Hf ratio comparably to the ilmenite-bearing granites of the GS1 unit (Naitza et al. 2017), while Nb/Ta generally indicates increased proportions of Nb, after Ta fractionation in ilmenite.

2021; Maia et al. 2022; Zhao et al. 2022). Since magnetite recurrently occurs in variable proportions in most economic subtypes of skarn deposits (Einaudi et al. 1981; Meinert et al. 2005), its trace elemental composition of magnetite could be potentially used as a pathfinder for

specific skarn mineralization. Therefore, we compared our samples to the trace elemental composition of magnetite from the Akesayi, Alvito and Azenhas Fe skarns (Meng et al. 2017; Dong et al. 2021; Maia et al. 2022) and from the Huangshaping W-Sn skarn deposit (Zhao et al. 2022) in order to

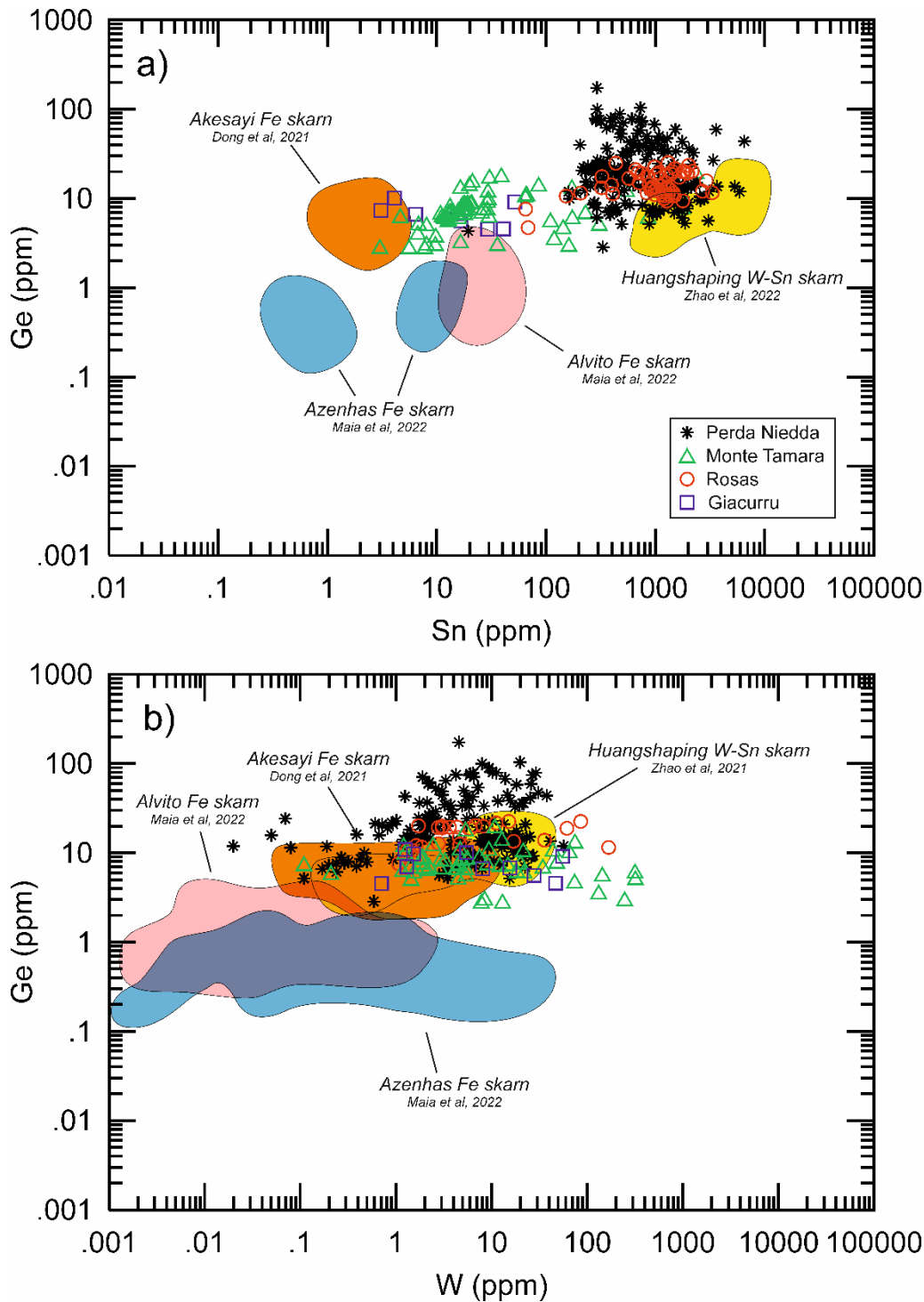


Figure 12 – Discrimination diagrams between W-Sn-bearing skarns, including data from our samples and Zhao et al. (2022), and Fe skarns, data from Dong et al. (2021) and Maia et al. (2022). In the Ge versus Sn (a) and Ge versus W (b) diagrams a good fitting between magnetite from Sardinia and from the Huangshaping W-Sn skarn can be highlighted.

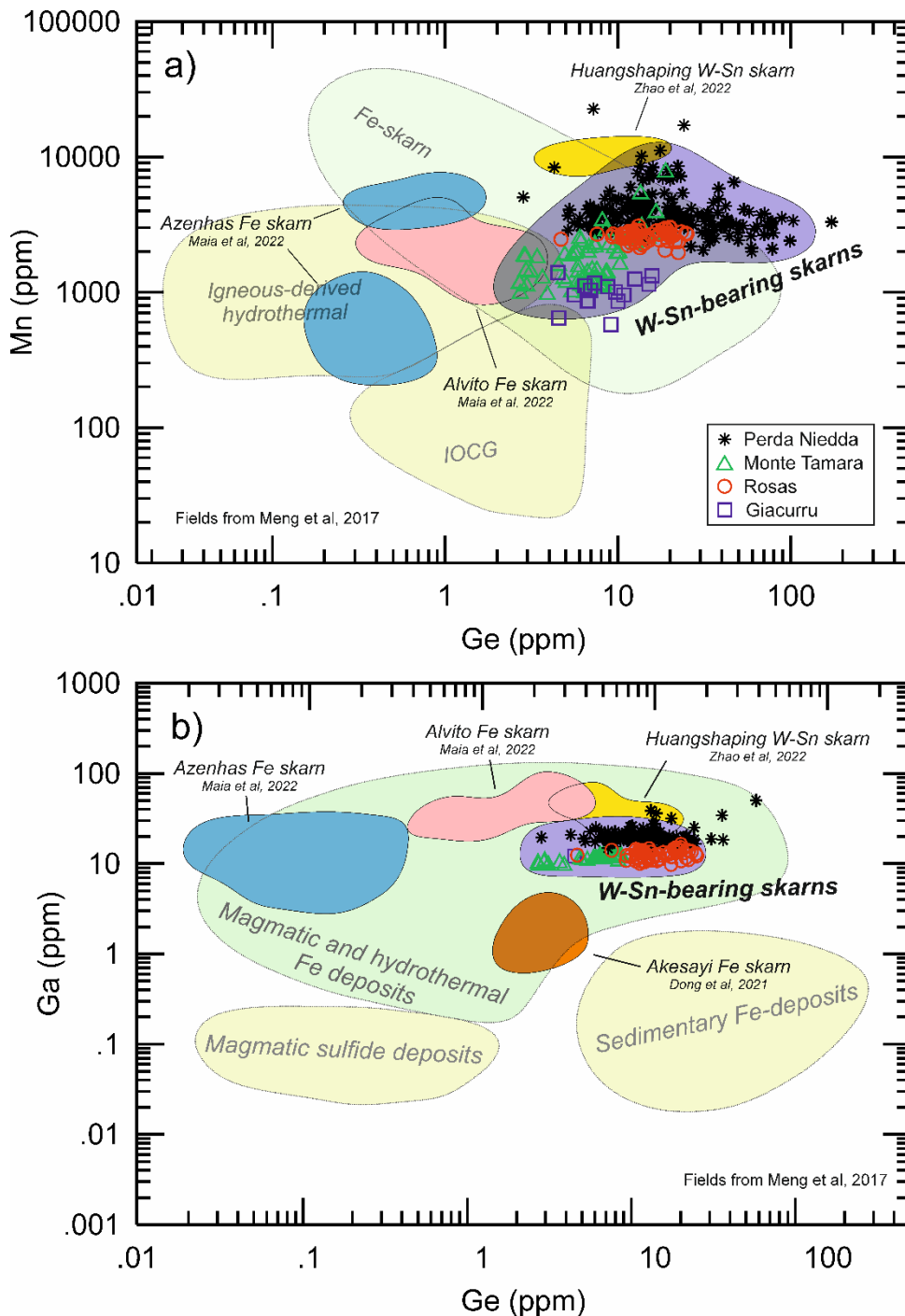


Figure 13 - Discrimination diagrams between W-Sn-bearing skarns, including data from our samples and Zhao et al. (2022), and Fe skarns, data from Dong et al. (2021) and Maia et al. (2022). The Mn versus Ge (a) and Ga versus Ge (b) diagrams (mod. after Meng et al. 2017) show that W-Sn-bearing skarns cluster within a narrower field in the Fe-skarn and magmatic and hydrothermal fields, with a good separation from Fe skarns. Therefore, we propose these diagrams as a tool to better identify W-Sn-bearing skarns.

identify possible discrimination and correlation trends. Magnetite from this study has been considered as representative of Sn-W-bearing skarns because of the documented association with cassiterite and scheelite.

The Ge and Sn diagram (Fig.12a) shows a

good correspondence between magnetite from the W-Sn skarns of Huangshaping (Zhao et al. 2022) and samples from Perda Niedda and Rosas. Magnetite from Monte Tamara and Giacurru, though, tend to lean more towards Fe-skarns, partially overlapping with magnetite from the

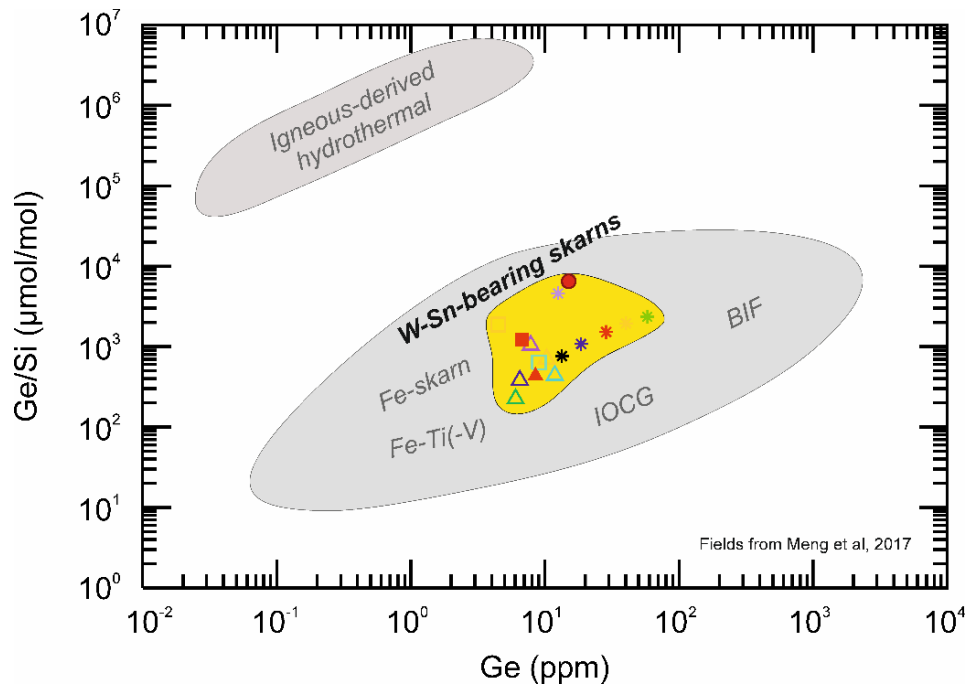


Figure 14 - Average values of magnetite from Sardinia in the Ge/Si ($\mu\text{mol/mol}$) versus Ge diagram, plotting within a narrow field between various types of Fe mineralization (Fe skarns, Fe-Ti(-V), IOCG and BIF; Meng et al. 2017).

Azenhas, Alvito (Maia et al. 2022) and Akesayi (Dong et al. 2021) deposits where cassiterite or scheelite mineralization are seemingly absent. However, such differentiation could be related to the relative abundance of cassiterite in the Perda Niedda and Rosas samples (Naitza et al. 2017; Cocco et al. 2022) with respect to Monte Tamara where, despite being in close association, scheelite prevails over cassiterite (Deidda et al. 2022). However, no significant changes to the topology of the diagram are obtained if Sn+W are plotted over Ge. Therefore, the timing of magnetite formation with respect to the Sn-bearing hydrothermal fluids may explain the decoupling between Sn and W. The Ge and W diagram (Fig.12b) shows a good correspondence between all magnetite samples from Sardinia and the Huangshaping. Both W-Sn bearing skarns separate well from the Azenhas and Alvito Fe skarns, though with an overlap with the Akesayi Fe skarn. Either way, W contents vary up over four orders of magnitude in samples from Azenhas and Sardinia,

proving to be not an effective discriminant. The best discrimination between Fe skarns and W-Sn-bearing skarns is obtained integrating the Ga and Mn versus Ge discrimination diagrams (Fig.13a-b) originally proposed by Meng et al. (2017). In the Mn versus Ge diagram (Fig.13a), magnetite from Sardinia and Huangshaping plot close to each other within the Fe-skarn field (Meng et al. 2017), separating from Fe skarns. It must be noted that the Ge concentrations in magnetite samples from Sardinia can be quite remarkable when compared to the Alvito, Azenhas and Akesayi Fe skarns (Maia et al. 2022, Dong et al. 2021). At the same time, the geochemical affinity between magnetite from Sardinian W-Sn bearing skarns and the more renowned W-Sn skarn of Huangshaping is highlighted (Zhao et al. 2022). These observations indicate that Ge and Ga could be very useful markers of magnetite from W-Sn-bearing skarns, in some cases more than W and Sn themselves. In fact, Sn contents are remarkably higher at Perda Niedda and

Rosas whereas magnetite from Monte Tamara has lower concentrations, despite the scheelite and cassiterite occurrence. However, the good clustering of Perda Niedda, Monte Tamara and Rosas samples in the Ga versus Ge diagram clearly points out that they could be grouped into a unitary W-Sn mineralizing system. On the other hand, the low Ge and Ga contents in magnetite from Giacurru seemingly suggest a different affinity of the mineralization, in terms of magmatic source and/or skarn system, despite its comparable W contents. Finally, the average sample and deposit Ge/Si ($\mu\text{mol/mol}$) and Ge contents have been plotted (Fig.14), defining again a narrower field for W-Sn-bearing skarns in the wider magmatic-hydrothermal Fe deposits by Meng et al. (2017).

Mechanisms of formation

In the last decade, the characterization of the different generations and compositional zoning have been used to better understand the mechanisms of formation of magnetite in various environments, including skarn (Xie et al. 2017; Wen et al. 2017; Chen et al. 2020; Sarjoughian et al. 2020; Dong et al. 2021; Maia et al. 2022; Zhao et al. 2022), IOCG (Hu et al. 2020; Tunnell et al. 2022), IOA (Broughm et al. 2017; Ovalle et al. 2022) and VMS (Makvandi et al. 2016). Following this direction, we present a representative case study based on the different textures and compositional features of magnetite from Perda Niedda.

The two textures of Perda Niedda magnetite, namely MagA and MagB (see *Petrographic and textural features* paragraph), seemingly suggest that MagA (e.g. rounded shapes, abundant silicate inclusions) represents a first magnetite generation, followed and overgrown by idiomorphic MagB. However, rather than

their textural differences, temperature is the most effective parameter to reveal different magnetite generations, as highlighted by the $T_{\text{Mg-Mag}}$ values calculated along EPMA profiles in MagA (PN5) and MagB surrounding Mag A (PN5), enclosed in garnet Sn-rich rims (PN3) and associated with cassiterite-fluorite-quartz-chlorite (wrigglite-type; PNB1) (Fig.15). In fact, the rounded MagA (PN5), formed under a range of 584-643°C (Fig.15a-b), comparable to the core of idiomorphic MagB enclosed in garnet (PN3), formed at 567-586°C (Fig.15c-d). Similarly, the 616-681°C temperature range of MagB surrounding MagA (Fig.15a-b; PN5) is instead comparable to the 592-687°C temperature range of idiomorphic MagB rim in garnet (Fig.15c-d; PN3). Thus, MagA is equivalent to the core of MagB, despite their different textures. Moreover, MagB from wrigglite-facies (PNB1) has markedly lower temperatures (Fig.15e-f) thereby representing a different magnetite generation.

The second consideration could be drawn from the core-to-rim profiles that indicate increasing temperatures of formation from MagA (from 567 to 643°C; Fig.15b-d) to MagB associated with garnets (from 592-606°C up to 687°C; Fig.15b-d), followed by the progressive temperature decrease of MagB in wrigglite-type facies (from 512 to 454°C; Fig.15f). Therefore, magnetite formation started during the prograde stage and continued for a broad time span throughout the retrograde stage. Similar temperature ranges have been reported and inferred for magnetite in other skarns worldwide (Zhao and Zhou 2015; Sarjoughian et al. 2020; Yan et al. 2021; Maia et al. 2022).

As a third consideration, Sn positively correlates with the temperatures of formation of magnetite. In fact, Sn contents slightly increase from negligible towards

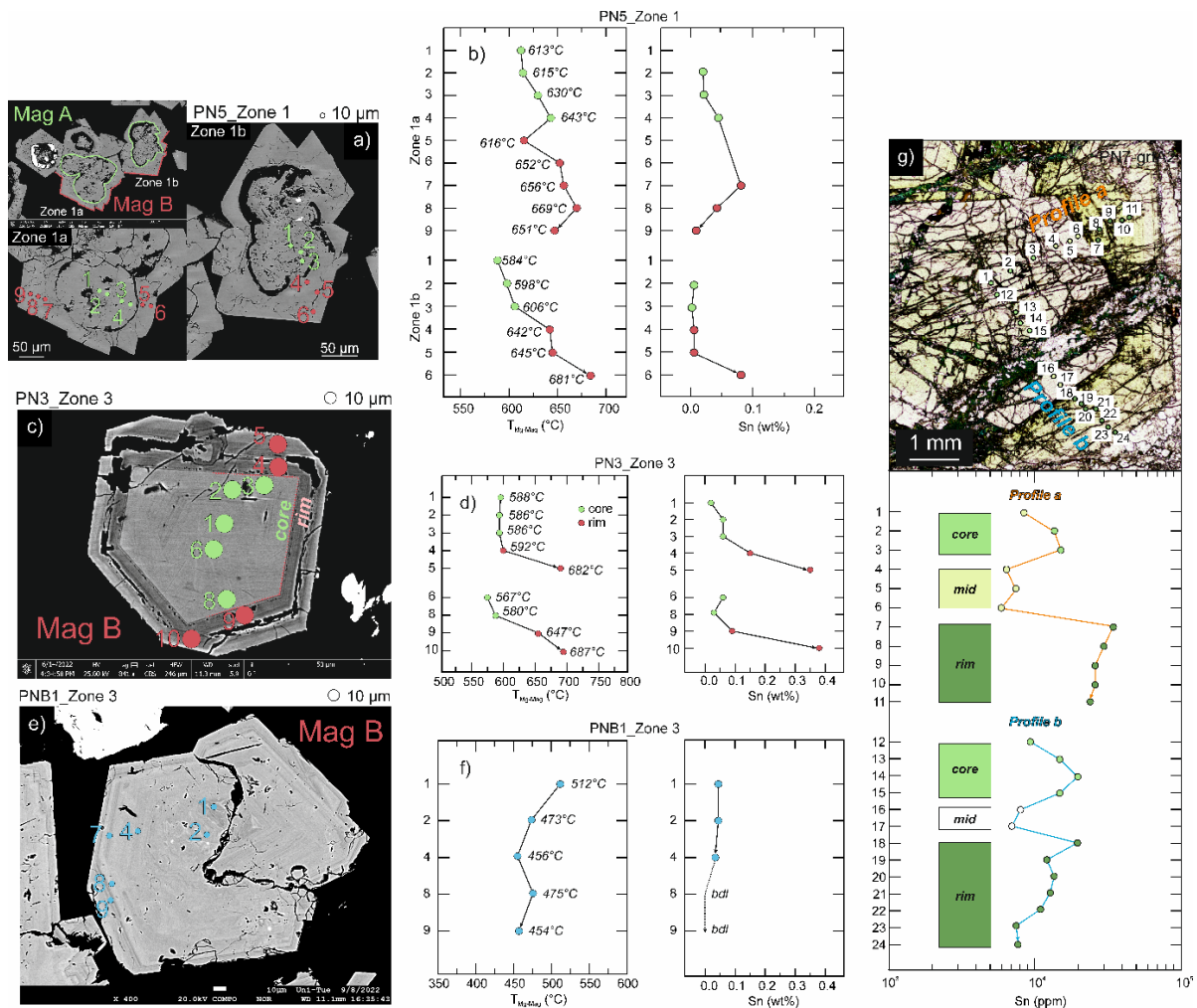


Figure 15 – Temperature and Sn profiles of representative magnetite crystals of the two different textures (MagA and MagB) from the Perda Niedda skarn (SW Sardinia). In (a), the EPMA spot analyses have been acquired along rounded and corroded MagA (green dots) and the surrounding idiomorphic MagB (PN5). In (b) the respective temperature and Sn values display a progressive increase from MagA to MagB. Profiles along Mag B (c; PN3), which is enclosed in garnet rims, show the correspondence between temperatures of MagB core (d) and Mag A. The rim of MagB shows a progressive temperature increase coupled with a sensible increase of Sn contents, testifying that Sn-enrichment occurred during the prograde hydrothermal evolution of magnetite. In the wrigglyite facies, MagB (e, PNB1) associated with cassiterite and fluorite shows a retrograde evolution and decreasing Sn contents (f). Representative LA-ICP-MS profiles on garnet crystals (g), exhibiting the rapid increase of Sn content in the rim (up to 3%).

peak values of 0.4 wt% at the peak of the prograde stage, namely where MagB, which is enclosed in the rims of garnet (PN5), records the highest temperatures (682-687°C; Fig.15b-d). Moreover, as shown in the LA-ICP-MS profile of garnet from the same deposit, Sn concentrations become remarkably high within garnet rims (Fig.15g), therefore suggesting the intake of a Sn-enriched hydrothermal fluid under prograde conditions of both garnet and MagB. It must be noted that Sn enrichments in MagB are not related with

the presence of cassiterite exsolutions or inclusions, but rather to the entrance of Sn in the magnetite crystal structure during this stage. The Sn increase corresponds to an increase of Si from core to rim of MagB (PN3), indicating that a temperature dependant behaviour, similarly to to Ti^{4+} , could be possible (Nadoll et al. 2014; Dare et al. 2014; Xie et al. 2017; Maia et al. 2022). Moreover, the high temperatures may have played a concurring role for Sn entrance in magnetite. Conversely, retrograde magnetite associated with

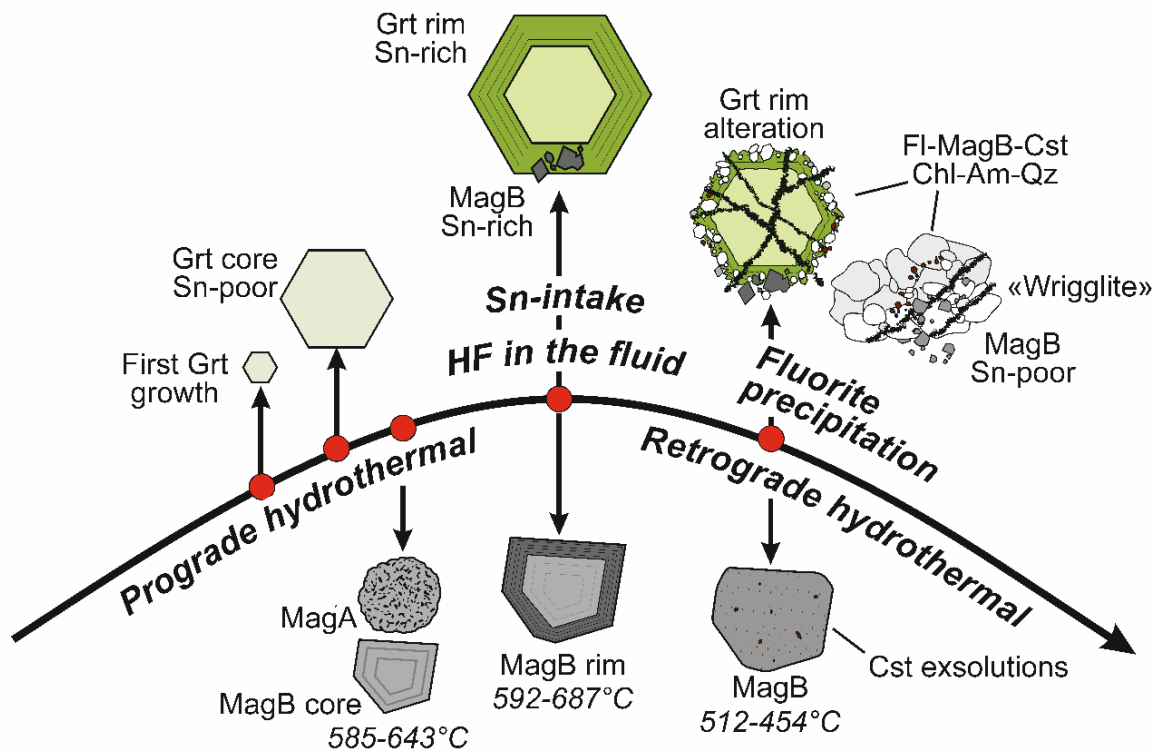


Figure 16 – Schematic illustration of magnetite crystallization process of the studied W-Sn-bearing skarns of Sardinia. During the prograde stage, garnet starts to grow and forms a moderately Sn-rich core. The first formation of MagA and the core of MagB occurred in the prograde hydrothermal stage under a temperature range from 584° to 643°C. At the thermal peak, the intake of Sn in the hydrothermal fluids led to the formation of garnet Sn-rich rims enclosing the Sn-enriched MagB, under a temperature range of 592° to 687°C. This moment corresponds to the first ingestion of HF in the fluid, enriching the Y/Ho ratio of Sn-enriched MagB. Eventually, during the retrograde hydrothermal stage (512-454°C), Sn-poor MagB. Moreover, the retrograde conditions led to the formation of cassiterite micro- and nano-scale exsolutions in MagB. The chemical aggression of garnet liberated Sn from its rims, thus forming cassiterite crystals as well. Consequently, fluorite extensively precipitated, fractionating Y and thus depleting the Y/Ho ratio of MagB, as observed in the altered garnet and wrigglyite facies.

cassiterite crystals in the wrigglyite-facies (PNB1), has negligible Sn contents, often below the detection limit. This may reflect a change in the physico-chemical conditions in the hydrothermal fluid triggering the precipitation of Sn as cassiterite (Schmidt 2018; Lehman 2022), rather than being trapped in other less-favourable hosts such as garnet or even magnetite.

Lastly, magnetite from Perda Niedda exhibit a good correlation between temperature and the Y/Ho ratio. Samples with higher Y/Ho ratio record higher average temperatures of formation (PN10, av. 674°C), whereas samples in the CHARAC field or slightly depleted in Y (PN-W, PN11, PN28B) have formed at lower

temperatures (PN-W, av. 490°C; PN11, av. 511°C; PN28B, av. 521°C). This evidence suggests that prograde magnetite (PN10, PN3, PN5) formed in presence of moderate concentrations of HF, able to mobilize yttrium, before fluorite precipitation. During this stage, garnet has favourable conditions for its growth, extracting Sn from the hydrothermal fluid. The Y/Ho range of retrograde magnetite plots within the CHARAC and reflects the formation after the reaction of HF with the host rock, thus after fluorite precipitation. Hydrothermal alteration of Sn-rich rims of garnet may have made Sn available for the precipitation of cassiterite and fluorite in the wrigglyite facies (PN-W, PN28B, PNB1).

These mechanisms are summarized in a schematic illustration in [Fig.16](#).

Conclusions

In the framework of the renewed interest for Critical Raw Materials in Europe, this study provides useful insights for W-Sn mineral exploration. We report the first characterization of the mineral chemistry of magnetite from skarn ores of Sardinia, which allowed to obtain further information regarding the metal endowment of a W-Sn-bearing skarn system and its mechanisms of formation. At the same time, this work offers potentially relevant cues, applicable on a broad scale to all W-Sn-bearing skarns. The main conclusions could be summarized as follows:

1. The metallogenic relationships between cassiterite- and scheelite-bearing skarns of Sardinia and the granites of the GS1 unit is confirmed, therefore aiding to the interpretation of such mineralization as parts of a unitary W-Sn mineral system.

2. The trace-elemental composition of magnetite represents a useful and powerful marker for W-Sn mineral exploration. The distinctive trace-elemental features of magnetite from W-Sn-bearing consist in their W-Sn-Ge enrichments, clearly diverging from Fe-skarns in the spider diagram proposed by [Dare et al. \(2014\)](#).

3. The comparison between our samples with other magnetite data from literature suggests that the Mn versus Ge and Ga versus Ge diagrams ([Meng et al. 2017](#)) could also be used to discriminate W-Sn-bearing skarns from Fe skarns. Therefore, Ge concentrations in magnetite play a major role in the identification of

potential undiscovered W-Sn mineralization.

4. The $T_{\text{Mg-Mag}}$ geothermometer ([Canil and Lacourse 2020](#)) allowed us to reconstruct the thermal evolution of magnetite formation which started under prograde hydrothermal conditions and continued throughout retrograde hydrothermal conditions.

5. A combined approach, considering the Y/Ho geochemical twin pair behaviour, the concentrations of Sn and the thermal evolution of magnetite, could provide very interesting informations about the complex formation mechanisms of skarn ores. In this sense, the intake of Sn occurred under prograde hydrothermal conditions before the precipitation of fluorite, leading to the formation of Sn-rich magnetite and garnet rims. Conversely, the subsequent alteration of Sn-rich garnet rims by an HF-rich hydrothermal fluid under retrograde conditions led to the precipitation of fluorite, followed by Sn-poor magnetite and cassiterite (wrigglite-facies).

Acknowledgements

M.L.D. gratefully acknowledges Sardinia Regional Government for financial support of his PhD scholarship (P.O.R. Sardegna F.S.E. Operational Programme of the Autonomous Region of Sardinia, European Social Fund 2007–2013 – Axis IV Human Resources, Objective 1.3, Line of Activity 1.3.1.), and the RAS/FdS grant “Sustainable land management: the tools of geology for the environment” (F72F16003080002). The EPMA analyses were performed using a microprobe (JEOL JXA-8230) which was partly funded by the German Research Foundation (DFG; grant INST 37/1026-1 FUGG).

References

- Akinfiyev, N. N., Korzhinskaya, V. S., Kotova, N. P., Redkin, A. F., & Zotov, A. V. (2020). Niobium and tantalum in hydrothermal fluids: Thermodynamic description of hydroxide and hydroxofluoride complexes. *Geochimica et Cosmochimica Acta*, 280, 102–115. <https://doi.org/10.1016/j.gca.2020.04.009>
- Atanasova P, Marks M A W, Frenzel M, et al (2020) Fractionation of geochemical twins (Zr/Hf, Nb/Ta and Y/Ho) and HREE-enrichment during magmatic and metamorphic processes in peralkaline nepheline syenites from Norra Kärr (Sweden). *Lithos*, 372–373. <https://doi.org/10.1016/j.lithos.2020.105667>
- Aponte F, Balassone G, Boni M, et al (1988) Variscan skarn ores in south-west Sardinia: their relationships with Cambro-Ordovician stratabound deposits. *Rend - Soc Ital di Mineral e Petrol* 43:445–462
- Bau M (1996) Controls on the fractionation of isovalent trace elements in magmatic and aqueous systems: evidence from Y/Ho, Zr/Hf, and lanthanide tetrad effect. *Contrib Mineral Petrol*, 123: 323–333. <https://doi.org/10.1007/s004100050317>
- Bau M, Dulski P (1995) Comparative study of yttrium and rare-earth element behaviours in fluorine-rich hydrothermal fluids. *Contributions to Mineralogy and Petrology*, 119(2–3): 213–223. <https://doi.org/10.1007/BF00307282>
- Bosi F, Biagioni C, Pasero M (2019) Nomenclature and classification of the spinel supergroup. *Eur J Mineral* 31:183–192. <https://doi.org/10.1127/ejm/2019/0031-2788>
- Boutroy E, Dare SAS, Beaudoin G, et al (2014) Magnetite composition in Ni-Cu-PGE deposits worldwide: Application to mineral exploration. *J Geochemical Explor* 145:64–81. <https://doi.org/10.1016/j.gexplo.2014.05.010>
- Broughm SG, Hanchar JM, Tornos F, et al (2017) Mineral chemistry of magnetite from magnetite-apatite mineralization and their host rocks: examples from Kiruna, Sweden, and El Laco, Chile. *Miner Depos* 52:1223–1244. <https://doi.org/10.1007/s00126-017-0718-8>
- Canil D, Lacourse T (2020) Geothermometry using minor and trace elements in igneous and hydrothermal magnetite. *Chem Geol* 541:119576. <https://doi.org/10.1016/j.chemgeo.2020.119576>
- Casini L, Cuccuru S, Puccini A, et al (2015) Evolution of the Corsica-Sardinia Batholith and late-orogenic shearing of the Variscides. *Tectonophysics* 646:65–78. <https://doi.org/10.1016/j.tecto.2015.01.017>
- Chen F, Deng J, Wang Q et al (2020) LA-ICP-MS trace element analysis of magnetite and pyrite from the Hetaoping Fe-Zn-Pb skarn deposit in Baoshan block, SW China: Implications for ore-forming processes. *Ore Geo Rev* 117. <https://doi.org/10.1016/j.oregeorev.2020.103309>
- Cocco F, Attardi A, Deidda ML, et al (2022) Passive Structural Control on Skarn Mineralization Localization: A Case Study from the Variscan Rosas Shear Zone (SW Sardinia, Italy). *Minerals* 12:272.

<https://doi.org/10.3390/min12020272>

- Conte AM, Cuccuru S, D'Antonio M, et al (2017) The post-collisional late Variscan ferroan granites of southern Sardinia (Italy): Inferences for inhomogeneity of lower crust. *Lithos* 294–295:263–282.
<https://doi.org/10.1016/j.lithos.2017.09.028>
- Dare SAS, Barnes SJ, Beaudoin G, et al (2014) Trace elements in magnetite as petrogenetic indicators. *Miner Depos* 49:785–796.
<https://doi.org/10.1007/s00126-014-0529-0>
- Dare SAS, Barnes SJ, Beaudoin G (2015) Did the massive magnetite “lava flows” of El Laco (Chile) form by magmatic or hydrothermal processes? New constraints from magnetite composition by LA-ICP-MS. *Miner Depos* 50:607–617.
<https://doi.org/10.1007/s00126-014-0560-1>
- Deidda ML, Naitza S, Moroni M, et al (2022) Mineralogy of the scheelite-bearing ores of Monte Tamara (SW Sardinia): Insights for the evolution of a Late Variscan W-Sn skarn system. *Mineral Mag* 1–23. <https://doi.org/10.1180/mgm.2022.119>
- Dong R, Wang H, Li W, et al (2021b) The geology, magnetite geochemistry, and oxygen isotopic composition of the Akesayi skarn iron deposit, Western Kunlun Orogenic Belt, Xinjiang, northwest China: Implications for ore genesis. *Ore Geol Rev* 130:..
<https://doi.org/10.1016/j.oregeorev.2020.103854>
- Dupuis C, Beaudoin G (2011) Discriminant diagrams for iron oxide trace element fingerprinting of mineral deposit types. *Miner Depos* 46:319–335.
<https://doi.org/10.1007/s00126-011-0334-y>
- Einaudi MT, Meinert LD, Newberry RJ (1981) Skarn deposits. SEG, *Econ Geol*, 75th Anniversary Volume, 317–391.
- Elicki O Pillola GL (2004) Cambrian microfauna and palaeoecology of the Campo Pisano Formation at Gutturu Pala (Iglesiente, SW Sardinia, Italy). *Boll Soc Pal It* 43:383–401.
- Bobba S, Carrara S, Huisman J et al. (2020) Critical Raw Materials for Strategic Technologies and Sectors in the EU. A Foresight Study. Publications Office of the European Union, Luxembourg, pp. 100.
- Frost, B.R., (1991). Introduction to oxygen fugacity and its petrologic importance. In: Donald L, *Oxide Minerals: Petrologic and Magnetic Significance*. Min Soc Am, 1-9.
- Funedda A (2009) Foreland- and hinterland-verging structures in fold-and-thrust belt: An example from the Variscan foreland of Sardinia. *Int J Earth Sci* 98:1625–1642.
<https://doi.org/10.1007/s00531-008-0327-y>
- Gao S, Liu X, Yuan H, et al (2002) Determination of Forty Two Major and Trace Elements in USGS and NIST SRM Glasses by Laser Ablation-Inductively Coupled Plasma-Mass Spectrometry: Geostandards and Geoanalytical Research, 26:181–196
- Green TH (1995) Significance of Nb / Ta as an indicator of geochemical processes in the crust-mantle system. 120:347-359.
doi:10.1111/j.1751-908X.2002.tb00886.x.
- Guillong M, Hametner K, Reusser E, et al (2005). Preliminary Characterisation of New Glass Reference Materials (GSA-1G, GSC-1G, GSD-1G and GSE-1G) by Laser Ablation-

- Inductively Coupled Plasma-Mass Spectrometry Using 193 nm, 213 nm and 266 nm Wavelengths. *Geostandards and Geoanalytical Research*, 29: 315-331.
<https://doi.org/10.1111/j.1751-908X.2005.tb00903.x>
- Hernández-Gómez P, Bendimya K, de Francisco C, et al (2001) Magnetic disaccommodation in Sn substituted magnetite. *Journal of Magnetism and Magnetic Minerals*. 226-230:1409-1411
- Hernández-Gómez P, Bendimya K, de Francisco C, et al (2006) Effect of tetravalent substitutions on the magnetic disaccommodation in magnetite. In: *Physica Status Solidi (C) Current Topics in Solid State Physics*. pp 3180–3183
- Hornig WS, Hess PC (2000) Partition coefficients of Nb and Ta between rutile and anhydrous haplogranite melts. *Contributions to Mineralogy and Petrology* 138:176–185.
<https://doi.org/10.1007/s004100050016>
- Horstwood, M.S.A. et al., 2016, Community-Derived Standards for LA-ICP-MS U-(Th-)Pb Geochronology – Uncertainty Propagation, Age Interpretation and Data Reporting: *Geostandards and Geoanalytical Research*, 40: 311–332.
[doi:10.1111/j.1751-908X.2016.00379.x](https://doi.org/10.1111/j.1751-908X.2016.00379.x)
- Hu X, Chen H, Beaudoin G, Zhang Y (2020) Textural and compositional evolution of iron oxides at Mina Justa (Peru): Implications for musketovite and formation of IOCG deposits. *American Mineralogist* 105:397–408.
<https://doi.org/10.2138/am-2020-7024>
- Hu H, Lentz D, Li JW, et al (2015) Riequilibrium processes in magnetite from iron skarn deposits. *Express letter. Econ Geol* 110:1–8.
<https://doi.org/10.2113/econgeo.110.1.1>
- Ishihara S (1981) The granitoid series and mineralization. SEG, *Econ Geol*, 75th Anniversary Volume, 458–484.
- Jochum K P, Weis U, Stoll B, et al (2011). Determination of reference values for NIST SRM 610-617 glasses following ISO guidelines. *Geostandards and Geoanalytical Research* 35, 397–429.
- Kwak TAP, Askins PW (1981) The nomenclature of carbonate replacement deposits, with emphasis on Sn-F(-Be-Zn) “wrigglite” skarns. *J Geol Soc Aust* 28:123–136.
<https://doi.org/10.1080/00167618108729151>
- Lehmann B (2021) Formation of tin ore deposits: A reassessment. *Lithos* 401-403.
<https://doi.org/10.1016/j.lithos.2020.105756>
- Lepage LD (2003) ILMAT: An Excel worksheet for ilmenite-magnetite geothermometry and geobarometry. *Comput Geosci* 29:673–678.
[https://doi.org/10.1016/S0098-3004\(03\)00042-6](https://doi.org/10.1016/S0098-3004(03)00042-6)
- Lindsley D, H. (1991) *Oxide Minerals: Petrologic and Magnetic Significance*. Min Soc of America, New York, USA.
- Linnen RL, Samson IM, Williams-Jones AE, Chakhmouradian AR (2013) *Geochemistry of the Rare-Earth Element, Nb, Ta, Hf, and Zr Deposits*, 2nd ed. Elsevier Ltd.
- Loi A, Cocco F, Oggiano G et al (2023) The Ordovician of Sardinia (Italy): from the ‘Sardic Phase’ to the end-Ordovician glaciation, palaeogeography and geodynamic context. *Geol*

Soc Lond, Spec Publ 532.

- Maia M, Barrulas P, Nogueira P, et al (2022) In situ LA-ICP-MS trace element analysis of deposits from SW Iberia (Ossa-Morena Zone). *J Geochem Explor* 234.
<https://doi.org/10.1016/j.gexplo.2021.106941>
- Makvandi S, Ghasemzadeh-Barvarz M, Beaudoin G, et al (2016) Partial least squares-discriminant analysis of trace element compositions of magnetite from various VMS deposit subtypes: Application to mineral exploration. *Ore Geol Rev* 78:388–408.
<https://doi.org/10.1016/j.oregeorev.2016.04.014>
- Meinert L D, Dipple G M, Nicolescu S (2005) World Skarn Deposits. *SEG*, Econ Geol, 100th Anniversary Volume, 299–336.
- Meloni MA, Oggiano G, Funedda A, et al (2017) Tectonics, ore bodies, and gamma-ray logging of the variscan basement, southern gennargentu massif (central Sardinia, Italy). *J Maps* 13:196–206.
<https://doi.org/10.1080/17445647.2017.1287601>
- Meng Y, Hu R, Huang X et al (2017) Germanium in Magnetite: Preliminary Review. *Acta Geol Sin* 91:711-726.
<https://doi.org/10.1111/1755-6724.13127>
- Nadoll P, Angerer T, Mauk JL, et al (2014) The chemistry of hydrothermal magnetite: A review. *Ore Geol Rev* 61:1–32.
<https://doi.org/10.1016/j.oregeorev.2013.12.013>
- Naitza S, Conte AM, Cuccuru S, et al (2017) A Late Variscan tin province associated to the ilmenite-series granites of the Sardinian Batholith (Italy): The Sn and Mo mineralisation around the Monte Linas ferroan granite. *Ore Geol Rev* 80:1259–1278.
<https://doi.org/10.1016/j.oregeorev.2016.09.013>
- Nistor CI, Boekema C, Van der Woude F, Sawatzky GA (1975) A Mössbauer study of doped magnetite. In: Hucl M, Zencik (1973) *Proc 5th Int Conf Mössbauer Spectrosc*, 1–3:99–103
- Ovalle JT, Reich M, Barra F, et al (2022) Magmatic-hydrothermal evolution of the El Laco iron deposit revealed by trace element geochemistry and high-resolution chemical mapping of magnetite assemblages. *Geochim Cosmochim Acta* 330:230–257.
<https://doi.org/10.1016/j.gca.2022.03.012>
- Paton, C., Hellstrom, J., Paul, B., et al (2011) Iolite: Freeware for the visualisation and processing of mass spectrometric data. *Journal of Analytical Atomic Spectrometry*.
doi:10.1039/c1ja10172b.
- Pillola GL (1991) Trilobites du Cambrien Inférieur du S.W. de la Sardaigne, Italie. *Palaeontographia Italica*, 78:1-74.
- Pirajno, F. (2009) *Hydrothermal Processes and Mineral Systems*. Springer, Dordrecht.
<https://doi.org/10.1007/978-1-4020-8613-7>
- Protano G, Riccobono F, Sabatini G (1996) Skarn formation and alteration-mineralization phenomena at Funtana Raminosa (Central Sardinia, Italy). Reconstruction of the thermal history from fluid inclusions. *Mineral Petrogr Acta* 231–249
- Ranta E, Wagner GST, Sturkell TFE, Skelton ETA (2018) Fluid – rock reactions in the 1.3 Ga

- siderite carbonatite of the Grønnedal – Íka alkaline complex, Southwest Greenland. *Contributions to Mineralogy and Petrology* 173:1–26.
<https://doi.org/10.1007/s00410-018-1505-y>
- Rossi P, Cocherie A (1991) Genesis of a Variscan batholith: Field, petrological and mineralogical evidence from the Corsica-Sardinia batholith. *Tectonophysics* 195:319–346.
[https://doi.org/10.1016/0040-1951\(91\)90219-I](https://doi.org/10.1016/0040-1951(91)90219-I)
- Sarjoughian F, Habibi I, Lentz DR, et al (2020) Magnetite compositions from the Baba Ali iron deposit in the Sanandaj-Sirjan zone, western Iran: Implications for ore genesis. *Ore Geol Rev* 126.
<https://doi.org/10.1016/j.oregeorev.2020.103728>
- Schmidt C (2018) Formation of hydrothermal tin deposits: Raman spectroscopic evidence for an important role of aqueous Sn(IV) species. *Geochim Cosmochim Acta* 220:499–511.
<https://doi.org/10.1016/j.gca.2017.10.011>
- Secchi F, Oggiano G, Cuccuru S, et al (2021) Geology of late-Variscan Sàrrabus pluton (south-eastern Sardinia, Italy). *J Maps* 17:591–605.
<https://doi.org/10.1080/17445647.2021.1982032>
- US Geological Survey (2021) Deposit Classification Scheme for the Critical Minerals Mapping Initiative Global Geochemical Database. U.S. Geological Survey Open-File Report 20211049:70.
- Veksler I V., Dorfman AM, Kamenetsky M, et al (2005) Partitioning of lanthanides and Y between immiscible silicate and fluoride melts, fluorite and cryolite and the origin of the lanthanide tetrad effect in igneous rocks. *Geochimica et Cosmochimica Acta*, 69:2847–2860.
<https://doi.org/10.1016/j.gca.2004.08.007>
- Verkaeren J. and Bartholomé P. (1979) Petrology of the San Leone Magnetite Skarn (S.W. Sardinia). *Econ Geol*, 74: 53–66.
- Wang RC, Yu A-P, Chen J et al (2012) Cassiterite exsolution with ilmenite lamellae in magnetite from the Huashan metaluminous tin granite in southern China. *Miner Petrol* 105:71–84.
<https://doi.org/10.1007/s00710-012-0194-x>
- Wen G, Li JW, Hofstra AH, et al (2017) Hydrothermal reequilibration of igneous magnetite in altered granitic plutons and its implications for magnetite classification schemes: Insights from the Handan-Xingtai iron district, North China Craton. *Geochim Cosmochim Acta* 213:255–270.
<https://doi.org/10.1016/j.gca.2017.06.043>
- Xie Q, Zhang Z, Hou T, et al (2017) Geochemistry and oxygen isotope composition of magnetite from the Zhangmatun deposit, North China Craton: Implications for the magmatic-hydrothermal evolution of Cornwall-type iron mineralization. *Ore Geol Rev* 88:57–70.
<https://doi.org/10.1016/j.oregeorev.2017.04.014>
- Yan H, Tian J, Yu D, et al (2021) Hydrothermal origin of the Naojiao Fe deposit in Lingxiang district, Eastern China: Evidence from in-situ LA-ICP-MS magnetite trace element analysis. *Solid Earth Sciences* 6:268–282.

<https://doi.org/10.1016/j.sesci.2021.06.004>

Zhao L, Shao Y, Zhang Y, Li H, Shah S A (2022) Differentiated enrichment of magnetite in the Jurassic W–Sn and Cu skarn deposits in the Nanling Range (South China) and their ore-forming processes: An example from the Huangshaping deposit. *Ore Geol Rev*, 148. <https://doi.org/10.1016/j.oregeorev.2022.105046>

Zhao WW, Zhou MF (2015) In-situ LA-ICP-MS trace elemental analyses of magnetite: The Mesozoic Tengtie skarn Fe deposit in the Nanling Range, South China. *Ore Geol Rev* 65:872–883. <https://doi.org/10.1016/j.oregeorev.2014.09.019>

APPENDIX I

Spatial and Metallogenic Relationships between Different Hydrothermal Vein Systems in the Southern Arburè District(SW Sardinia)

Matteo L. Deidda^{1*}, Dario Fancello¹, Marilena Moroni², Stefano Naitza¹, and
Ignazio Scano¹

¹ Department of Chemical and Geological Sciences, University of Cagliari, 09042, Monserrato (CA), Italy

² Dipartimento di Scienze della Terra, Università degli Studi di Milano, Via Luigi Mangiagalli, 34, 20133 Milano
MI, Italy

Published 25 February 2021

Environmental Science Proceedings - MDPI

Proceedings

Spatial and Metallogenic Relationships between Different Hydrothermal Vein Systems in the Southern Arburèse District (SW Sardinia) [†]

Matteo Luca Deidda ^{1,*}, Dario Fancello ¹, Marilena Moroni ², Stefano Naitza ¹ and Ignazio Scano ¹

¹ Dipartimento di Scienze Chimiche e Geologiche, Università degli Studi di Cagliari, 09124 Cagliari, Italy; dario.fancello@unica.it (D.F.); snaitza@unica.it (S.N.); iscano91@gmail.com (I.S.)

² Dipartimento di Scienze della Terra, Università degli Studi di Milano, 20122 Milano, Italy; marilena.moroni@unimi.it

* Correspondence: deiddam.geo@gmail.com

[†] Presented at the 2nd International Electronic Conference on Mineral Science, 1–15 March 2021; Available online: <https://iecms2021.sciforum.net/>.

Abstract: The SW Sardinian basement hosts various ore deposits linked to geological processes active from Cambrian to post-Variscan times. In particular, the Southern Arburèse district hosts several granite-related W-Sn-Mo deposits and a 10 km-long system of Ni-Co-As-Bi-Ag ± Au bearing five-element veins. New investigations into the eastern and central parts of the district (Pira Inferida mine sector) were performed to understand the poorly documented spatial and metallogenic relationships between these systems. The granite-related deposits consist of massive wolframite-quartz (W-Bi-Te-Au) and molybdenite-quartz veins, linked to the early Permian (289 ± 1 Ma) Mt. Linas granite, that are cross-cut by the five-element veins. The wolframite-quartz veins, observed by optical and electron (SEM-EDS) microscopy, show abundant native Bi, Bi-Te phases and native Au suggesting a W-Bi-Te-Au hydrothermal system. The five-element veins exhibit breccia and cockade textures, enveloping clasts of the Ordovician host-rocks and locally small fragments of the earlier W-Mo-quartz veins. The five-element vein paragenesis includes three main stages, from older to younger: (1) native elements (Bi ± Au); (2) Ni-Co arsenides-sulfarsenides in quartz gangue; and (3) Pb-Zn-Cu ± Ag sulfides in siderite gangue. The mineralogical, geochemical and isotopic features of the five-element vein swarm are closely comparable to five-element deposits elsewhere in Europe (Germany, Switzerland, Italian Alps). While the source of Ni and Co is still unknown, the high Bi contents, as well as Au enrichment in the five-element veins, suggest selective remobilization of these elements, and perhaps others, from the granite-related W-Bi-Te-Au veins. The five-element vein system was likely formed during a post-289 ± 1 Ma and post-Variscan metallogenic event.

Citation: Deidda, M.L.; Fancello, D.; Moroni, M.; Naitza, S.; Scano, I. Spatial and Metallogenic Relationships between Different Hydrothermal Vein Systems in the Southern Arburèse District (SW Sardinia). *Environ. Sci. Proc.* **2021**, *6*, 13. <https://doi.org/10.3390/iecms2021-09363>

Published: 25 February 2021

Publisher's Note: MDPI stays neutral with regard to jurisdictional claims in published maps and institutional affiliations.



Copyright: © 2021 by the authors. Licensee MDPI, Basel, Switzerland. This article is an open access article distributed under the terms and conditions of the Creative Commons Attribution (CC BY) license (<http://creativecommons.org/licenses/by/4.0/>).

Keywords: five-element veins; granite-related deposits; Ni-Co arsenides; native Bi; late Variscan metallogenesis

1. Introduction

In recent years the five element (Ni-Co-As-Bi-Ag) class of hydrothermal vein deposits [1] has been the object of renewed interest, primarily due to its relevant contents in critical elements such as Co and Bi [2]. Past and current mining surveys and exploitation in the major districts worldwide (e.g., Cobalt, Ontario; Great Bear Lake, WT; Bou Azzer, Morocco; Kongsberg, Norway; Erzgebirge, Germany; Jachimov, Czech Republic, Batopilas, Mexico, etc.) revealed the metallogenic intricacies of these systems, commonly characterized by a complex geochemical association (also including Sb, U, Hg and base metals), by exceptional enrichments of Ni-Co arsenides-sulfarsenides and native

elements (Ag, Bi) and by a typical carbonate gangue [3]. These peculiar characters raised several questions about the sources of these metals, the chemo-physical conditions regulating their regional-scale transport by low-temperature hydrothermal fluid systems and their deposition in vein-type deposits at shallow crustal levels. In recent studies focused on the genetic aspects of this class of deposits, abrupt redox variations and intake of hydrocarbons in fluids in tectonically active environments have been identified as the main controlling factors [4,5]. This general frame, albeit with differences related to regional and/or local geological conditions, has been confirmed by further studies on European deposits in Germany, Switzerland, Italian Alps and Sardinia [6–8]. The SW Sardinia (Italy) is characterized by multiple metallogenic events that originated different types of ore deposits ranging in age from Cambrian to post-Variscan times [9]. The northern side of this region, the Arburèse district (Figure 1a), hosts several kinds of deposits including: a) skarns, greisens and veins related to the emplacement of the late Variscan (289 ± 1 Ma) Monte Linas granite [10]; b) the large Zn-Pb Montevecchio vein swarm, and a 10-km long five-element vein system formerly considered to be related to the emplacement of the older Arbus pluton at 304 ± 1 Ma [9]. Our study is set in the old Pira Inferida mine, in the central section of the Southern Arburèse district, a key area due to the simultaneous occurrence of large Ni-Co-As-Bi-Ag \pm Au five-element veins and a wide granite-related quartz-wolframite vein swarm (“Togoro” veins in Figure 1b,c), both hosted in Ordovician very low-grade metasediments–metasiltstones. The mine operated during the 1930’s and only the Ni-Co arsenide and Pb-Zn sulfide ores have been systematically exploited; the five-element veins of Pira Inferida were included and briefly described in a recent study of the Southern Arburèse district by [8]. Conversely, very little data are available from the poorly studied wolframite-bearing veins. New surveys and mineralogical studies were performed in the area to acquire new data on both types of ores and to investigate their mutual and hitherto poorly constrained spatial and metallogenic relationships.

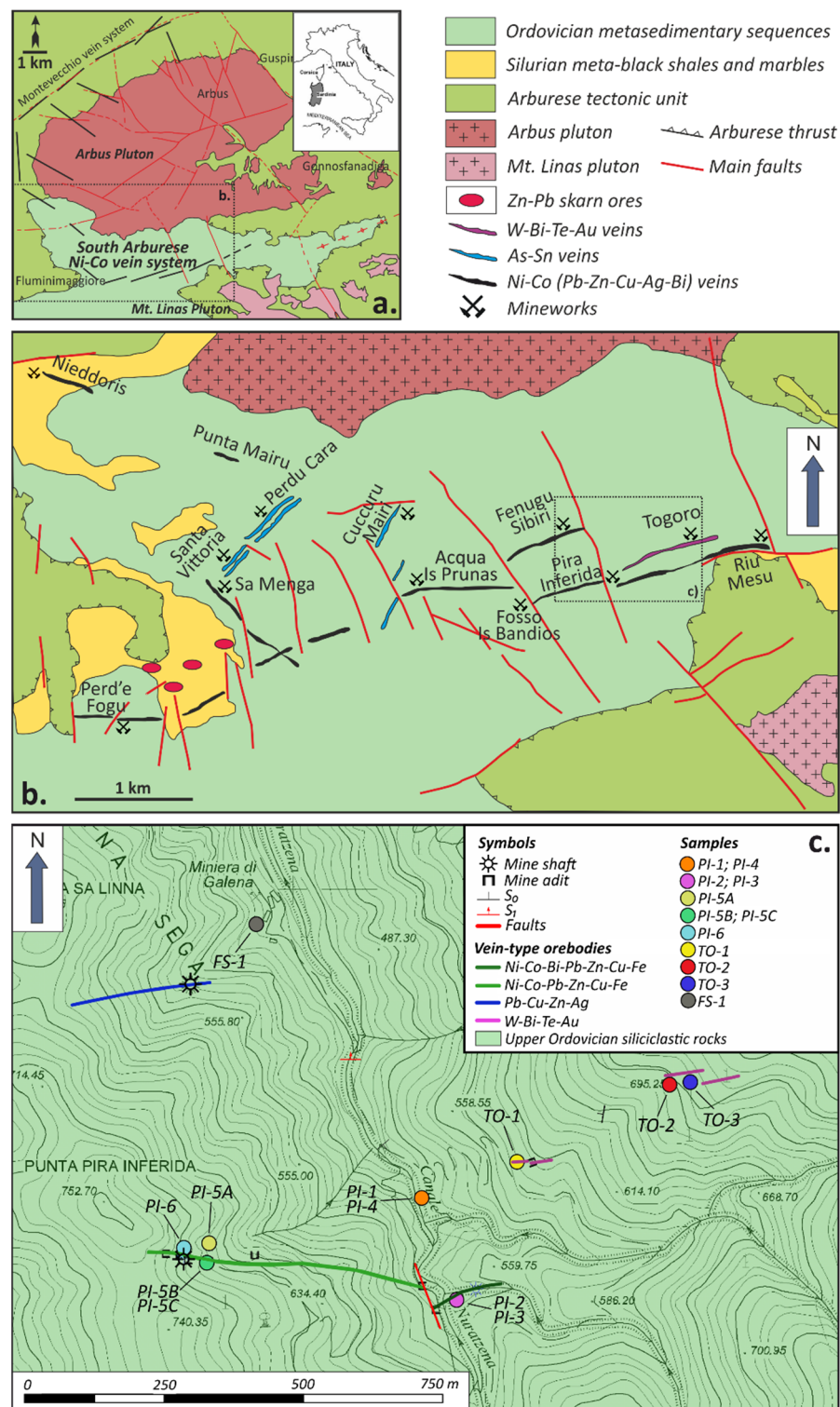


Figure 1. Geological sketch of the South Arburès area: (a) large-scale geological sketch showing the spatial relationships between the Arbus (304 Ma) and Linas plutons (289 Ma) and the orebodies (mod. after Moroni et al., 2019); (b) detail of the different vein-type orebodies of the area, including Ni-Co five-element type, As-Sn and W veins (mod. after Moroni et al., 2019); (c) small-scale geological sketch of the study area showing the location of the Pira Inferida five-elements type and Togoro W-Bi-Te-Au veins and the sampling sites.

2. Materials and Methods

Field surveys and samplings were performed in the old mine area of Pira Inferida (Figure 1c). Samples were collected at different mine levels, from the outcrops and from the dumps close to the main (mostly collapsed) adits. Several sub-sets of samples (PI-1, PI-2, PI-3, PI-4, PI-5, PI-6) were selected based on their location and different ore and gangue mineral associations. Samples of the quartz-wolframite veins were collected from small mineworks and trenches set at three different levels along the vertical development of the vein swarm (TO-1; TO-2; TO-3). Thin and polished sections from hand-selected samples were studied under transmitted and reflected light (RL) Optical Microscopy (OM). Further investigations were performed by SEM-EDS spot analyses and elemental mapping using a FEI Quanta 200 equipped with a ThermoFisher Ultradry EDS detector at the CeSAR laboratory at Università di Cagliari under high vacuum conditions, acceleration voltage 25–30 Kv, spot size 5 μm .

3. Results

3.1. Field Relationships

The investigated five-element veins comprise a series of 1–3 m thick, E-W striking and S-dipping veins outcropping discontinuously for over 500 m along their strike (Figure 1c). The veins crosscut a thick sequence of very low-grade metasandstones and meta-siltites of the late Ordovician age (Rio San Marco Fm. [11]); evidence of contact-metamorphism (i.e., andalusite-bearing spotted schists) are widespread, suggesting a relative proximity of underlying intrusions. A series of mineworks intercepted the orebodies at different levels: in the lower parts, the veins are well exposed with evident banded, brecciated and cockade textures (Figure 2); a thick, well-developed oxidation zone with vuggy quartz can be observed in the uppermost levels (Figure 2a–c). The Togoro wolframite ores occur as a NNE-SSW and N-dipping swarm of sub-parallel quartz veins whose thickness varies from 15 cm to 1 m; the mineralized zone is roughly 50 m wide and can be followed for over 1 km. The veins display a massive texture of white quartz enveloping idiomorphic, millimetric to pluricentimetric wolframite bladed crystals (Figure 2d). Overall, the orientation of the veins suggests crosscutting relationships between the two systems, although the bad outcrop preservation does not allow the direct recognition of their interaction. Such a situation is similar to what is reported in other mineralized sites along the Southern Arburès district (e.g., Sa Menga and Acqua is Prunas mines [8]), where greisen-type orebodies and five-element vein swarms are contiguous but not well exposed, thereby questioning the succession of mineralizing events.

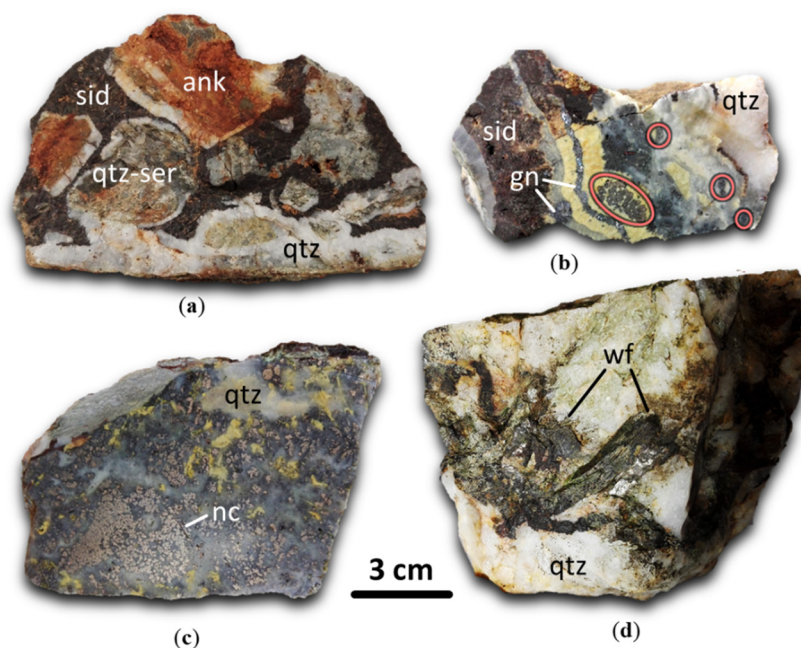


Figure 2. Hand specimens from the five-element veins at Pira Inferida and from the Togoro wolframite-bearing veins: (a) typical brecciated textures of the quartz and carbonate (siderite-ankerite) gangue (Pira Inferida, PI-1); (b) Bi and Ni-Co arsenide-sulfarsenide nests (in red) and thin galena veins in the siderite-quartz matrix (Pira Inferida, PI-5); (c) niccolite aggregates in the quartz matrix (Pira Inferida, PI-2); (d) idiomorphic wolframite crystals up to 6 cm in length in quartz gangue (Togoro, TO-2). nc = niccolite; qtz = quartz; sid = siderite; ank = ankerite; gn = galena; wf = wolframite.

3.2. The Five-Element Vein-Type Ore

The mineralogy of the five-element veins of Pira Inferida includes native Bi, Ni-Co arsenides and sulfarsenides, Zn-Cu-Fe-Pb sulfides and quartz-sericite-siderite gangue. Vein textures indicate multiple brecciation events between and during the mineralizing stages. At the selvages, host rocks are diffusely fractured, silicified and sericitized, with fractures filled by thin quartz veinlets. Incipient fracture opening is testified by the abundant host rock fragments into the vein mass. Remarkably, small fragments of older quartz veins were detected into the breccia in many samples; in these fragments, RL OM studies recognized the presence of rutile crystals with high W contents revealed by SEM-EDS. On the basis of the preliminary observations by OM and SEM-EDS, the five-element ore mineralizing stages may be schematized as follows: (1) native element stage (native Bi \pm native Au); (2) arsenide-sulfarsenide stage (niccolite \pm breithauptite \pm löllingite \rightarrow gersdorffite \pm cobaltite \pm ullmannite \pm bismuthinite \pm arsenopyrite) with quartz; (3) sulfide stage (sphalerite \pm pyrite \rightarrow chalcopyrite + tetrahedrite + galena) with siderite-ankerite. Focusing on the first two stages of mineralization, the paragenetic succession of native elements and Ni-Co arsenides-sulfarsenides can be clearly inferred from the zoned textures of the ore nodules, with native Bi cores extensively overgrown by niccolite aggregates with a mosaic or radial texture, in turn rimmed and substituted by gersdorffite and, less frequently, by ullmannite (Figures 3 and 4). Rare, rounded grains of native Au in gersdorffite have been also attributed to these early ore stages [8]. Local breithauptite intergrowths in niccolite and late bismuth-rich infillings along microcracks in the arsenides-sulfarsenides are also observed, with frequent substitution of native Bi by late bismuthinite; löllingite crystals are overgrown by arsenopyrite. Every major ore stage in the five-element veins is marked by strong brecciation and fragmentation of the previously crystallized assemblages, providing the evidence of a remarkably dynamic mineralizing process. Hence, the native Bi-bearing Ni-Co arsenide-sulfarsenide ore occur throughout the veins as irregular fragments and masses enveloped by later base metal sulfides and quartz/carbonate gangue

minerals; the Bi-Ni-Co aggregates are more abundant in oreshoot zones that were the main targets of former mining operations.

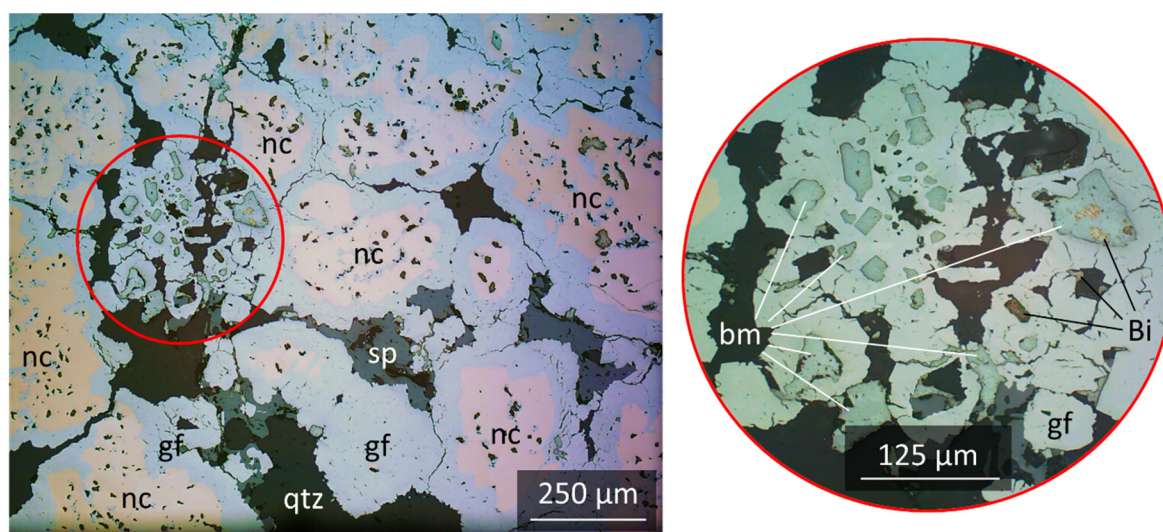


Figure 3. RL microscope images showing the textural relationships between native elements and Ni-Co arsenides-sulfarsenides of the five-element vein of Pira Inferida: native Bi grains with bismuthinite (bis) overgrowths are enclosed in the niccolite and gersdorffite aggregates (PI-2, 10–20×). nc = niccolite; gf = gersdorffite; Bi = bismuth; bm = bismuthinite; sp = sphalerite qtz = quartz.

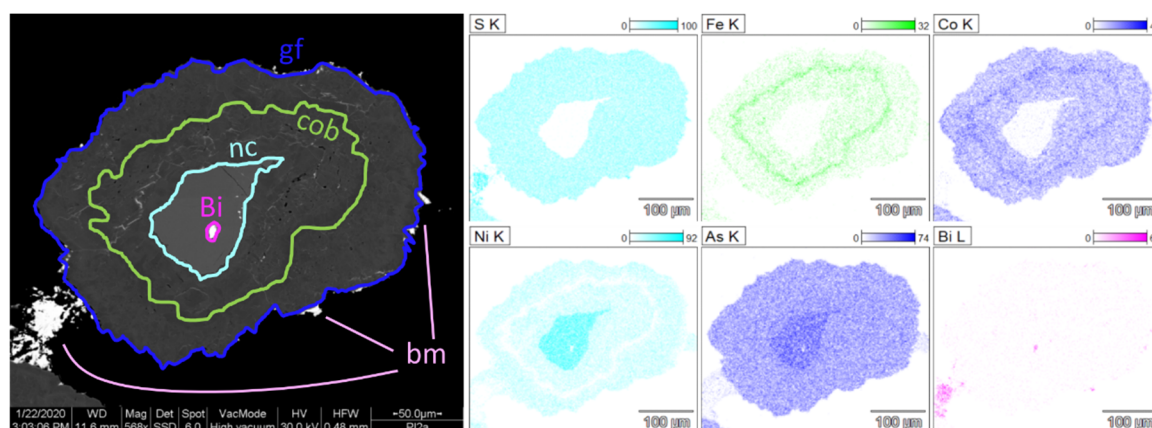


Figure 4. SEM-EDS elemental maps of Ni-Co arsenides-sulfarsenides of Pira Inferida: niccolite with native Bi inclusions surrounded by gersdorffite and cobaltite; fine-grained bismuthinite occurs on the edges of the Ni-Co ore minerals (PI-2). nc = niccolite; gf = gersdorffite; cob = cobaltite; Bi = bismuth; bm = bismuthinite.

3.3. The Wolframite Ore

The mineralogical association of the Togoro wolframite-bearing veins comprises wolframite in a granoblastic quartz and white mica gangue. Radial aggregates of mica are common both interstitial to quartz and along the vein selvages. Wolframite crystals are idiomorphic and tabular-shaped; their dimensions vary from 100 μm up to 6 cm in length. The lack of internal reflections and the weak anisotropy, coupled with the Fe-rich and Mn-low composition provided by SEM-EDS analyses, suggest a ferberite term. Scheelite pseudomorphs with relict wolframite are frequent; thin cross-cutting scheelite veins extend in both wolframite and quartz. Late-stage goethite-hematite alteration is also frequent, occasionally forming perfect pseudomorphs on wolframite and probable arsenopyrite. Numerous zoned Bi phases were observed as microinclusions both in the goethite-hematite pseudomorphs on wolframite and in the quartz gangue. SEM-EDS spot analyses and elemental mapping on Bi-phases in the quartz gangue showed Bi-rich cores with complex associations of bismuth tungstate (probable russellite), up to 500 μm in size, and

sulfotellurides, up to 100 μm surrounded by bismite alteration (Figure 5a). Occasionally, native bismuth occurs in the quartz gangue. The presence of native Au/electrum grains, previously observed under OM (Figure 5b), was confirmed by SEM-EDS analyses. Small (10–15 μm) Au $^{+/-}$ Ag blebs occur in close association with native Bi, Bi-W (Figure 5c) and Bi-Te-S phases included in wolframite and in the quartz matrix. Sulfides are rare and are represented only by pyrite and bismuthinite. Accordingly, a paragenetic succession of the W-Bi-Te-Au ore may be proposed with an initial precipitation of native Au, Bi-tellurides and wolframite in a quartz gangue with subordinate white micas, followed by scheelite and Bi-tungstate substituting wolframite and Bi-tellurides, respectively.

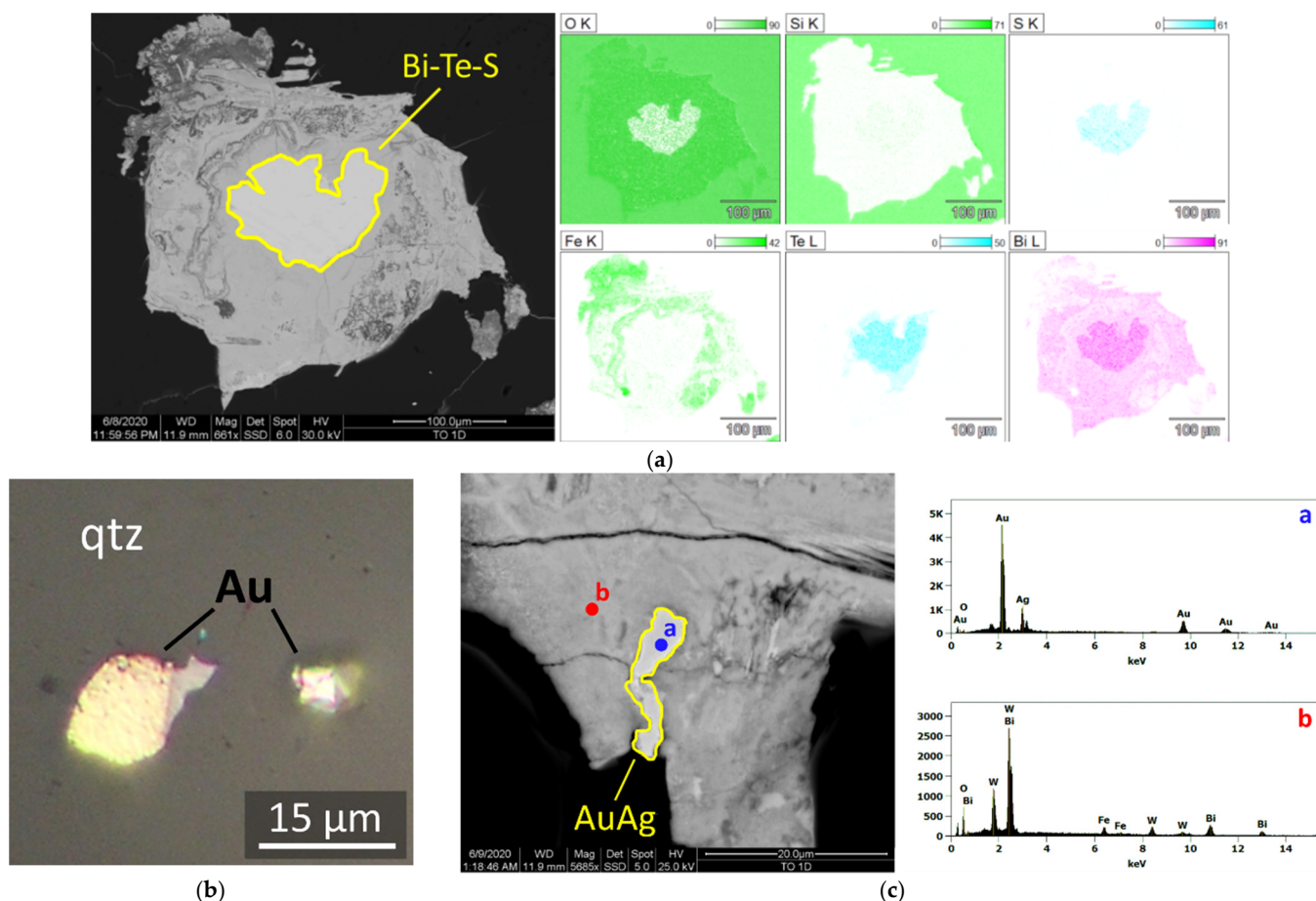


Figure 5. Bi-Te-Au mineralization from the Togoro wolframite veins: (a) Bi-sulfotelluride grain surrounded by bismite alteration (TO-1); (b) visible μm -scale gold grains enclosed in quartz (TO-1, 50 \times); (c) SEM-EDS spot analysis showing electrum (AuAg) grains, point a, enclosed in a Bi-tungstate, point b (TO-1).

4. Discussion and Conclusions

In this study, new mapping and sampling, OM and SEM-EDS analyses allow us to envisage a relationship between the wolframite-bearing veins and the polymetallic five-element vein system of the Pira Inferida mine sector and to locate these vein systems within a framework of successive mineralizing events that occurred in the Southern Arbùrese district during and after the emplacement of the Monte Linas granite. The wolframite-bearing veins are part of the magmatic hydrothermal systems of Monte Linas pluton, which belongs to a suite of early Permian (289 ± 1 Ma) F-bearing, ilmenite-series granites widely represented in SW Sardinia and associated with several Mo-W-Sn skarn, greisen and vein deposits [10]. Although fluid inclusion data on the Togoro vein system are not yet available, cassiterite and quartz microthermometry performed in other veins related to the Monte Linas granite (Perdu Cara in Figure 1b, and Perd'e Pibera deposits) assessed hypothermal to mesothermal conditions (410–320 $^{\circ}\text{C}$) for their main Sn-(W) and

Mo-(W) ore stages, at a depth corresponding to the shallow emplacement of the pluton (1 kbar) [10]. The detection of previously unrecognized Bi-Te-Au mineralization associated with the granite-related wolframite ore expands the knowledge on the metallogenic endowment of the area. More detailed mineral chemistry studies on Bi-Te phases will evaluate composition and distribution of Bi-tellurides and their relationship with Au enrichment in the vein system [12], the latter being a feature of high economic relevance and worthy of further investigation. Moreover, the presence of abundant Bi phases in the wolframite veins can contribute to defining their metallogenic relationships with the contiguous Ni-Co-As-Bi- Ag \pm Au, five-element vein system. The paragenetic succession established in the five-element ore at Pira Inferida approaches the general models [3–5], and broadly matches the depositional sequence in many similar deposits in alpine Italy and in Europe [6–8]. Few data reported for fluid inclusions in quartz [8] document low-temperature (<110 °C) and highly saline (20%NaCleq) fluids, presumably related to late mineralizing stages. The first two stages of mineralization likely represent rapidly changing physico-chemical conditions, causing the fast and abundant precipitation of native Bi “drop-lets”, followed by sudden precipitation of arsenides and, in turn, sulfarsenides, thereby forming zoned aggregates. Diffuse brecciation and cockade textures testify tectonic-driven fluid flow and hydrofracturing of host rocks. The absence of a pre-native element sulfide stage [4] may be ascribed to initial very low S contents in mineralizing fluids [5]; only after the As-dominated stage and precipitation of abundant siderite/ankerite gangue, do sulfides became dominant in the ore. The absence of early siderite, the high Ni/Co ratios and the low Ag contents reflect local peculiarities distinguishing the five-element veins of the Southern Arburèse district from many analogous systems worldwide [3]. Moreover, according to the most recent studies, the interaction between hydrothermal fluids and methane-, graphite- or Fe²⁺-rich rocks cause abrupt redox changes and triggers metal precipitation [4–6]. Methane has not been detected so far in fluid inclusions from the studied system; however, the late Ordovician metasediments and Silurian carbonaceous black shales, both pyrite-bearing and deposited in oxygen-poor environments [11], may be potential sources of methane and other reducing agents. In the Southern Arburèse district, the polymetallic five-element vein system might have cut across the granite-related veins. At Pira Inferida the crosscutting spatial relationships between the two vein systems are inferred by geometry of the orebodies and are documented by vein breccia fragments enveloped in the gangue of five-element veins. The latter feature is actually reported in other parts of the district, such as the Acqua is Prunas mine area, 4 km W from Pira Inferida, where small fragments of a quartz-molybdenite ore was observed in the five-element vein breccia [8]. These new evidences may have metallogenic implications in tracing the sources of metals of the five-element system. Such sources remain largely hypothetical, particularly for Ni and Co, tentatively ascribed to mafic rocks related to the older Arbus pluton [8]; however, the discovery of a notable Bi and Au mineralization in the wolframite veins suggests that the latter may have had a role as local sources of these metals. Bi and, to some extent, Au, may have been selectively remobilized from wolframite-bearing veins and re-precipitated in the native element stage of the five-element ores. This idea is strongly supported by the high Bi (native Bi + bismuthinite) contents of five-element ores in the highly mineralized intersection zone between the two systems within the mine; Bi contents decrease rapidly moving away from this sector. There is a final issue regarding the timing of the metallogenic events in the district. No geochronological data are so far available for the five-element veins, whereas the age of wolframite-bearing veins may be close to the 289 \pm 1 Ma age of the Monte Linas granite. The diffuse presence of cockades in five-element vein textures support the idea of mineralization along a regional-scale fault network during repeated seismic cycles at very low depths (<2 km) [13], indicating that, at the time of the five-element metallogenic event, the Monte Linas pluton and related deposits underwent an exhumation of almost 0.5 kbar. This supports the idea that the five-element vein system may instead belong to a late or possibly post-Variscan metallogenic event similar to the large-scale ones recorded in various mining poles across

Europe [14–17]. Such an event might have been developed at a regional scale and involved hypersaline fluids like those which caused the formation of the giant hydrothermal vein system of the Montevecchio district located just north of the five-element veins [18].

Author Contributions: Conceptualization, M.L.D., S.N., I.S., M.M., D.F.; methodology, S.N., M.M.; analysis, D.F., I.S., M.M.; field investigation, I.S., M.L.D., S.N., D.F.; data curation, M.L.D., I.S., D.F.; writing M.L.D., S.N., M.M.; funding acquisition, S.N., M.M. All authors have read and agreed to the published version of the manuscript.

Funding: This research was funded by RAS L.R. 7/2007 research program ‘Il blocco Sardo-Corso: area chiave per la ricostruzione della geodinamica varisica’ CUP J81G17000110002, and by RAS/FdS research program ‘Geogenic and anthropogenic sources of minerals and elements: fate and persistency over space and time in sediments’ CUP F74I19000960007. Matteo Luca Deidda gratefully acknowledges Sardinia Regional Government for the financial support of his PhD scholarship (P.O.R. Sardegna F.S.E. Operational Programme of the Autonomous Region of Sardinia, European Social Fund 2007–2013—Axis IV Human Resources, Objective 1.3, Line of Activity 1.3.1.).

Institutional Review Board Statement: Not applicable.

Informed Consent Statement: Not applicable.

Data Availability Statement: The data presented in this study are available on request from the corresponding author.

Conflicts of Interest: The authors declare no conflict of interest.

References

- Halls, C.; Stumpfl, E. The five-element (Ag-Bi-Co-Ni-As) vein deposit—A critical appraisal of the geological environments in which it occurs and of the theories affecting its origin. In Proceedings of the 24th International Geological Congress, Montreal, QC, Canada, August 1972; Section 4, p. 540.
- Horn, S.; Gunn, A.; Petavratzi, E.; Shaw, R.; Eilu, P.; Törmänen, T.; Bjerkgård, T.; Sandstad, J.; Jonsson, E.; Kountourelis, S.; et al. Cobalt resources in Europe and the potential for new discoveries. *Ore Geol. Rev.* **2021**, *130*, 103915, doi:10.1016/j.oregeorev.2020.103915.
- Kissin, S.A. Five-element (Ni-Co-As-Ag-Bi) veins. *Geosci. Can.* **1992**, *19*, 113–124.
- Markl, G.; Burisch, M.; Neumann, U. Natural fracking and the genesis of five-element veins. *Miner. Deposita* **2016**, *51*, 703–712, doi:10.1007/s00126-016-0662-z.
- Scharrer, M.; Kreissl, S.; Markl, G. The mineralogical variability of hydrothermal native element-arsenide (five-element) associations and the role of physicochemical and kinetic factors concerning sulfur and arsenic. *Ore Geol. Rev.* **2019**, *113*, 1–28, doi:10.1016/j.oregeorev.2019.103025.
- Burisch, M.; Gerdes, A.; Walter, B.F.; Neumann, U.; Fettel, M.; Markl, G. Methane and the origin of five-element veins: Mineralogy, age, fluid inclusion chemistry and ore forming processes in the Odenwald, SW Germany. *Ore Geol. Rev.* **2017**, *81*, 42–61.
- Kreissl, S.; Gerdes, A.; Walter, B.F.; Neumann, U.; Wenzel, T. Reconstruction of a >200 Ma multi-stage “five element” Bi-Co-Ni-Fe-As-S system in the Penninic Alps, Switzerland. *Ore Geol. Rev.* **2018**, *95*, 746–788.
- Moroni, M.; Rossetti, P.; Naitza, S.; Magnani, L.; Ruggieri, G.; Aquino, A.; Tartarotti, P.; Franklin, A.; Ferrari, E.; Castelli, D.; et al. Factors Controlling Hydrothermal Nickel and Cobalt Mineralization—Some Suggestions from Historical Ore Deposits in Italy. *Minerals* **2019**, *9*, 429.
- Cuccuru, S.; Naitza, S.; Secchi, F.; Puccini, A.; Casini, L.; Pavanetto, P.; Linnemann, U.; Hofmann, M.; Oggiano, G. Structural and metallogenic map of late Variscan Arbus Pluton (SW Sardinia, Italy). *J. Maps* **2015**, *12*, 860–865, doi:10.1080/17445647.2015.1091750.
- Naitza, S.; Conte, A.M.; Cuccuru, S.; Oggiano, G.; Secchi, F.; Tecce, F. A Late Variscan tin province associated to the ilmenite-series granites of the Sardinian Batholith (Italy): The Sn and Mo mineralization around the Monte Linas ferroan granite. *Ore Geol. Rev.* **2017**, *80*, 1259–1278.
- Leone, F.; Ferretti, A.; Hamman, W.; Loi, A.; Pillola, G.L.; Serpagli, E. A general view on the post-Sardic Ordovician sequence from SW Sardinia. *Rend. Soc. Paleont. Ital.* **2002**, *1*, 51–68.
- Ciobanu, C.L.; Cook, N.J.; Pring, A.; Brugger, J.; Danyushevsky, L.V.; Shimizu, M. “Invisible gold” in bismuth chalcogenides. *Geochim. Cosmochim. Acta* **2009**, *73*, 1970–1999.
- Masoch, S.; Fondriest, M.; Preto, N.; Secco, M.; Di Toro, G. Seismic cycle recorded in cockade-bearing faults (Col de Teghime, Alpine Corsica). *J. Struct. Geol.* **2019**, *129*, 103889.
- Munoz, M.; Boyce, A.J.; Corjault-Jade, P.; Fallick, A.E.; Tollon, F. Multi-stage fluid inclusion in the Palaeozoic base-ment-hosted Saint-Salvy ore deposit (NW Montagne Noire, southern France). *Appl. Geochem.* **1994**, *9*, 609–626.

15. Munoz, M.; Baron, S.; Boucher, A.; Béziat, D.; Salvi, S. Mesozoic vein-type Pb–Zn mineralization in the Pyrenees: Lead isotopic and fluid inclusion evidence from the Les Argentières and Lacore deposits. *C. R. Geosci.* **2016**, *348*, 322–332.
16. Muchez, P.; Heijlen, W.; Banks, D.; Blundell, D.; Boni, M.; Grandia, F. 7: Extensional tectonics and the timing and formation of basin-hosted deposits in Europe. *Ore Geol. Rev.* **2005**, *27*, 241–267, doi:10.1016/j.oregeorev.2005.07.013.
17. Ostendorf, J.; Henjes-Kunst, F.; Seifert, T.; Gutzmer, J. Age and genesis of polymetallic veins in the Freiberg district, Erzgebirge, Germany: Constraints from radiogenic isotopes. *Miner. Depos.* **2018**, *54*, 217–236, doi:10.1007/s00126-018-0841-1.
18. Moroni, M.; Naitza, S.; Ruggieri, G.; Aquino, A.; Costagliola, P.; De Giudici, G.; Caruso, S.; Ferrari, E.; Fiorentini, M.; Lattanzi, P.; et al. The Pb–Zn–Ag vein system at Montevecchio-Ingurtosu, southwestern Sardinia, Italy: A summary of previous knowledge and new mineralogical, fluid inclusion, and isotopic data. *Ore Geol. Rev.* **2019**, *115*, 103194, doi:10.1016/j.oregeorev.2019.103194.

APPENDIX II

Bi-minerals occurrence in various ore deposits of Southern Sardinia: a short review

Matteo L. Deidda^{1*}, Dario Fancello¹, Stefano Naitza¹, Marilena Moroni² and Ignazio Scano¹

¹ Department of Chemical and Geological Sciences, University of Cagliari, 09042, Monserrato (CA), Italy

² Dipartimento di Scienze della Terra, Università degli Studi di Milano, Via Luigi Mangiagalli, 34, 20133 Milano MI, Italy

Published 19 April 2022

Presented at EGU General Assembly 2022



Bi-minerals occurrence in various ore deposits of Southern Sardinia: a short review.

Matteo Luca Deidda¹, Dario Fancello¹, Naitza Stefano¹, Marilena Moroni², and Ignazio Scano¹

¹Università degli Studi di Cagliari, Dipartimento di Scienze Chimiche e Geologiche, Monserrato, Italy

²Università degli Studi di Milano, Dipartimento di Scienze della Terra, Milano, Italy

Bismuth is recognized as a Critical Raw Material by the EU Commission and it is found in many ore deposits across the world. In Southwestern (SWS) and Southeastern (SES) Sardinia, Bi-minerals are commonly found in two main groups of ore deposit: 1) late Variscan granite-related orebodies including greisens, W-Mo(-Sn) HT hydrothermal veins, skarns and hornfelses; and 2) late- to post-Variscan five-element (Ni-Co-As-Bi-Ag) LT hydrothermal veins.

In the first group, greisens (Flumini Binu prospect, SWS) and HT hydrothermal W-Mo(-Sn) veins (Perd'e Pibera mine and Togoro prospect, SWS; Perda Majori-Brunco Spangas prospects, SES) typically host native Bi, bismuthinite and, subordinately, Pb-Ag-Bi-sulfosalts interstitial to molybdenite and/or scattered in the quartz-feldspar(-fluorite-topaz) gangue. Locally, maldonite (Au₂Bi), Bi-tellurides (hedleyite Bi₇Te₃, and Bi₂Te) and probable russellite (Bi₂WO₆) are abundant in wolframite-rich veins (Togoro prospect), associated with native Au. Small grains of native Bi have also been found in some poorly mineralized garnet-vesuvianite-epidote calc-silicate hornfelses (Domus De Maria, SWS). Besides native Bi and bismuthinite, skarn orebodies frequently host wider assemblages consisting of Bi-Pb-Ag-Cu-sulfosalts intergrowths, once again associated with wolframates (scheelite at Monte Tamara prospect and Sa Marchesa mine, SWS) and molybdenite (Monte Tamara, Sa Marchesa and Morettu prospect, SWS). As a reference, the Monte Tamara assemblage includes "phase 88.6" (Cu_{0.33}Pb_{0.33}Bi_{7.67}S₁₂), pekoite (PbCuBi₁₁S₁₆Se₂), salzburgite-paarite (Cu_{1.58-1.67}Fe²⁺_{0.03-0.01}Pb_{1.65-1.72}Bi_{6.38-6.3}S_{12-12.06}), gustavite (PbAgBi₃S₆) xilingolite-lillianite (Pb₃Bi₂S₆), cosalite (Pb₂Bi₂S₆), berryite (Cu₃Ag₂Pb₃Bi₇S₁₆), ourayite (Pb₄Ag₃Bi₅S₁₃) and cupropavonite (Cu_{0.9}Ag_{0.5}Pb_{0.6}Bi_{2.5}S₅), identified by means of EPMA analyses. Moreover, since high Bi(-Ag-Te) contents have been detected in sulfides (sphalerite, galena, arsenopyrite), micro-inclusions of -sulfosalts and/or -tellurides may also occur. In the same area, wittichenite ((Bi,Cu)₂S₃) and hammariite (Pb₂Cu₂Bi₄S₉) have been previously identified, while schapbachite (AgBiS₂) has been reported at the Sa Marchesa mine.

The second group of Bi-bearing orebodies includes the five-element veins of the Arburès district (Pira Inferida, Acqua Is Prunas and Sa Menga mines, SWS), where native Bi and bismuthinite typically occur at the core of Ni-Co arsenides-sulfarsenides (e.g. nickeline and gersdorffite-cobaltite) concentric growths.

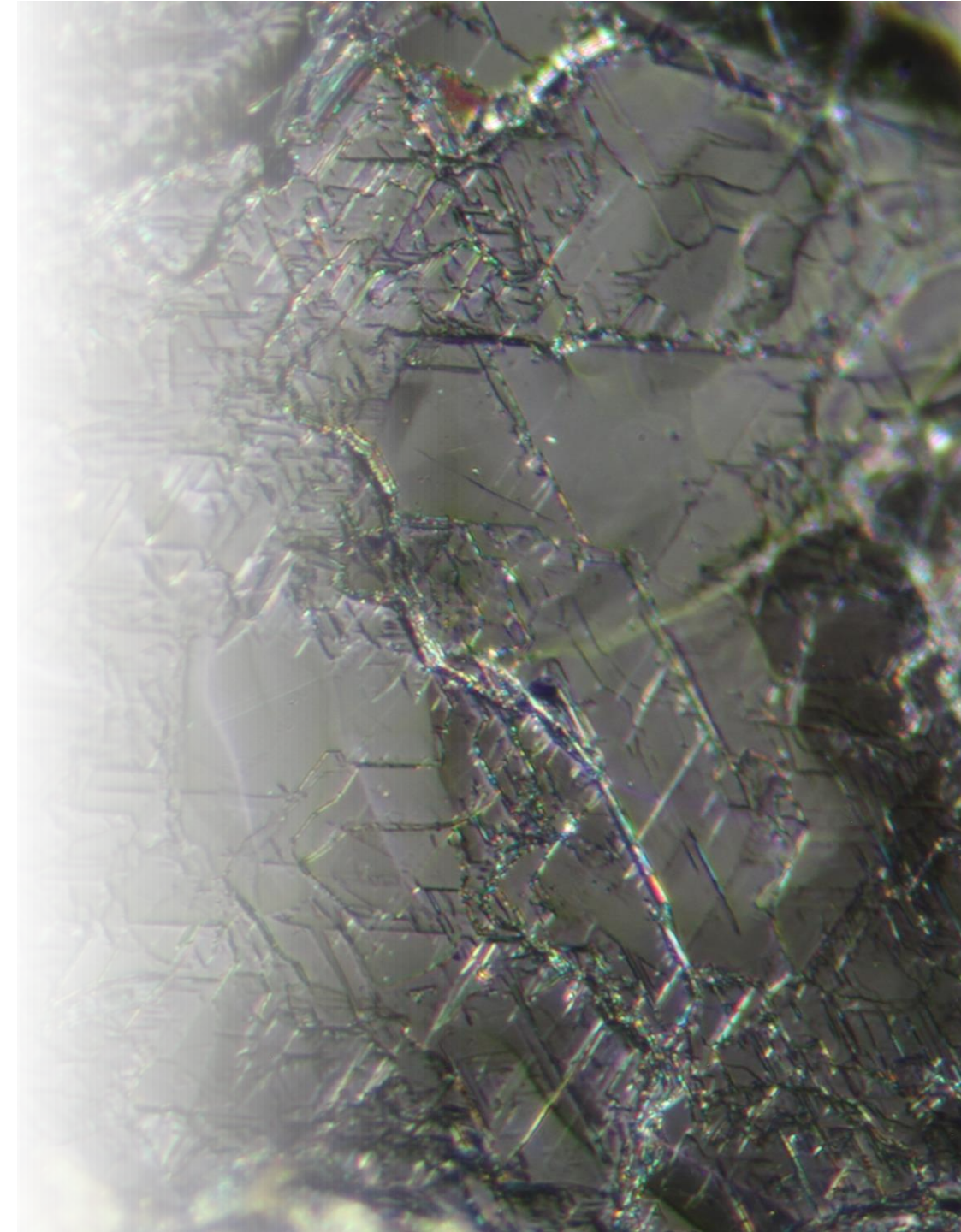
Therefore, the strong affinity of bismuth for granite-related W-Mo(-Sn) deposits of Southern

Sardinia indicates that the late-Variscan (Early Permian) granites represent its main metallogenic source. However, the formation of such diverse Bi-minerals assemblages is seemingly controlled by local-scale conditions. In skarn ores, the Bi-Pb-Ag-Cu-sulfosalts intergrowths formed during the sulfide stages, apparently after the interaction between primary Bi-phases and Pb-Ag-Cu-bearing hydrothermal fluids and under oscillatory variations of metals availability and stability. Conversely, in W-Mo(-Sn) hydrothermal veins and greisens, where sulfides are apparently more scarce, the array of Bi-phases is usually more limited. Furthermore, field and analytical data point towards a selective remobilization of bismuth from the primary native and -tellurides assemblage of HT wolframite-quartz veins (Togoro, SWS) by late cross-cutting LT five-element veins, suggesting that multiple, spaced over time hydrothermal-veining events occurred in the same area. In conclusion, bismuth and related mineral phases could serve as important markers, providing useful qualitative indications regarding the source of metals, the ore-forming processes and the relationships between different ore deposits at the district-scale.



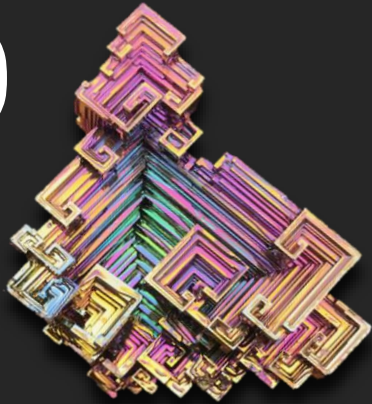
Bi-minerals occurrence in various ore deposits of Southern Sardinia: a short review.

Matteo Luca Deidda¹, Dario Fancello¹, Stefano Naitza¹, Marilena Moroni², Ignazio Scano¹



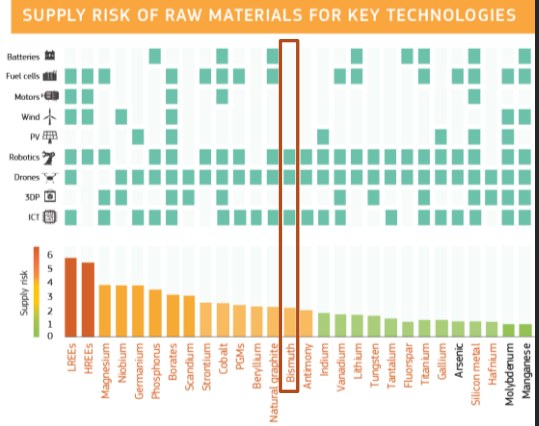
Bismuth (Bi)

It's a heavy, non-toxic, white-pinkish metal, with similar chemical properties to arsenic and antimony.



| | | | |
|---|---|---------------------------------------|---|
| 31 Ga gallium 69.723 | 32 Ge germanium 72.630(8) | 33 As arsenic 74.922 | 34 Se selenium 78.971(8) |
| 49 In indium 114.82 | 50 Sn tin 118.71 | 51 Sb antimony 121.76 | 52 Te tellurium 127.60(3) |
| 81 Tl thallium 204.38 [204.38, 204.39] | 82 Pb lead 207.2 | 83 Bi bismuth 208.98 | 84 Po polonium |
| 113 Nh nihonium | 114 Fl flerovium | 115 Mc moscovium | 116 Lv livermorium |

It is mostly used as an important raw material in the production of low-melting point alloys, cosmetics, paints and pharmaceuticals.



Bismuth has been recently included in the list of CRM.

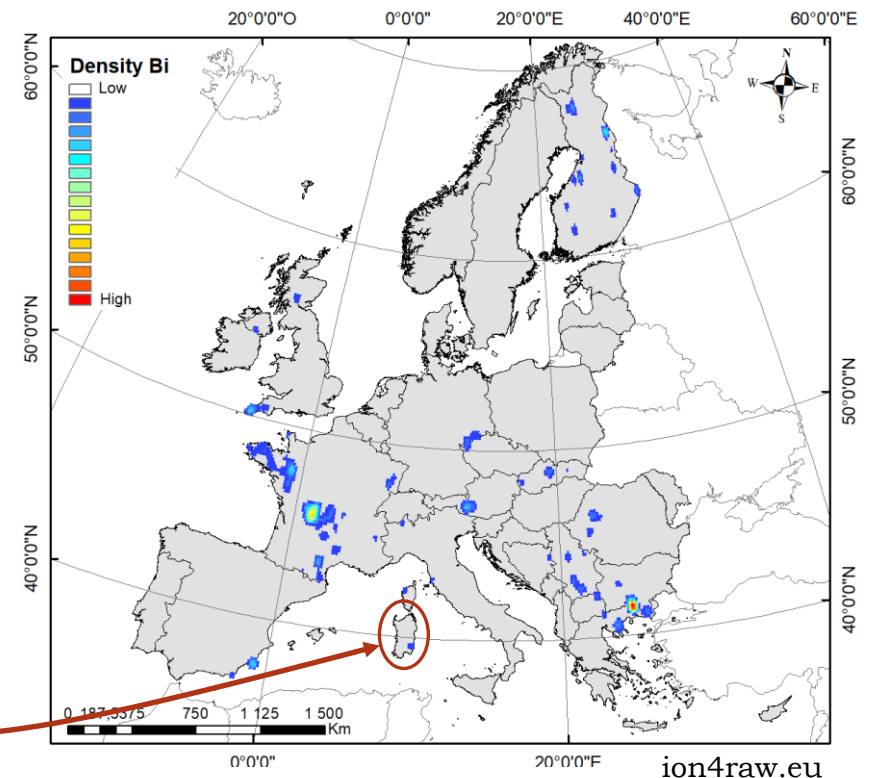
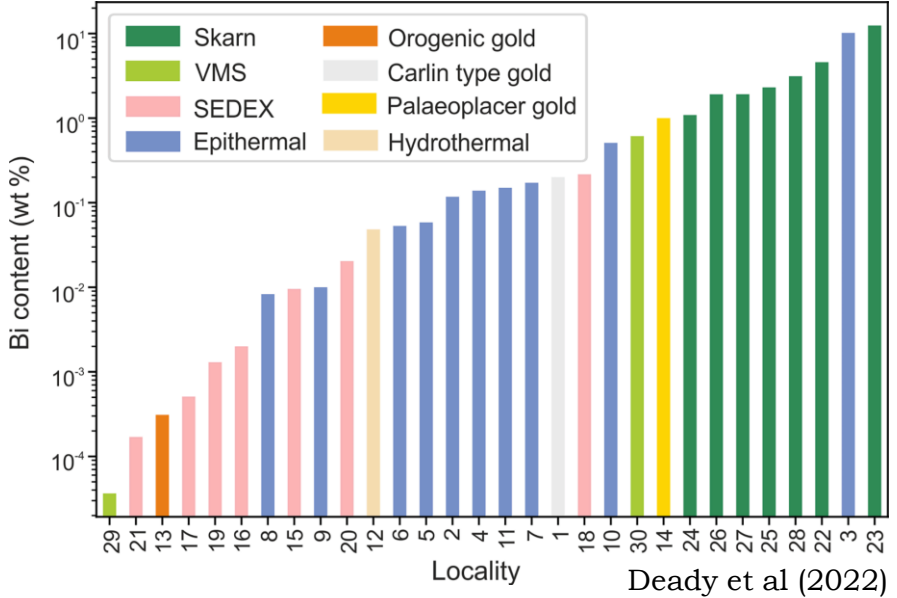
Mod. after European Commission's annual report on CRM (2020).

It occurs in its native form or in a wide variety of minerals (sulfides, sulfosalts, tellurides, oxides, etc)...

...and in many geologic environments and ore deposit types, including (Deady et al, 2022):

- Skarn
- Granite-related veins and greisens
- RIRGD (?)
- Porphyry/epithermal
- IOCG
- Pegmatites
- Five-element veins
- Orogenic gold
- VMS
- SEDEX




In Europe, Bi is frequently hosted in Variscan granite-related ore deposits, including those of **Sardinia**.

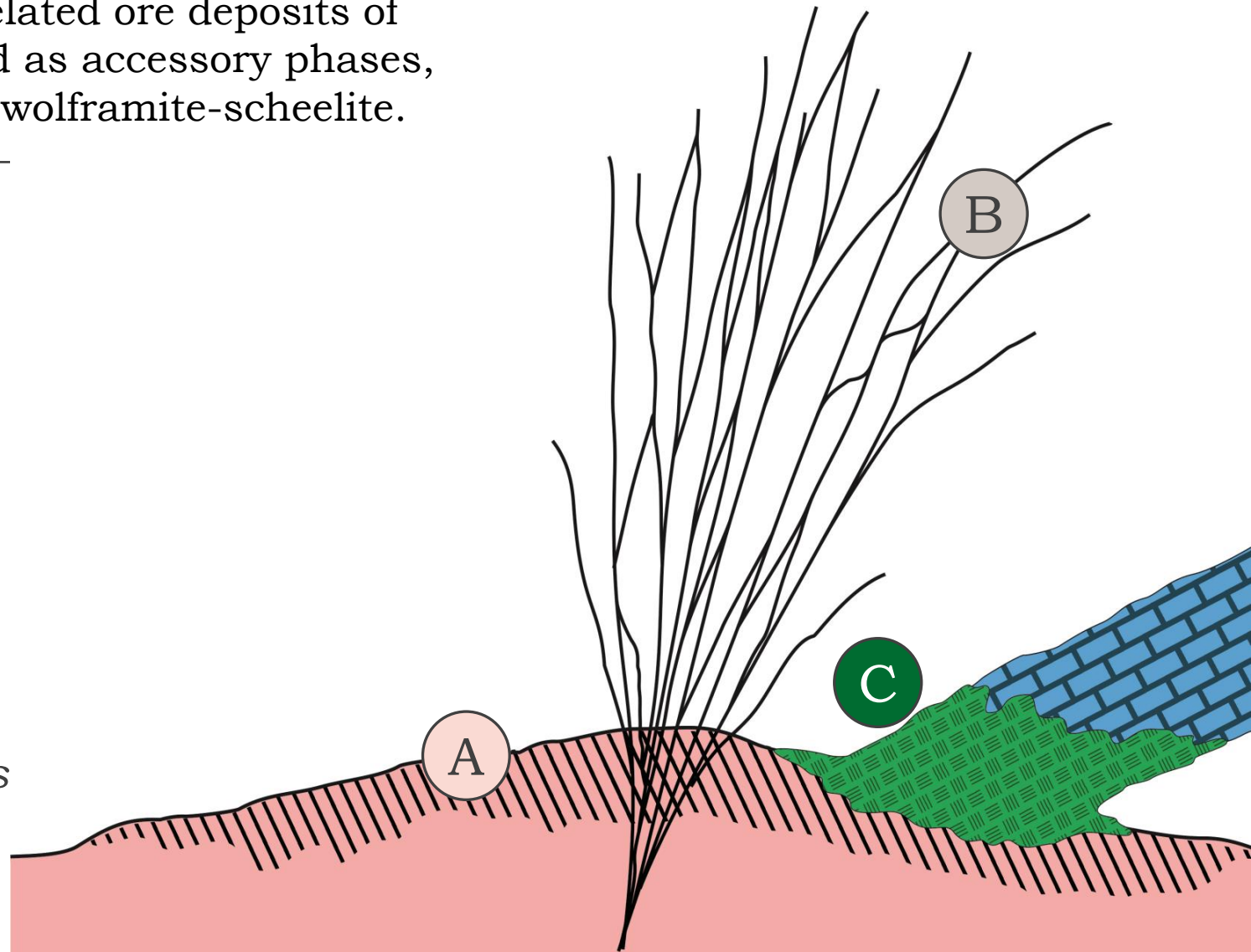


Bi-minerals in ore deposits of Sardinia

In late-Variscan (289-286 Ma) granite-related ore deposits of Sardinia, Bi-minerals are commonly found as accessory phases, mostly associated with molybdenite and wolframite-scheelite.

*Late-Variscan granite-related ores
(289-286 Ma)*

-  *Sn-W(-Mo) skarns*
-  *Mo-W(-Sn) HT hydrothermal veins*
-  *Mo(-W-Sn) Greisen*



Bi-minerals in ore deposits of Sardinia

In five-element veins, Bi-phases form at the early mineralizing stages.

The higher concentrations correspond to ore shoots in the proximity of granite-related Mo-W(-Sn) HT hydrothermal veins

*Post-Variscan? ores
(cross-cutting relationships)*

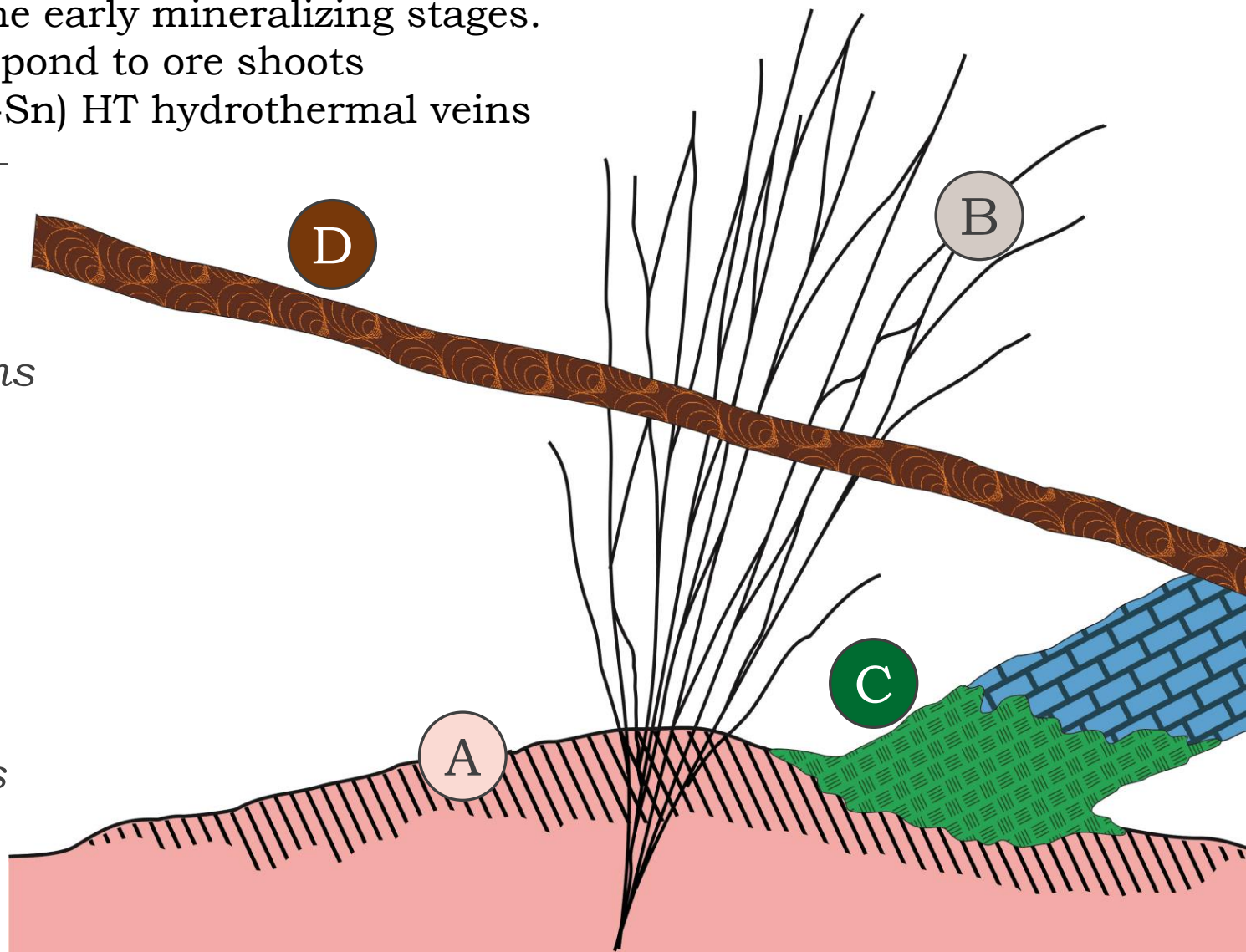
D *Five-element (Ni-Co-Bi-As-Ag) veins*

*Late-Variscan granite-related ores
(289-286 Ma)*

C *Sn-W(-Mo) skarns*

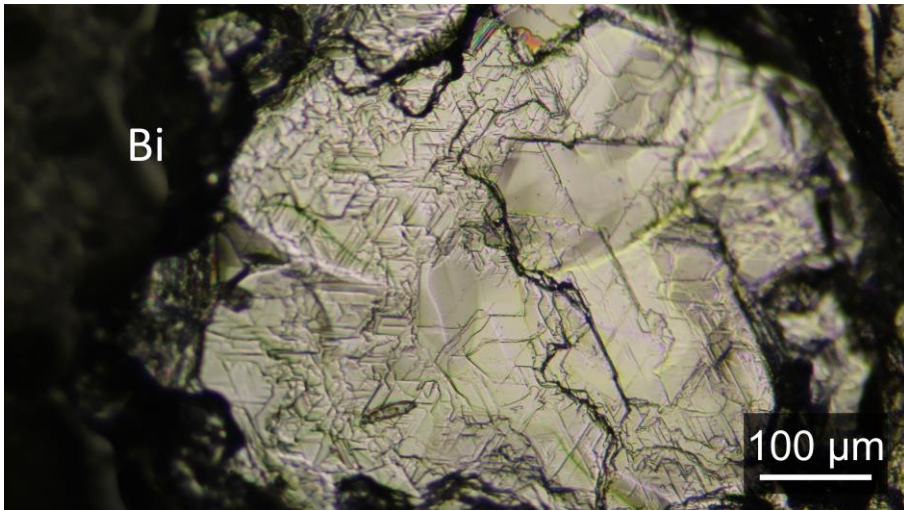
B *Mo-W(-Sn) HT hydrothermal veins*

A *Mo(-W-Sn) Greisen*



A Mo(-W-Sn) greisens

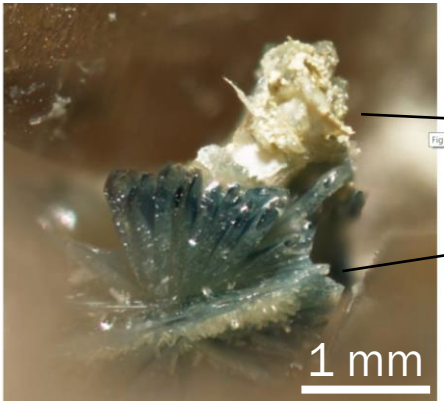
Molybdenite scattered in the greisen matrix, composed of quartz, K-feldspar, muscovite. Accessory tourmaline, rutile, monazite and **wolframite**. Sulfides are very rare (mostly pyrite and chalcopyrite).



Native Bi and Bi-Pb-sulfosalts in the intergranular spaces of molybdenite (Flumini Binu)...

...and newly discovered secondary Bi-molybdates like «gelosaite», «sardignaite», «suseinargiuite» and «mambertiite» (Su Seinargiu)

American Mineralogist, Volume 96, pages 268–273, 2011



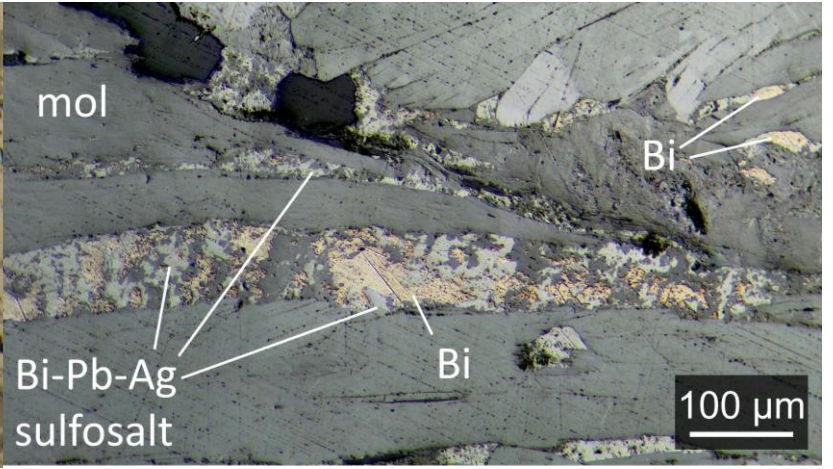
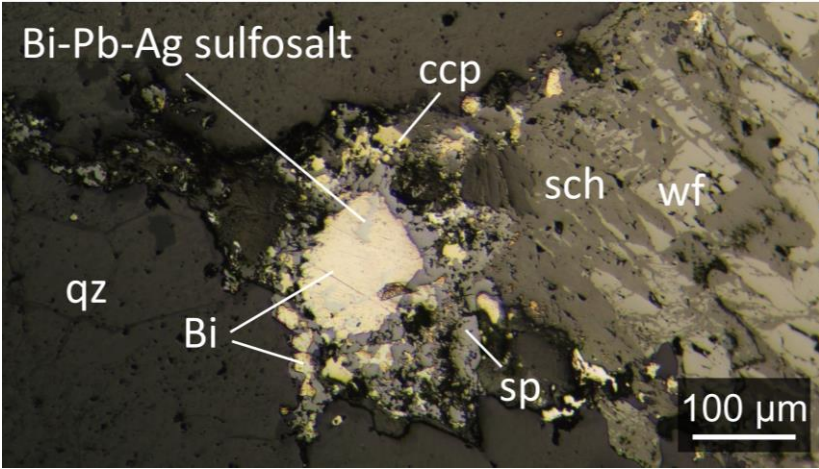
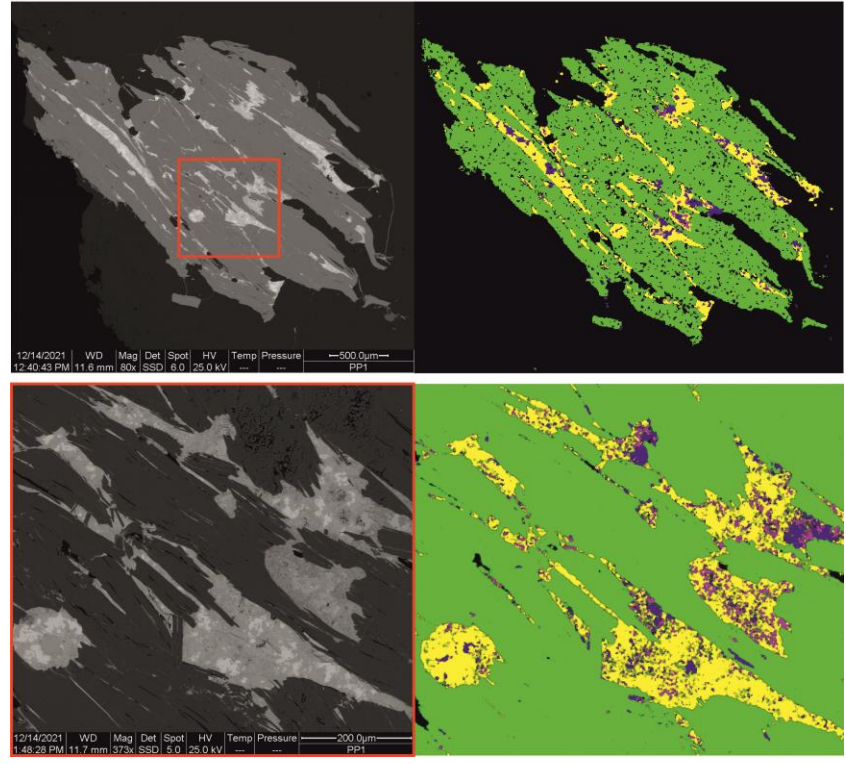
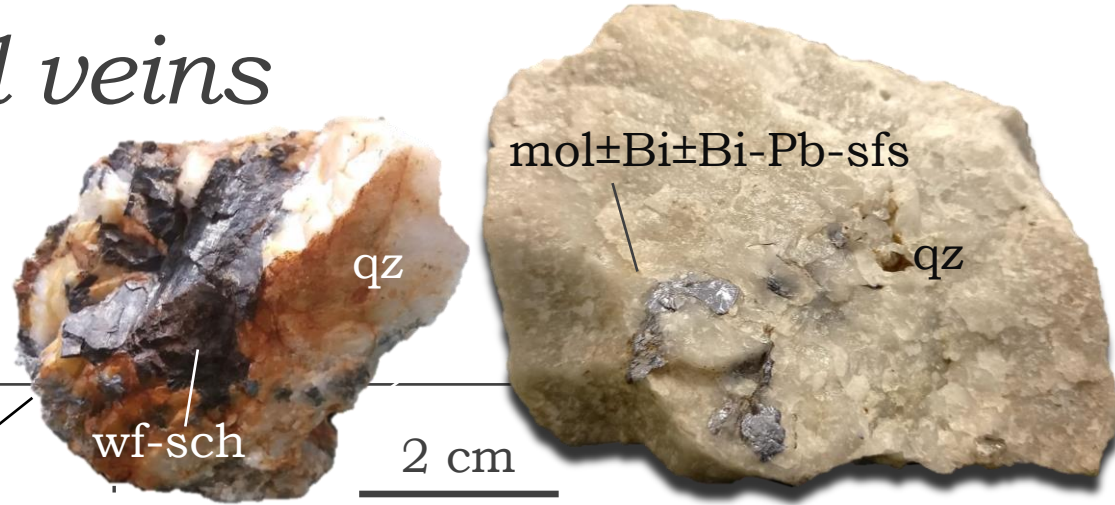
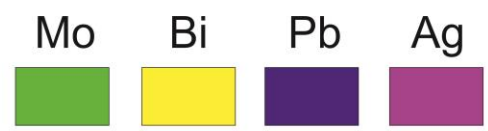
bismutite
gelosaite
mod. after Orlandi et al, 2011

Gelosaite, $\text{BiMo}_{(2-5x)}^{6+}\text{Mo}_{6x}^{5+}\text{O}_7(\text{OH})\cdot\text{H}_2\text{O}$ ($0 \leq x \leq 0.4$), a new mineral from Su Senargiu (CA), Sardinia, Italy, and a second occurrence from Kingsgate, New England, Australia

PAOLO ORLANDI,¹ FRANCESCO DEMARTIN,^{2,*} MARCO PASERO,¹ PETER LEVERETT,³ PETER A. WILLIAMS,³ AND DAVID E. HIBBS⁴

B Mo-W(-Sn) HT hydrothermal veins

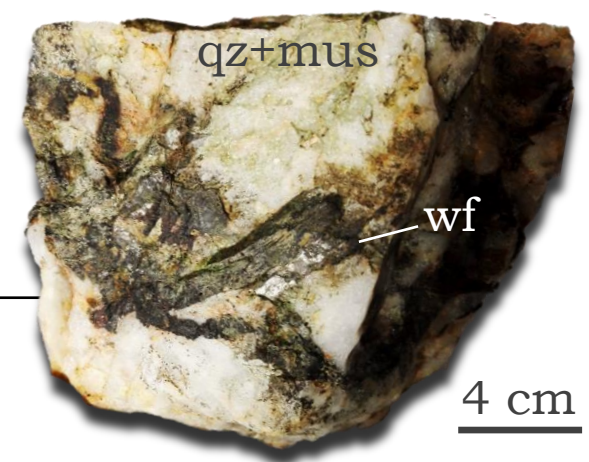
Quartz veins hosted in granites and metasandstones with **molybdenite and wolframite**. Accessory tourmaline, rutile, fluorite, feldspar, muscovite, topaz, uraninite, scheelite. Subordinate pyrite, sphalerite, galena, chalcocopyrite.



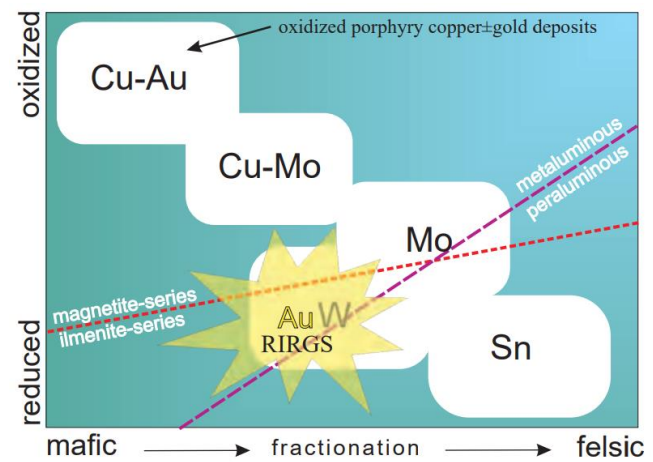
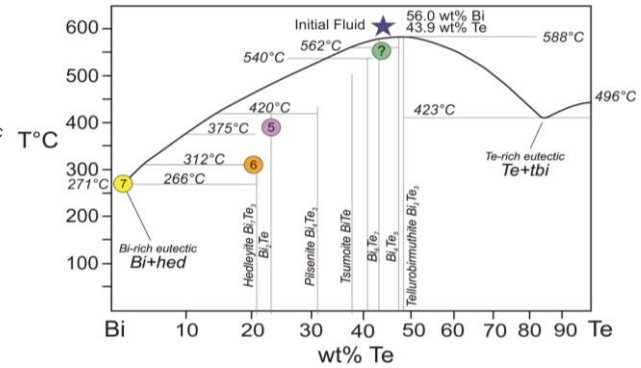
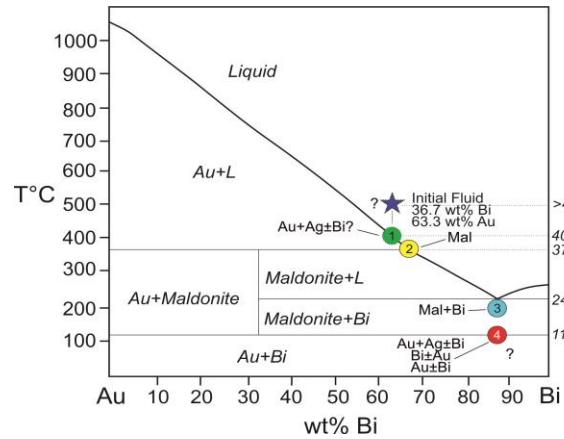
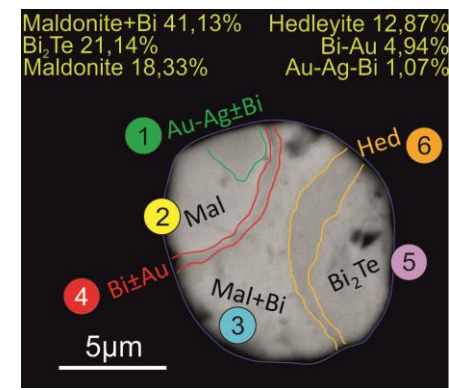
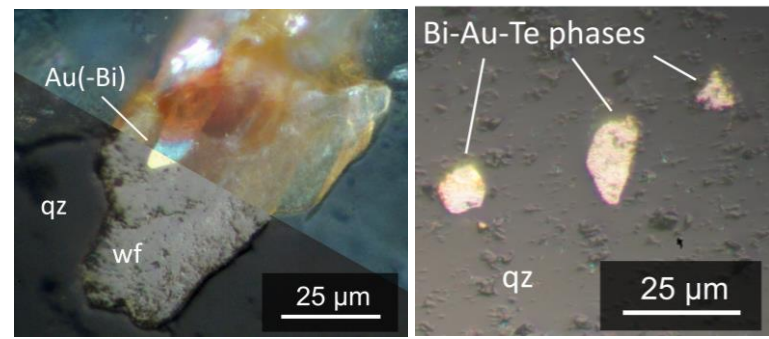
Native Bi, bismuthinite and Bi-Pb-Ag-sulfosalts in the intergranular spaces of molybdenite and at the edges of wolframite. Sulfosalts probably belong to the **bismuthinite-aikinite series** (similar to gustavite $PbAgBi_3S_6$)

B Mo-W(-Sn) HT hydrothermal veins

Wolframite-quartz veins (Togoro). Muscovite at the selvages. Molybdenite and cassiterite are absent; very rare sulfides (pyrite-arsenopyrite). **Scheelite** and goethite alteration of wolframite.

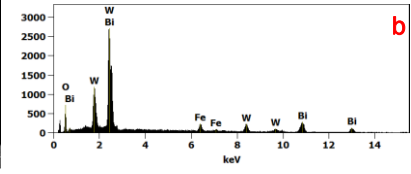
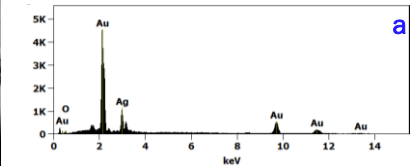
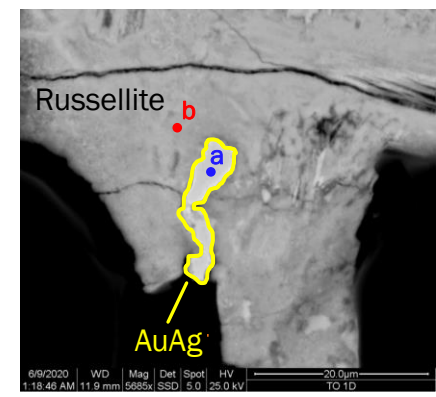


Complex «**gold scavenging**» paragenesis (Ciobanu, 2003): **maldonite** (Au_2Bi), **native Bi**, **Bi-tellurides (hedleyite Bi_7Te_3 ; Bi_2Te)**, **russellite** (Bi_2WO_6).



Some affinities with RIRGD (Hart, 2007):

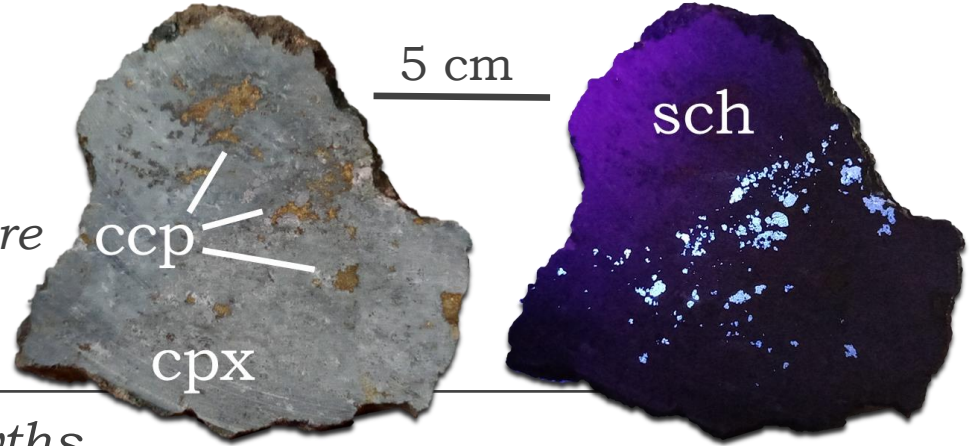
- Ilmenite series granites
- W-Bi-Te-Au association
- Rare sulfides
- Ag-Pb-Zn veins in the proximity





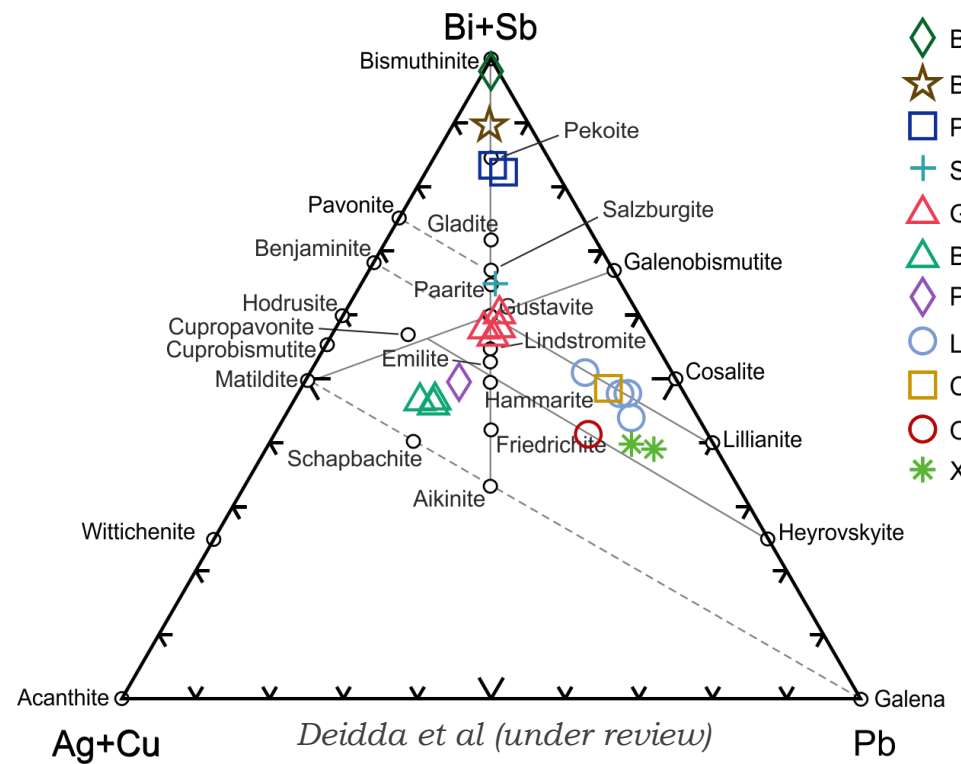
W-Sn(-Mo) skarns

Garnet-clinopyroxene skarns with disseminated **scheelite** and subordinate **cassiterite-stannite** and **molybdenite**. Sulfides are very abundant (arsenopyrite, sphalerite, chalcopyrite, galena, pyrrhotite, pyrite).

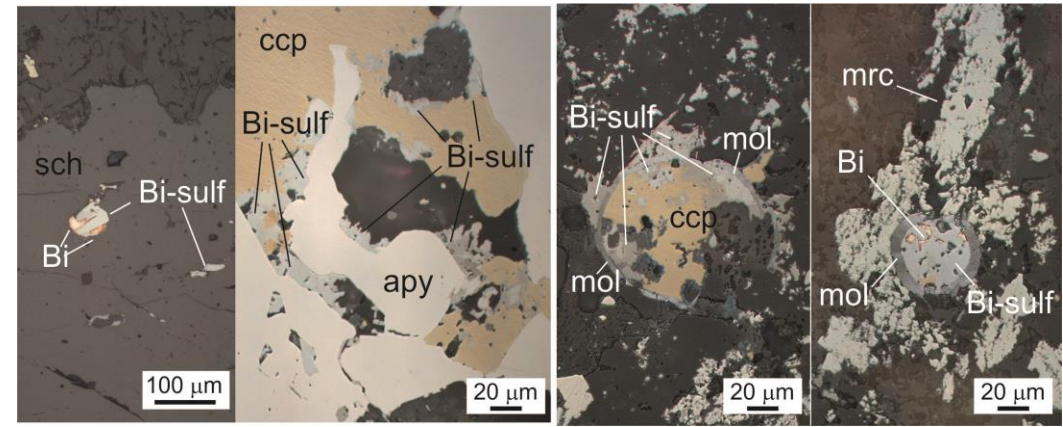


Deidda et al (under review)

Complex **native Bi** and **Bi-Pb-Ag-Cu-sulfosalts** intergrowths. Often enveloped in molybdenite «rings»; also enclosed in garnets and scheelite.

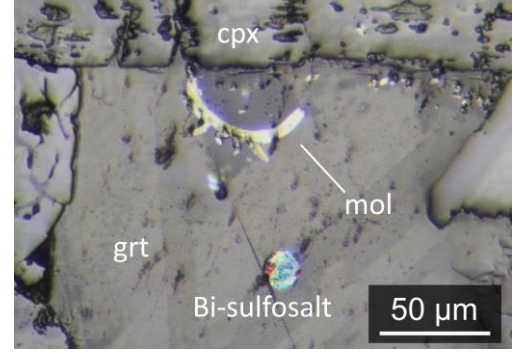


Deidda et al (under review)



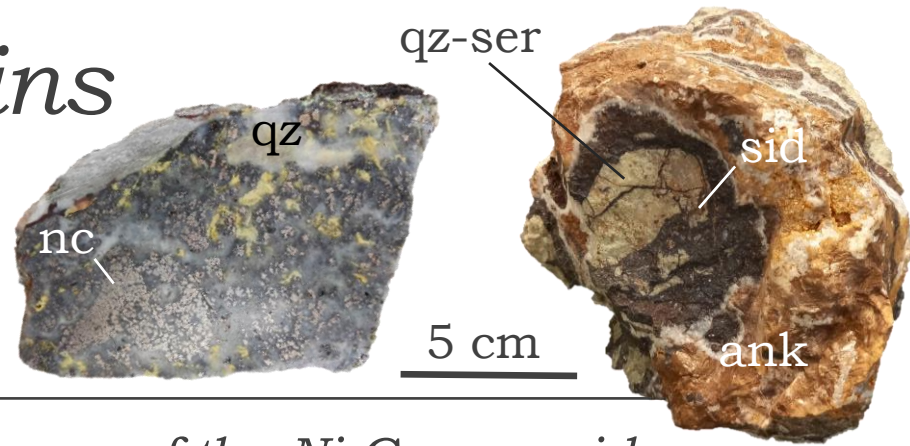
Deidda et al (under review)

High Bi-Te contents in galena, probably due to Bi-tellurides micro-inclusions (George et al, 2015)

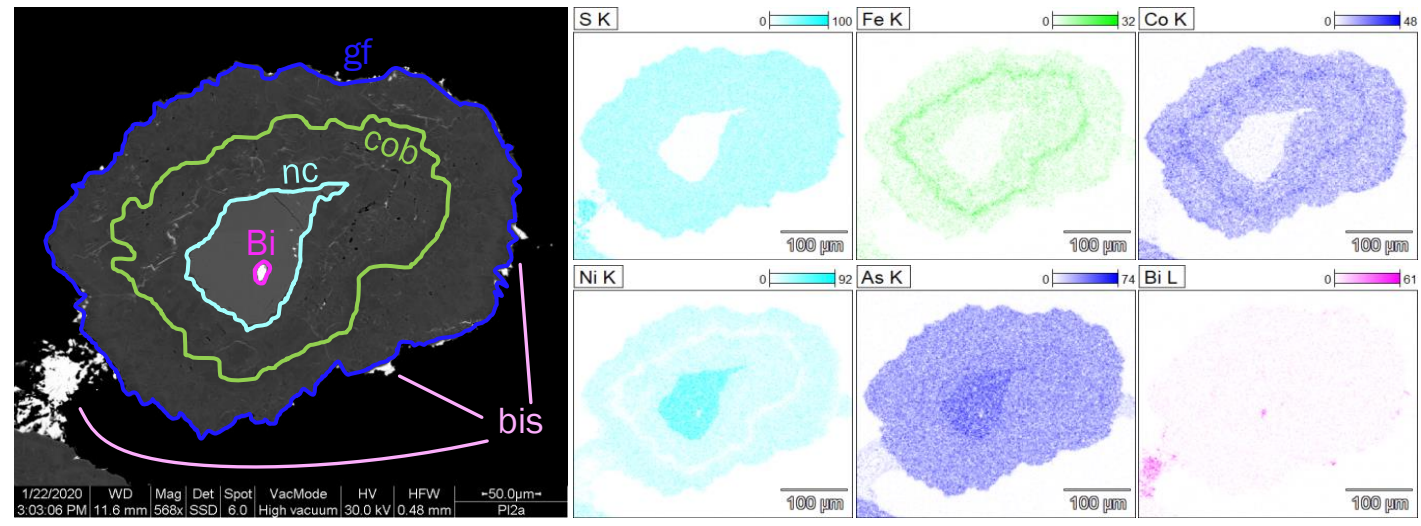
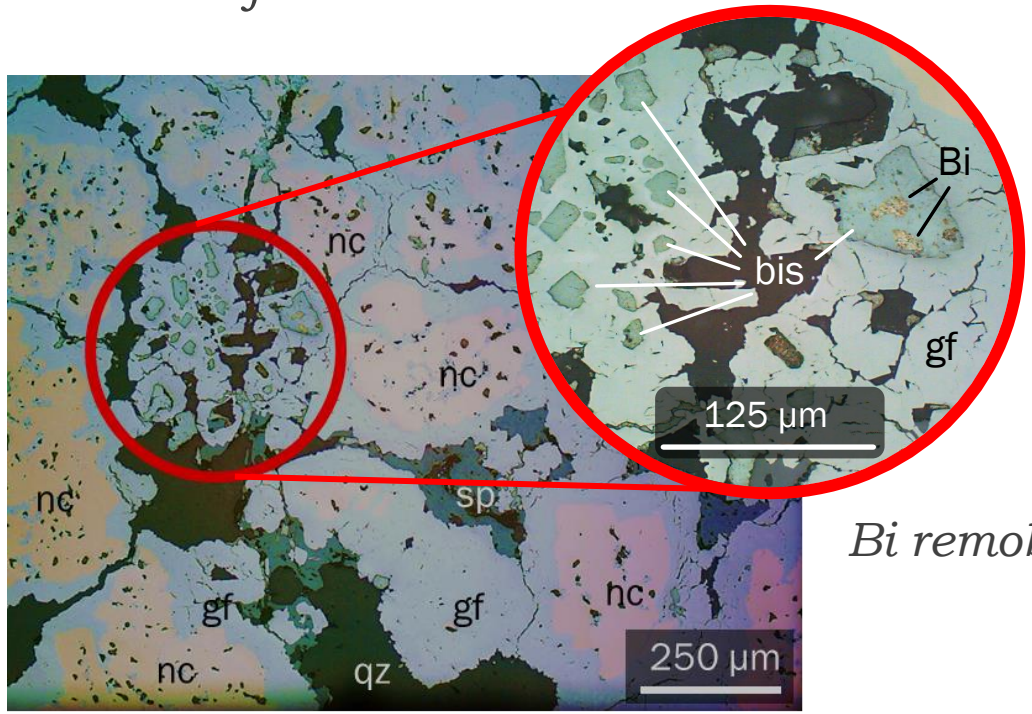


D Five-element (Ni-Co-Bi-As-Ag) veins

LT hydrothermal veins with brecciated-cockade textures. Concentric growths of **Ni-Co-arsenides and -sulfarsenides; siderite-ankerite-dolomite and quartz gangue**. Sulfides are moderately abundant (galena, sphalerite, pyrite, chalcopyrite)



Native Bi with **bismuthinite** replacements recurrently at the core of the Ni-Co-arsenides and -sulfarsenides.



Bi remobilization from the late-Variscan, HT W-Bi-Te-Au veins (Togoro):

- geometry and ore shoots
- breccia fragments (W-rich rutile)
- post-Variscan age of five-element systems of Europe (Erzgebirge/ Krušné Hory; Guilcher et al, 2021)

mod. after Deidda et al, 2011

Conclusions

1

1

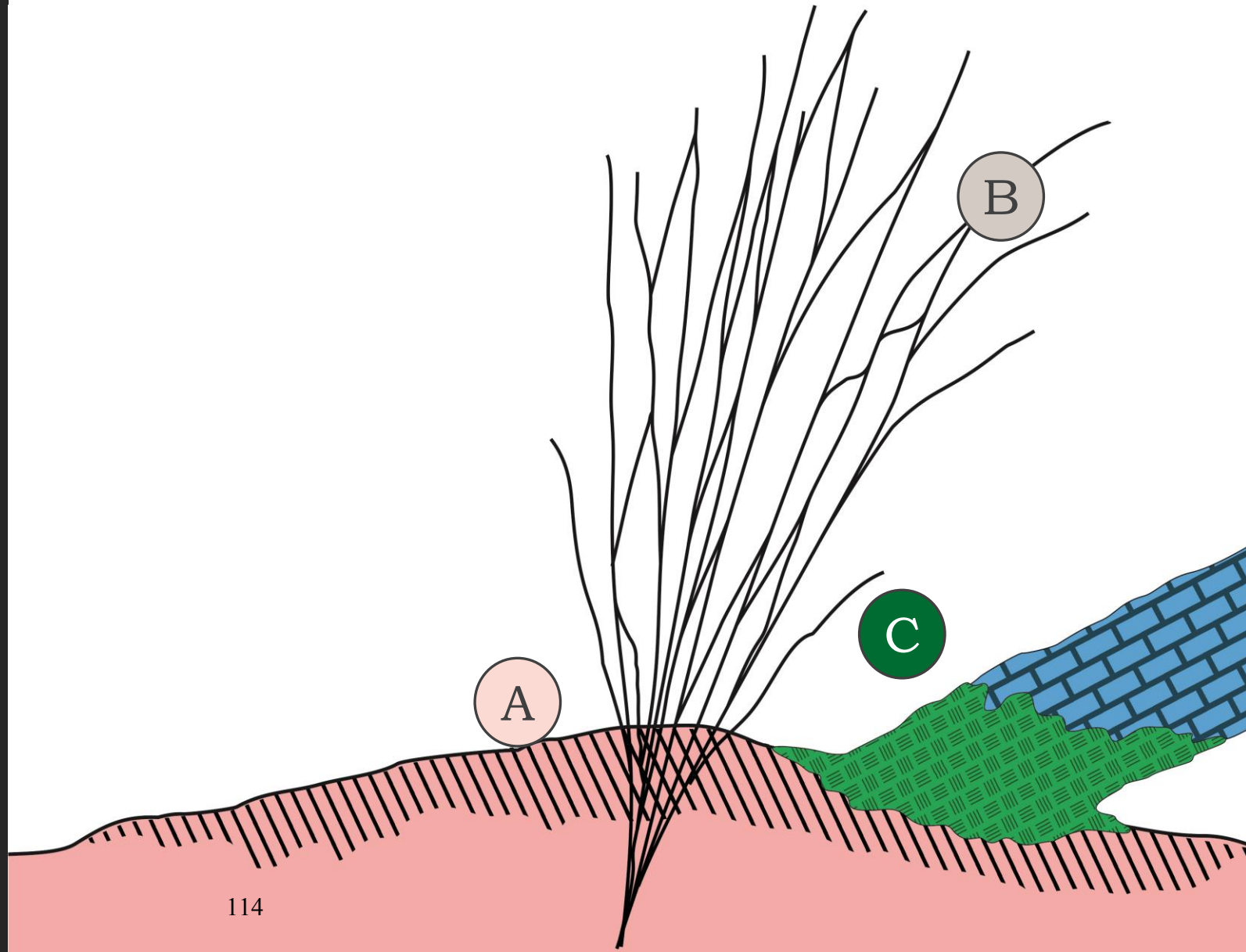
In Sardinia, Bi is more recurrently observed in granite-related deposits.

The late-Variscan granite suite represents the main metallogenic source of bismuth.

Bismuth could serve as a useful marker of granite-related mineralization...

...or as a qualitative tool to evaluate various relationships between granite-related deposits and other systems

The assemblages of Bi-bearing phases reflect local scale formation mechanisms.



Conclusions

2

1

In Sardinia, Bi is more recurrently observed in granite-related deposits.

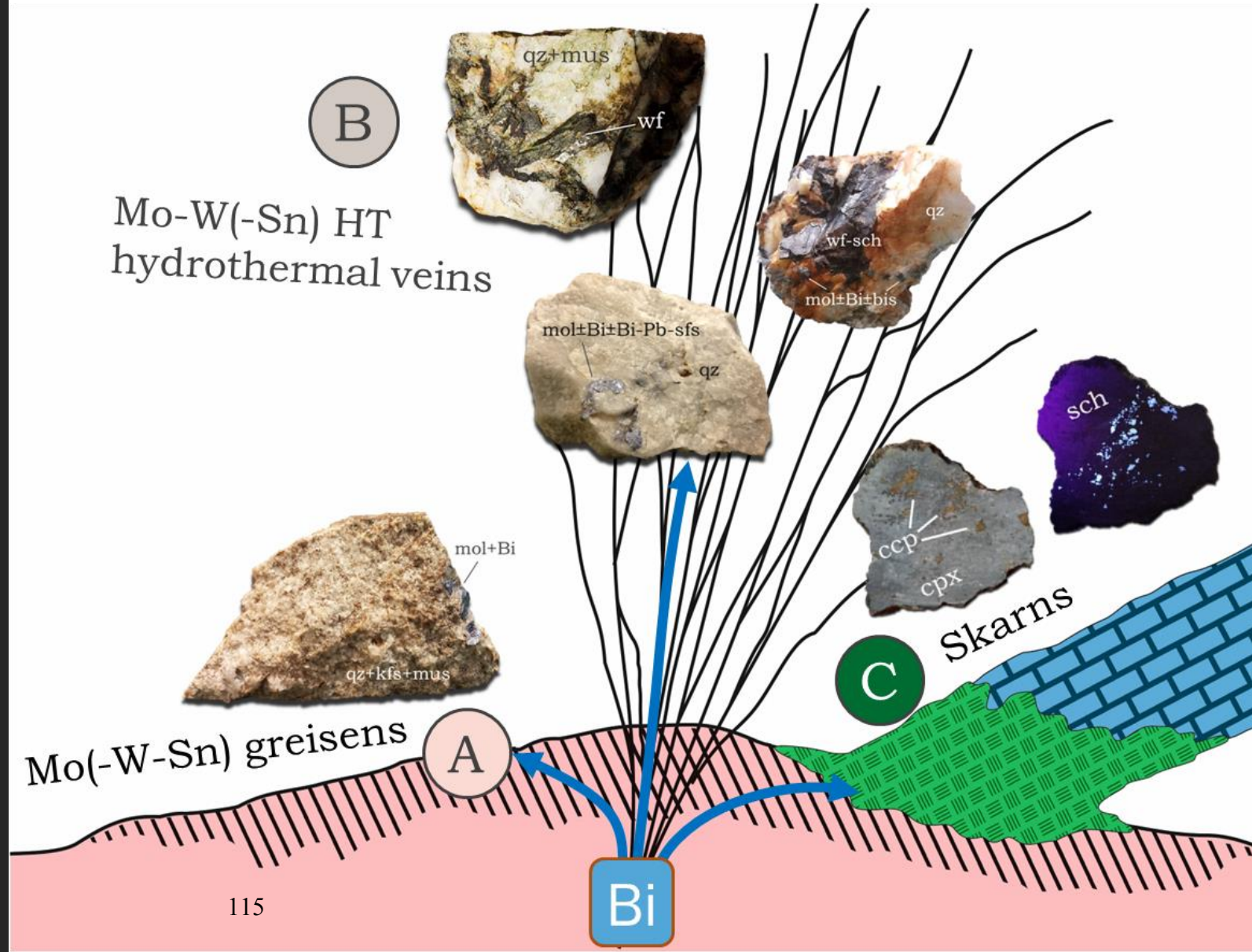
2

The late-Variscan granite suite represents the main metallogenic source of bismuth.

Bismuth could serve as a useful marker of granite-related mineralization...

...or as a qualitative tool to evaluate various relationships between granite-related deposits and other systems

The assemblages of Bi-bearing phases reflect local scale formation mechanisms.



Conclusions

3

1

In Sardinia, Bi is more recurrently observed in granite-related deposits.

2

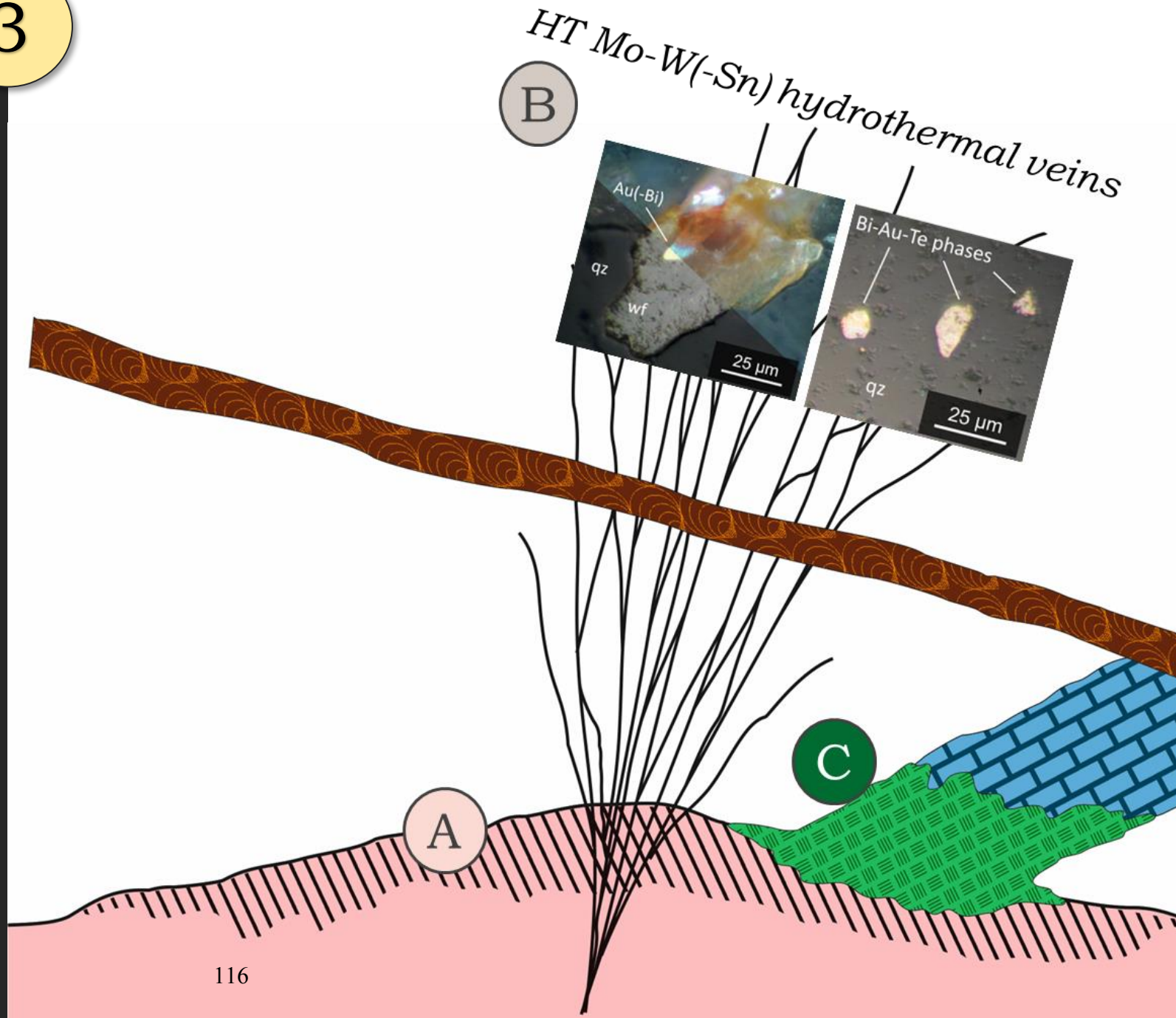
The late-Variscan granite suite represents the main metallogenic source of bismuth.

3

Bismuth could serve as a useful marker of granite-related mineralization...

...or as a qualitative tool to evaluate various relationships between granite-related deposits and other systems

The assemblages of Bi-bearing phases reflect local scale formation mechanisms.



Conclusions

4

1

In Sardinia, Bi is more recurrently observed in granite-related deposits.

2

The late-Variscan granite suite represents the main metallogenic source of bismuth.

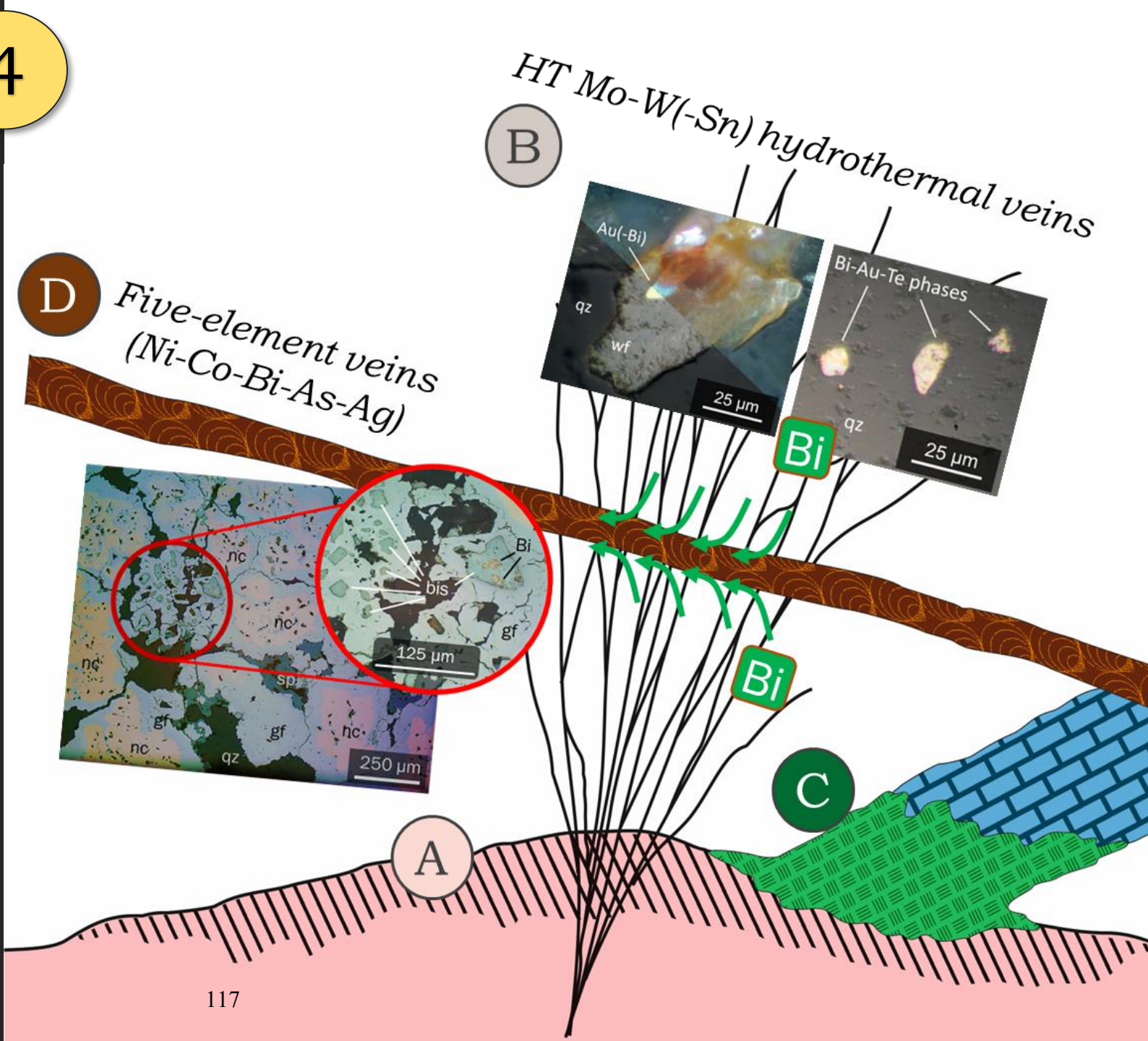
3

Bismuth could serve as a useful marker of granite-related mineralization...

4

...or as a qualitative tool to evaluate various relationships between granite-related deposits and other systems

The assemblages of Bi-bearing phases reflect local scale formation mechanisms.



Conclusions

1

In Sardinia, Bi is more recurrently observed in granite-related deposits.

2

The late-Variscan granite suite represents the main metallogenic source of bismuth.

3

Bismuth could serve as a useful marker of granite-related mineralization...

4

...or as a qualitative tool to evaluate various relationships between granite-related deposits and other systems

5

The assemblages of Bi-bearing phases reflect local scale formation mechanisms.

5

HT Mo-W(-Sn) hydrothermal veins

Less abundant
Cu-Zn-Pb-Fe sulfides

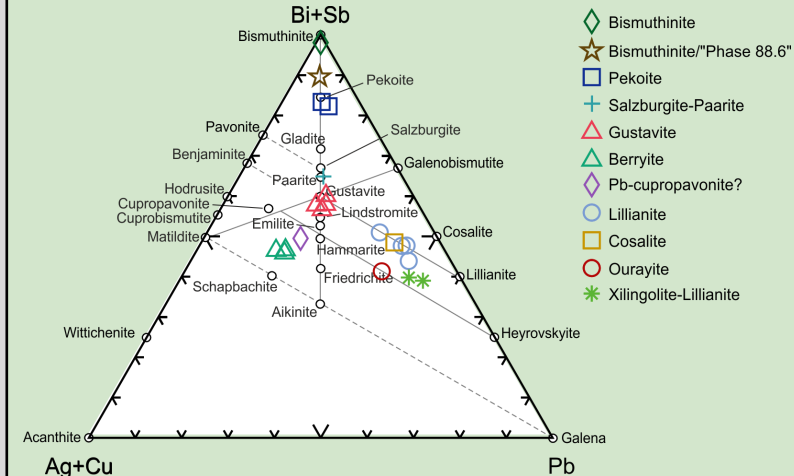
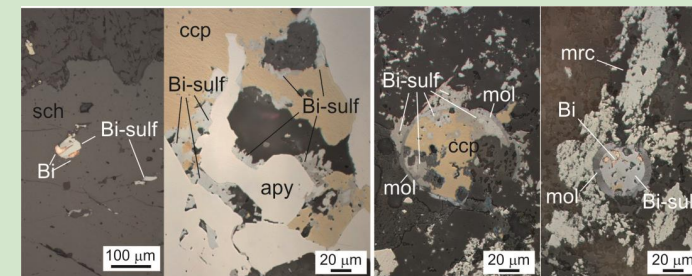
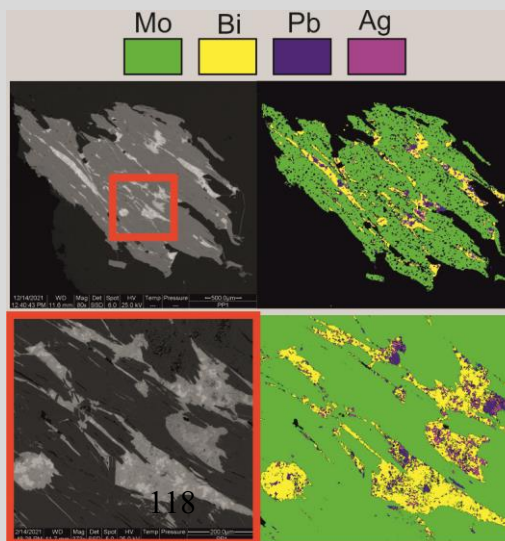
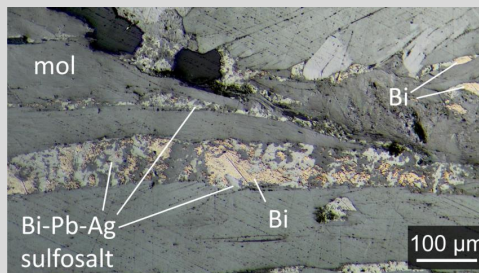
VS

Skarn deposits

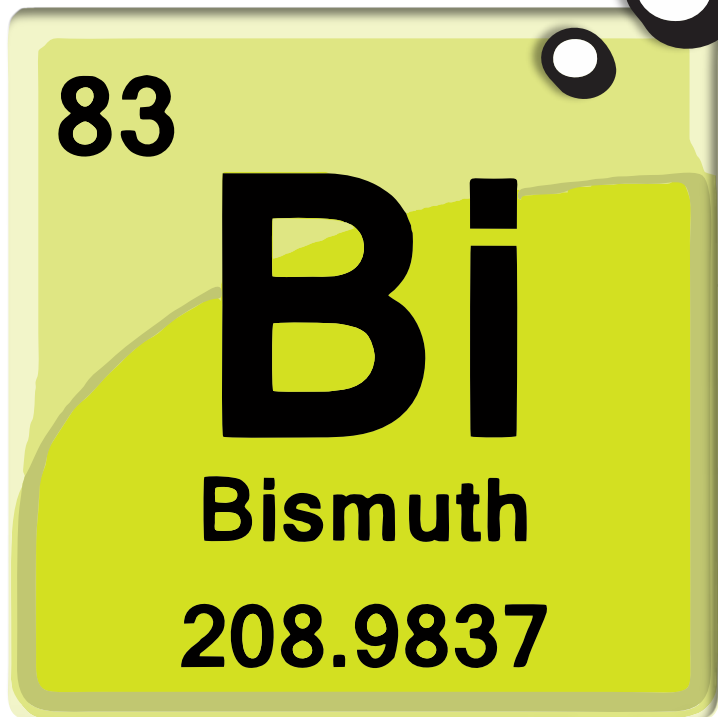
Abundant
Cu-Zn-Pb-Fe sulfides

Apparently more limited array of native Bi, bismuthinite and Bi-Pb-Ag-sulfosalts

Complex intergrowths of native Bi, bismuthinite and Bi-Pb-Ag-Cu-sulfosalts



Thanks for your
attention!



APPENDIX III

Towards the definition of a Sn-W-Mo late Variscan skarn-system in Southwestern Sardinia: evidence from key-areas in the Sulcis-Iglesiente district

Matteo L. Deidda¹, Giovanni B. De Giudici¹, Dario Fancello¹, Lorenzo
Tavazzani² and Kalin Kouzmanov²

¹ Department of Chemical and Geological Sciences, University of Cagliari, 09042, Monserrato (CA), Italy

² ETH Zürich, Department of Earth Sciences, Institute for Geochemistry and Petrology, Zürich, Switzerland

³ Department of Earth Sciences, University of Geneva, CH-1205 Geneva, Switzerland

Submitted 4 May 2022

Presented at SGI-SIMP, Geoscience for a Sustainable Future, Torino, 19-21 September 2022

Towards the definition of a Sn-W-Mo late Variscan skarn-system in Southwestern Sardinia: evidence from key-areas in the Sulcis-Iglesiente district

Deidda M.L.*¹, De Giudici G.B.¹, Fancello D.¹, Idini A.¹, Tavazzani L.² & Kouzmanov K.³

¹ Dipartimento di Scienze Chimiche e Geologiche, Università di Cagliari. ² Institute of Geochemistry and Petrology, ETH Zürich (Switzerland). ³ Department of Earth Sciences, University of Geneva (Switzerland).

Corresponding author e-mail: deiddam.geo@gmail.com

Keywords: skarn, Sn-W-Mo, Variscan.

The SW portion of Sardinia (Sulcis-Iglesiente district) hosts many skarn orebodies, spatially and genetically associated to a suite of late-Variscan (289-286 Ma) ilmenite-series granites with a Sn-W-Mo metallogenic signature (Naitza et al., 2017). In order to frame different skarn-forming processes under a regional-scale metallogenic model, three key-areas (the old mines of Perda Niedda, Monte Tamara and Rosas) have been studied. Hosted in the same, variably metasomatized Cambrian carbonate unit (Gonnesa Fm.), these orebodies show a distinctive ore mineral assemblage, including magnetite, Zn-As-Pb-Cu-Fe sulfides - in part referable to pre-existent concentrations in the host rocks (Aponte et al., 1988) - and, as markers of the magmatic source, variable proportions of cassiterite, scheelite, molybdenite and Bi-phases.

The Perda Niedda skarn represents the proximal member of the system. Among prograde and retrograde silicates, garnet and axinite are Sn-rich; hydrothermal alteration of columbo-tantalite-bearing garnet resulted in a magnetite-fluorite-amphibole-chlorite assemblage with abundant cassiterite. Cassiterite and sphalerite are In-rich; magnetite is W-bearing.

Mineralization at Monte Tamara belong to a complex skarn system at variable distance from the causative intrusion. The ores include: 1. a proximal clinopyroxene-garnet-epidote skarn with magnetite, scheelite, cassiterite-stannite, molybdenite, Bi-Pb-Cu-Ag sulfosalts and Zn-Pb-Cu-Fe sulfides (San Pietro); 2. a relatively distal hydrothermal scheelite-arsenopyrite-sphalerite vein with quartz-carbonate gangue (Sinibidraxiu). Here, scheelite prevails over cassiterite (also In-bearing); garnet and epidote are also Sn-enriched.

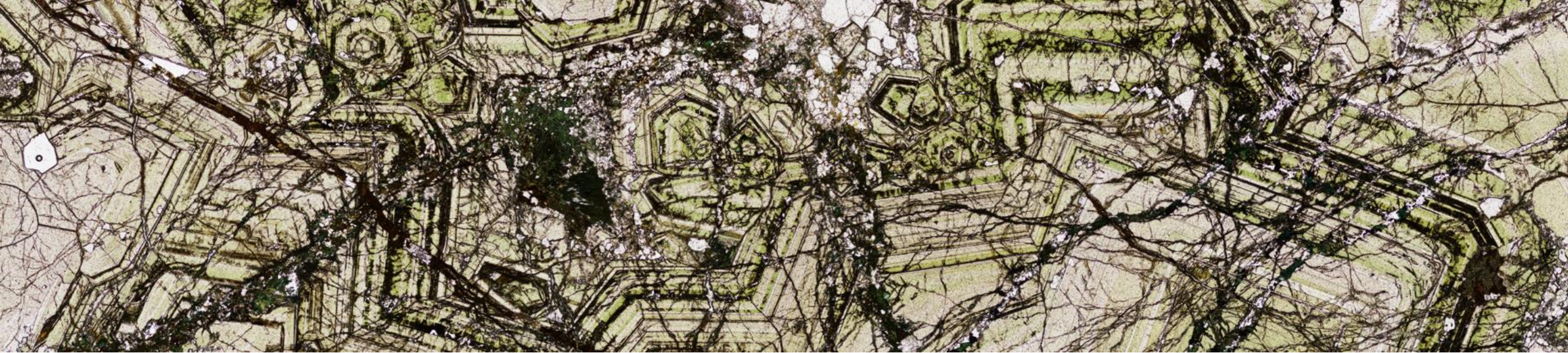
The Rosas orebodies represent a more distal part of the system. Large-scale fluid circulation exploited a series of structures at the tectonized footwall of the Rosas Shear Zone (Cocco et al., 2022); mineralization mainly occurred in tectonic slices of Cambrian carbonates. Therefore, garnet is subordinate to Mn-rich clinopyroxene and Sn-poor epidote. The main ores consist of Zn-Pb-Cu-Fe sulfides and locally Ag-sulfides. Cassiterite-magnetite-fluorite seams are rare, Bi-phases very rare and scheelite undetected so far.

In conclusion, skarn orebodies of SW Sardinia can be considered as parts of a regional-scale metallogenic system, related to a specific late-Variscan intrusive suite and developed in the same metasomatized host rocks. This implies that different features between skarn orebodies may reflect local factors (e.g., distality, structural asset, chemical controls related to facies variability in host rocks) within a single skarn system. Based on these evidences, we argue that an updated model for skarn mineralization of SW Sardinia could support further W-Sn-Mo mineral exploration in the future, not only in the deeper parts of these key-areas but also in the many, recurrent and promising skarn occurrences of the whole district.

Aponte F., Balassone G., Boni M., Costamagna L. & Di Maio G. (1988) - Variscan Skarn Ores in South-West Sardinia: their relationships with Cambro-Ordovician stratabound deposits. *Rend. Soc. Ital. Mineral. Petrol.*, 43, 445-462.

Cocco F., Attardi A., Deidda M.L., Fancello D., Funedda A. & Naitza S. (2022) - Passive Structural Control on Skarn Mineralization Localization: A Case Study from the Variscan Rosas Shear Zone (SW Sardinia, Italy). *Minerals*, 12, 272.

Naitza S., Conte A.M., Cuccuru S., Oggiano G., Secchi F. & Tecce F. (2017) - A Late Variscan tin province associated to the ilmenite-series granites of the Sardinian Batholith (Italy): The Sn and Mo mineralisation around the Monte Linas ferroan granite. *Ore Geol. Rev.*, 80, 1259-1278.



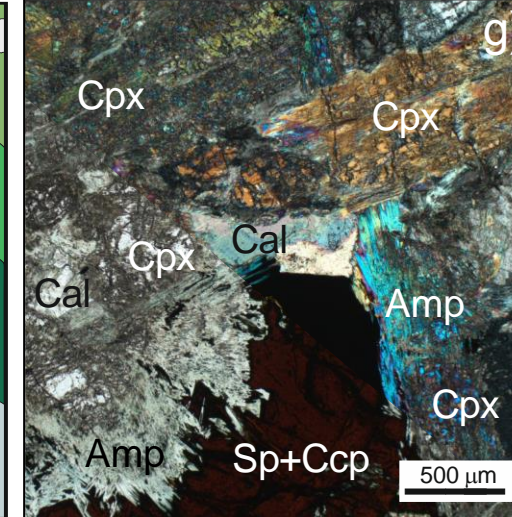
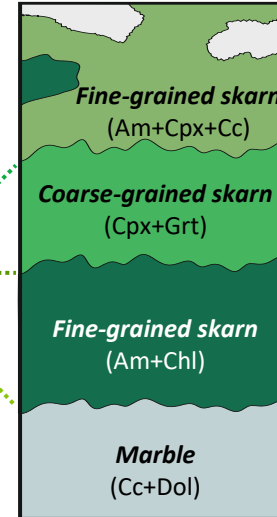
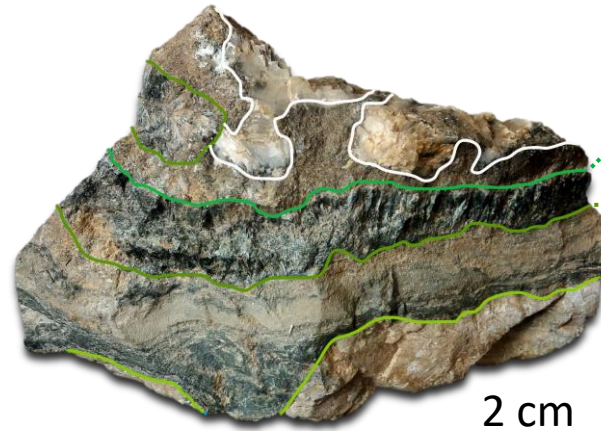
***Towards the definition of a Sn-W-Mo late Variscan skarn-system
in Southwestern Sardinia:
evidence from key-areas in the Sulcis-Iglesiente district***

Deidda M.L.* , De Giudici G.B., Fancello D., Idini A., Tavazzani L. & Kouzmanov K.



What is a skarn?

- Metasomatism
- Magmatic-hydrothermal fluids
- Reactive protoliths
- Calcsilicate minerals
- Decreasing temperatures
- Polyphase
- Overprinting textures (*prograde vs «retrograde»*)
- Zoning patterns
- Mineralization

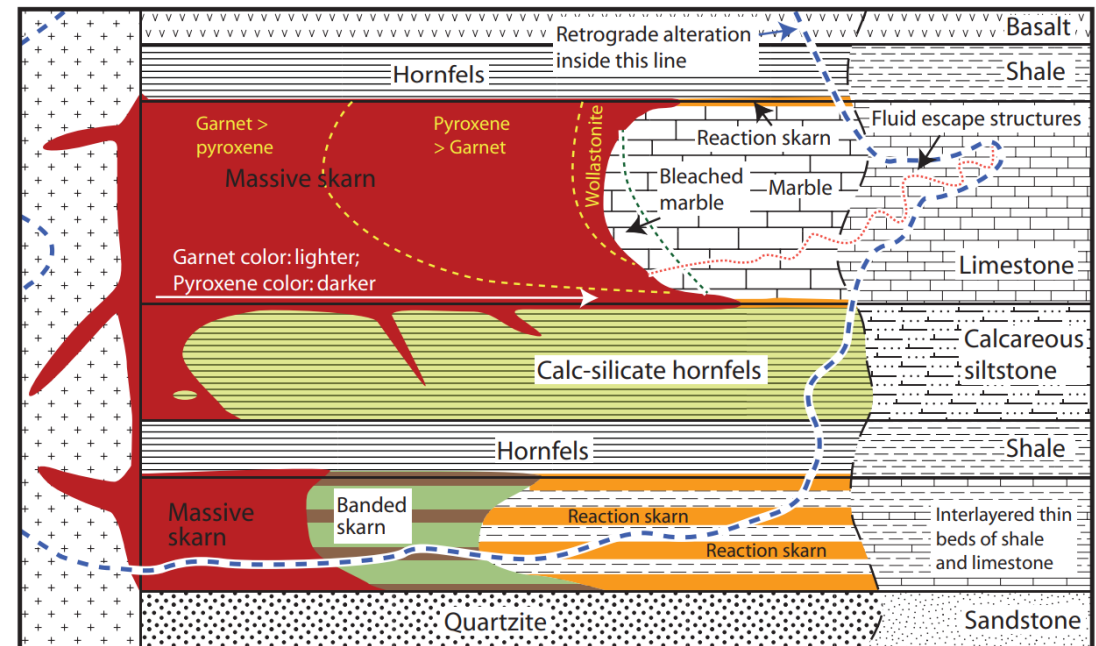
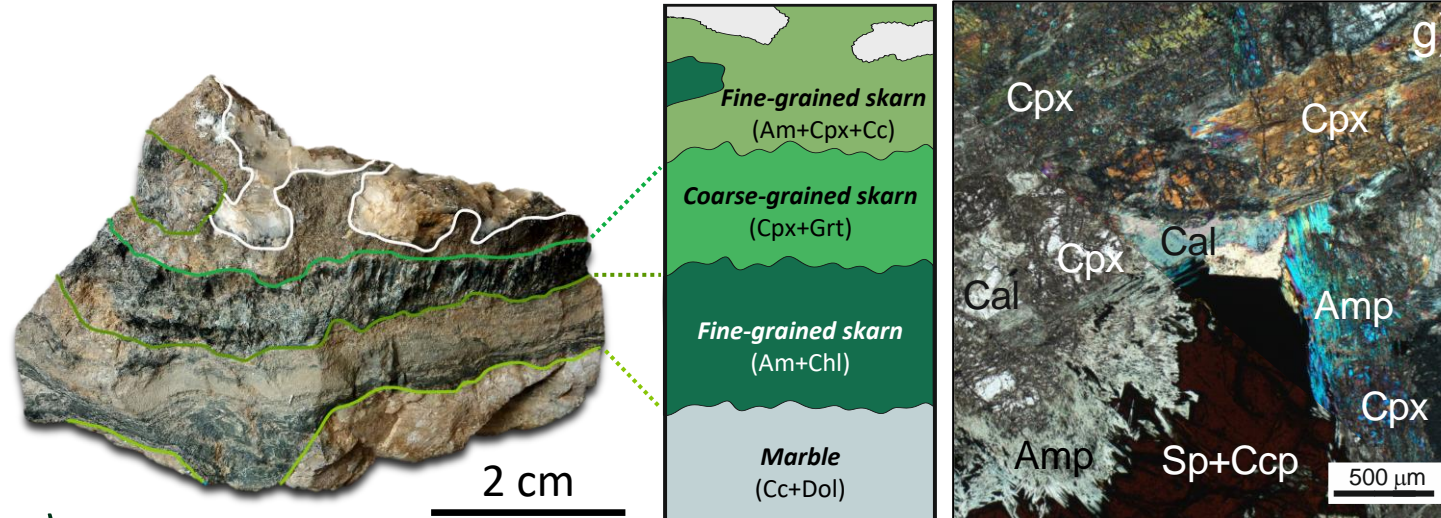


What is a skarn?

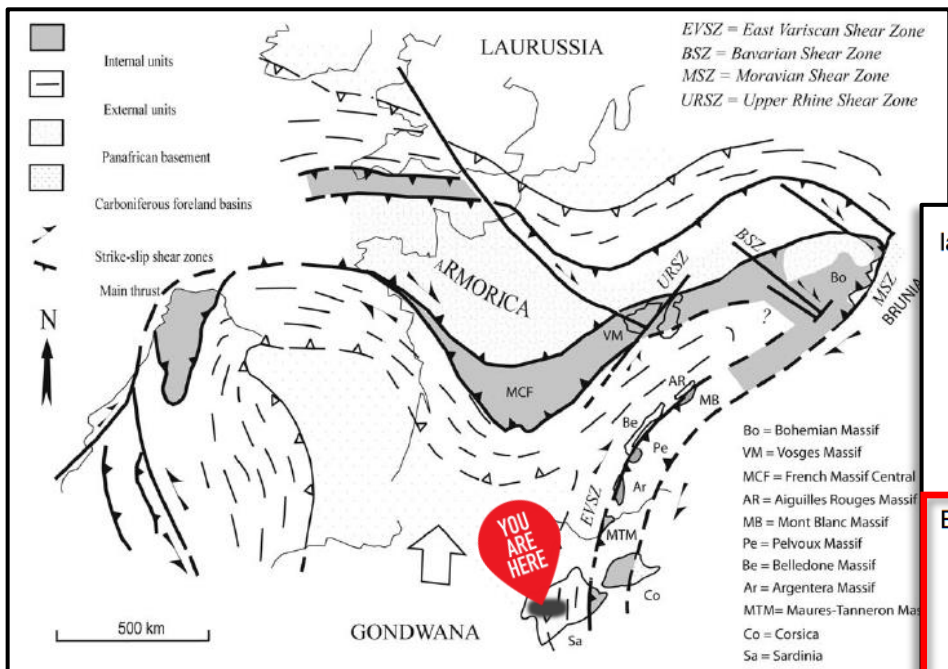
- Metasomatism
- Magmatic-hydrothermal fluids
- Reactive protoliths
- Calcsilicate minerals
- Decreasing temperatures
- Polyphase
- Overprinting textures (*prograde vs «retrograde»*)
- Zoning patterns
- Mineralization

Why are skarn deposits important?

- One of the main sources of W-Sn
- Small sized but high grades
- Zoning patterns are useful prospection guides

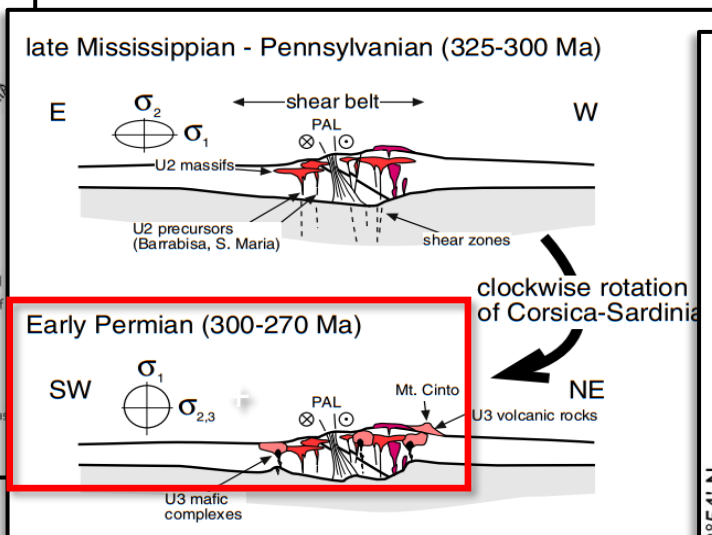


Chang et al, 2019



Corsini & Rolland, 2009

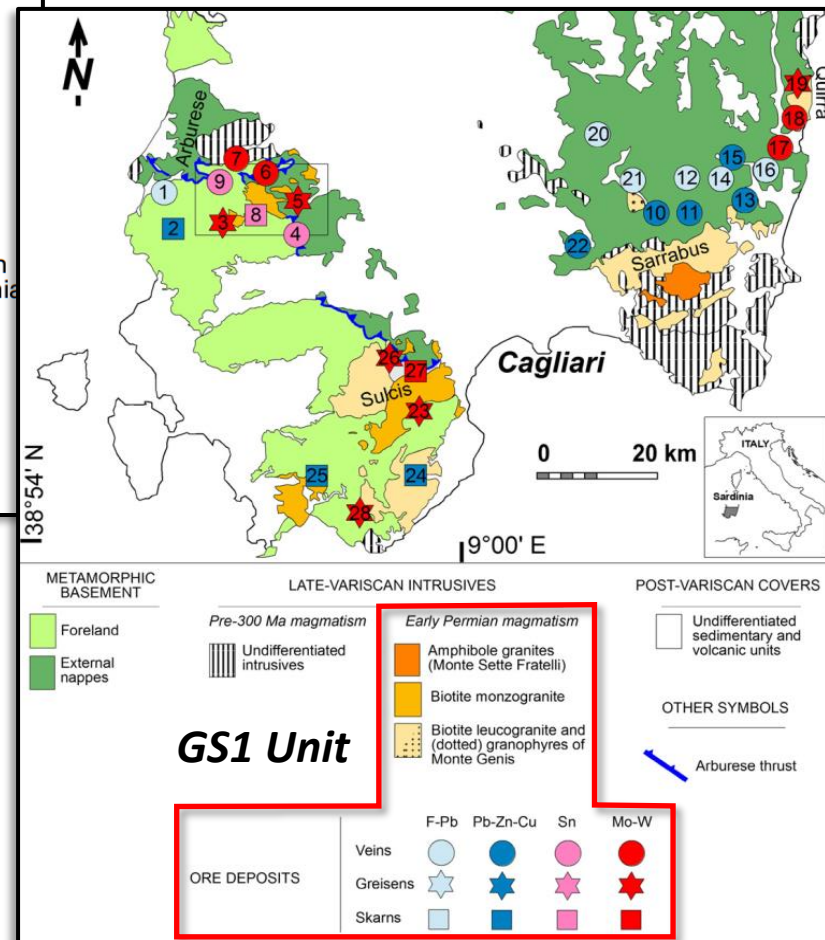
A composite batholith (the CSB) emplaced during late-Variscan times, producing contact metamorphism on the pre-Variscan low-grade metasedimentary units.



Casini et al, 2015

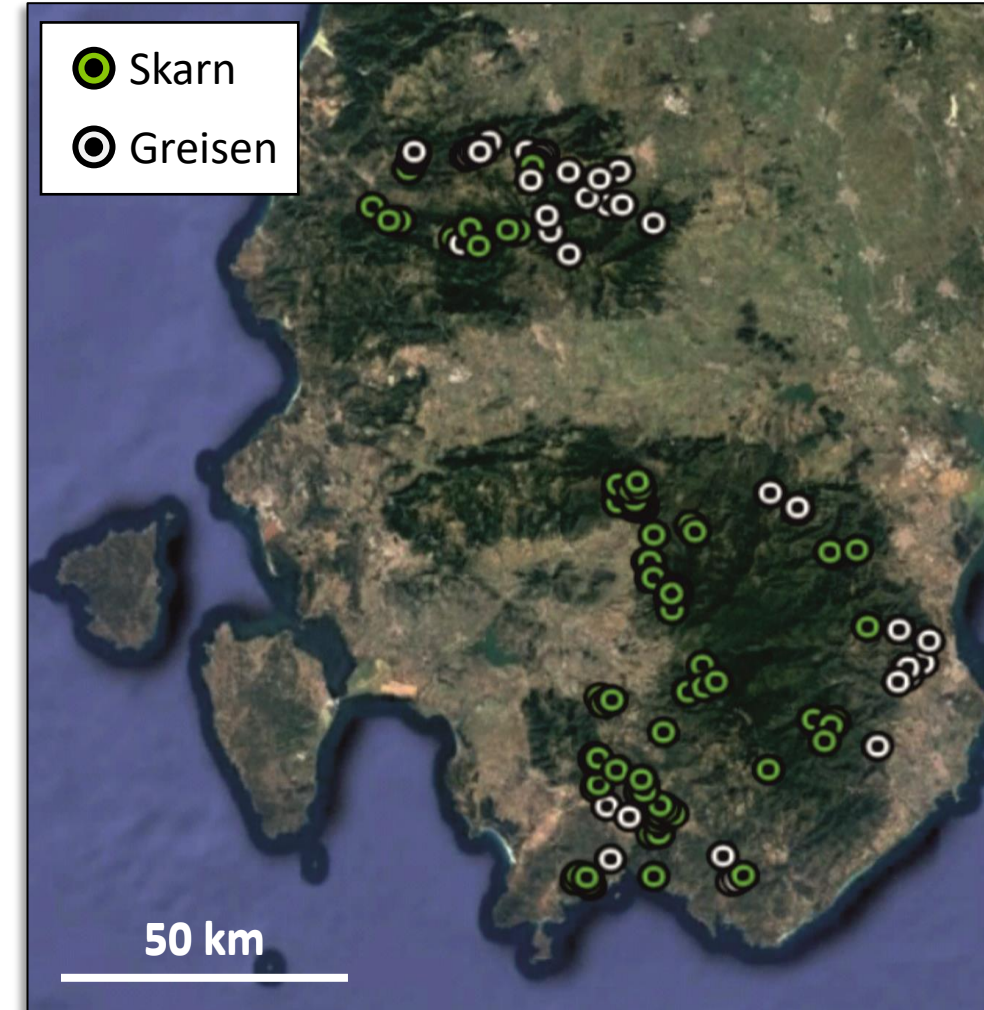
Granites of the GS1 unit (289-286 Ma) have been recognized to be responsible for several W-Sn-Mo mineralization in SW Sardinia, including greisen, skarns and hydrothermal veins (Naitza et al, 2017).

Naitza et al, 2017



Where to target for further W-Sn mineral prospecting in SW Sardinia?

Understanding skarns within a unitary regional-scale metallogenic system is essential.



Where to target for further W-Sn mineral prospecting in SW Sardinia?

Understanding skarns within a single regional scale metallogenic system is essential.

3 key-areas

1. Oridda
2. Monte Tamara
3. Rosas

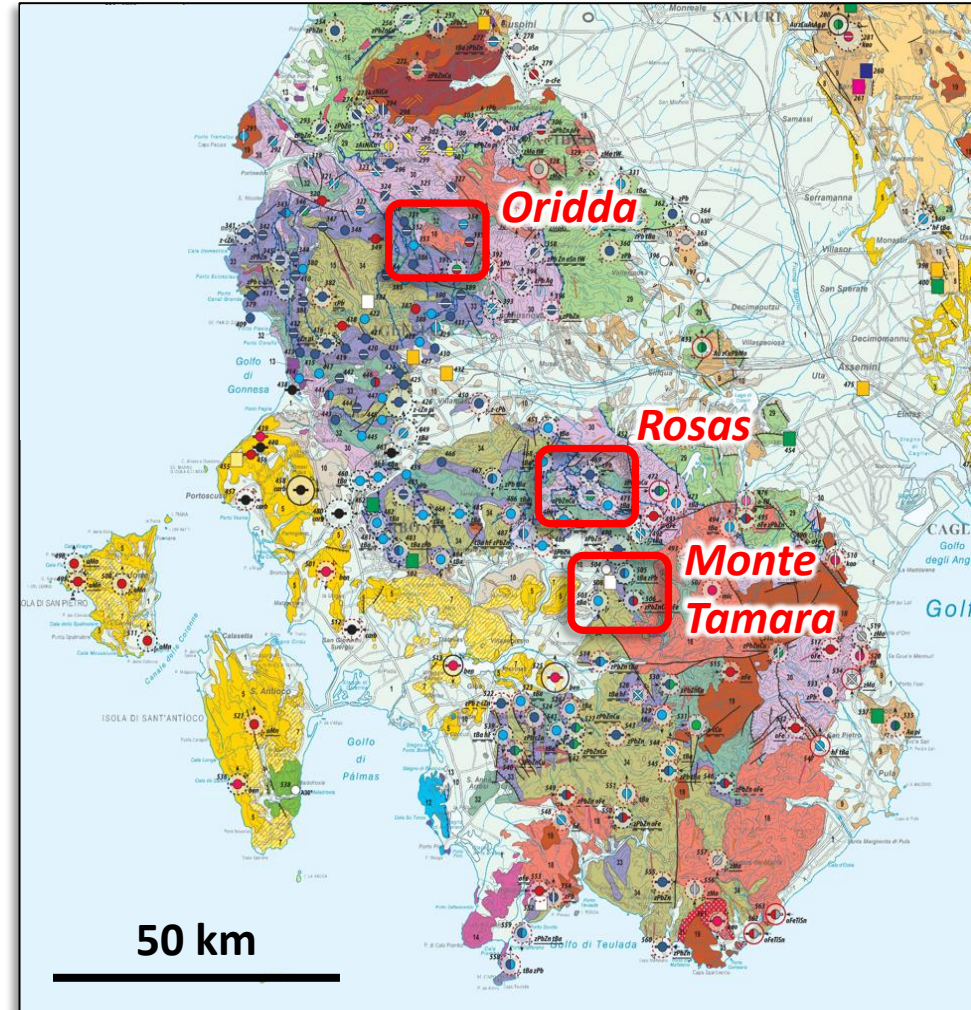
Same Protoliths (Cambrian limestones)

Same causative intrusive suite (GS1)

Comparable skarn and ore minerals

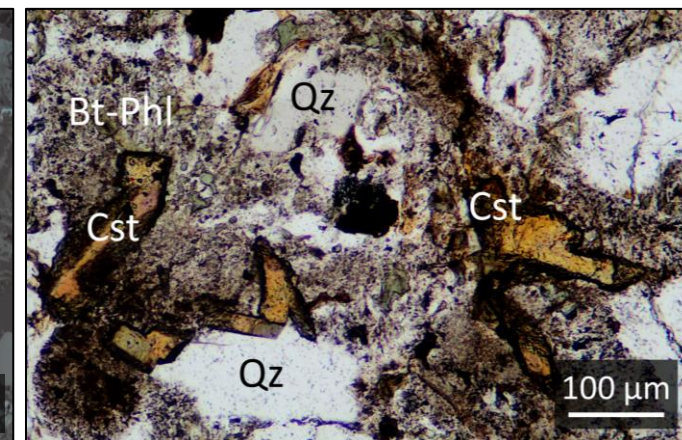
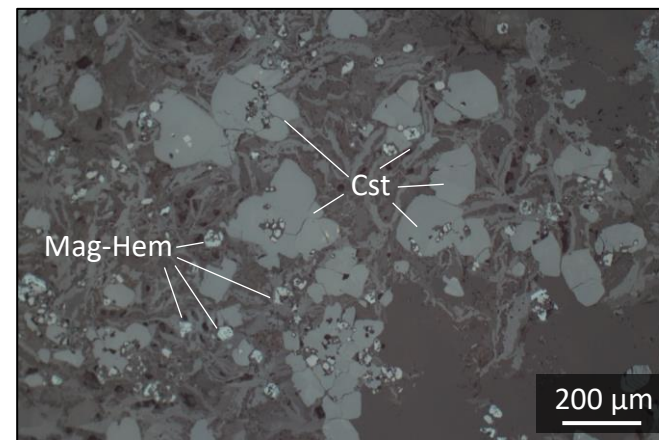
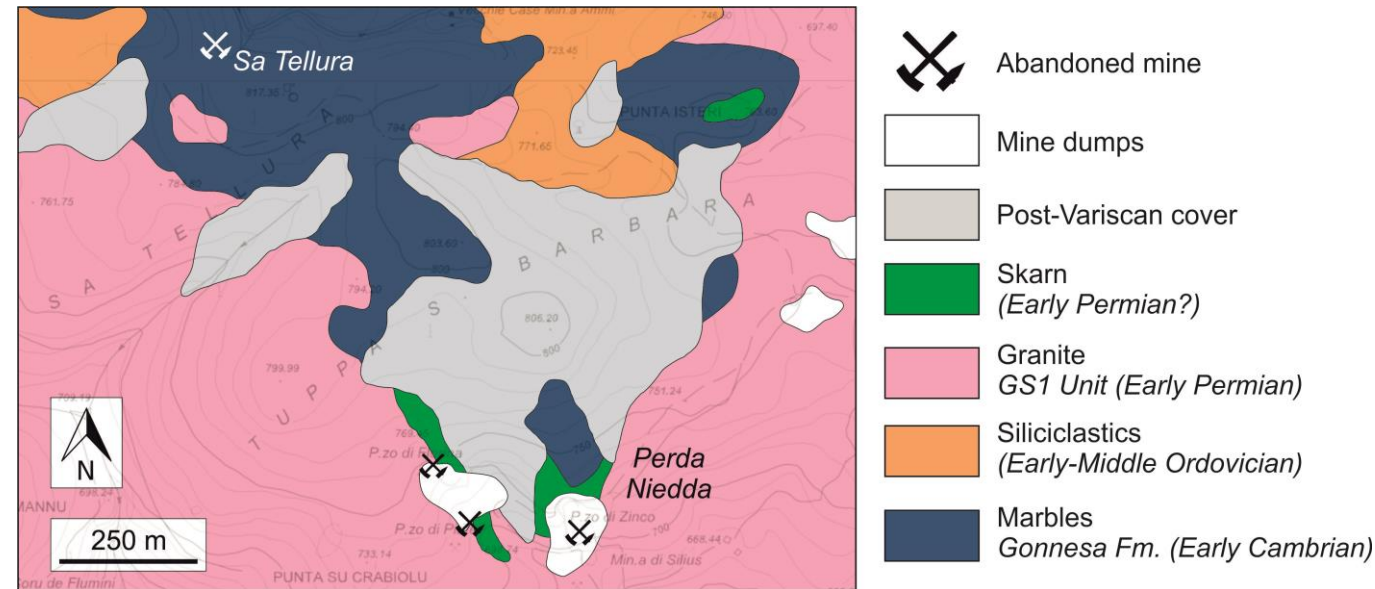
Same index minerals (e.g. cassiterite and/or scheelite)

Different structural context



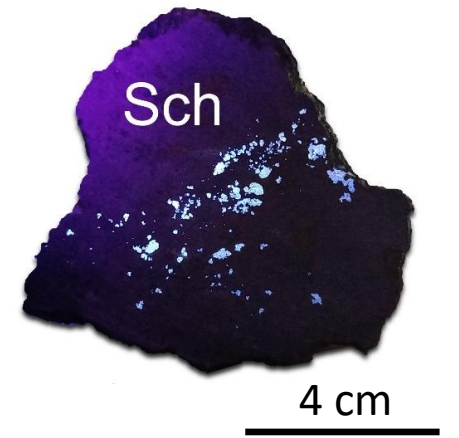
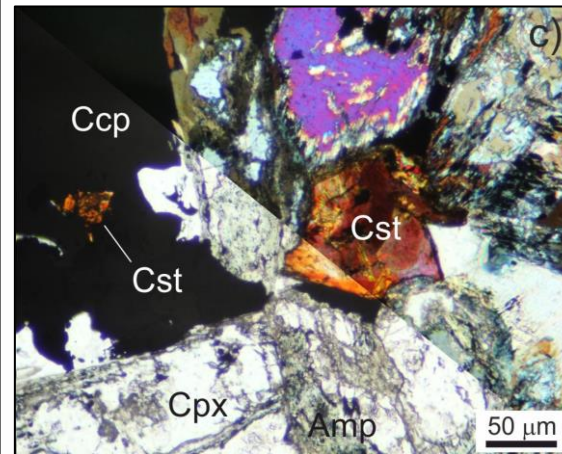
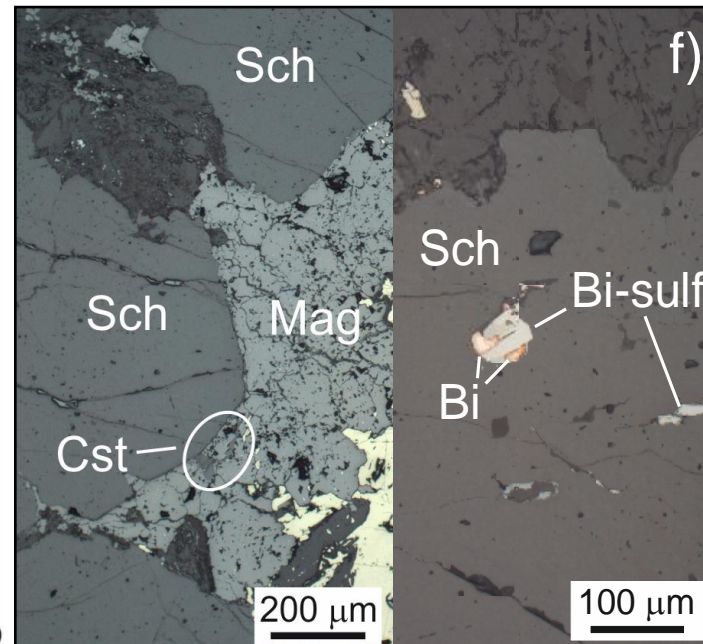
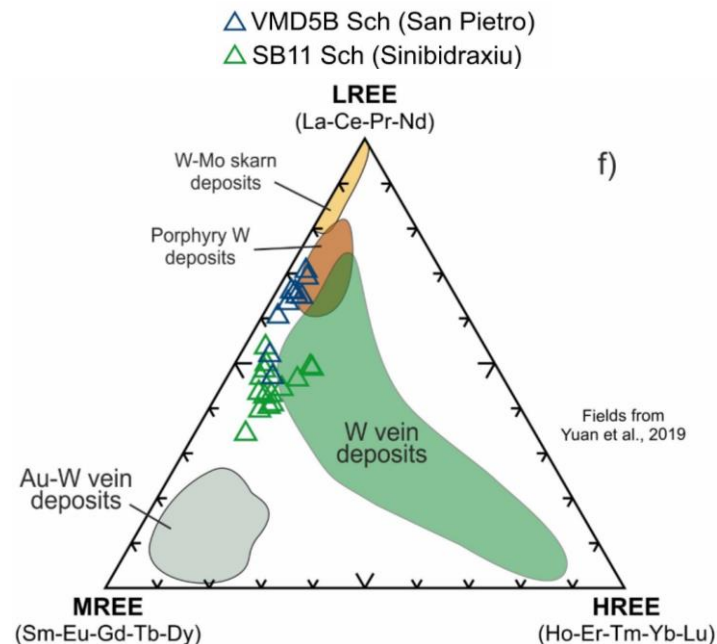
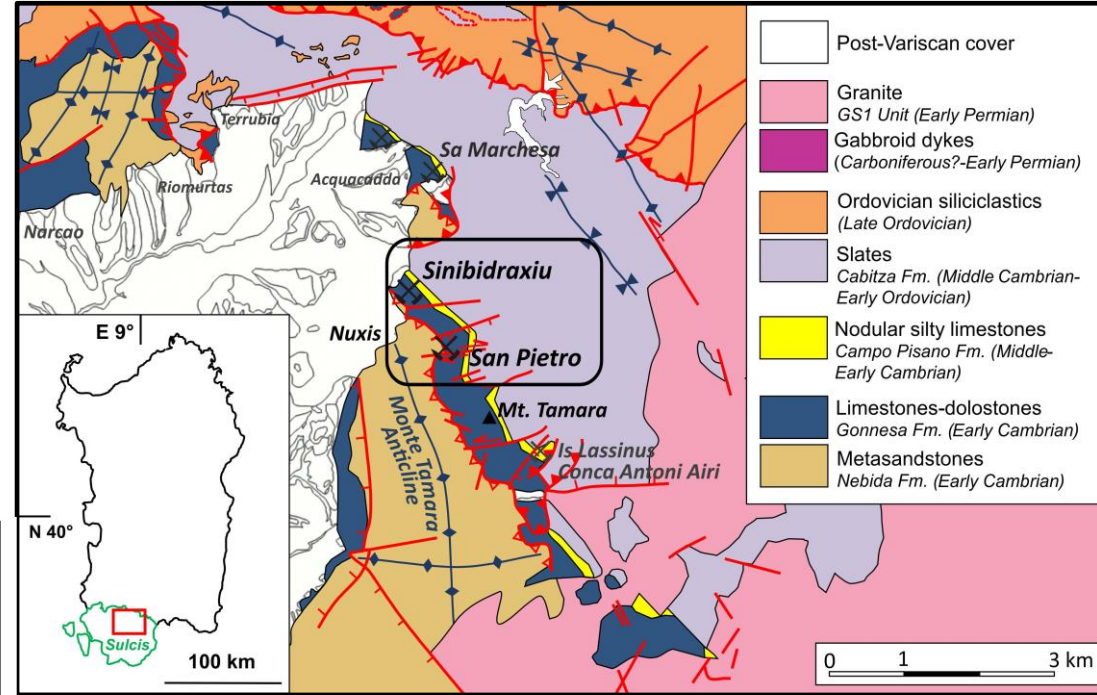
Key area #1: Oridda

- Sn-bearing Fe-Zn skarns (Perda Niedda) and satellite orebodies (Sa Tellura)
- Exposed contact with GS1 granites
- Endoskarn and exoskarn
- Garnet > clinopyroxene
- Magnetite, fluorite, sphalerite, **cassiterite**



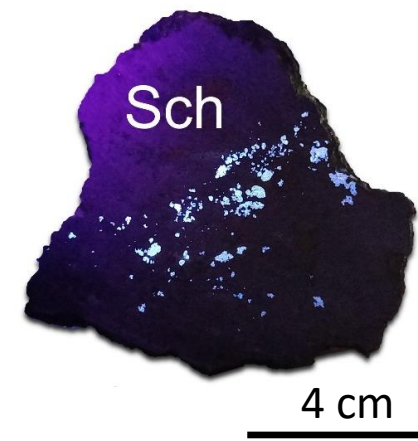
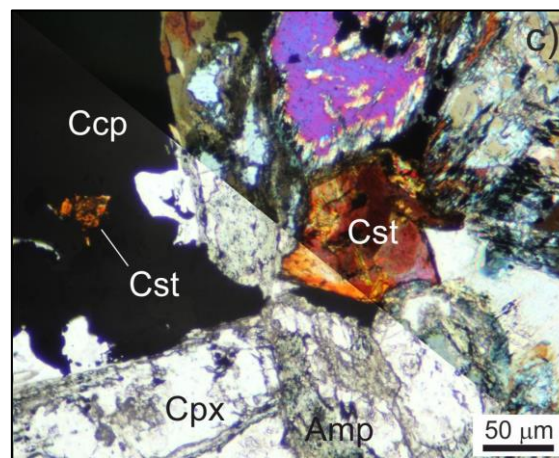
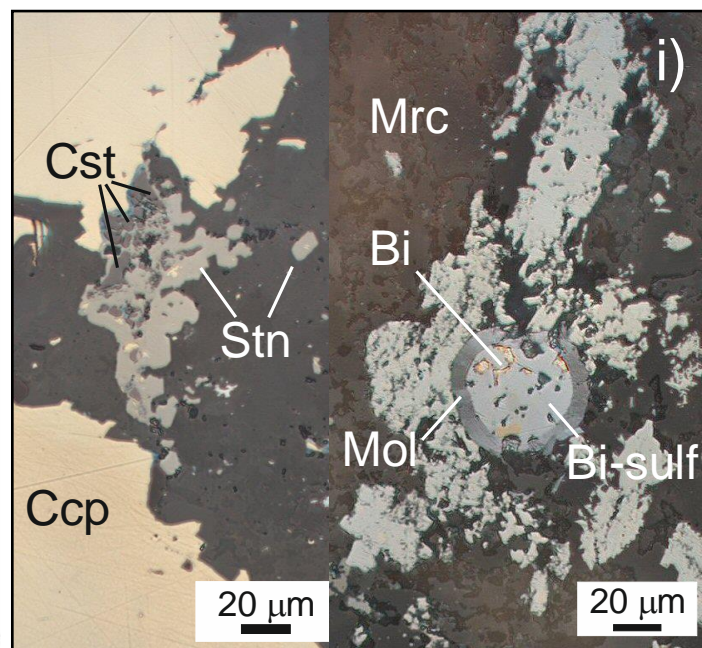
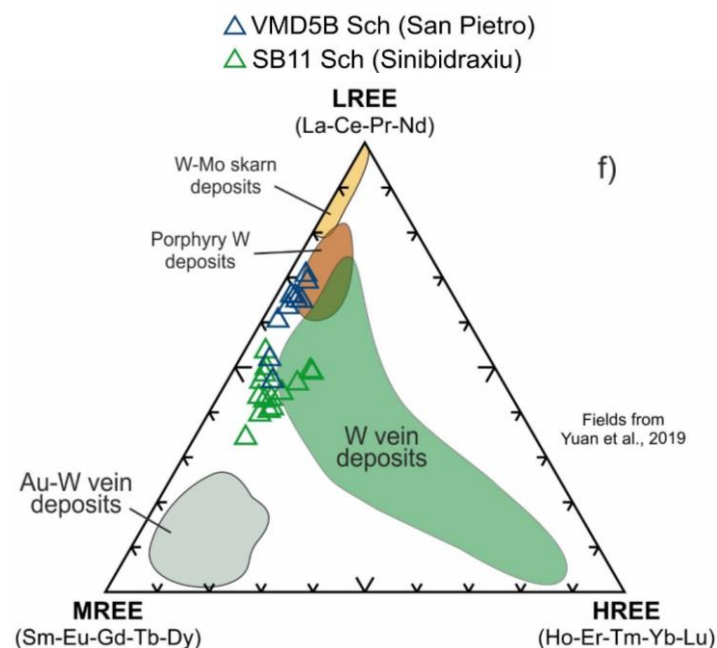
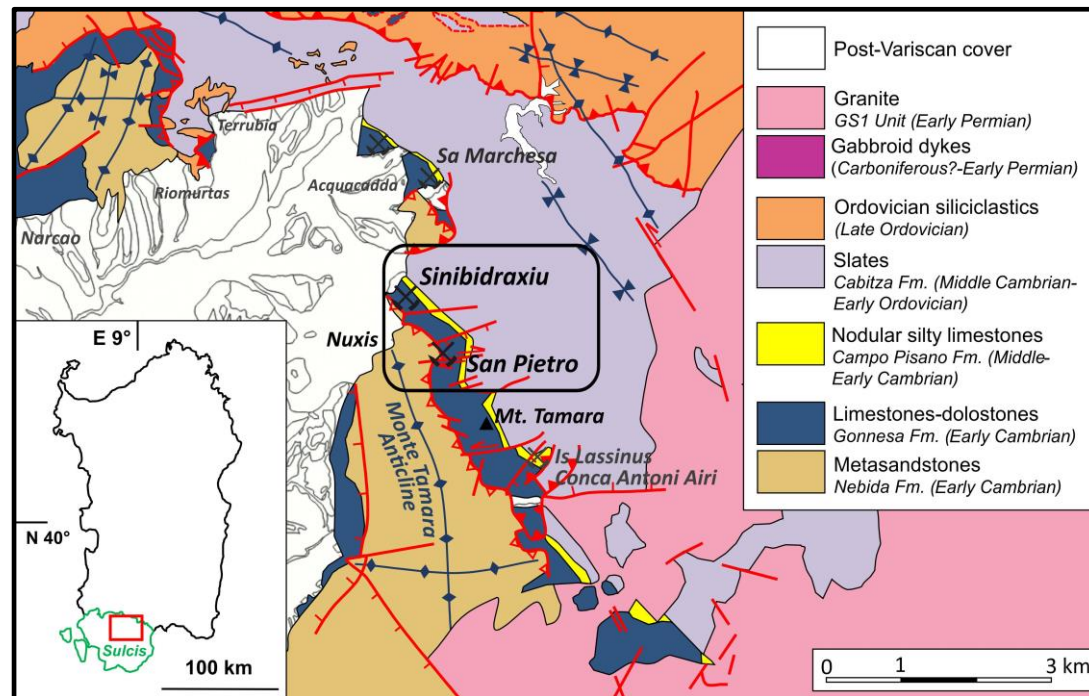
Key area #2: Monte Tamara

- W-bearing Zn-Pb-Cu-Fe skarn orebodies
- Contact with GS1 not exposed
- **Clinopyroxene \geq garnet**
- Complex ore mineral assemblage
- Sphalerite, galena, chalcopyrite, magnetite, **scheelite**, **cassiterite**, **Bi-phases**, **stannite**, **molybdenite**



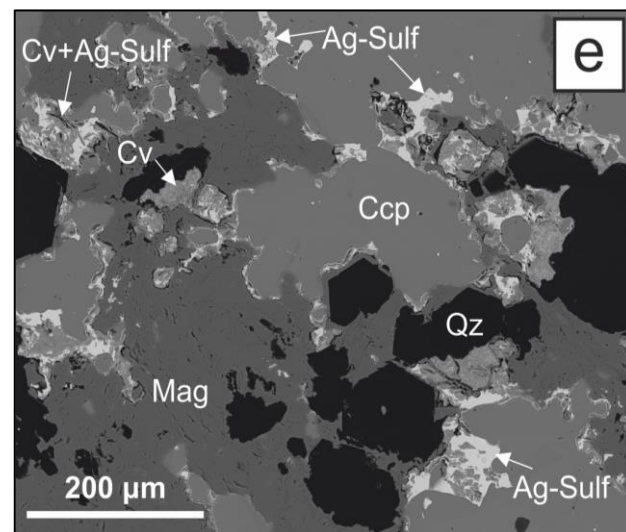
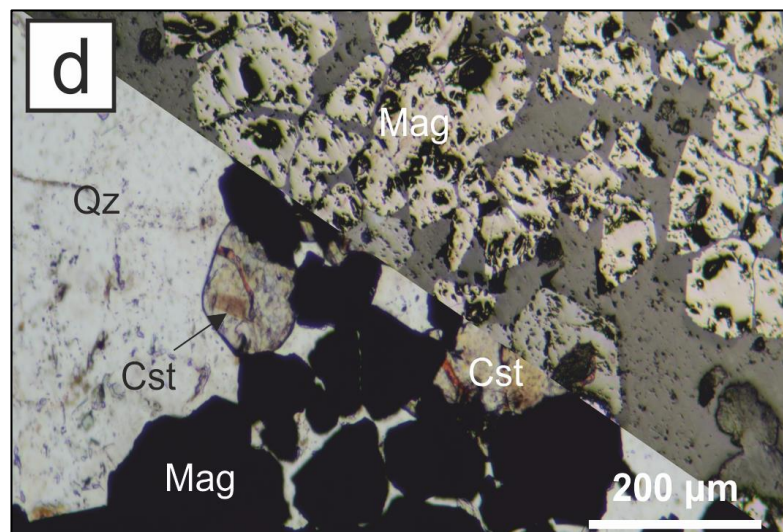
Key area #2: Monte Tamara

- W-bearing Zn-Pb-Cu-Fe skarn orebodies
- Contact with GS1 not exposed
- **Clinopyroxene** \geq garnet
- Complex ore mineral assemblage
- Sphalerite, galena, chalcopyrite, magnetite, **scheelite**, **cassiterite**, **Bi-phases**, **stannite**, **molybdenite**

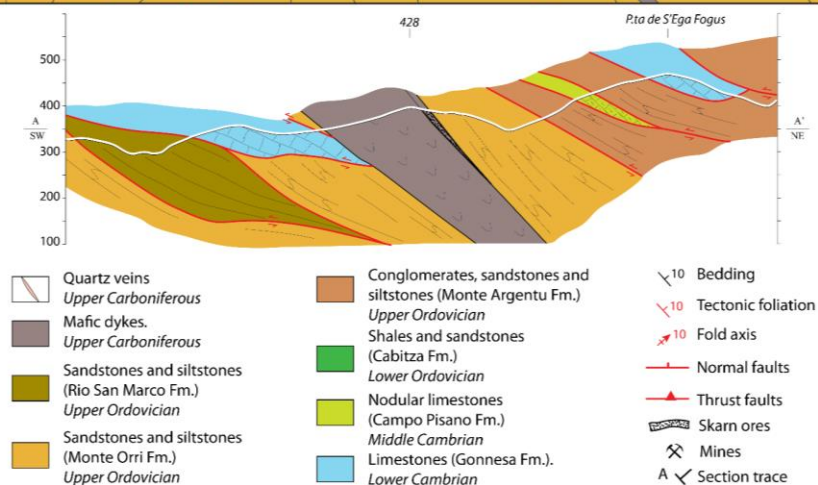
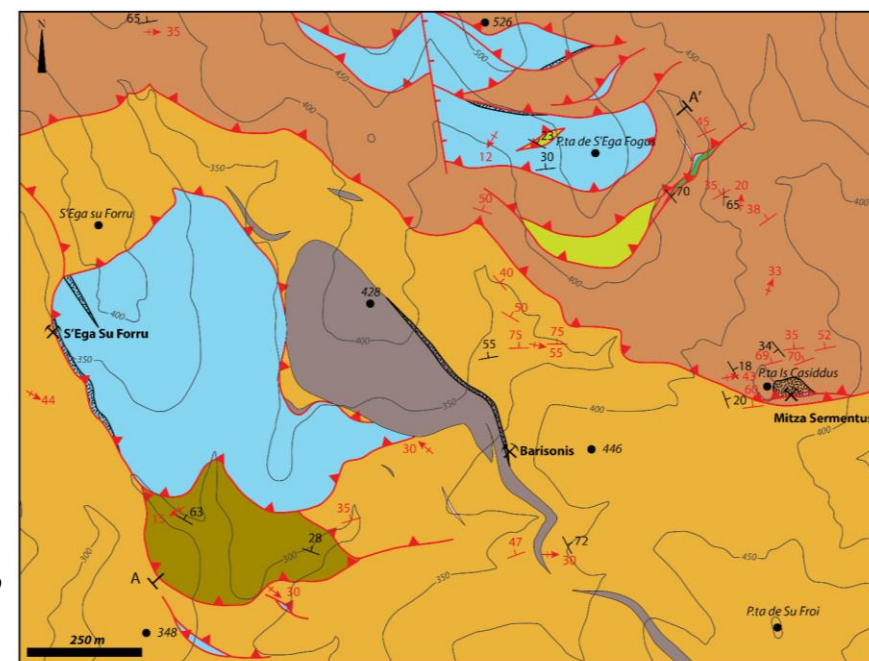


Key area #3: Rosas

- Skarns along a shear zone
- Passive structural control
- Contact with GS1 granites **not exposed**
- **Clinopyroxene > garnet**
- **Prevalence of Zn-Pb-Cu-Fe(-Ag) sulfides**; subordinate magnetite and rare cassiterite



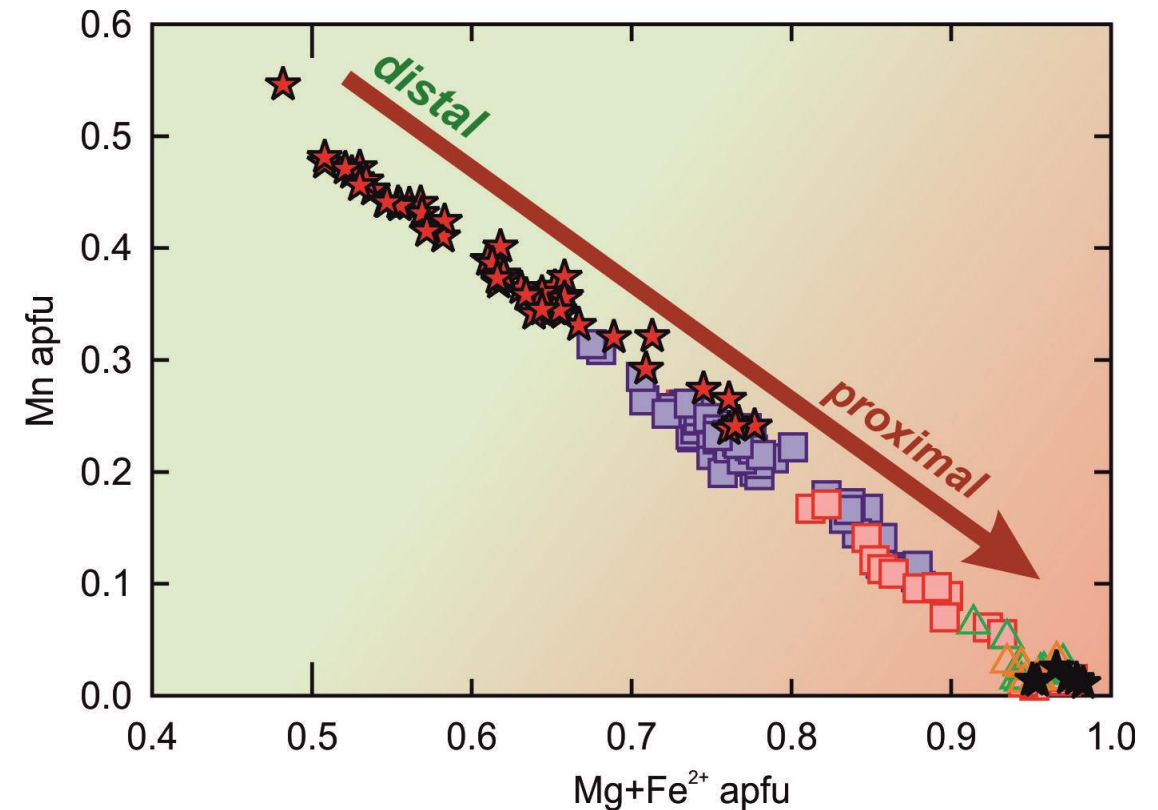
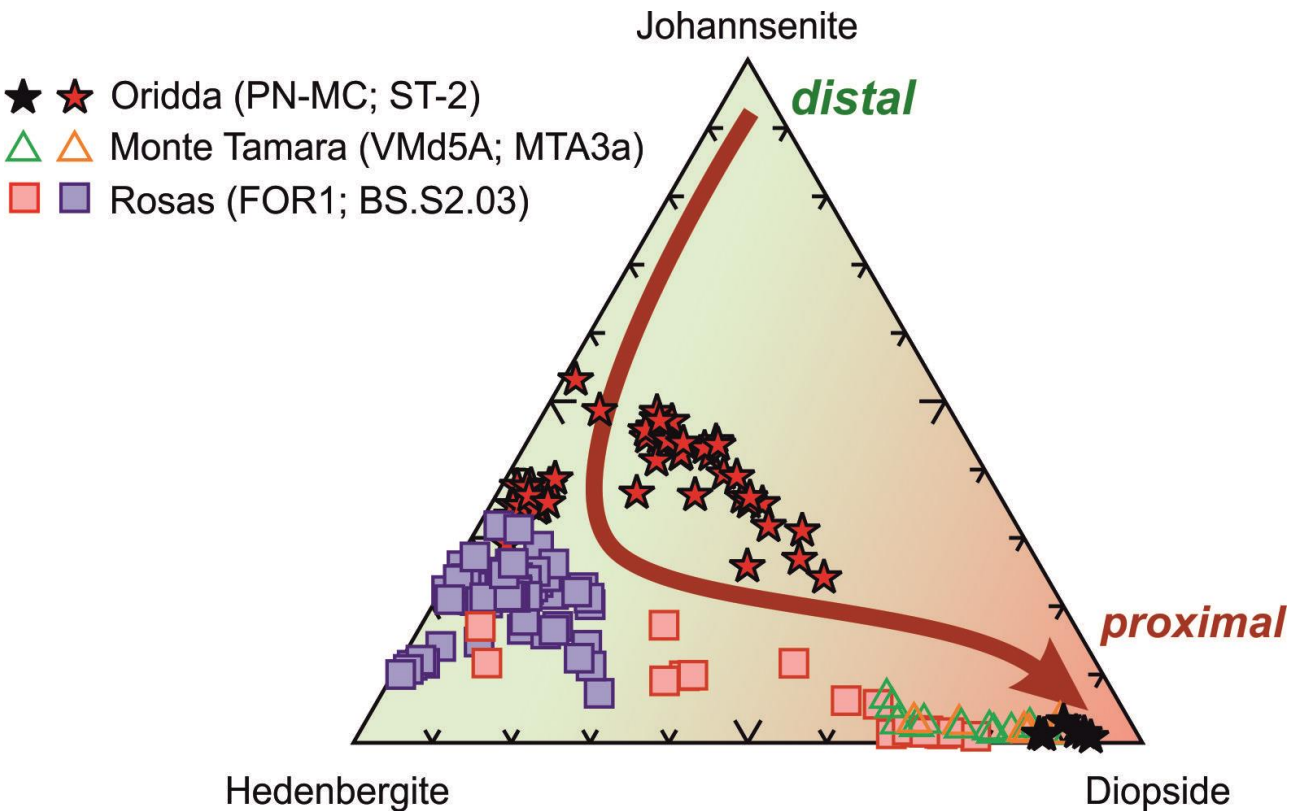
Cocco et al, 2022



Mn-Fe in clinopyroxene

Mn \longrightarrow > Johannsenite ($\text{CaMn}^{2+}\text{Si}_2\text{O}_6$) away from the intrusion (Meinert et al, 2005; Chang, 2019)

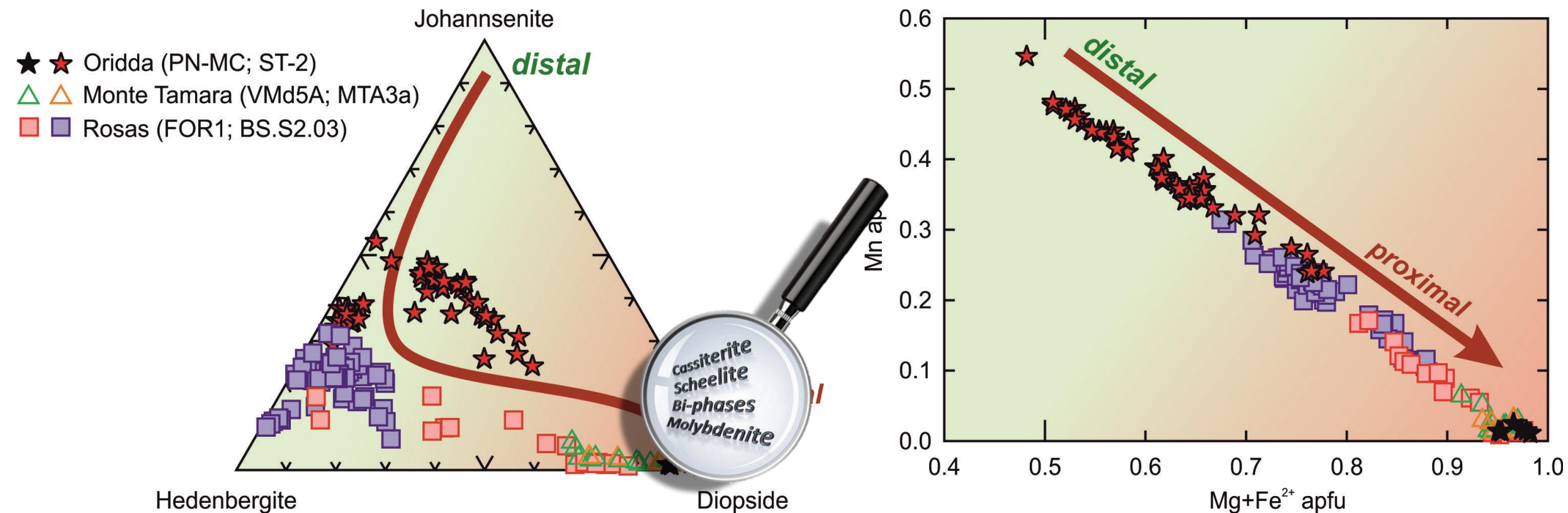
Fe \longrightarrow > Hedenbergite ($\text{CaFe}^{2+}\text{Si}_2\text{O}_6$) at higher distance than diopside ($\text{CaMgSi}_2\text{O}_6$) (Chang, 2019):



Mn-Fe in clinopyroxene

Mn \longrightarrow > Johannsenite ($\text{CaMn}^{2+}\text{Si}_2\text{O}_6$) away from the intrusion (Meinert et al, 2005; Chang, 2019)

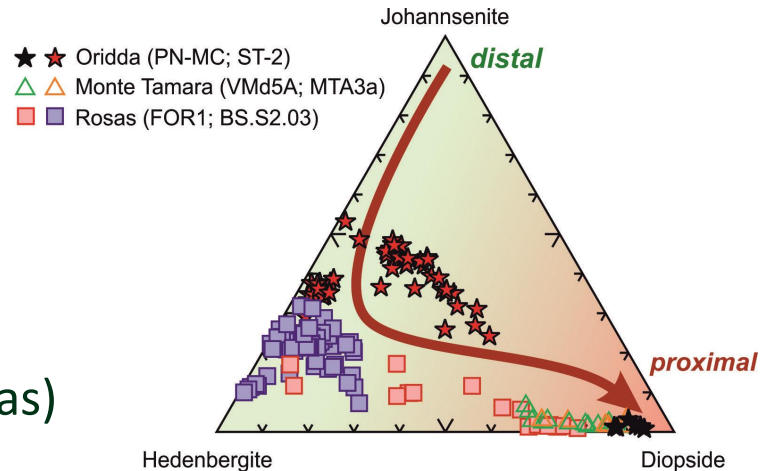
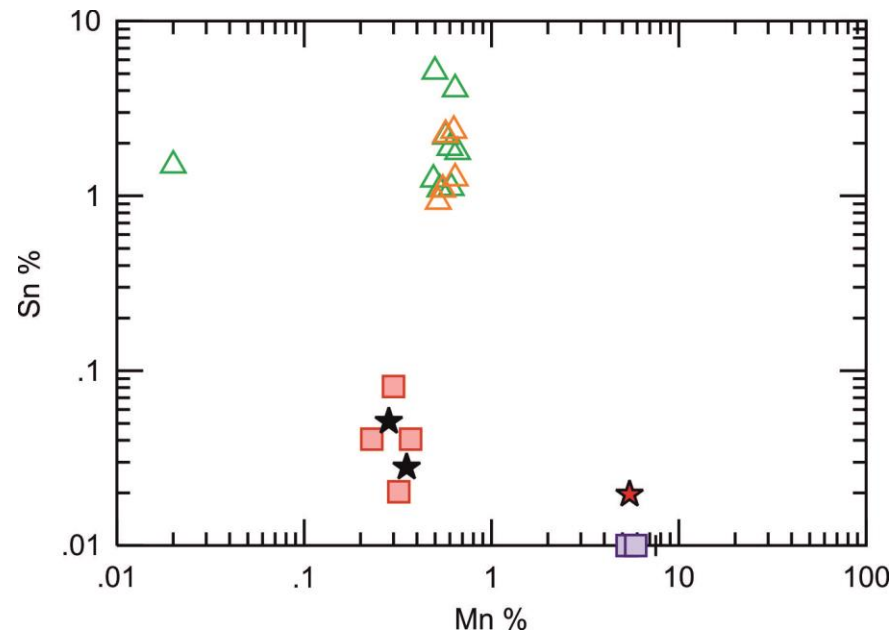
Fe \longrightarrow > Hedenbergite ($\text{CaFe}^{2+}\text{Si}_2\text{O}_6$) at higher distance than diopside ($\text{CaMgSi}_2\text{O}_6$) (Chang, 2019):



Sn and W vs Mn in clinopyroxene

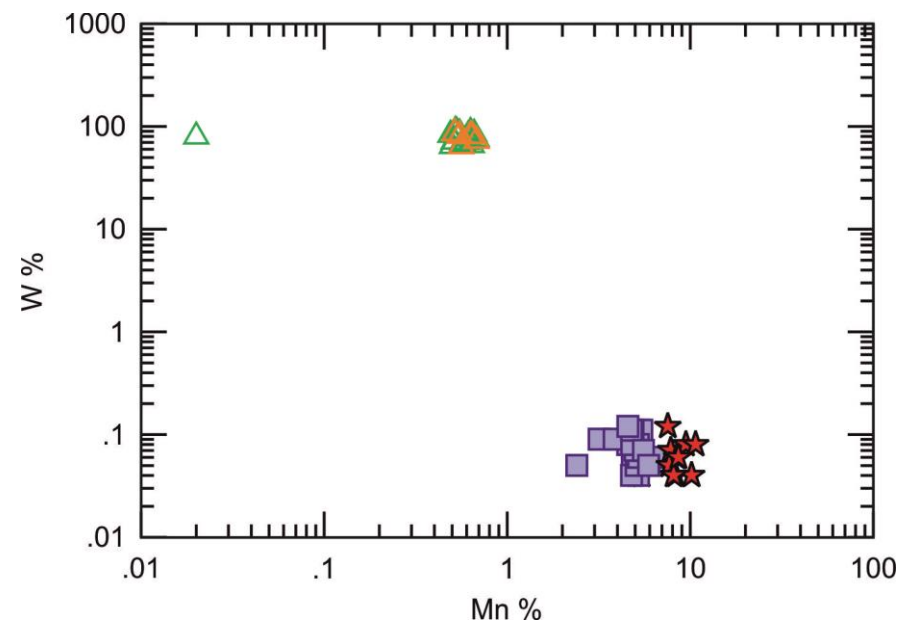
Sn vs Mn

Higher Sn values in most proximal,
Mn-poor clinopyroxene
(Monte Tamara and Perda Niedda-Rosas)



W vs Mn

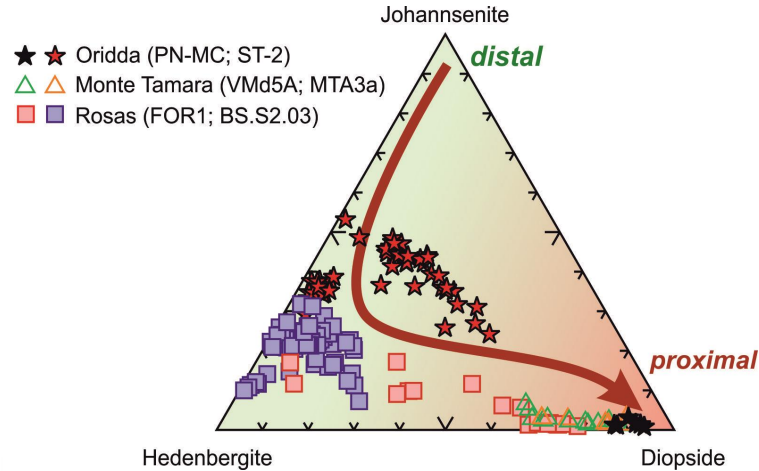
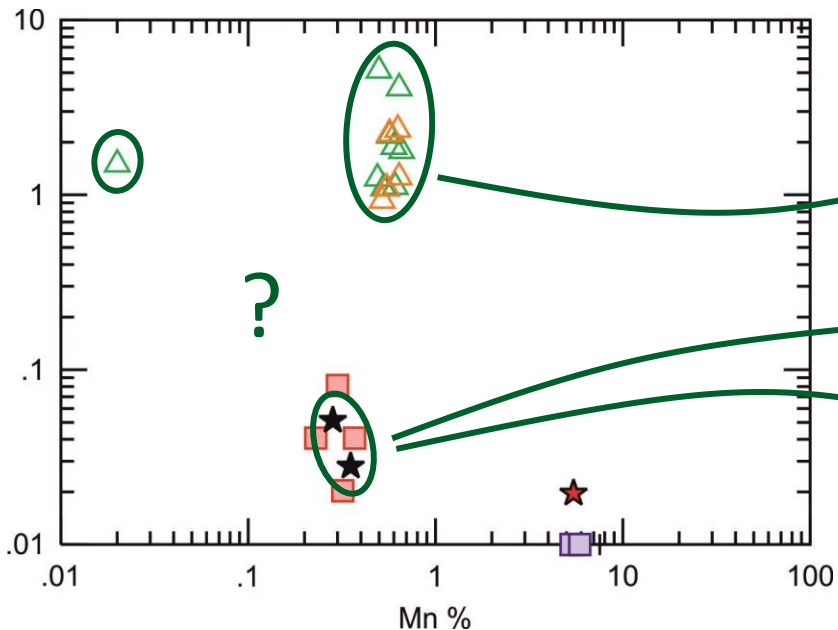
Highest W values in W-bearing
skarns (Monte Tamara),
independent from distality



Sn and W vs Mn in clinopyroxene

Sn vs Mn

Why such a difference between Monte Tamara and Perda Niedda?

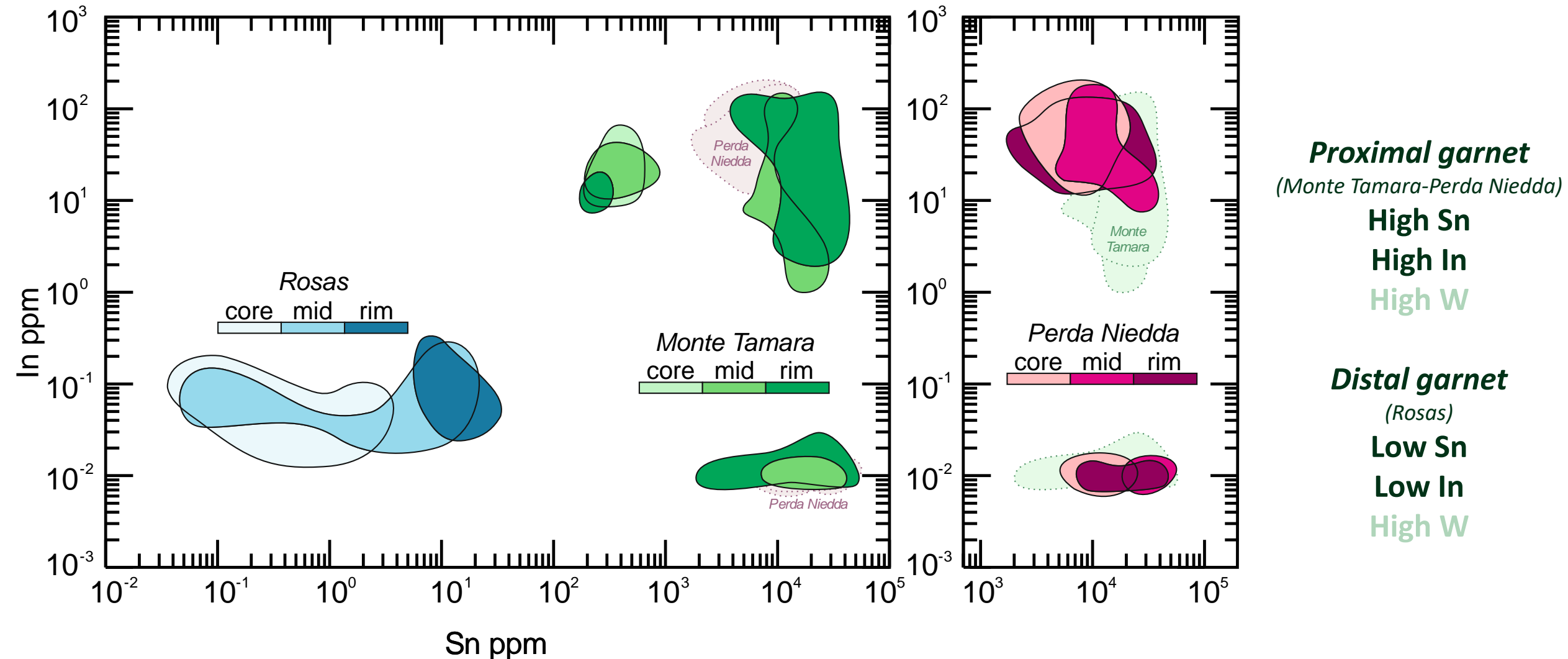


Good timing?
Nano-inclusions?

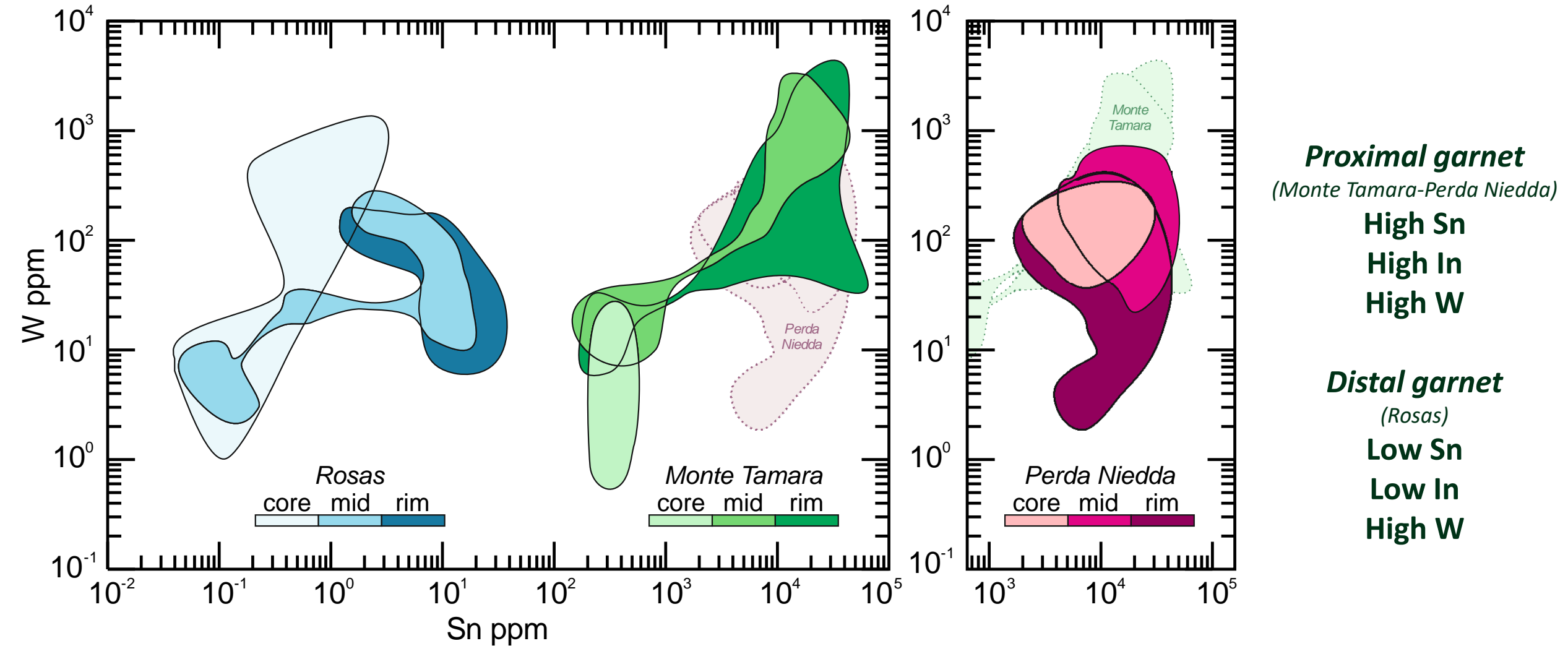
Short timing? Sn input from the fluids after clinopyroxene formation

Bad timing? Most Sn already incorporated in garnet lattice

Tin, indium and tungsten in garnet

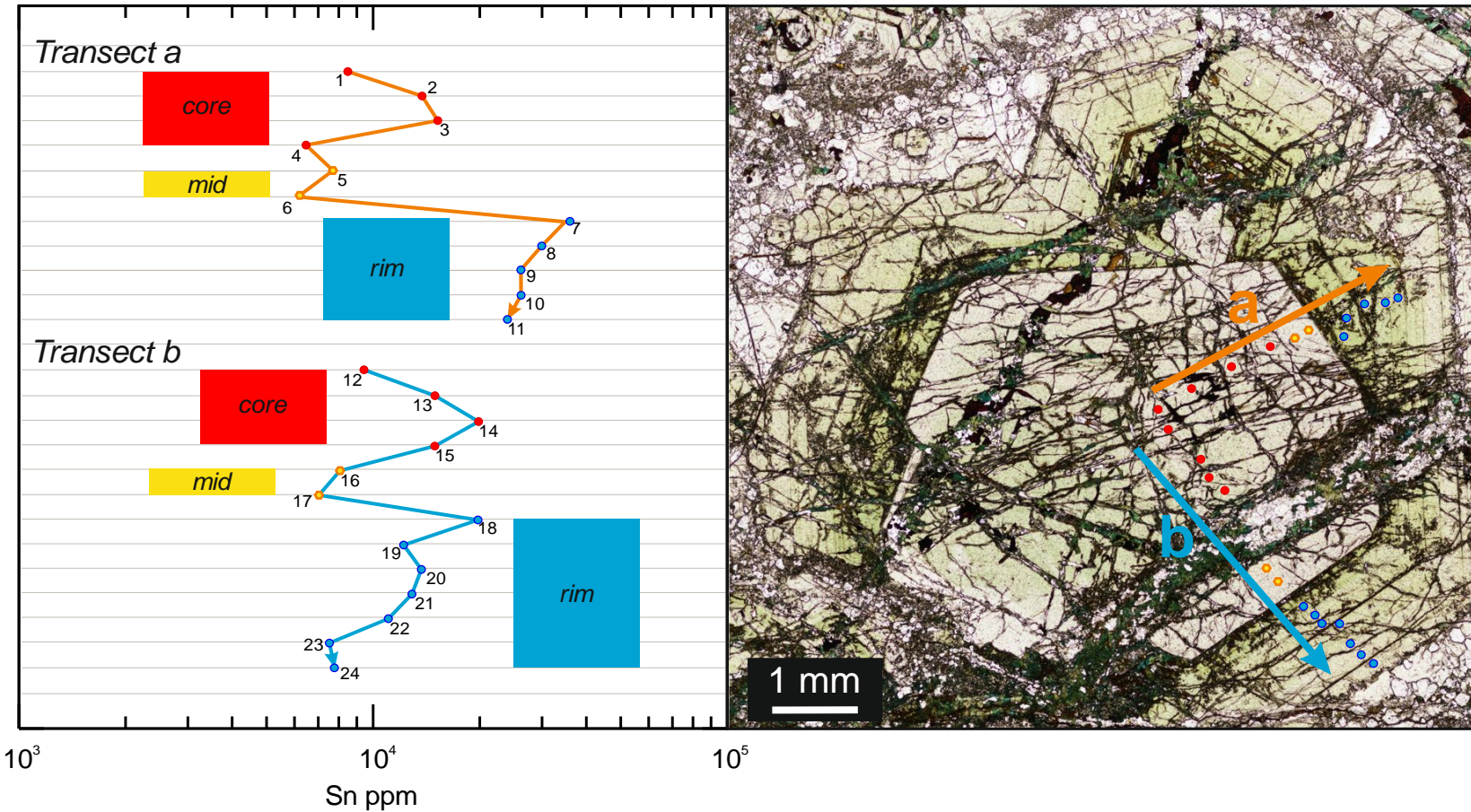


Tin, indium and tungsten in garnet



Tin distribution in garnet (Perda Niedda)

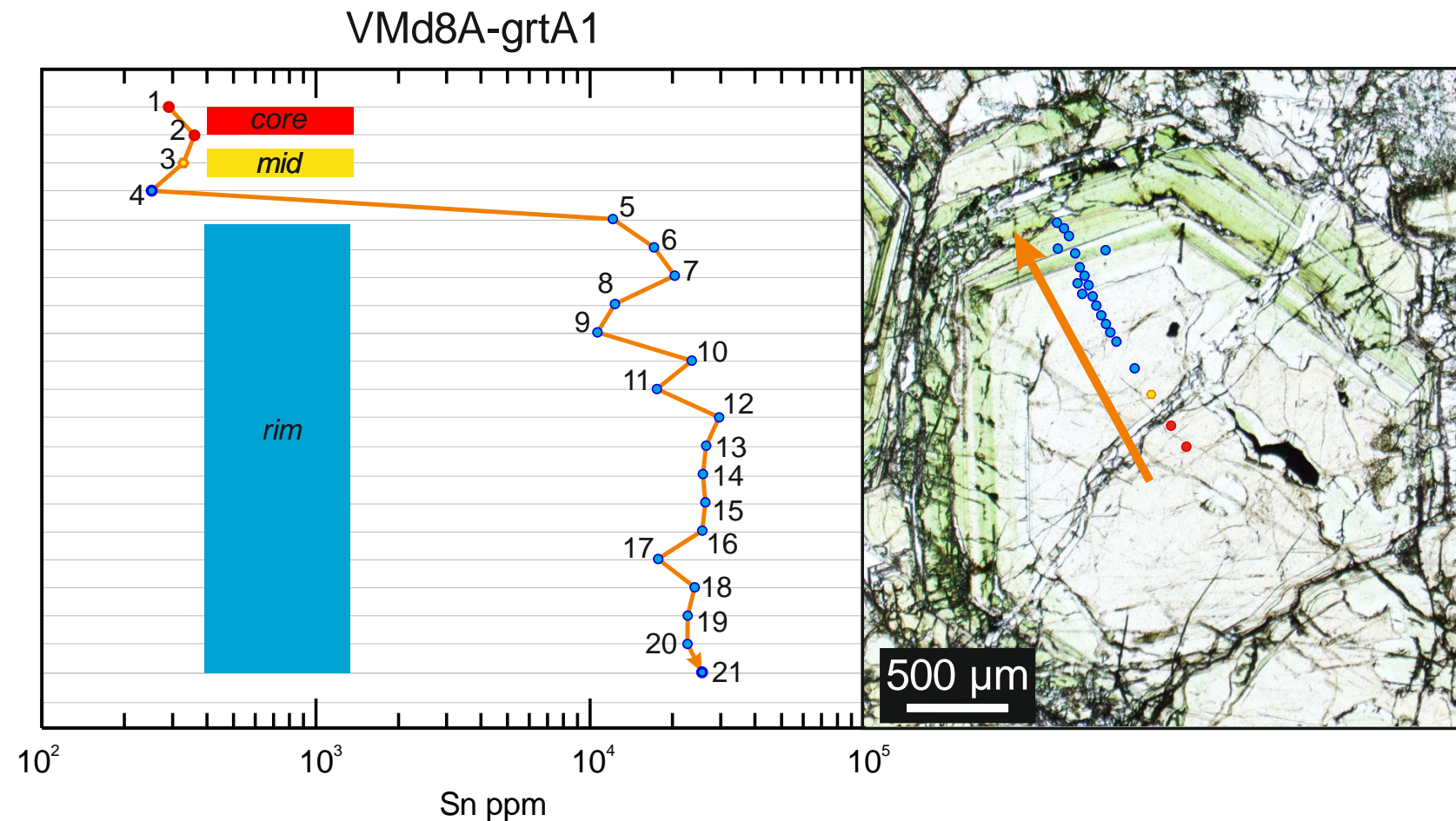
PN7-grtA2



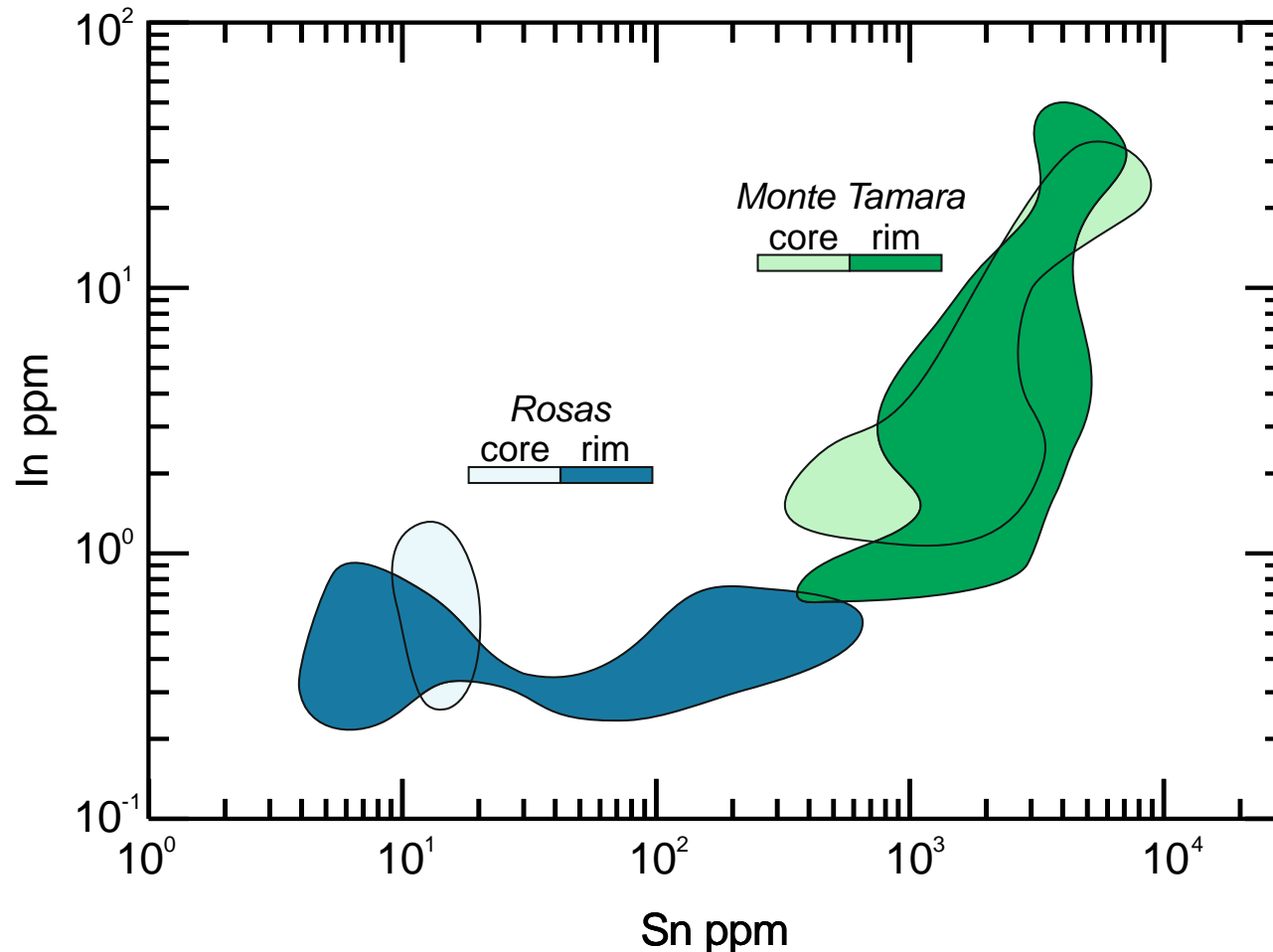
- Sn-rich cores
- Sn-rich mids and rims
- Polyphase
- Potentially > Sn remobilization

Tin distribution in garnet (Monte Tamara)

- Sn-poor cores
- Sn-rich mid and rims
- Polyphase enrichments
- Potentially < Sn remobilization



Tin and indium in epidote



Proximal deposits (Monte Tamara)

- Sn-rich (300 ppm to 1%)
- Higher In (1-50 ppm)
- No rim-to-core variations (patchy zoning)
- Inherited from retrograde alteration of garnet

Distal deposits (Rosas)

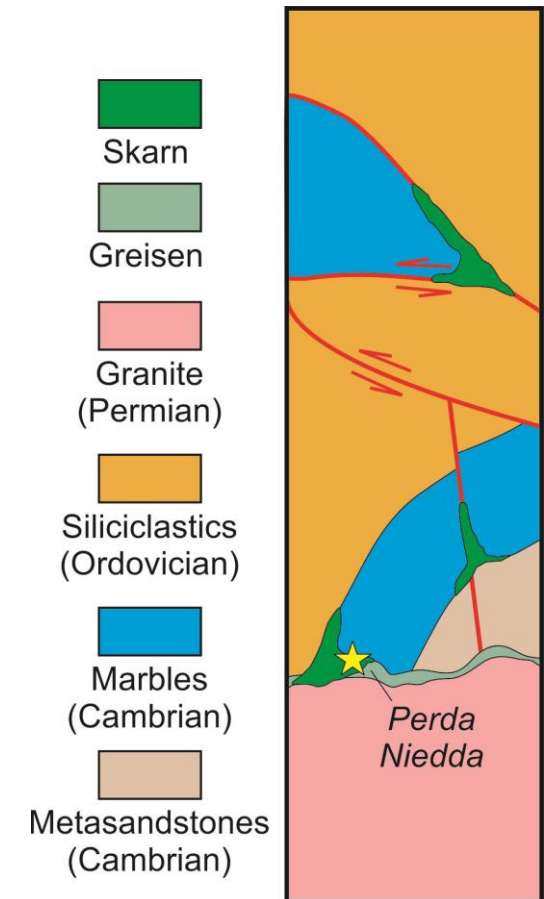
- Moderate Sn-enrichment (up to 600 ppm)
- Sn-enriched rims
- Low In (up to 1 ppm)
- Negligible inheritance from garnets

Skarn orebodies of SW Sardinia can be considered as parts of a regional-scale metallogenic system.

Within this model...

...Perda Niedda is the most proximal deposit.

- Exposed contact with granites
- Endoskarn-greisenizing evidence
- Cassiterite relatively abundant
- Garnet > clinopyroxene
- Diopsidic clinopyroxene (low-Mn, low-Fe)
- High Sn contents in garnet (core-to-rim)
- Higher In in garnet

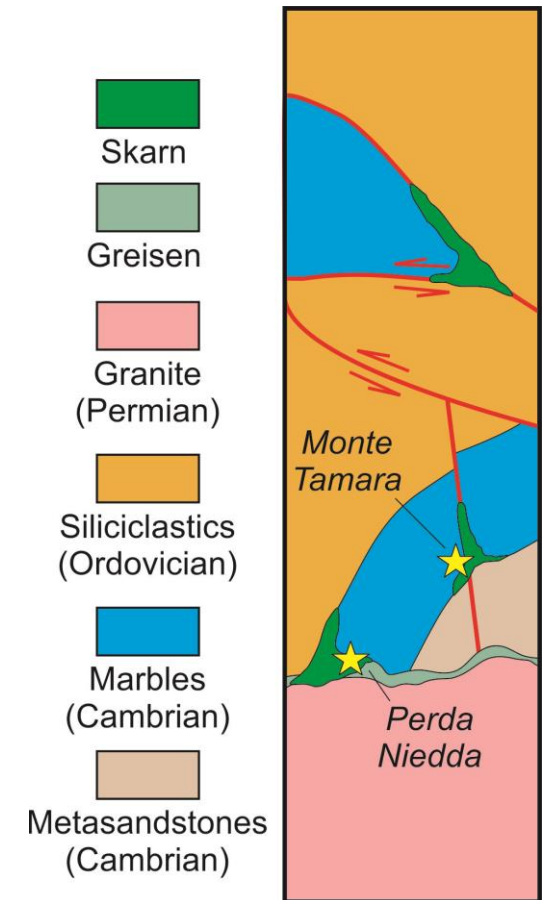


Skarn orebodies of SW Sardinia can be considered as parts of a regional-scale metallogenic system.

Within this model...

...Monte Tamara is also a relatively proximal deposit.

- No evident contact with granites
- Scheelite more common than cassiterite
- Clinopyroxene \geq garnet
- Diopsidic clinopyroxene (low-Mn, low-Fe)
- High Sn and W in clinopyroxene
- High Sn contents in garnet (mid and rim)
- High Sn-In in epidote
- Molybdenite, native Bi and Bi-sulfosalts

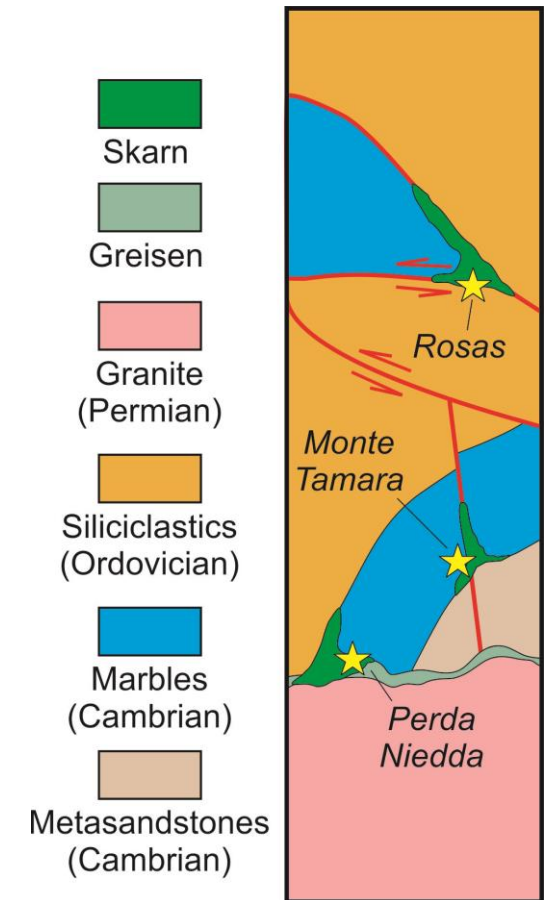


Skarn orebodies of SW Sardinia can be considered as parts of a regional-scale metallogenic system.

Within this model...

...Rosas is a more **distal deposit**.

- Passive structural control
- Extensive metasomatism at larger distance
- Cassiterite is rare
- Scheelite, molybdenite, Bi-phases seemingly absent
- Clinopyroxene > garnet
- Hedenbergite-Johansennite clinopyroxene
- Low Sn contents in garnet
- Lower Sn contents in epidote



Final considerations

- Understanding the **variability of skarn deposits within a modern unitary regional-scale metallogenic system is essential.**



Final considerations

- Understanding the **variability of skarn deposits within a modern unitary regional-scale metallogenic system is essential.**
- In this view, **the Oridda, Monte Tamara and Rosas skarns represent the first terms of comparison for future studies.**



Final considerations

- Understanding the **variability of skarn deposits within a modern unitary regional-scale metallogenic system is essential.**
 - In this view, **the Oridda, Monte Tamara and Rosas skarns represent the first terms of comparison for future studies.**
- The same approach **could be applied to the several skarn orebodies of SW Sardinia associated with the same intrusive suite, protolith and calcsilicate assemblages.**



Final considerations

- Understanding the **variability of skarn deposits within a modern unitary regional-scale metallogenic system is essential.**
 - In this view, **the Oridda, Monte Tamara and Rosas skarns represent the first terms of comparison for future studies.**
- The same approach **could be applied to the several skarn orebodies of SW Sardinia associated with the same intrusive suite, protolith and calcsilicate assemblages.**
 - **Further Sn-W (and possibly Bi-In-Mo) mineral exploration in SW Sardinia could provide interesting results**





Thanks for your attention!



Paragenetical sequences

Perda Niedda

| | STAGE I Prograde | STAGE II Retrograde/sulfide | STAGE III Late stage |
|---------------|---------------------|--------------------------------|-------------------------|
| garnet | ██████████ | | |
| clinopyroxene | | | |
| wollastonite | ██ | | |
| amphibole | | ██████████ | |
| fluorite | | ██████████ | |
| chlorite | | ██████████ | |
| quartz | | ██████████ | |
| epidote | | | |
| calcite | | | |
| talc | | | ██████████ |
| magnetite | ██████████ | | |
| cassiterite | ██ | ██ | |
| pyrrhotite | ██ | ██ | |
| löllingite | ██ | ██ | |
| sphalerite | | ██████████ | |
| arsenopyrite | | | |
| chalcopyrite | | ██████████ | |
| galena | | ██ | ██ |
| hematite | | ██ | ██ |
| pyrite | | ██████████ | |

Monte Tamara

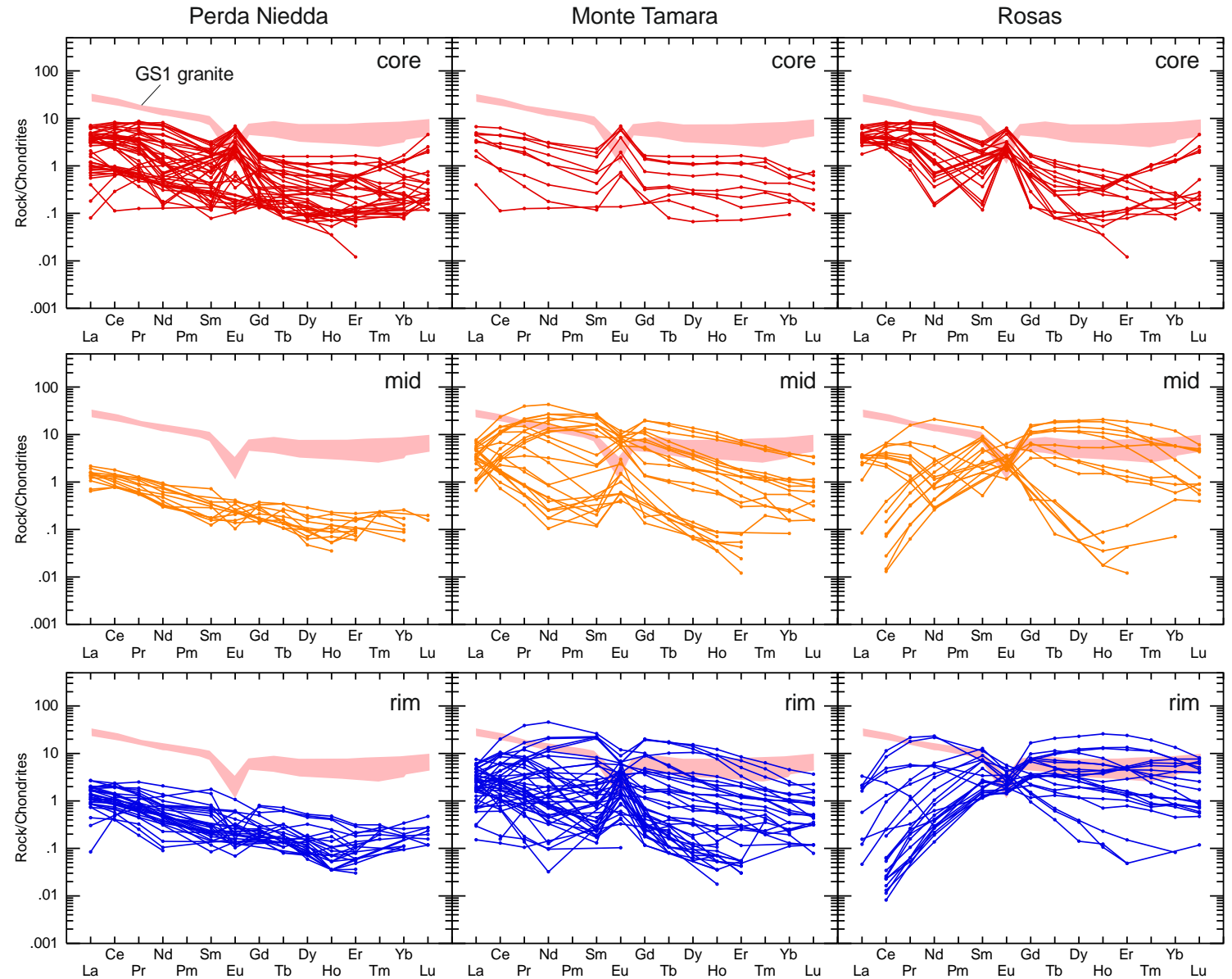
| | STAGE I Prograde | STAGE II Retrograde/sulfide |
|---------------|---------------------|--------------------------------|
| wollastonite | ██████████ | |
| clinopyroxene | ██████████ | |
| garnet | ██████████ | |
| amphibole | | ██████████ |
| epidote | | ██████████ |
| calcite | | ██████████ |
| quartz | | ██████████ |
| chlorite | | ██████████ |
| scheelite | ██ | |
| hematite | ██ | |
| magnetite | | ██ |
| cassiterite | | ██ |
| native Bi | | ██ |
| chalcopyrite | | ██████████ |
| sphalerite | | ██████████ |
| arsenopyrite | | ██████████ |
| pyrrhotite | | ██ |
| Bi-sulfosalts | | ██ |
| molybdenite | | ██ |
| stannite | | ██ |
| pyrite | | ██████████ |
| galena | | ██████████ |
| marcasite | | ██████████ |

Rosas

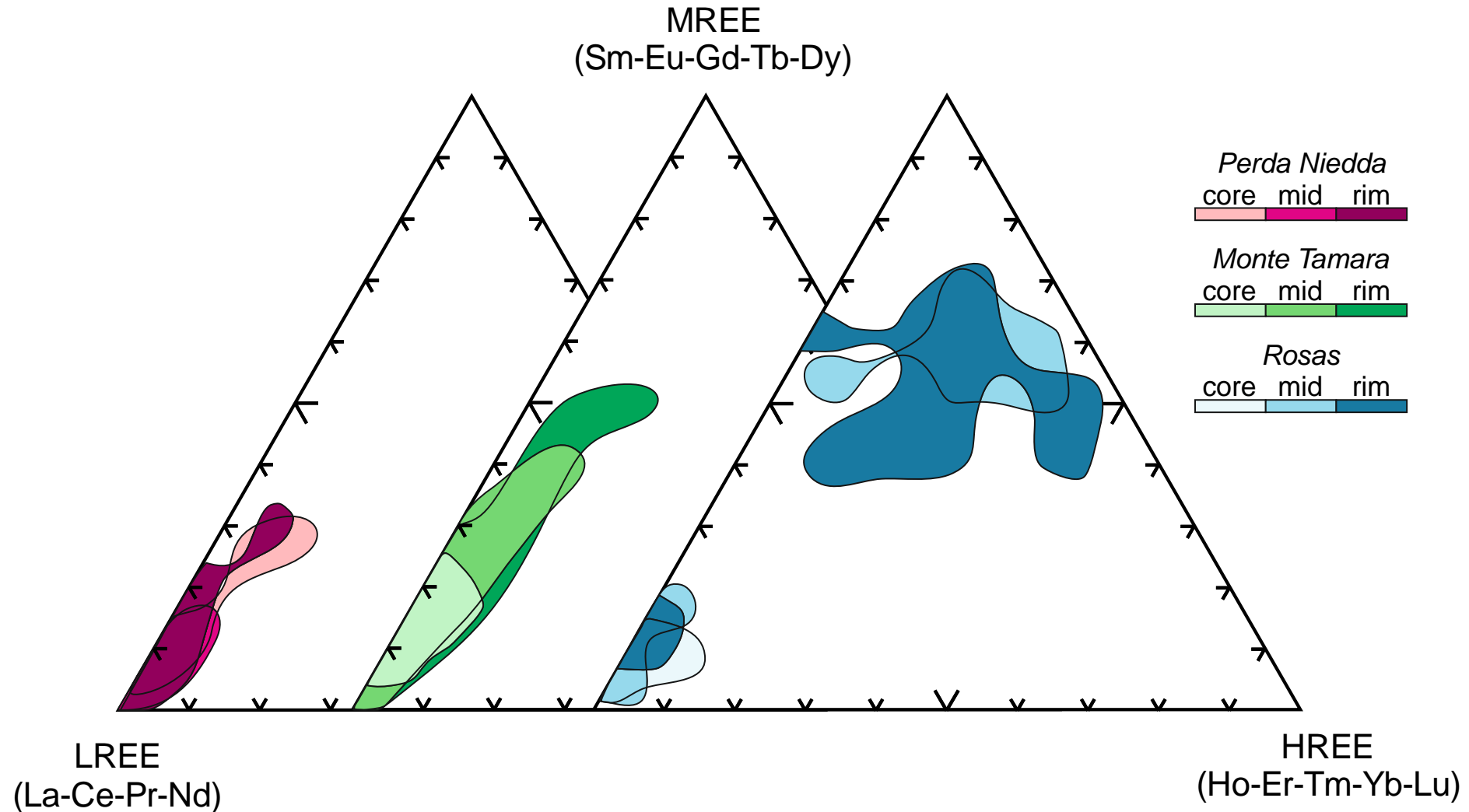
| | STAGE I Prograde | STAGE II Retrograde/sulfide | STAGE III Late stage |
|---------------|---------------------|--------------------------------|-------------------------|
| garnet | | | |
| clinopyroxene | ██████████ | | |
| wollastonite | | | |
| amphibole | | ██████████ | |
| epidote | | ██████████ | |
| chlorite | | ██████████ | |
| fluorite | | ██ | |
| quartz | | ██████████ | |
| calcite | | ██████████ | |
| magnetite | | ██ | |
| cassiterite | | ██ | |
| sphalerite | | ██████████ | |
| chalcopyrite | | ██████████ | |
| galena | | ██ | |
| pyrite | | ██ | |
| tetrahedrite | | ██ | |
| gold | | ██ | |
| bornite | | | ██ |
| covellite | | | ██████████ |
| Ag-sulfides | | | ██████████ |



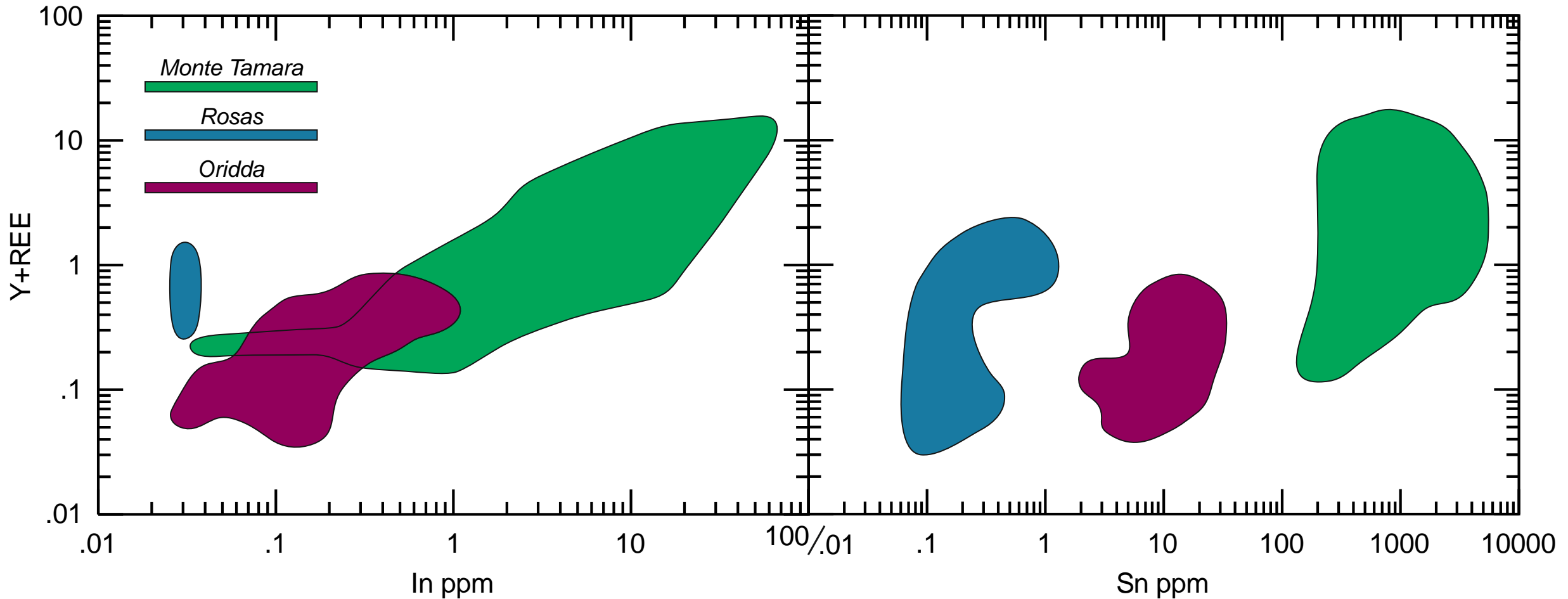
REE in garnet



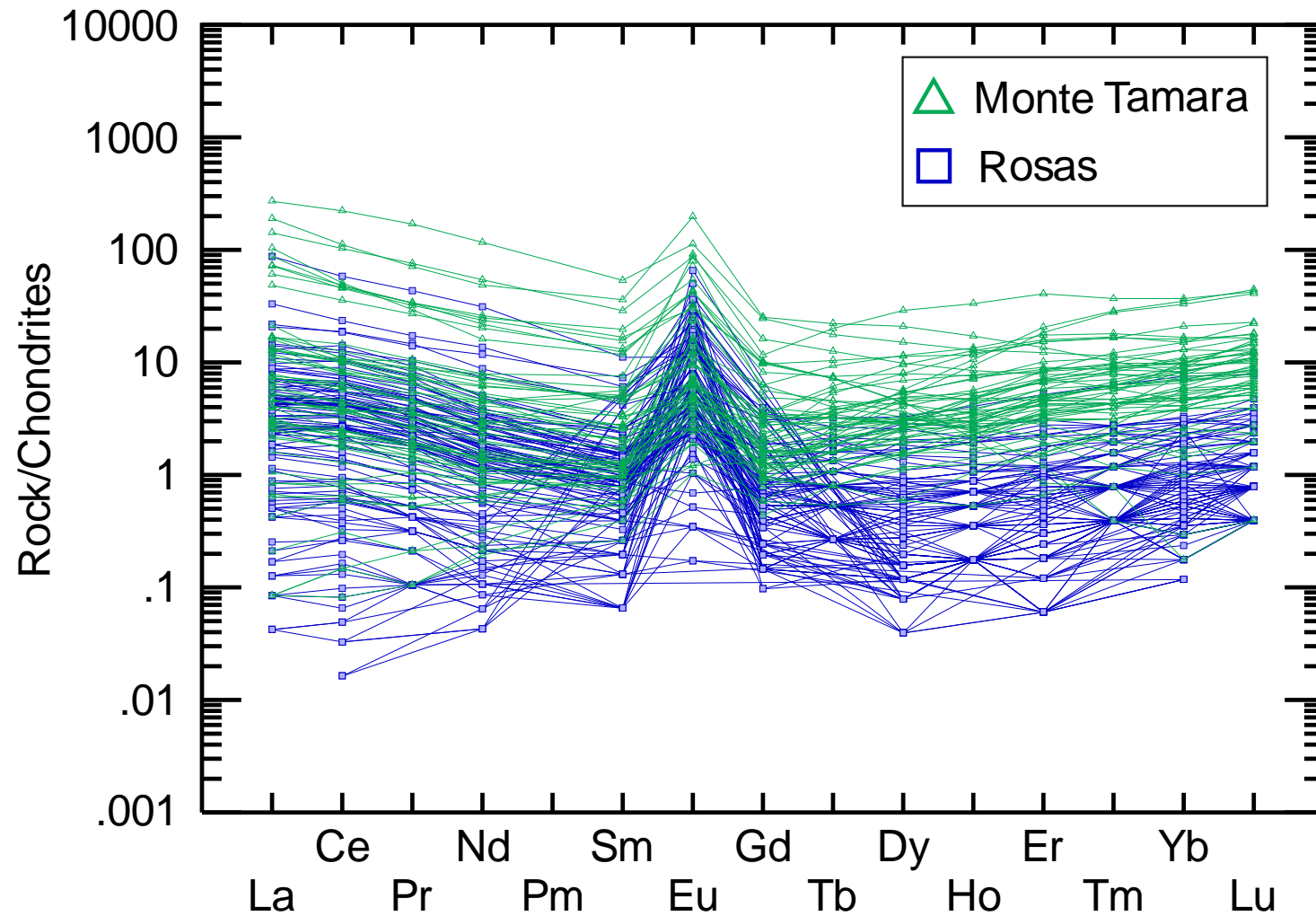
LREE-MREE-HREE distribution in garnet



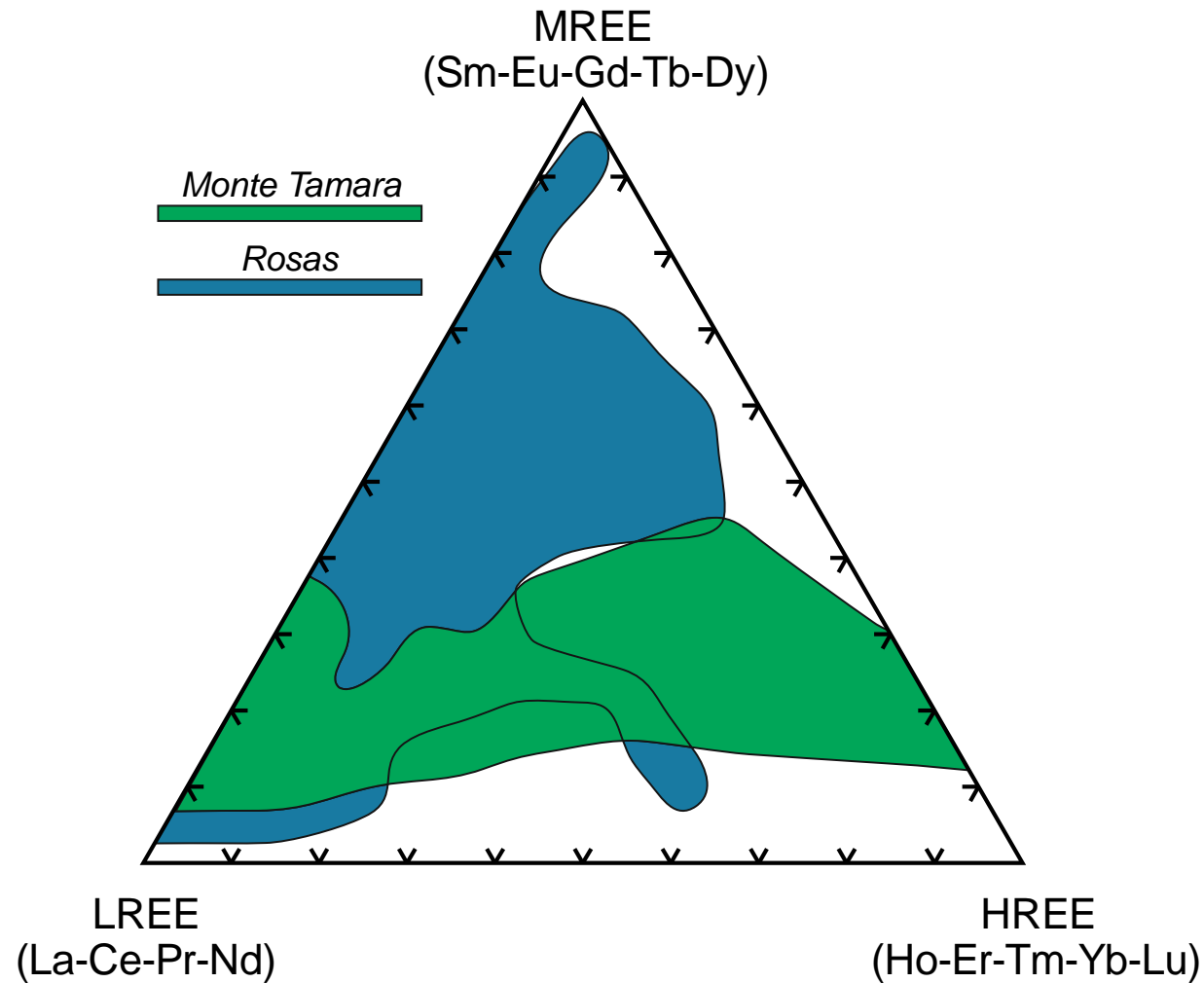
REE+Y vs In and Sn in clinopyroxene



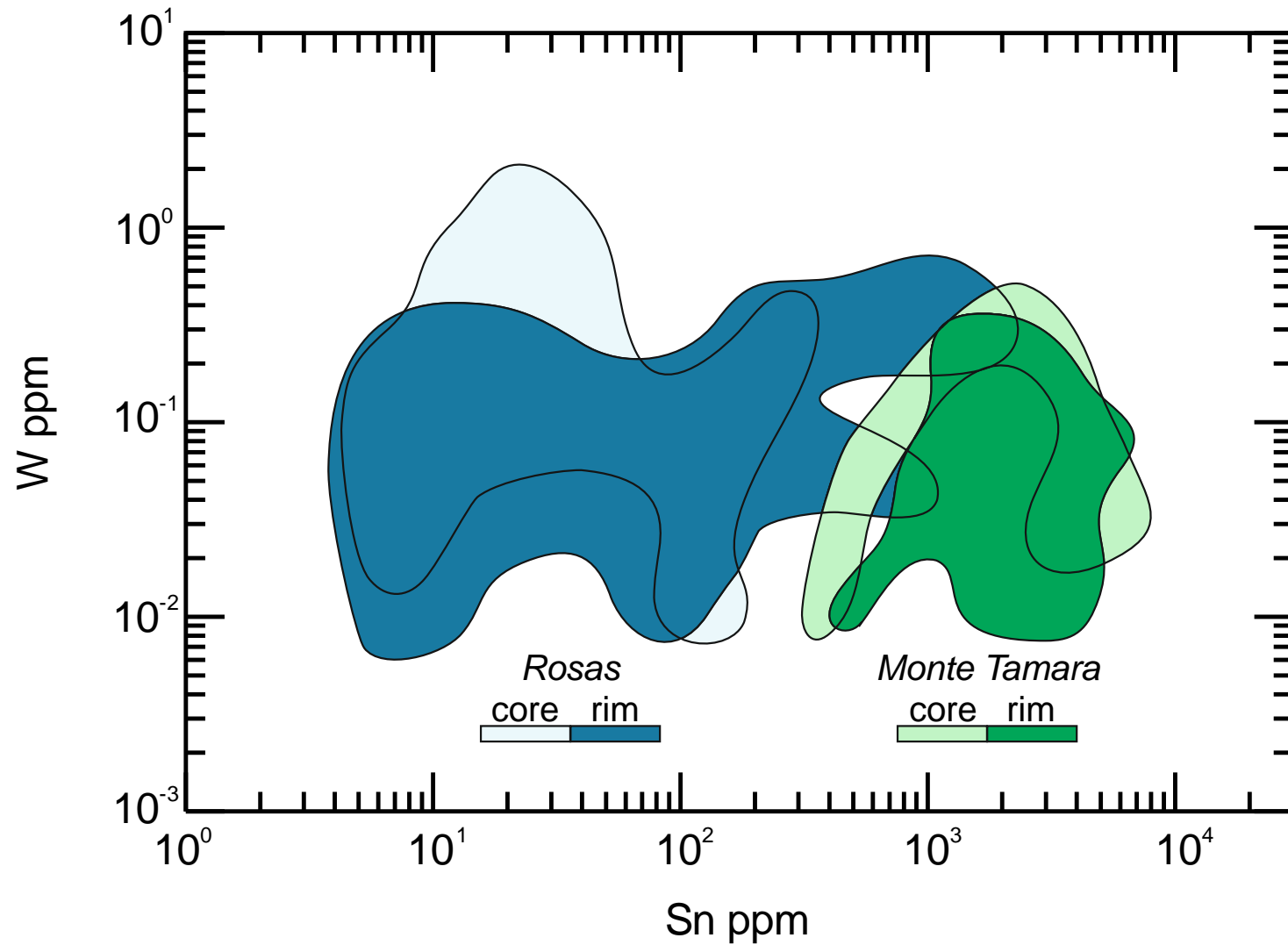
REE in epidote



LREE-MREE-HREE distribution in epidote



Sn and W in epidote



Conclusions

The present PhD project successfully accomplished the aim of obtaining more knowledge regarding the CRM mineralization in skarn deposits of Sardinia. Given the limited number of modern studies on ore deposits of Sardinia, among which skarns have rarely been considered worth studying, this work could be considered as a starting point in setting the ground for other investigations on the same topic.

As a first consideration, in line with the directives of the European Commission, this research testified the presence in skarns and other granite-related mineralization of CRM, like W, Sn and Bi. Moreover, the occurrence of traces of potentially interesting elements like Ge, In and Te were documented here for the first time, therefore expanding the set of CRM associated with the causative GS1 intrusive unit.

In more than one case, this project enlightened the potentialities of Sardinian skarn ore deposits as significant case studies. This consideration does not merely apply to skarns but to the many ore deposit types occurring in the region, all of which have many shady areas to be further investigated and could serve as reference points to scientific researchers worldwide. Lastly, this project tried to offer a detailed characterization of field relationships, mineral assemblages, chemical features of skarn ores with the goal of understanding and model the mechanisms of formation of such complex deposits. With this purpose, the study provided several useful indications which could be crucial for future W-Sn-Bi and possibly Ge-In mineral explorations on skarn deposits.

Acknowledgments

“Matteo Deidda gratefully acknowledges the Sardinian Regional Government for the financial support of her/his PhD scholarship (P.O.R. Sardegna F.S.E. - Operational Programme of the Autonomous Region of Sardinia, European Social Fund 2014-2020 - Axis III Education and training, Thematic goal 10, Investment Priority 10ii), Specific goal 10.5”.



